THE UNIVERSITY of ADELAIDE

Quantifying the Compressive Ductility of Concrete in RC Members through Shear Friction Mechanics

Yongjian Chen

B.E. Civil and Structural Engineering (Hons)

A thesis submitted for the degree of doctor of philosophy

Department of Civil, Environment and Mining Engineering

The University of Adelaide, Australia

October 2014

Table of Contents

Abstract

This thesis contains a series of journal papers in which the compressive ductility of concrete in RC members has been quantified through shear friction mechanics.

Firstly, the size dependent stress-strain models for unconfined and actively confined concrete are derived based on the fundamental mechanics of shear friction theory. At this stage, the shear friction properties, that is the relationship between the shear stress, normal stress, crack widening and interface slip across the sliding plane, are not specifically required. It is shown how the stress-strain from cylinder tests of one specific length can be modified to determine that for any size of cylinder. Moreover, it is shown that the proposed approach can be used to make existing generic stress/axial-strain relationships size dependent and these size dependent relationships can be directly used to determine the corresponding size dependent stress/lateral-strain relationship. Being mechanics based, size dependent stress-strain models reduce the reliance on vast experimental testing as only one size of specimen needs be tested to obtain stress-strain relationships for all sizes.

Secondly, the shear friction properties, that is the relationship between the shear stress, normal stress, crack widening and interface slip across the sliding plane is derived and presented in a generic form suitable for application. These generic shear-friction material properties are then used to simulate and quantify the shear-sliding behaviour of initially uncracked concrete generally obtained directly from relatively expensive tests. In addition, it is also shown how these shear-sliding capacities can then be used to quantify the shear capacity of RC beams without stirrups and without the need for size factors as the mechanics based approach automatically, through mechanics, allows for member size.

Thirdly, the generic shear-friction material properties derived in Chapter 3 are used to simulate passive confinement in FRP confined cylinders. Importantly, two distinct cylinder failure modes have been identified and examined: that of the circumferential wedge that is common in standard cylinders with aspect ratios of 2:1; and that of the single sliding plane that occurs at higher aspect ratios. It shows the mechanics solutions for the influence of specimen size, that is both diameter and height, on the stress-strain relationship of axially loaded FRP confined concrete cylindrical specimens and how small scale FRP wrapped specimens suitable for compression testing can be designed so that the stress/strain relationship of the full scale member under pure compression can be extracted from those of the small test specimen.

Finally, a series test of steel tube confined concrete columns is designed to verify the accuracy of the size effect expressions proposed in previous chapters. Importantly, it shows that because the standard material test always adopts small scale 2:1 aspect ratio specimens, the majority failure mode in material test specimens is the circumferential wedge failure. Consequently it is for this wedge failure mode that most axial-stress/global-axial-strain relationships are developed. However, similar to the specimens studied in this test program, the aspect ratio of most practical steel tube confinement columns is more than 2. Hence only in a minority of cases does the circumferential wedge failure occur in practice. Therefore, the empirical or semi-empirical equations developed from small scale concrete specimens are not truly representative of the actual behaviour of full-scale columns which have aspect ratios markedly different from the 2:1 ratio most commonly tested.

Statement of Originality

This work contains no material which has been accepted for the award of any other degree or diploma in any university or any tertiary institution to Yongjian Chen and, to the best of my knowledge and belief, contains no material previously published or written by another person, except where due reference has been made in the text.

I give consent to this copy of my thesis when deposited in the University Library, being made available for load and photocopying, subject to the provisions of the Copyright Act 1968.

The author acknowledges that copyright of published works contained within this thesis (as listed below) resides with the copyright holder(s) of those works.

I also give permission for the digital version of my thesis to be made available on the web, via the University's digital research repository, the Library catalogue, the Australasian Digital Theses Program (ADTP) and also through web search engines, unless permission has been granted by the University to restrict access for a period of time.

…… ……

Yongjian Chen Date

List of Publications

Oehlers, D.J., Visintin, P,. Zhang, T., Chen, Y., and Knight, D. (2012). “Flexural Rigidity of Reinforced Concrete Members Using a Deformation Based Analysis.” Concrete in Australia, 38(4), 50-56.

Chen, Y., Visintin, P., Oehlers, D.J., and Alengaram, U. (2014). “Size dependent stress-strain model for unconfined concrete.” Journal of Structural Engineering, 140(4), 10.1061/(ASCE)ST.1943-541X.0000869.

Visintin, P., Chen, Y., and Oehlers, D.J. (2014). “Size dependent axial and lateral stress strain relationships for actively confined concrete.” Accepted for publication by Advances in Structural Engineering on 05/06/2014.

Chen, Y., Visintin, P., and Oehlers, D.J. (2014). “Concrete shear-friction material properties: derivation from actively confined compression cylinder tests.” Submitted to Advances in Structural Engineering on 26/03/2014.

Chen, Y., Zhang, T., Visintin, P., and Oehlers, D.J. (2014). “Concrete shear-friction material properties: application to shear capacity of RC beams of all sizes.” Submitted to Advances in Structural Engineering on 26/03/2014.

Visintin, P., Chen, Y., and Oehlers, D.J. (2014). “Simulating the behaviour of FRP confined cylinders using the shear friction mechanism.” Submitted to ASCE Composites for Construction on 10/10/2014.

Chen, Y., Visintin, P., and Oehlers, D.J. (2014). “Extracting size dependent stress/strain relationships from FRP confined concrete cylinders for varying diameters and heights.” To be submitted to Composite Structures.

Chen, Y., Visintin, P., and Oehlers, D.J. (2014). “Test of Steel tube confined concrete columns.” Text in Manuscript.

Acknowledgements

Firstly, my sincerest thanks go to Emeritus Professor Deric Oehlers and Dr Phillip Visintin; this thesis could not have been achieved without their special knowledge and patient supervision. I would also like to thank Associate Professor Hamid Sheikh and Dr Matthew Haskett for their input and guidance.

Secondly, special thanks goes to Sherry, Gateway, Apd, Mike, Zuo, Rob, Marj, Steve, John and James. You are nice Australians who gave me such a kind and important helping hand when I was almost lost in this new country.

Finally, dedicated thanks and love go to my father, my mother, my wife, and my child who so desired for me the Dr title, sometimes even more than I did. You are always the whole world for me.

Introduction and General Overview

The axial-stress/axial-strain behaviour of concrete under compression is crucial in determining both the strength and ductility of reinforced concrete members. In this thesis, it is shown that concrete deformation due to compression is both a material property and a shear-friction mechanism and that by taking into account both of these deformations a size dependent stress-strain relationship can be derived.

This thesis contains a collection of manuscripts published, accepted or submitted to internationally recognised journals. Each of the chapters 1 to 4, which are titled according to the research objective, contain: an introduction explaining the aim of the chapter and how the work fits into the overall objective; a list of manuscripts contained within the chapter; and finally the presentation of each manuscript.

Chapter 1 introduces the fundamental mechanisms of the developed segmental deformation approach for the generic analysis of reinforced concrete (RC) beams incorporating: a size-dependent stress-strain model to simulate the concrete wedge formation associated with concrete softening; and residual strain partial-interaction (PI) theory to directly simulate the effects of tension-stiffening as the internal bonded reinforcement pulls from the crack face. This background paper shows the overall project of our research group of which this thesis mainly focuses on the analysis of size-dependent stress-strain models.

Chapter 2 contains two journal papers which use the mechanics of shear friction theory to simulate the formation and displacement of sliding planes as concrete softens and then derives size dependent stress-strain models. The first paper extracts size dependent strains at the peak stress from 380 published tests on unconfined concrete and then uses it in existing curve fitting models to produce size dependent stress-strain models for unconfined concrete. The second paper has reanalysed 692 published test results on confined concrete to provide size dependent stress/strain relationships for both axial and dilatory strains in both the ascending and falling branches and for a wide range of confinements. The new approach in these two papers considerably reduces the amount of testing required for new concretes as only one size of specimen is required to be tested for obtaining stress-strain relationships for all sizes.

Chapter 3 focuses on the shear-friction material properties across potential sliding planes, that is the relationship between the shear stress, normal stress, crack widening and interface slip across an initially uncracked concrete sliding plane. It shows how the shear-friction material properties can be quantified from relatively readily available and inexpensive compression tests, and then presented in a generic form which is directly applicable for the papers in Chapter 4.

Chapter 4 consists of three papers that show the applications of shear friction properties proposed in Chapter 3. The first paper shows how these shear-friction material properties can be used directly to quantify the shear-sliding capacity and also how these shear-friction material properties can also be used to analyse standard shear-sliding tests in order to extract more accurate shear-sliding capacities. It is then shown how these shear-sliding capacities can be used as the failure criteria to quantify the shear capacities of reinforced concrete beams. The main aim of the first paper is to show that the use of mechanics and shear-friction material properties can not only quantify apparently diverse behaviours such as the shear capacity and flexural ductility but also reduce the cost of developing new RC

products and in developing more accurate and less conservative design rules. In the second paper, two distinct cylinder failure modes have been examined: that of the circumferential wedge that is common in standard cylinders with aspect ratios of 2:1; and that of the single sliding plane that occurs at higher aspect ratios. Importantly, from this is shown that although each mechanism is defined by the same shear friction material properties different stress strain relationships result and this may explain some of the scatter of test results. In the third paper, mechanics solutions have been developed to show the influence of specimen size, that is both diameter and height, on the stress-strain relationship of axially loaded FRP confined concrete cylindrical specimens using shear friction theory. Due to the capacities of the testing machines, it is often quite difficult to test large or full-scale FRP wrapped specimens under pure compression in order to extract their axial-stress/axial-strain relationships. The third paper shows that through the mechanics of shear friction, how small scale FRP wrapped specimens suitable for compression testing can be designed so that the stress/strain relationship of the full scale member under pure compression can be extracted from those of the small test specimen.

Chapter 5 is the experimental work for steel tube confined concrete of which the test data can be used to verify the axial and lateral size expressions proposed in Chapters 2 and 4 respectively. It also shows that the proposed expression of the sliding angle α that is dependent on the confinement stress and proposed in Chapter 2 of this thesis has a very good correlation with the experimental results. Importantly, as the standard material test always adopts small scale 2:1 aspect ratio specimens, the majority of the failure modes in material test specimens is the circumferential wedge failure and from which most axial-stress/global-axial-strain relationships are developed. However, similar to the specimens studied in this test program, the aspect ratio of most practical steel tube confinement columns is more than 2, so only in a minority of cases does the circumferential wedge failure occur. Therefore, the empirical or semi-empirical equations developed from small scale concrete specimens are not truly representative of the actual behaviour of full-scale columns which have aspect ratios markedly different from the 2:1 ratio most commonly tested.

Chapter 6 shows the concluding remarks of this research. The applications of size dependent models and shear-friction material properties for passively confined RC members provides a novel technique in simulating what is actually observed in practice. The generic approach proposed in this thesis can easily be repeated and updated by following researchers for new types of concrete.

Chapter 1: Background

Introduction

Chapter 1 presents the first manuscript “Flexural rigidity of reinforced concrete members using a deformation based analysis” which provides a background to the existing research in the area and highlights the overall need for this research. The fundamental mechanisms which form the basis of this research for the remainder of the thesis which can simulate the mechanisms of tension-stiffening, wedge softening and shear failure. Being mechanics based, it is shown how the approach reduces the reliance on vast experimental testing and hence can help refine existing design models and help expedite the development of new products.

List of manuscripts

Oehlers, DJ., Visintin, P,. Zhang, T., Chen, Y., and Knight, D. (2012). “Flexural Rigidity of Reinforced Concrete Members Using a Deformation Based Analysis.” Concrete in Australia, 38(4), 50-56.

Statement of Authorship

Flexural Rigidity of Reinforced Concrete Members Using a Deformation Based Analysis. Concrete in Australia 2012, 38(4) 50-56.

Oehlers, DJ

Compiled manuscript and supervised research

I hereby certify that the statement of contribution is accurate and I give permission for the inclusion of the paper in this thesis

Signed……..Date……

Visintin, P

Supervised and contributed to research

I hereby certify that the statement of contribution is accurate and I give permission for the inclusion of the paper in this thesis

Signed……..Date……

Zhang, T

Contributed to research

I hereby certify that the statement of contribution is accurate and I give permission for the inclusion of the paper in this thesis

Signed……..Date……

Chen, Y (Candidate)

Contributed to research

I hereby certify that the statement of contribution is accurate and I give permission for the inclusion of the paper in this thesis

Signed……..Date……

Knight, D

Contributed to research

I hereby certify that the statement of contribution is accurate and I give permission for the inclusion of the paper in this thesis

Signed……..Date……

Flexural Rigidity of Reinforced Concrete Members Using a Deformation Based Analysis

D. J. Oehlers, P. Visintin, T. Zhang, Y. Chen, and D. Knight

School of Civil and Environmental & Mining Engineering, The University of Adelaide

Abstract: The flexural rigidity (EI) of a member section is intrinsic to structural engineering methods of analysis and design of reinforced concrete (RC). Central to determining EI is the strain based moment-curvature (M-χ) approach. The problem with the M-χ approach is that being strain based it is two-dimensional and, hence, cannot cope directly with the mechanisms that control both tension-stiffening and concrete softening due to wedge-sliding. To overcome this problem, the M-χ approach uses empirically based approximations such as effective EIs or hinge lengths, which, not being mechanics based, are only approximations and can only be used within the bounds of the tests from which they were developed. Consequently they are generally inaccurate, conservative, have limited use and have to be repeatedly determined for new products. This empirical approach has held back the development of new products and the refinement of existing approaches. A deformation based moment-rotation (M-θ) approach is described which being three-dimensional can simulate the mechanisms of tension-stiffening, wedge softening and shear failure. Being mechanics based, it can predict the flexural rigidities, of sections with any type of materials, with any residual strains, and at all stages of loading, for use in the analysis of the member. As this approach requires considerably less testing and is mechanics based, it should help refine existing design models and help expedite the development of new products.

1.0 INTRODUCTION

The flexural analysis and design of RC members is based on the Euler-Bernoulli principle of plane sections remaining plane. The linear strain profile used in the M-χ approach is a corollary of the Euler-Bernoulli principle and is referred to as a strain based approach. Hence to use the M-χ approach all deformations, whether they occur in the materials, or are due to mechanisms, have to be input in the form of strains and stresses.

The flexural behaviour of reinforced concrete flexural members depends on the material properties which are determined experimentally, such as the stress-strain (σ-ε) behaviour of the concrete and reinforcement. However, the flexural behaviour also depends on the partial-interaction mechanism of tension-stiffening (Muhamad et al 2011; Oehlers et al 2011a; Muhamad et al 2012; Knight et al 2012) and the partial-interaction mechanism of wedge sliding which is associated with concrete softening (Visintin et al 2012a; Visintin et al 2012c; Chen et al 2012). While the M-χ approach can cope with variations in the material σ-

ε relationships it cannot cope with the mechanics of tension-stiffening and concrete softening through the formation of wedges (Oehlers 2010; Oehlers et al 2011b; Oehlers et al 2012a). These gaps in the mechanics of the M-χ model are filled in with experimental approximations. Consequently the M-χ approach requires two distinct forms of testing: *material testing* such as the σ-ε material properties which is straightforward; and *mechanics testing* to develop components of the mechanics model such as hinge lengths and effective flexural rigidities. *Material testing* is relatively straightforward and inexpensive. *Mechanics testing* is however very expensive as it has to cover the wide range of parameters associated with RC members and even then the results used in design may have to be highly conservative to cover the large scatter. After the development of the design or analysis model, a separate series of tests is often carried out to validate the model prior to application that is *validation testing*. *Validation testing* is always required as a safeguard and it is neither part of *mechanics testing* nor *material testing*.

Mechanics testing has been a bane for RC developers due to the huge cost, which has subsequently held back the development of RC. The results of *mechanics testing* have been a bane for reinforced concrete structural engineers as they generally lead to very conservative and restrictive designs. In contrast, *mechanics testing* has been a boon to reinforced concrete researchers around the world who have had a field day getting grants to apply old techniques to try to find simple empirical solutions that do not exist (Oehlers 2010; Oehlers et al 2011b; Oehlers et al 2012a). *Mechanics testing* should not be required if the mechanics model truly simulates all aspects of RC behaviour. In this paper a deformation based M-θ mechanics model is described which eliminates the need for *mechanics testing* and consequently has the potential to considerably reduce the cost of development, as well as provide more accurate design solutions with a greater range.

A M-θ displacement based technique (Oehlers et al 2011a; Knight et al 2012; Visintin et al 2012a; Visintin et al 2012c; Chen et al 2012; Oehlers et al 2012a; Mohamed Ali M.S. 2012; Visintin et al 2012b), as opposed to the M-χ strain based technique, is described which goes back to the original Euler-Bernoulli principle of plane sections remaining plane. It is shown that prior to the mechanisms of concrete softening and the occurrence of concrete cracking, the displacement based M-θ and the strain based M-χ approaches give exactly the same results. However after cracking and/or softening, the M-θ approach gives mechanics solutions and, hence, obviates the need for *mechanics testing*. It will also be shown that: the results of the M-θ can be easily converted to variations in moment-curvature (M/χ) and moment-flexural-rigidity (M/EI) which can then be used in the analysis of flexural members at all stages of loading that is at serviceability, ultimate, collapse and cyclic loads (Visintin et al 2012b; Oehlers et al 2012b); that this approach can cope with residual strains at all stages of loading including after cracking and after softening (Knight et al 2012); and, furthermore, can then be used to quantify the shear capacity of flexural members (Lucas et al 2011; Lucas et al 2012) further obviating the need for *mechanics testing* in an area currently even more ridden by the cost of *mechanics testing*.

In this paper, two size-dependent mechanisms, which the M-χ approach cannot deal with directly, are first described: the concrete softening mechanism; and the tension-stiffening mechanism. It is then shown how these size-dependent mechanisms can be included in a size-dependent deformation based analysis to determine, through mechanics, the variation in the sectional properties and, hence, obviate the need for *mechanics testing*. Then to conclude, it is shown how the shear capacity of an RC member can be extracted from a deformation based analysis further obviating the need for *mechanics testing*.

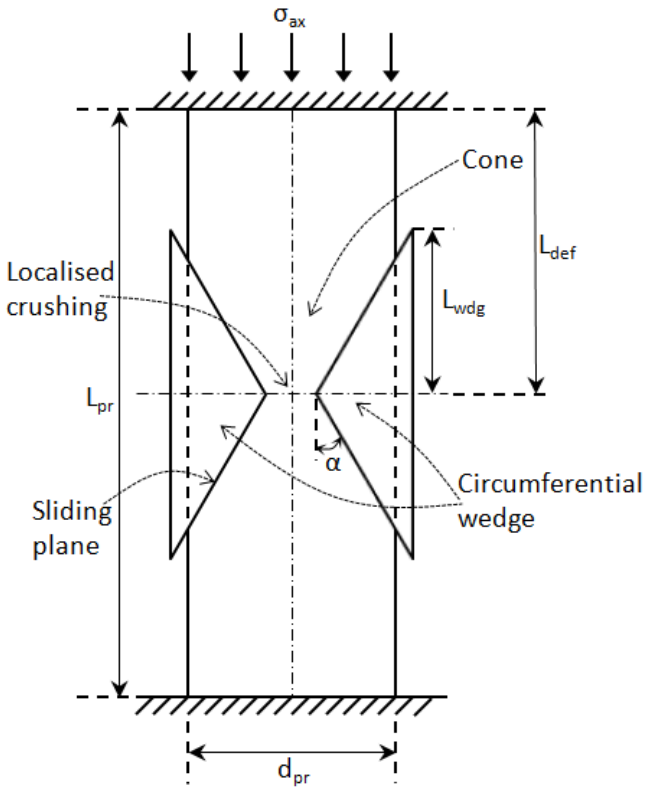

Figure 1. Compression test

2.0 CONCRETE SOFTENING MECHANISM (Chen et al 2012)

A compression test of height L_{pr} and width d_{pr} is subjected to an axial stress σ_{ax} in Figure 1. Because the stresses do not vary along the length L_{pr}, this test resembles the behaviour in a constant moment region in a beam. Softening is associated with slip along sliding planes, forming a wedge at an angle α, which encompasses an inner cone as shown; the occurrence of interface slip means that this is a partial-interaction problem. Strain gauges could be placed well away from the sliding planes in Figure 1 which would then register the material strain ε_{mat} and this could be used to determine the material stress-strain (σ-ε) property. Global strains ε_{gl} could be measured by dividing total contraction over the total length L_{pr} by L_{pr} and this could be used to determine the global σ-ε relationship. As the stresses are increased, the material strains ε_{mat} and global strains ε_{gl} diverge and tests have shown that

this divergence depends on the shape of the specimen L_{pr}/d_{pr} and the length of the specimen L_{pr}.

Consider the deformation of a quadrant of the specimen of length L_{def} as in Figure 2. The natural angle α of the wedge is about 26° which means that the natural angle of the wedge can occur in specimens in which $L_{pr}/d_{pr} \geq 2$ such as in Figure 1 where $L_{def} > L_{wdg}$. The wedge slides a distance Δ in Figure 2 which has an axial component H_{wdg}. From shear-friction theory, the slip Δ depends on both σ_{ax} and α. Hence in specimens in which $L_{pr}/d_{pr} \geq 2$ in which α is constant at 26°, the slip Δ and consequently the axial contraction H_{wdg} only depends on σ_{ax}. Hence the effect of shape L_{pr}/d_{pr} on the stress-strain relationship can be eliminated by ensuring that $L_{pr}/d_{pr} \geq 2$. This leaves the size dependency.

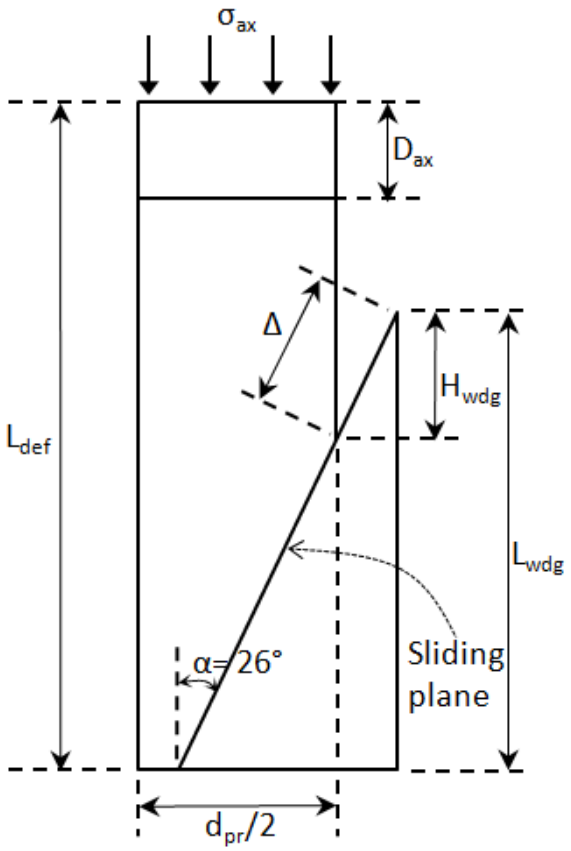

Figure 2. Compression analysis

The contraction of the quadrant D_{ax} in Figure 2 is due to the material contraction $\varepsilon_{mat}L_{def}$ and that due to sliding H_{wdg}. Dividing these contractions by L_{def} gives the global strain as

$$\varepsilon_{gl} = \varepsilon_{mat} + \varepsilon_{wdg} \qquad (1a)$$

where

$$\varepsilon_{wdg} = \frac{H_{wdg}}{L_{def}} \qquad (1b)$$

where H_{wdg}/L_{def} is the effective strain due to wedge sliding ε_{wdg}. The slip Δ, and consequently H_{wdg}, is a shear-friction material property and, therefore, independent of the member size L_{def}. Hence it is the sliding component of contraction in Equation (1) which is size-dependent and if this can be extracted from test results it can be used to derive size-dependent relationships as follows.

Let us assume that the stress-strain relationship in Figure 3 labelled (L_{pr}) is that derived from a specimen in which $L_{pr}/d_{pr} \geq 2$ so that we can assume that ε_{wdg} is only dependent on σ_{ax}. Strain gauges were used to measure the material properties *o-a-b-c* which is shown as linear for convenience but could just as easily be non-linear. Furthermore, the total deformation of the prism was used to derive the global stress-strain relationship *o-a-d-e*. Hence from Equation (1) at stress level σ_n, the material strain is ε_{mat} as shown and the effective strain due to wedge sliding is ε_{wdg} as shown. If the prism length is doubled to $2L_{pr}$ then from Equation (1) the sliding component ε_{wdg} is halved but ε_{mat} stays the same which produces the curve marked ($2L_{pr}$) in which the stress-strain becomes more brittle. Conversely, if the prism length is halved, but the width adjusted if necessary to ensure that $L_{pr}/d_{pr} \geq 2$, then the stress-strain becomes more ductile.

It can be seen in Figure 3 that only one size of specimen needs to be tested to determine the size dependent stress-strain properties which should help reduce the cost of testing. However and much more importantly, it will be shown that these size-dependent stress-strain material properties can then be used in a size dependent analysis to quantify sectional properties for use in member analyses and eliminate *mechanics testing*.

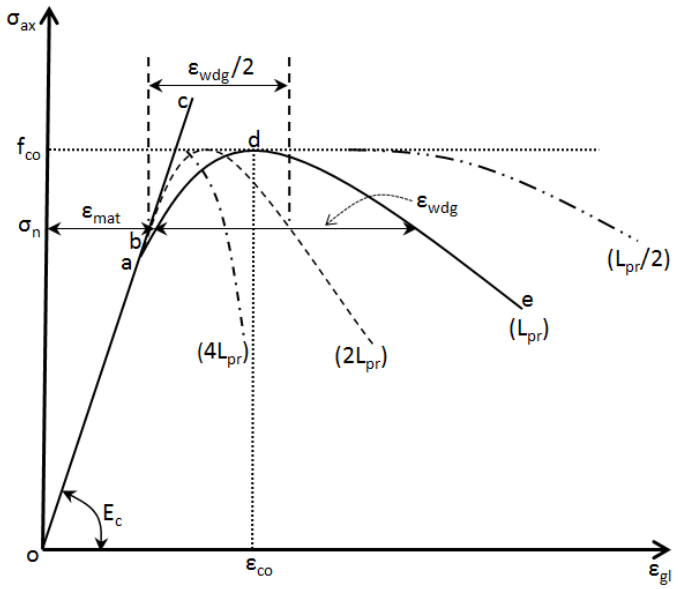

Figure 3. Size dependent σ-ε

3.0 TENSION STIFFENING MECHANISM (Knight et al 2012)

A typical tension-stiffening test is illustrated in Figure 4. The prism is of length L_{pr} and depth d_{prt} and is concentrically loaded to ensure no bending. As the axial load P is constant over the length of the prism it resembles the constant moment region in a beam. For a given axial load P, the stresses in the concrete increase from zero at the ends to a maximum near mid-length. As the load P is increased, the stresses build up in the concrete until a single crack, which will be referred to as the *initial crack*, occurs. With the applied load P, which is also and obviously the force in the reinforcement at the initial crack, sliding between the reinforcement and the adjacent concrete at their interface causes a slip at the crack face Δ_{cr} such that the total crack width w_{cr} is 2 Δ_{cr} at the level of reinforcement load P. To quantify this slip and the forces it induces, requires a partial-interaction theory that incorporates the bond-slip (τ-s) relationship. There are numerous closed form or numerical solutions readily available that can quantify the variation in interface slip *s* or interface slip-strain *ds/dx* along the member and the only difference in the solutions are the required boundary conditions.

Let us first consider the behaviour at the initial crack in Figure 4 which is shown in Figure 5(d) and labelled *single crack* to distinguish it from analyses in which there are multiple cracks. Partial-interaction theory, which requires the bond-slip properties (τ-s) can be used to: quantify the variation in the slip-strain ds/dx in Figure 5(a) in which ds/dx is the difference in strain across the bond interface, that is ε_r-ε_c in Figure 5(d); the variation in the bond shear stress τ along the prism as in Figure 5(b); and the variation in slip *s* as in Figure 5(c).

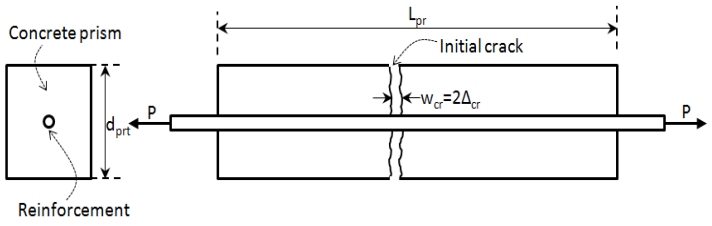

Figure 4. Tension-stiffening test

For a long length of reinforcing bar, the boundary condition required for the single crack analysis in Figure 5(d) is that at some point distance L_{prim} from the crack face both ds/dx and *s* tend to zero as shown in Figure 5(d). The partial-interaction analysis in Figure 5(d) can predict the minimum position at which the next crack could occur, should the concrete stresses be large enough, which is also L_{prim} and the load in the reinforcement to cause it to occur P_{prim}. This gives the minimum spacing of the primary cracks L_{prim}. Once primary cracks occur, the partial-interaction analysis is that of a symmetrically loaded prism in Figure 5(e) of length L_{prim} where by symmetry the slip at $L_{prim}/2$ is zero which is the new boundary condition. The analysis of this prism can be used to predict when cracking could occur at the mid-length $L_{prim}/2$ and should these secondary cracks occur the analysis is that shown in Figure 5(f).

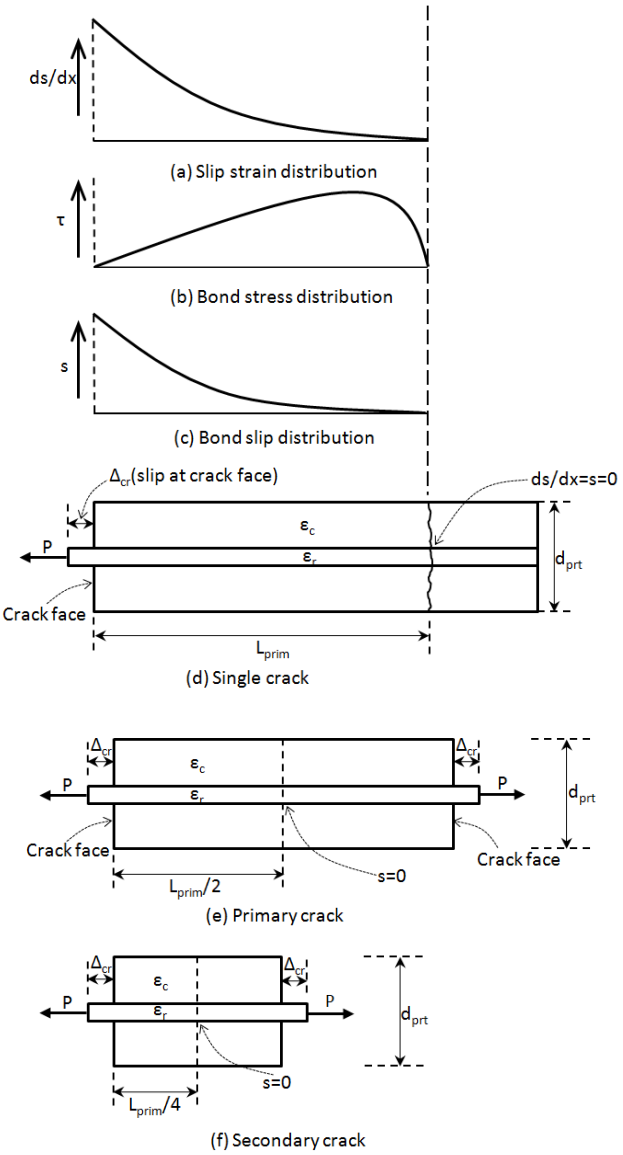

Figure 5. Tension-stiffening analysis

It can be seen that the only requirements for this mechanics model are the material properties of the concrete and reinforcement and in particular the bond properties. Hence the model can cope with any type of reinforcement with any type of concrete with any type of bond properties. Furthermore it will be shown that this size-dependent mechanism can be incorporated into a size-dependent analysis which obviates the need for *mechanics testing* to allow simple design approaches to be developed. It may also be worth noting that the model can cope with residual strains such as prestress, shrinkage and thermal gradients as well as creep and relaxation before and after cracking.

4.0 DEFORMATION BASED ANALYSIS (Visintin et al 2012a and 2012b)

The aim is to extract the sectional properties such as χ and EI which can then be used in a member analysis. To do this, let us consider a segment of the member of length $2L_{def}$ as shown in Figure 6 which is subjected to a constant moment. The segment is subjected to an Euler-Bernoulli deformation at is ends which cause the rotations θ. The size-dependent tension-stiffening model and the size-dependent concrete-softening model, described previously, are applicable in regions where the axial forces are constant and, hence, they can be incorporated directly into the segment as this is subjected to a constant moment region.

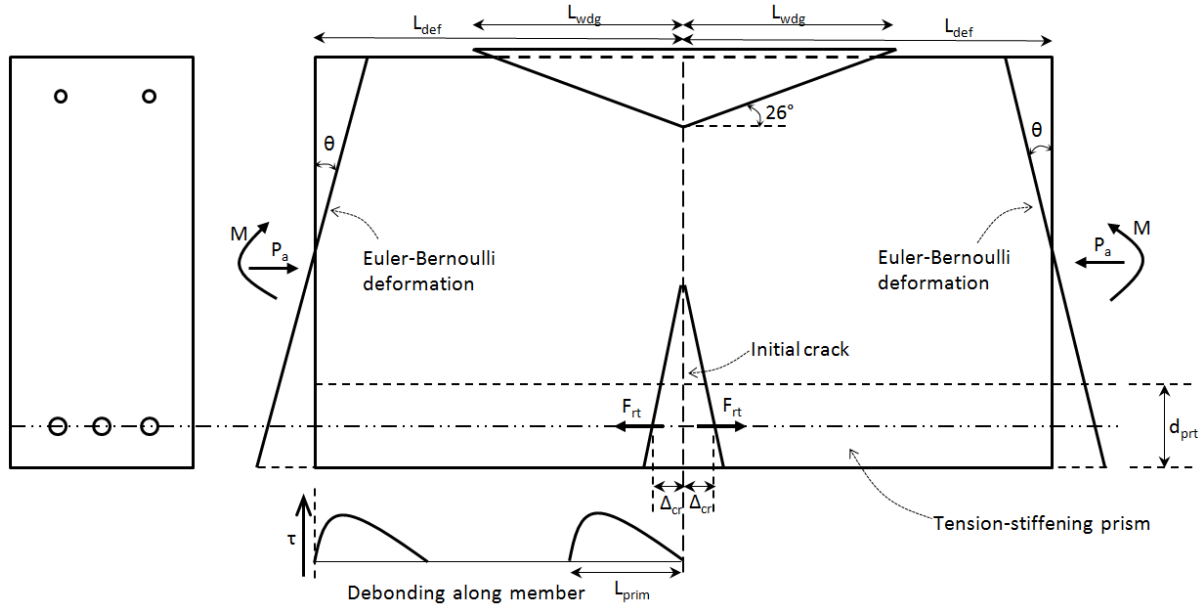

Figure 6. M/ϑ single crack

The analysis in Figure 6 is for a segment with a single crack. Hence the tension-stiffening analysis with the boundary conditions in Figure 5(d) applies. This can be used to quantify the relationship between P and Δ_{cr} at the initial crack in Fig. 6. This form of analysis also allows for debonding along the member as illustrated at the bottom of Figure 6 and, hence, is useful for reinforcements with weak bond such as in FRP reinforcement. Hence if debonding does not need to be accounted for, L_{def} needs only be equal to L_{prim}, otherwise, it should be greater to simulate debonding along the member. If softening is to be accounted for, then L_{def} must be greater than the length of the wedge L_{wdg} as shown.

The analysis in Figure 5(d) gives the force in the reinforcement to cause the concrete to crack that is the reinforcement force to cause primary cracking P_{prim} as well as the minimum spacing of these primary cracks L_{prim}. Once these primary cracks occur, the segment has two cracks at its ends and a length L_{prim} as in Figure 7 and the P/Δ_{cr} relationship is given by the analysis in Figure 5(e). The analysis in Figure 5(e) also gives the reinforcement force to cause secondary cracks, then if they do occur the analysis is the same as in Figure 7 except that the length of the segment is now $L_{prim}/2$ and P/Δ_{cr} given by Figure 5(f).

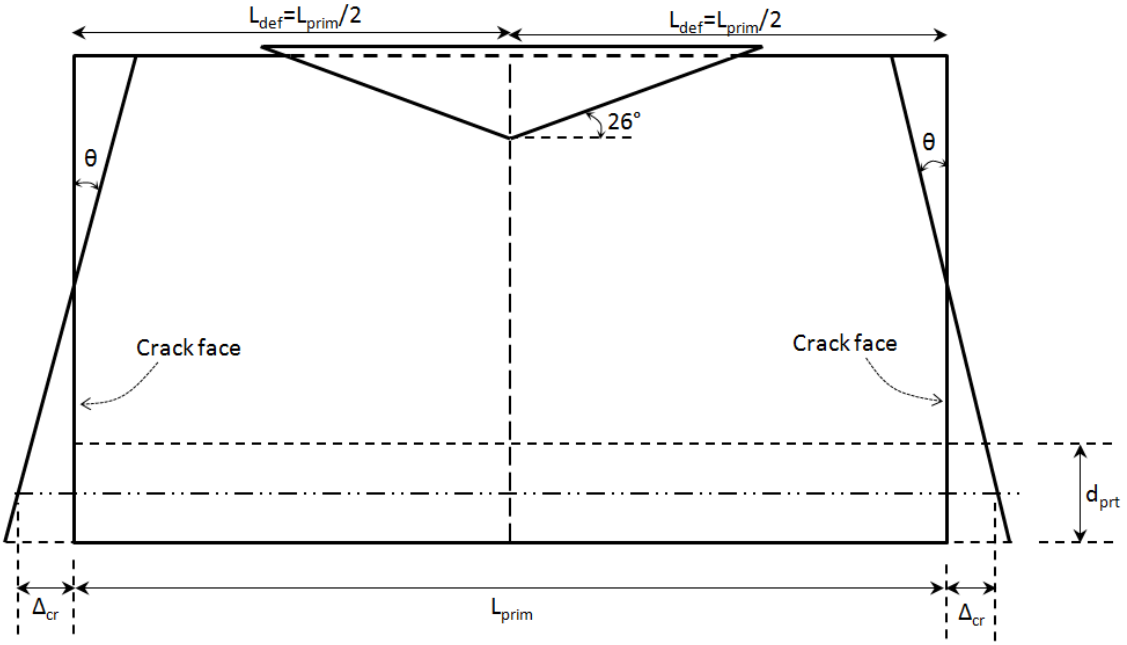

Figure 7. M/ϑ multiple primary cracks

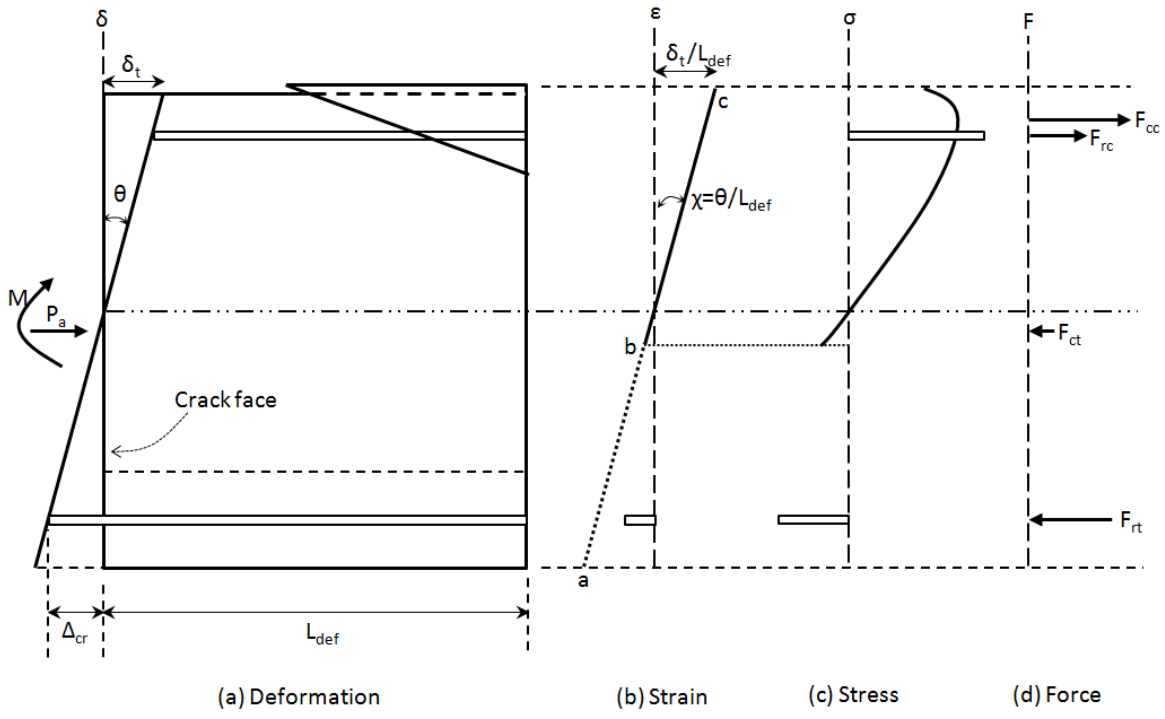

Figure 8. M/ϑ analysis

The M/θ analysis for the segments in Figures 6 and 7 is depicted in Figure 8 where only half a segment needs to be analysed as the other half is a mirror image. A deformation is imposed as in Figure 8(a). If the concrete is uncracked and not softening, then there is a linear strain profile *a-b-c* as in Figure 8(b) and the standard M/χ analysis ensues such that: the stresses in Figure 8(c) are strain based that is determined from the material stress-strain

relationship; from which the forces in Figure 8(d) can be derived; and it is a question of moving the strain profile in Figure 8(b) up and down at the fixed χ until equilibrium is achieved.

If cracking occurs in the analysis in Figure 8, then the force in the reinforcement F_{rt} in Figure 8(d) can be derived from the tension-stiffening analyses in Figures 5(d), (e) and (f) depending on their boundary conditions, and the remaining forces from the strain profile *b-c* in Figure 8(b). If softening occurs, then F_{cc} in Figure 8(d) is now derived using a size-dependent stress-strain relationship in which L_{pr} in Figure 3 is equal to $2L_{def}$ in Figures 6 or 7.

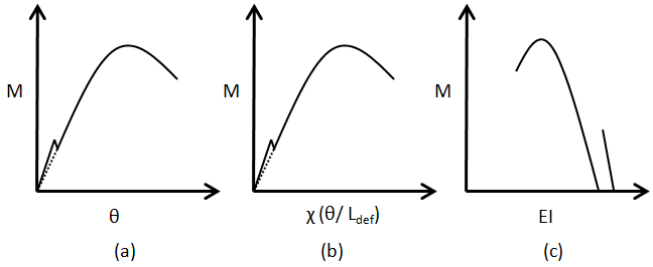

Figure 9. Sectional properties

The results of the M/θ analysis quantify the behaviour at all levels of loading as in Figure 9(a) which includes serviceability, ultimate and failure. The analyses can include the effects of prestress, creep, shrinkage and relaxation. The analysis can be applied to any concrete and any reinforcement and can allow for changes in these properties as might occur through degradation. Only *material testing* is required and there is no need for the gross expense of *mechanics testing*.

The results of the M/θ analysis as depicted in Figure 9(a) can be converted to M/χ variations as in Figure 9(b) by simply dividing θ by L_{def}. From the secant stiffness of the M/χ variation, can be determined the M/EI variation in Figure 9. Either the curvature or the flexural rigidity can then be used in a member analysis.

5.0 SHEAR FAILURE OF DEFORMATION BASED ANALYSIS (Lucas et al 2011)

The deformation based analysis in Figure 8 can readily be applied to inclined diagonal cracks as shown in Figure 10 where: the diagonal crack is inclined at an angle β; the force in the stirrup F_{st} can be derived from the partial-interaction analysis in Figure 5(d) or where the boundary condition is that the slip is zero at the bend of the stirrup. The displacement based flexural analysis gives the forces acting along the potential sliding plane A-A. Importantly, from the normal component of these forces on the sliding plane, can be derived the normal compressive force across this sliding plane as it is this force which quantifies through shear-friction the capacity of this sliding plane to resist shear and consequently the shear capacity of the member.

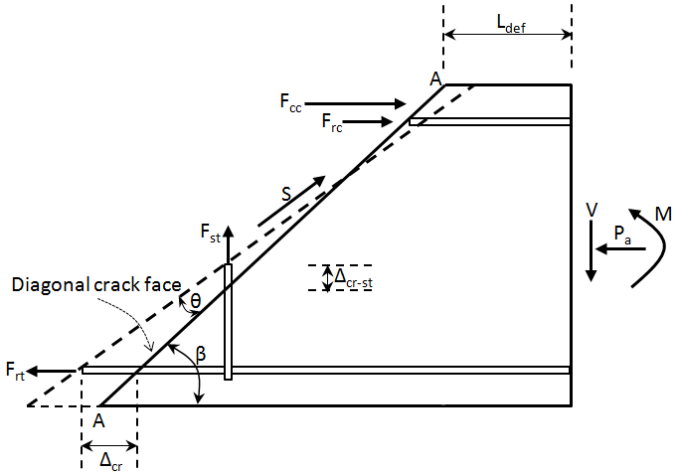

Figure 10. M/ϑ diagonal crack

It can be seen in Figure 10 that the shear capacity depends on the forces engendered by flexure and that a mechanics solution is now available to quantify the shear capacity which should no doubt further reduce the cost of developing new products by reducing the amount of *mechanics testing* required.

6.0 CONCLUSIONS

There are three types of testing required in reinforced concrete structural development and design: *material testing* to determine the fundamental and basic material properties; *mechanics testing* to find empirical solutions where there are gaps in the understanding of the mechanics; and *validation testing* to ensure safe use. The problem with reinforced concrete is that much of the expense of development is in *mechanics testing* simply because current design and analysis models are unable to simulate mechanisms that are known to occur such as tension-stiffening, concrete softening and shear failure.

Structural design should be easy. There should be a structural mechanics model that simulates all modes of behaviour and failure and the only experimental input should be the material properties. The model could then be used: to develop simple and efficient design rules for codes; by structural engineers to analyse and design complex members; and by developers who should only need to measure the material properties. Nothing more than material testing should be required if the structural mechanics model truly simulates the behaviour. Unfortunately this is not the case in reinforced concrete and it is this lack of a mechanics model which has considerably increased the cost of development and limited the accuracy and width of design.

A deformation based flexural analysis has been described which can simulate the mechanics involved in concrete-softening, tension-stiffening and shear failure. The aim is to develop this mechanics model to such an extent that the cost of *mechanics testing* is removed or considerably reduced which should help in the development of new products or techniques and provide much more accurate analysis techniques.

7.0 ACKNOWLEDGEMENTS

The financial support of the Australian research Council ARC Discovery project DP0985828 'A unified reinforced concrete model for flexure and shear' is gratefully acknowledged.

8.0 NOTATION

D_{ax} total axial deformation

d_{pr} width of prism

d_{prt} depth of tension stiffening prism

ds/dx slip-strain; ε_r-ε_c

E_c concrete modulus

EI flexural rigidity

F force profile

F_{cc} concrete compressive force

f_{co} concrete compressive strength

F_{ct} concrete tensile force

F_{rc} force in compression reinforcement

F_{rt} tensile force in reinforcement

F_{st} force in stirrup

H_{wdg} axial component of Δ

L_{def} deformation length

L_{pr} length of prism

L_{prim} primary crack spacing

L_{wdg} length of wedge

M moment

P reinforcement force

P_a axial force

P_{prim} reinforcement force to cause primary cracks

RC reinforced concrete

S shear force along inclined plane

s slip

V vertical shear force

w_{cr} width of crack at level of reinforcement

α wedge angle

β inclination of diagonal crack

Δ slip along sliding plane

Δ_{cr} reinforcement slip at crack face

$\Delta_{cr\text{-}st}$ stirrup reinforcement slip at crack face

δ deformation profile

δ_t contraction at top surface

ε strain; strain profile

ε_c concrete strain adjacent to reinforcement

ε_{co} strain at f_{co}

ε_{gl} global strain; total strain over L_{pr}

ε_{mat} material strain

ε_{r} reinforcement strain

ε_{wdg} effective strain due to Δ

θ rotation

σ stress; stress profile

σ_{ax} axial stress

σ_{n} n^{th} level of axial stress

τ shear stress

χ curvature

9.0 REFERENCES

Chen, Y., Visintin, P., Oehlers, D.J., and Johnson, A.U., (2012.) "Size dependent stress-strain model for unconfined concrete" Submitted to ASCE Structures.

Knight. D., Visintin, P., Oehlers, D.J., Jumaat, M.Z., (2012). "Incorporating residual strains in the flexural rigidity of RC members with varying degrees of prestress and cracking". Submitted Advances in Structural Engineering.

Lucas, W., Oehlers, D.J. and Mohamed Ali M.S. (2011) "Formulation of a shear resistance mechanism for inclined cracks in RC beams". ASCE Journal of Structural Engineering, Vol. 137, Issue 12, Dec., pp1480-1488.

Lucas, W., Oehlers, D.J., Mohamed Ali, M.S. and Griffith, M.C., (2012) "The FRP reinforced concrete shear-friction mechanism". Advances in Structural Engineering, Vol. 15, Issue 4, SI, April, pp615-623.

Mohamed Ali M.S., Oehlers, D.J., Haskett, M., and Griffith, M.C.. (2012) "The discrete rotation in reinforced concrete beams". ASCE Journal of Engineering Mechanics. Accepted 24/3/12.

Muhamad, R., Mohamed Ali M.S., Oehlers, D.J. and Sheikh, A.H.. (2011) "Load-slip relationship of tension reinforcement in reinforced concrete members". Engineering Structures, 33, pp1098-1106.

Muhamad, R., Mohamed Ali, M.S., Oehlers, D.J., and Griffith, M.C., (2012) "The tension stiffening mechanism in reinforced concrete prisms". International Journal of Advances in Structural Engineering. Accepted 10/2/12.

Oehlers, D.J., (2010) “The hunt for the elusive concept”. Len Hollaway’s special edition of Advances in Structural Engineering. Vol. 13, No. 5, September, pp755-772.

Oehlers, D.J., Mohamed Ali M.S., Haskett, M., Lucas, W., Muhamad, R., and Visintin, P., (2011a) “FRP reinforced concrete beams – a unified approach based on IC theory”. ASCE Composites for Construction , May/June, Vol. 15, No. 3, pp293-303.

Oehlers, D.J, Haskett, M., Mohamed Ali M.S., Lucas, W., and Muhamad, R., (2011b) “Our obsession with curvature in reinforced concrete modelling”. Advances in Structural Engineering, Vol. 14, No. 3, pp 399-412.

Oehlers, D.J., Mohamed Ali M.S., Griffith, M.C., Haskett, M., and Lucas, W., (2012a) “A generic unified reinforced concrete model”, Proc. ICE , Structures and Buildings, Vol. 165, Issue SB1, February, pp 27-49.

Oehlers, D.J., Visintin, P. And Haskett, M., (2012b) “The ideal bond characteristics for reinforced concrete members”. Bond in Concrete Conference, Brescia, Italy. 18/6/12 – 20/6/12.

Visintin, P., Oehlers, D.J., Wu, C., and Haskett, M., (2012a) “A mechanics solution for hinges in RC beams with multiple cracks”. Engineering Structures, Vol. 36, pp 61-69.

Visintin, P., Oehlers, D.J., Wu, C., and Griffith, M.C. (2012b) “The Cyclic Behaviour of Reinforced Concrete Beam Hinges”, Earthquake Engineering and Structural Dynamics, Vol. 31, Issue 12, pp 1591-1608.

Visintin, P., Oehlers, D.J., Haskett, M., Wu C. and Chen, J.F. (2012c) “A mechanics based hinge analysis for reinforced concrete columns”. ASCE Journal of Structural Engineering. Accepted subject to minor changes 29/8/12.

Chapter 2: Size Dependent Models for Concrete in Compression

Introduction

This chapter contains two published journal papers in which it is shown how the fundamental mechanics of shear friction theory can be used to describe the mechanism of size effect in un-confined and actively confined concrete.

In the first paper “Size dependent stress-strain model for unconfined concrete” it is shown that concrete deformation due to compression is both a material property and a shear-friction mechanism and that by taking into account of both of these deformations it is possible to derive a stress-strain relationship that is size dependent. It is also shown how the stress-strain from cylinder tests of one specific length can be modified to determine that for any size of cylinder.

In the second paper “Size dependent axial and lateral stress strain relationships for actively confined concrete” the shear friction mechanism used to describe size effect described in the first paper is extended to actively confined concrete.. Moreover, it is shown that the proposed approach can be used to make existing generic stress-axial strain relationships size dependent and these size dependent relationships can be directly used to determine the corresponding size dependent stress/lateral-strain relationship which is often difficult to measure as compared to the axial contraction.

List of manuscripts

Chen, Y., Visintin, P., Oehlers, D., and Alengaram, U. (2014). ”Size dependent stress-strain model for unconfined concrete.” Journal of Structural Engineering, 140(4), 10.1061/(ASCE)ST.1943-541X.0000869.

Visintin, P., Chen, Y., and Oehlers, D. (2014). “Size dependent axial and lateral stress strain relationships for actively confined concrete.” Accepted for publication by Advances in Structural Engineering on 05/06/2014.

Statement of Authorship

Size dependent stress-strain model for unconfined concrete. Journal of Structural Engineering 2014, 140(4), 10.1061/(ASCE)ST.1943-541X.0000869.

Chen, Y (Candidate)

Performed analyses and developed model

I hereby certify that the statement of contribution is accurate and I give permission for the inclusion of the paper in this thesis

Signed……..Date……

Visintin, P

Supervised and contributed to research

I hereby certify that the statement of contribution is accurate and I give permission for the inclusion of the paper in this thesis

Signed……Date……

Oehlers, DJ

Supervised and contributed to research

I hereby certify that the statement of contribution is accurate and I give permission for the inclusion of the paper in this thesis

Signed……Date……

Alengaram, U.

Contributed to research

I hereby certify that the statement of contribution is accurate and I give permission for the inclusion of the paper in this thesis

Signed……Date……

Size Dependent Stress-Strain Model for Unconfined Concrete

Chen, Y., Visintin, P., Oehlers, D.J., and Alengaram, U.J

Abstract: The stress-strain behaviour of concrete under compression, both in the ascending and descending branches, is crucial in determining both the strength and ductility of reinforced concrete members. This material property is generally determined directly from compression tests of cylinders or prisms. However, it is widely recognised that this material property depends on both the size and shape of the test specimen and the method of measurement. In this paper, it is shown that concrete deformation due to compression is both a material property and a shear-friction mechanism and that by taking into account of both of these deformations it is possible to derive a stress-strain relationship that is size dependent. It is also shown how the stress-strain from cylinder tests of one specific length can be modified to determine that for any size of cylinder. With this new procedure, the results from 380 published tests on unconfined concrete have been reanalysed to extract size dependent strains at the peak stress which are then used in existing curve fitting models to produce size dependent stress-strain models for unconfined concrete. It is shown how these size dependent stress-strain models can be used in a size-dependent deformation based approach to quantify both the strength and ductility of reinforced concrete members.

Author keywords: Unconfined concrete; Unconfined concrete properties; Stress-strain concrete; Size dependent concrete properties; Deformation based model.

Introduction

The compressive axial stress-strain (σ_{ax}-ε_{ax}) properties of concrete, both the ascending and descending branches, are an intrinsic component of reinforced concrete analysis and design. In general, these σ_{ax}-ε_{ax} properties are obtained directly from compression tests on concentrically loaded cylinders or prisms, herewith referred to as prisms, such as in Fig. 1 where L_{pr} is the length of the specimen and d_{pr} the diameter or width. However, these measured σ_{ax}-ε_{ax} properties can vary widely depending on the method of measurement and the shape and size of the concrete specimens. For example, when an axial stress σ_{ax} is applied which causes a total axial shortening D_{ax} as shown, then the global strain D_{ax}/L_{pr} (ε_{axgl}) can be determined by measuring the total contraction between the platen and base; this gives the global stress-strain relationship (σ_{ax}-ε_{axgl}). However, if the strains are measured locally (ε_{axlc}) such as by using strain gauges at positions A or B, then the local stress-strain relationship σ_{ax}-ε_{axlc} will not be the same as the global stress-strain relationship σ_{ax}-ε_{axgl}. Even if the local strains are measured at demec points such as at C-D and D-E which averages the strains over these regions, then these local average stress-strain relations (σ_{ax}-ε_{axlc}) will vary along the length of the specimen L_{pr}. This problem of the variability of the strains due to the measuring techniques has been long

recognised (Sangha and Dhir 1972, Kotsovos 1983, Ahmad and Shah 1985; Van Mier 1986a and 1986b, Shah and Sankar 1987, Jansen et al 1997).

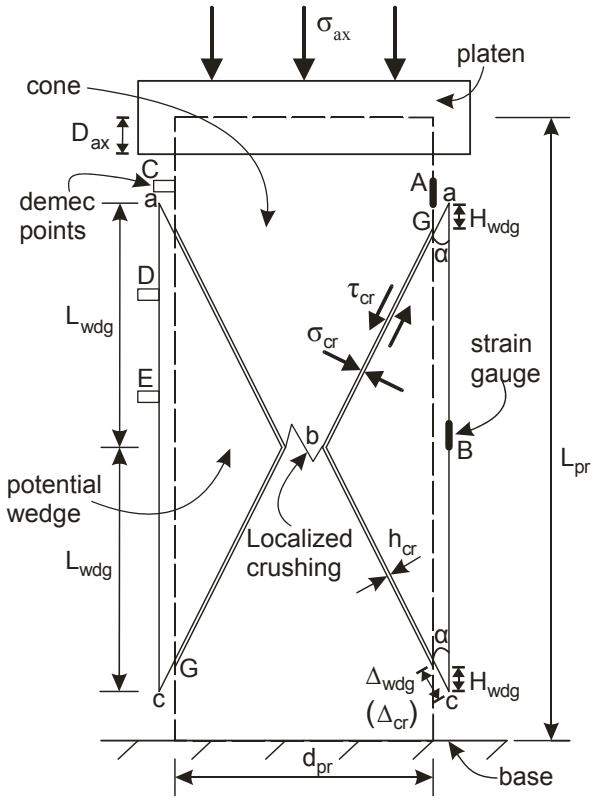

Fig. 1. Compression tests

As well as depending on the method of measuring the strain, tests have shown that the global stress-strain relationships (σ_{ax}-ε_{axgl}) depends on both the shape which will be defined as

$$\mu = \frac{L_{pr}}{d_{pr}} \tag{1}$$

and the size of the specimen which will be defined as

$$\eta = \frac{L_{pr-1}}{L_{pr-2}} \tag{2}$$

that is the ratio of the prism lengths. For example, standard compression cylinder tests in which the slenderness factor μ equals 2, fail at a lower peak stress f_{co} than those from standard cube

tests in which μ equals 1, and codes (British Standards 1996; CEB-FIP1990) give conversion factors to relate these strengths. Furthermore, tests have shown that in specimens in which μ exceeds 2, the strength f_{co} hardly varies, if at all, when the length is increased, that is the strength is independent of the size factor η. In contrast for the same specimens, the strain at the peak stress ε_{co} as well as those on the descending branch reduce when the length is increased, that is the strain depends on the size factor η. This has led to the recognition that there are different zones of behaviour that govern compression failure and such techniques such as energy (Sangha and Dhir 1972; Kotsovos 1983; Van Mier 1984; Shah and Sankar 1987; Hillerborg 1989, 1990; Torrenti et al. 1993; Bazant et al 1994; Markset and Hillerborg 1995; Lee et al 1995; Jansen and Shah 1997) or sliding and shear-friction (Fantilli et al 2007; Mohamed Ali M.S. 2010; Haskett et al 2010; and Haskett et al 2011) have been used to quantify the compressive behaviour in zones where there are large deformations such as where wedges of length L_{wdg} may form as shown in Fig. 1.

This paper follows the zone approach in particular the excellent and original sliding mechanism proposed by Fantilli et al (2007) but not directly their method of analysis. It is assumed that the global strain ε_{axgl} due to the overall contraction D_{ax} in Fig. 1 is due to: material strains ε_{mat} along the length of the member L_{pr} which can be measured through the use of strain gauges, such as at A and B, and which cause a contraction $\varepsilon_{mat}L_{pr}$; and the effective strain due to the mechanism of sliding of the wedges which cause the axial movement H_{wdg} as shown and consequently an effective strain $2H_{wdg}/L_{pr}$ (ε_{wdg}) and which can only be measured through the total contraction, that is not through strain gauges. It is this latter component of strain, the effective strain due to wedge sliding ε_{wdg}, which makes the stress-strain relationship both size and shape dependent. This principle is first used to develop a strain adjustment factor for directly converting tests of a specific size (L_{pr-1}) for use in specimens of any size (L_{pr-2}) and these are then compared with test results. This size-dependent strain adjustment factor is then applied to the reanalysis of 380 published test results to produce generic stress-strain (σ_{ax}-ε_{axgl}) relationships for use in any size of specimen. As these generic stress-strain relationships are size dependent, they are not suitable for the standard moment-curvature (M/χ) approach as it is strain based and simply cannot cope with specimen sizes unless a hinge length or constant moment length (Fantilli et al 2007) is assumed. Instead a moment-rotation (M/θ) approach is described which being deformation based can readily accept size dependent stress-strain relationships.

SIZE DEPENDENT STRAIN

The size dependent component of the strain ε_{wdg} can be quantified through the use of shear-friction theory of initially uncracked concrete.

Shear friction mechanism

The shear-friction mechanism of concrete softening is illustrated in Fig. 1. A circumferential double wedge *a-b-c* of length $2L_{wdg}$ and at an angle α forms around a cone. The sliding planes *a-b* and *b-c* are initially uncracked and sliding Δ_{wdg} occurs as shown. Furthermore, for sliding to

occur requires localised crushing at the apex *b* of the cones. Occasionally for slender prisms, sliding occurs across a diagonal sliding plane such as G-G which does not require localised crushing. However, this rarely occurs in the standard prism in which the slenderness μ equals 2 and, furthermore, rarely occurs in reinforced concrete members, so this case will not be considered.

The natural angle of the sliding plane, that is when the end restraints of the platen and base do not affect the angle of the wedge α in Fig. 1 depends on the Mohr-Coulomb frictional component of concrete (Mohamed Ali M.S. et al 2010). Tests have shown (Balmer et al. 1949; Mattock 1974; Cusson and Paultre 1995; Rutland and Wang 1997; Harmon et al. 1998; Gebran and Mazen 2009; Mohamed Ali M.S. et al 2010) that for normal concrete this natural angle α_{nat} is about 26^o that is L_{wdg} is very close to d_{pr}. Hence the natural angle of the wedge at 26^o can occur in prisms in which L_{pr} is greater than or equal to $2d_{pr}$, that is the angle of the wedge remains constant when

$$\mu \geq 2 \tag{3}$$

Hence the standard compression cylinder test in which the height of the prism is twice the diameter and prisms with greater slenderness as in Fig. 1 allow for the natural angle of the wedge α_{nat} to occur. In contrast, the end restraints in compressive cube tests in which μ = 1 do not allow wedges to form at α_{nat} (26^o) but force α to be 45^o (Domone and Illston 2001). Hence, the effective strain ε_{wdg} from cube tests will be different from those measured from standard cylinder tests and in cylinder tests in which μ exceeds 2.

For a fixed angle α in Fig. 1, from equilibrium there is a direct relationship between the axial stress σ_{ax}, the normal stress to the sliding plane σ_{cr} and the shear stress along the sliding planes τ_{cr} (Visintin et al 2012a; Visintin et al 2012b). The shear-friction material properties quantify the relationship across a potential initially uncracked sliding plane between: the shear stress τ_{cr}; normal stress σ_{cr}; crack width h_{cr}; and sliding along the plane Δ_{cr} which is also shown in Fig. 1 as Δ_{wdg} (Haskett et al 2010; Haskett et al 2011). Hence shear-friction material properties can be used to quantify Δ_{wdg} and consequently H_{wdg} and consequently ε_{wdg} (Visintin et al 2012a; Visintin et al 2012b). For example, this could be used to quantify the behaviour of cubes in which α is 45^o but this would be of no use in the analysis of RC members where α_{nat}, at about 26^o, occurs. However all prisms with the slenderness in Eq. 3 have the same natural angle of wedge so that the relationship between σ_{ax}, σ_{cr}, τ_{cr}, Δ_{cr} and H_{wdg} is the same in all of these prisms. Hence they will have the same relationship between σ_{ax} and ε_{wdg}. This could be derived from shear-friction material properties (Haskett et al 2010; Haskett et al 2011; Visintin et al 2012a; Visintin et al 2012b) or directly from the test results themselves as follows.

Size dependent strain

The axial contraction of the prism $(D_{ax})_n$ in Fig. 1 when the n^{th} value of stress $(\sigma_{ax})_n$ is applied is due to the axial contraction of the concrete material $(D_{mat})_n$ and the axial contraction due to sliding of the wedges $(D_{wdg})_n$, that is

$$(D_{ax})_n = (D_{mat})_n + \left(D_{wdg}\right)_n \tag{4}$$

such that

$$(D_{ax})_n = \left(\varepsilon_{axgl}\right)_n L_{pr} \tag{5}$$

and in which

$$(D_{mat})_n = (\varepsilon_{mat})_n L_{pr} \tag{6}$$

where $(\varepsilon_{mat})_n$ is the material strain in the concrete, that is the stress $(\sigma_{ax})_n$ divided by the material secant modulus for that stress $(E_c)_n$ and where

$$\left(D_{wdg}\right)_n = 2\left(H_{wdg}\right)_n \tag{7}$$

Substituting Eqs. 5-7 into Eq. 4 gives

$$2\left(H_{wdg}\right)_n = \left(\left(\varepsilon_{axgl}\right)_n - (\varepsilon_{mat})_n\right) L_{pr} \tag{8}$$

Hence for a prism of length L_{pr-1} and subjected to an axial stress $(\sigma_{ax})_n$ which produces a material strain $(\varepsilon_{mat})_n$, the contraction due to sliding in a wedge is given by

$$2\left(H_{wdg-1}\right)_n = \left(\left(\varepsilon_{axgl-1}\right)_n - (\varepsilon_{mat})_n\right)\left(L_{pr-1}\right) \tag{9}$$

Similarly for a prism with a different length L_{pr-2}

$$2\left(H_{wdg-2}\right)_n = \left(\left(\varepsilon_{axgl-2}\right)_n - (\varepsilon_{mat})_n\right)\left(L_{pr-2}\right) \tag{10}$$

However from shear-friction material properties as described in the previous section, for the same axial stress $(\sigma_{ax})_n$ and the same angle of wedge α_{nat}, the slip across the sliding plane $(\Delta_{wdg})_n$ and consequently the contraction due to sliding $2(H_{wdg})_n$ is the same. Hence equating Eqs. 9 and 10 gives the size dependent global strain

$$\left(\varepsilon_{axgl-2}\right)_n = \left(\left(\varepsilon_{axgl-1}\right)_n - (\varepsilon_{mat})_n\right)\frac{L_{pr-1}}{L_{pr-2}} + (\varepsilon_{mat})_n \tag{11}$$

Equation 11 is shown diagrammatically in Fig. 2 for the stress level $(\sigma_{ax})_n$. The number in brackets is the size factor η in Eq. 2 that is L_{pr-1}/L_{pr-2} which also occurs in Eq. 11. The stress-strain curve marked (η = 1) can be considered to be the test result of a prism of a specific length L_{pr-1} which could be of a standard cylinder of 200 mm and, importantly, in which the slenderness in Eq. 3 applies. At the stress level $(\sigma_{ax})_n$, the material strain is $(\varepsilon_{mat})_n$; in this figure we have assumed that the material stress-strain is linear elastic with a modulus of E_c but this property could have been measured with the strain gauges in Fig. 1. The global strain in the ascending branch is $[(\varepsilon_{axgl-1})_n]_{asc}$ and that in the descending branch $[(\varepsilon_{axgl-1})_n]_{des}$.

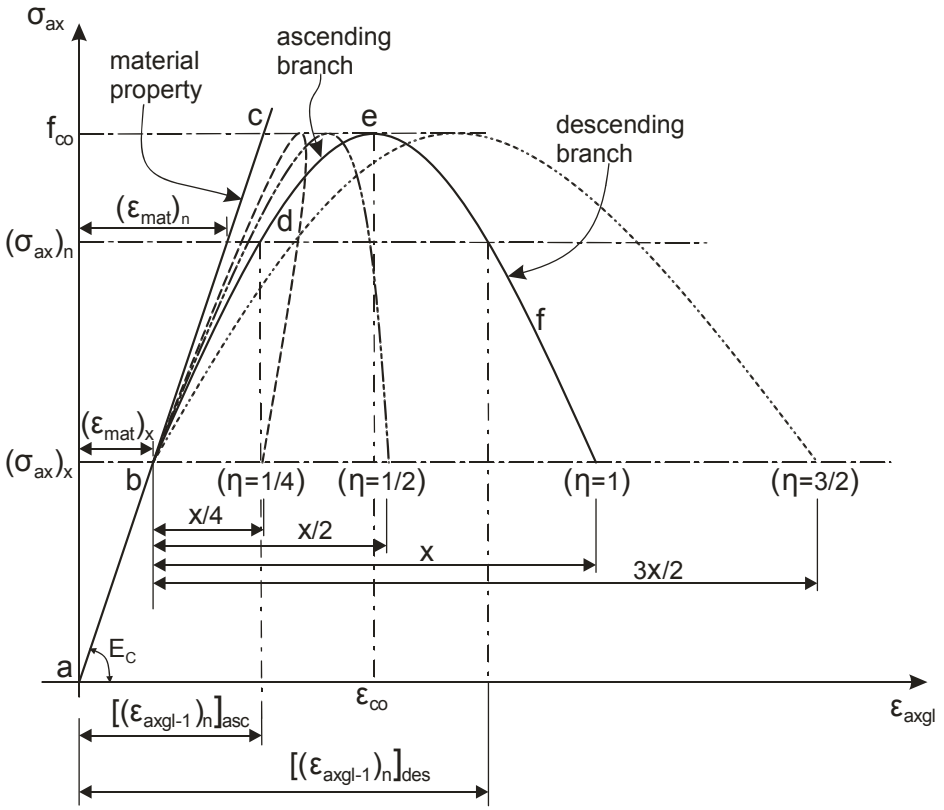

Fig. 2 Size dependent σ_{ax}-ε_{axgl}

The test results labelled (η = 1) in Fig.2 can be used in Eq. 11 to plot the stress-strain relationships for different lengths of prism L_{pr-2}. For example, doubling the length of the prism from 200 mm to 400 mm gives the curve marked (η = 1/2) which has a reduced ductility but the same strength f_{co}. Doubling the length of the prism again to 800 mm gives the curve marked (η = 1/4) with a further reduction in ductility and which shows the classical snap-back condition which is known to occur in tests. In contrast, reducing the length of the prism by a third, that is from 200 mm to 133 mm, produces the curve marked (η = 1½) where the ductility increases; bearing in mind that the width of the prism must be less than or equal to 133/2 to satisfy Eq. 3.

The behaviour given by Eq. 11 is further illustrated at the stress level $(\sigma_{ax})_x$ in Fig. 2. At this stress level, all the specimens have the same material strain $(\varepsilon_{mat})_x$ and the specimen labelled (η = 1) has an effective strain due to sliding $(\varepsilon_{wdg})_{x-1}$ which is shown as *x*. When the prism is doubled in length from η = 1 to η = ½, then the effective strain due to the wedge halves to *x*/2 as shown. A further doubling of the prism length halves the effective strain due to wedge sliding to *x*/4 as shown. It can be seen that it is only necessary to test one specific size of specimen in which the slenderness is greater or equal to two (Eq. 3) to obtain the size-dependent strain-strain relationship of the concrete for any size of prism.

Comparison with test results

Jansen et al (1997) tested prisms which satisfied the slenderness requirement of Eq. 3 that is μ ≥ 2, which ensures that the wedges occur throughout at their natural angle α_{nat}. The results of these tests are summarised in Table 1 in the Appendix. There is a group of 13 results in which the peak strength averaged 48 MPa and these are plotted in Fig. 3 as *Exp.*; the ordinate has been non-dimensionalised in terms of the strength of the specimen f_{co}. The slenderness μ ranged from 2 to 5.5 and the prism lengths L_{pr} ranged from 200 mm to 550 mm.

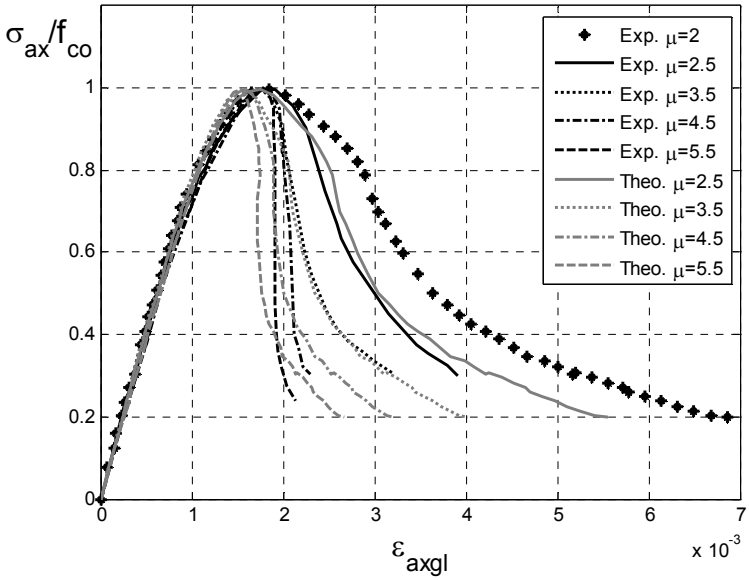

Fig. 3 Jansen (1997) 48 MPa series

Any of the experimental results in Fig. 3 can be used as a base line for calculating the size-dependent stress-strain relationships using Eq. 11. Let us use the experimental results for $\mu = 2$ as the base line as this is the standard cylinder test of a 200 mm prism of diameter 100 mm. For this base line, for Eq. 11 and for the n^{th} stress level: $L_{pr\text{-}1}$ is fixed at 200 mm; $L_{pr\text{-}2}$ is the length of prism length for which the size-dependent stress-strain relationship is being determined; ε_{mat} is the material strain using the experimentally derived moduli in Table 1; $\varepsilon_{axgl\text{-}1}$ is the strain in the 200 mm prism determined experimentally; and $\varepsilon_{axgl\text{-}2}$ is the theoretical strain for the prism of length $L_{pr\text{-}2}$. Using Eq. 11, the theoretical size-dependent stress-strain relationships have been plotted in Fig. 3 as *Theo*. It can be seen that there is good correlation with the experimental results and in particular with regard to the shapes of the curves.

From Table 1, Jansen et al (1997) also tested a group of tests in which the strengths averaged 90 MPa and these are shown in Fig. 4, and Shanga and Dhir (1997) tested specimens with an average strength of 41 MPa which are shown in Fig. 5. These results have been analysed as above using the base lines at $\mu = 2$. Once again there is good correlation. Furthermore, it can be seen in Fig. 4 that the theoretical results can also simulate snap-back.

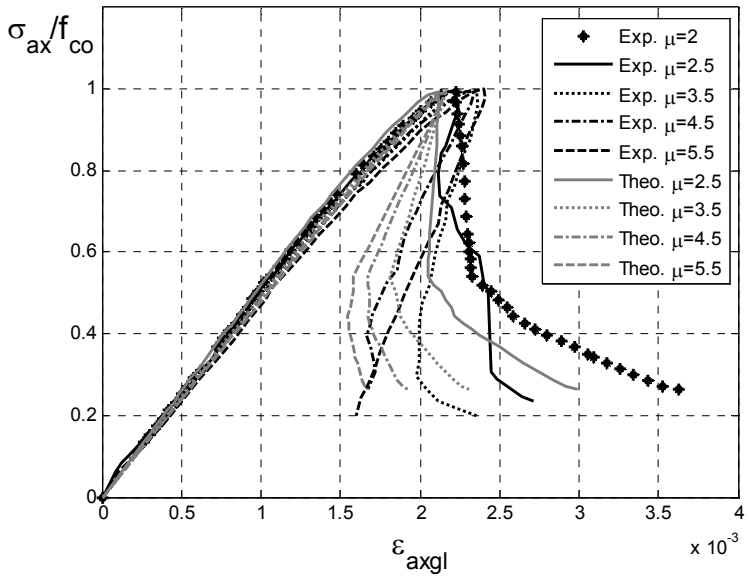

Fig.4 Jansen (1997) 90 MPa series

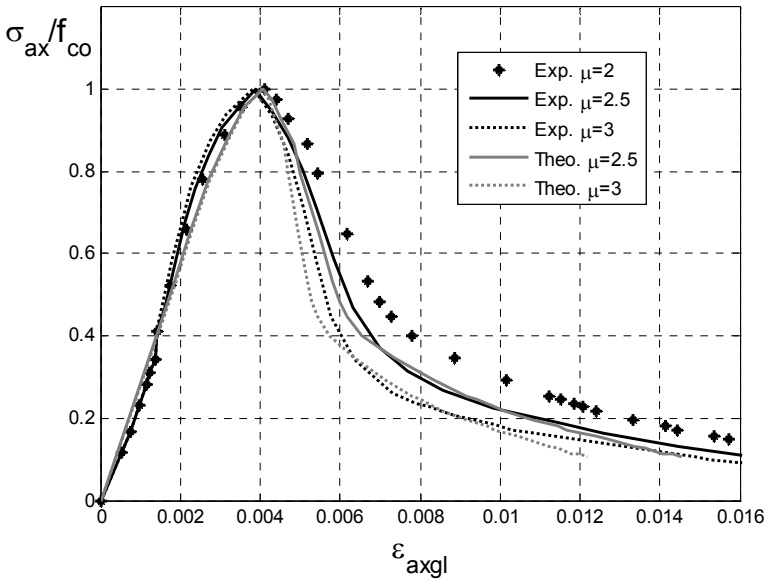

Fig. 5 Sangha and Dhir (1972) 41 MPa series

The implication of this research is that the stress-strain relationship for prisms of any size can be obtained from testing only one size of specimen in which the slenderness is greater than or equal to 2 (Eq.1) and in which the total deformation D_{ax} in Fig. 1 and consequently global strain

(ε_{axgl}) is measured. This provides an additional technique for not only refining existing stress-strain models but of reducing the amount of experimental research required in developing new types of concrete such as those which use oil palm kernels for aggregate and steel and polymer fibre concrete.

GENERIC SIZE DEPENDENT STRESS-STRAIN

Deriving the size-dependent stress-strain relationship directly from tests as described above is probably the most efficient and accurate method of determining the size-dependent stress-strain relationship for a specific concrete mix. The alternative is to develop a generic stress-strain relationship for use in analysis and design which is the subject of this section.

Strain at peak stress (ε_{co})

It is accepted practice (Wee et al 1996; Tasdemir et al 1998; Shah et al 1985; Popovics 1973; Tadros 1970; Carreira and Chu 1985; Ros 1950; Nicolo et al 1994; Attard and Setunge 1996) that the main parameters that control the stress-strain relationship of unconfined concrete are the secant modulus E_c and the strain ε_{co} at the peak stress f_{co} as shown in Fig. 2. Out of a total of 855 published test results, 475 had to be discarded (Ansari and Li 1998; Assa et al 2001; Benzaid et al. 2010; Berthet et al 2005; Bischoff and Perry 1995; Carrasquillo et al 1981; Dilger et al 1984; Imran and Pantazopoulou 1996; Lu and Hsu 2006; Jiang and Teng 2007; Karabinis and Rousakis 2002; Kshirsagar 2000; Matthys et al 2005; Markeset and Hillerborg 1995; Pessiki et al 2001; Ramesh et al 2003; Richart et al 1928; Richart et al 1929; Rokugo and Koyanagi 1992; Nanni and Bradford 1995; Toutanji 1999; Shahawy et al. 2000; Shehata et al 2002; Silva and Rodrigues 2006; Smith and Young 1956; Van Mier et al. 1997; Vonk 1992; Watstein 1953; Xiao and Wu 2000; Xiao et al 2010; Youssef et al. 2006; Zhang and Gjorv 1991) mainly because: the global strain ε_{axgl} had not been measured; or the slenderness requirement of Eq. 3 did not apply; and in the remainder the strains had not been reported. The remaining 380 results (Lahlou et al 1992; Jansen et al 1995; Jansen and Shah 1997; Amir 1996; Ahmad and Shah 1982; Sangha and Dhir 1972; Sfer et al 2002; Xie et al 1995; Candappa et al 2001; Gardener 1969; Attard and Setunge 1996; Ahmad and Shah 1985; Wee et al 1996; Wang et al 1978;) are listed in Table 1: where *No.* in Column 2 is the number in the group of tests in which the mean result is given; occasionally the modulus E_c was not recorded or could not be extracted from the test results in which case E_c is estimated using that recommended by the ACI (363R-92) and this is shown as an asterisk in Column 8 in Table 1.

From Eq. 11, the global strain ε_{axgl} is size dependent, that is it depends on the size factor η in Eq. 2. Hence to remove the scatter due to size-dependency, all of the results in Table 1 were converted to a specimen size of 200 mm; any size could have been chosen but this is the most common. To do this, Eq. 11 can be written in the form

$$\left(\varepsilon_{axgl-200}\right)_n = \left(\left(\varepsilon_{axgl-test}\right)_n - \left(\varepsilon_{mat}\right)_n\right)\frac{L_{pr-test}}{L_{pr-200}} + \left(\varepsilon_{mat}\right)_n \qquad (12)$$

where for the n^{th} stress level $\varepsilon_{axgl\text{-}200}$ is the predicted global strain in a specimen of length 200 mm, $\varepsilon_{axgl\text{-}test}$ is the measured global strain in the test, $L_{pr\text{-}test}$ is the length of the test specimen and $L_{pr\text{-}200}$ is the length to be converted to, which in this case is 200 mm. Equation 12 applies at all stress levels. However, for the specific strain ε_{co} at the peak stress f_{co}, Eq. 12 can be written as

$$\varepsilon_{co-200} = \left(\varepsilon_{co-test} - \frac{f_{co}}{E_c}\right)\frac{L_{pr-test}}{200} + \frac{f_{co}}{E_c} \tag{13}$$

where $\varepsilon_{co\text{-}200}$ is the global strain at the peak stress f_{co} when adjusted to a specimen of length 200 mm, $\varepsilon_{co\text{-}test}$ is the measured global strain at the peak stress in the test. Hence the test results can be converted to that of a 200 mm specimen using Eq. 13 and these converted strains are shown in Column 9 in Table 1 as $\varepsilon_{co\text{-}200}$.

To determine the effect of the variation in size only, the results $\varepsilon_{co\text{-}200}$ in Table 1 in which the size was varied or in which the prism size was not 200 mm were used in Fig. 6. A linear regression analysis has been plotted which has a coefficient of variation of 0.158. The unadjusted results ε_{co} for the same tests in Table 1 are analysed in Fig. 7 and this has a coefficient of variation of 0.219. Hence without the size-effect adjustment from Eq. 13, the scatter has increased by 39% which would suggest that the size-dependent adjustment has had a major positive influence.

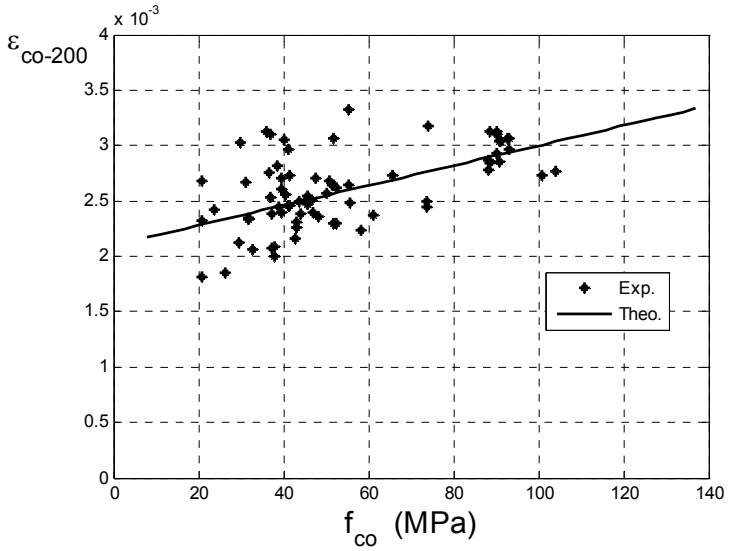

Fig. 6 $\varepsilon_{co\text{-}200}$ for specimens with varying size

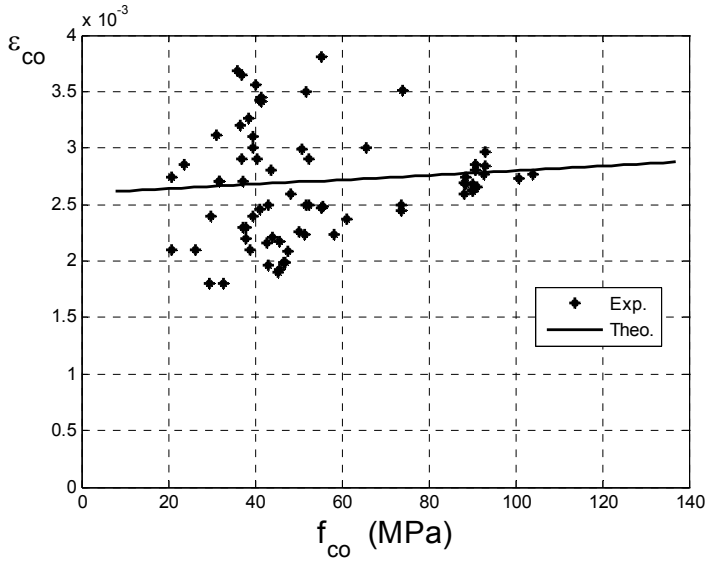

Fig. 7 ε_{co} for specimens with varying size

To determine the best relationship between ε_{co200} and f_{co}, all the results from Table 1 were analysed in Fig. 8 which gave the linear regression

$$\varepsilon_{co-200} = 4.76 \times 10^{-6} f_{co} + 2.13 \times 10^{-3} \quad (14)$$

where the stress is measured in MPa and which has a coefficient of variation of 0.140. The unadjusted values ε_{co} in Column 7 are shown in Fig. 9 in which the linear regression analysis gave

$$\varepsilon_{co} = 1.74 \times 10^{-6} f_{co} + 2.41 \times 10^{-3} \quad (15)$$

where the stress is in MPa and the coefficient of variation was 0.176 that is 26% larger than that of the adjusted results from Eq. 14. It can be seen by comparing Eqs. 14 and 15 that adjusting ε_{co} for size has significantly increased the slope of the regression. It may also be worth bearing in mind that the regression analyses in Figs. 8 and 9 allowed for the fact that some of the results plotted are the mean of a group (Column 2 in Table 1), as opposed to an individual result, and therefore have a higher weighting.

Published variations of the unadjusted strains ε_{co} with f_{co} are also plotted in Fig. 9 which helps to emphasise the large scatter associated with the unadjusted raw data associated with ε_{co}. However, these published variations are also plotted with the adjusted strains ε_{co-200} in Fig. 8 and the trends are reasonably close.

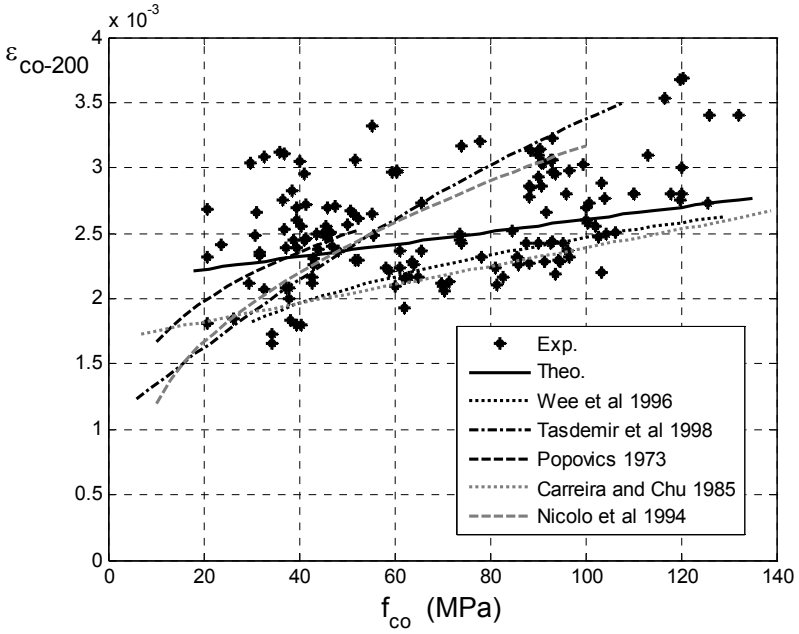

Fig.8 All values of $\varepsilon_{co\text{-}200}$ adjusted for size

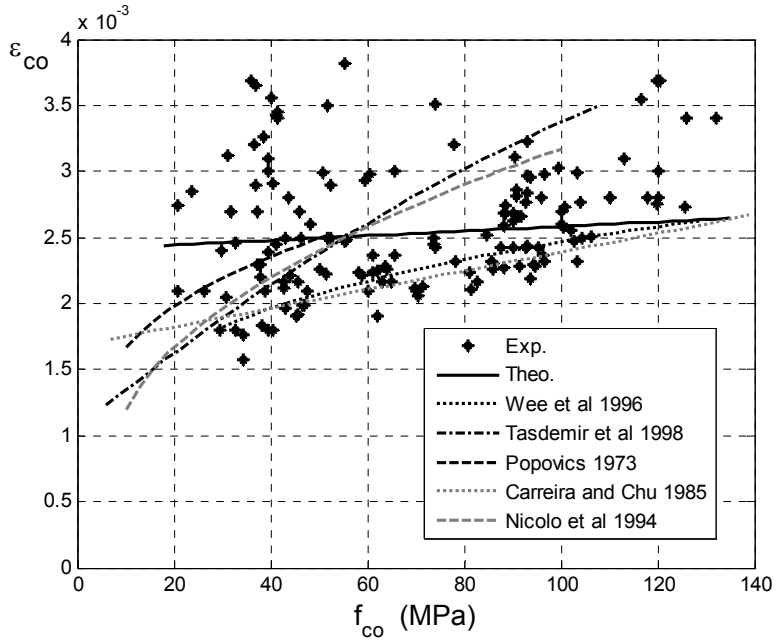

Fig. 9 All values of ε_{co} unadjusted

The scatter of the adjusted results in Fig. 8, even though it has been substantially reduced by the size dependent factor from that in Fig. 9, is still quite large. It is suggested that a part of this

scatter is due to the difficulty of measuring the global stress-strain relationship particularly at the onset of the descending branch when controlling the rig is difficult. Furthermore, it is felt that a major component of the error is the omission of the parameters that affect the shear-friction properties. Currently it is assumed that the stress-strain relationship is only a function of the concrete strength. However the behaviour along a sliding plane as in Fig. 1is also controlled by the shear friction properties which depend on the aggregate size and the strength of the aggregate (Bazant 1984; Kim and Eo 1990) and it is felt that if this was taken into account it would further reduce the scatter.

Generic stress-strain unconfined concrete

Good curve fits to the stress-strain relationship (Sargin et al 1971; Attard and Setunge 1996; Assa et al 2001; Hognested 1951; Kent and Park 1971; Saatcioglu and Razvi 1992; Mendis et al 2000; Popovics 1973; Mander et al 1988; Wee et al 1996) already exist. We will assume that these apply to 200 mm cylinders as this is a common specimen size. As an example, let us consider that by Popovics (1973) which can be written in the form:

$$(\sigma_{ax}) = f_{co}\frac{\left(\frac{(\varepsilon ax)pop}{\varepsilon_{co-200}}\right)r}{r-1+\left(\frac{(\varepsilon ax)pop}{\varepsilon_{co-200}}\right)^{r}} \quad (16)$$

Where $(\varepsilon_{ax})_{pop}$ is the strain in Popovics' expression, r is a factor which controls the ductility of the concrete and is given by $r=E_c/[E_c-(f_{co}/\varepsilon_{co\text{-}200})]$ and $\varepsilon_{co\text{-}200}$ is the strain given by Eq. 14 as we are assuming the expression came from tests on cylinders of length 200 mm. Hence Eq. 16 can be used to plot the stress-strain relationship for a 200 mm cylinder such as that for η = 1 in Fig. 2. This may be considered to be a test result which can then be used to derive the stress-strain relationship for any size of specimen using Eq. 11 in the following form.

$$\varepsilon_{axgl} = \left((\varepsilon_{ax})_{pop} - \varepsilon_{mat}\right)\frac{200}{L_{pr}} + \varepsilon_{mat} \quad (17)$$

This procedure has previously been described in deriving the size dependent stress-strain relationships in Fig. 2 such as the curve (η = ½) from the curve (η=1). All that is being done is the replacement of the test result at η=1 by Popovics' variation. Hence the size-dependent factor η in Eq. 2 can be easily incorporated into existing stress-strain relationships for use in member analyses as follows.

DEFORMATION BASED ANALYSIS

In order to incorporate a size-dependent stress-strain relationship, a size dependent member analysis is required. As the moment-curvature approach is strain based, it is not size dependent and, consequently, cannot incorporate the effects of size due to the mechanisms of tension-stiffening and concrete softening (Oehlers 2010; Oehlers et al 2011a; Oehlers et al 2011b; Oehlers et al 2012a). In contrast, a moment-rotation approach (Visintin et al 2012a; Visintin et al 2012b; Visintin et al 2012c) first proposed by Bachman (1970) is deformation based and consequently size dependent and can, therefore, incorporate the mechanics of size into the analysis.

The moment-rotation mechanism is illustrated in Fig. 10. A segment of length L_{seg} is subjected to a constant moment region as shown. A wedge can form anywhere within the segment but for convenience of explanation it will be shown symmetrical about the centre line, so that the left hand side of length L_{def} is the mirror image of the right hand side such that L_{def} is equal to half L_{seg}. Both ends of the segment are subject to an Euler-Bernoulli deformation, plane sections remaining plane; this causes a rotation θ so that the deformation, shown shaded, depends on the length of the segment L_{def} that is it is size dependent. Prior to concrete softening, L_{def} can be any size and it is convenient, but not essential, to choose a length which is a multiple of the crack spacing S_{cr} (Visintin et al 2112a; Visintin et al 2012b).

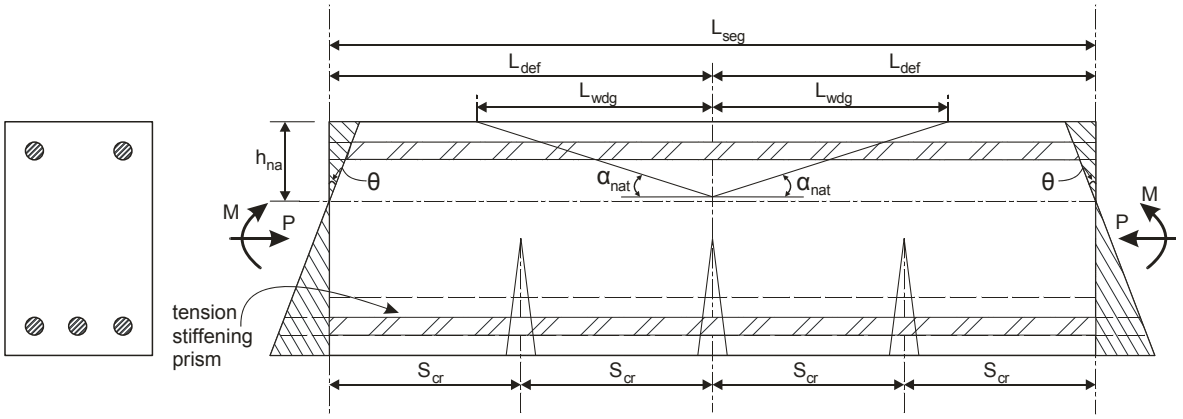

Fig. 10 Deformation based mechanism

Let us now consider the inclusion of softening. As described previously, the natural angle of the wedge α_{nat} can be determined from shear-friction properties and is about 26^o for normal concrete. Hence the length of the wedge L_{wdg} is approximately $h_{na}/\tan\alpha_{nat}$ where h_{na} is the neutral axis depth. It is important to ensure that the chosen segment length L_{def} is greater than L_{wdg} when it is intended to include the softening mechanism.

If a constant moment region is being analysed, then $2L_{def}$ in Fig. 10 is equal to the width of the constant moment region just as long as this exceeds $2L_{wdg}$. If on the other hand a variable moment region is being analysed as in Fig. 11, then part of the region *a*-*b* of length L_{def} must include the wedge and consequently be assumed to be a constant moment region and remainder *c*-*d* a variable moment region. As the distribution of moment shown shaded as *a*-*b*-*c*

overestimates the applied moment and consequently leads to a greater rotation, this can be considered to be a conservative approach. The conservatism can be reduced by making L_{def} as small as possible that is close to L_{wdg}.

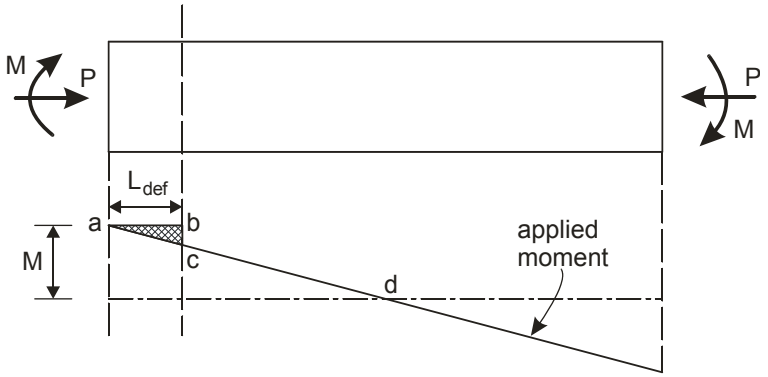

Fig. 11 Variable moment region

The deformation based analysis is shown in Fig. 12. The imposed deformations in Fig. 12(b) can be divided by L_{def} to get the strain distribution in Fig. 12(c). In the tension region, the force in the reinforcement can be derived from the strain distribution which is exactly the same approach as the strain based moment-curvature approach and, hence, ignores tension-stiffening. Alternatively, tension-stiffening can be included by deriving the force in the reinforcement through the partial-interaction analysis of the tension-stiffening prism in Fig. 12(b) (Haskett et al 2009; Haskett et al 2009b; Haskett et al 2009c; Mohamed Ali, M.S. 2012).

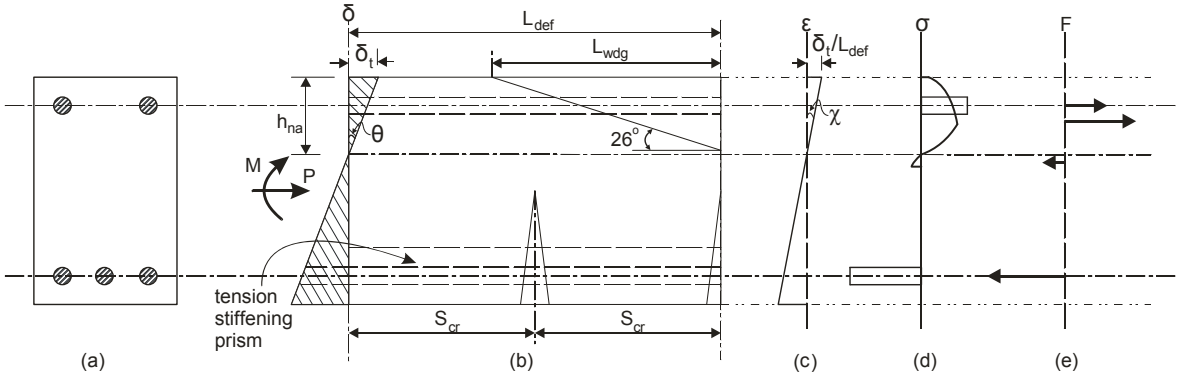

Fig. 12 Deformation based analysis

In the compression region in Fig. 12, the wedge mechanism is automatically accounted for by using a size-dependent stress-strain relationship which depends on the length of the segment

L_{def}. From the segmental analysis in Fig. 10, L_{def} is $L_{seg}/2$ which is equivalent to $L_{pr}/2$. Hence Eq. 14 which applies when the prism length is 200 mm, such that L_{def} is 100 mm, can be written as

$$(\varepsilon_{co})_{L_{def}=100} = 4.76 \times 10^{-6} f_{co} + 2.13 \times 10^{-3} \quad (18)$$

and Eq. 17 can be written as

$$(\varepsilon_{axgl}) = ((\varepsilon_{ax})_{pop} - \varepsilon_{mat}) \frac{100}{(L_{def})_{mem}} + \varepsilon_{mat} \quad (19)$$

where the units are in N and mm.

It can be seen in Fig. 12 that the components (c), (d) and (e) of the deformation based analysis are exactly the same as the standard moment-curvature analysis except that the concrete compressive properties are now size-dependent. The analysis in Fig. 12 can be used to derive the variation of the moment-rotation as in Fig. 13(a), which are derived using the stress-strain relationships for 25, 50, 75 and 100MPa concrete as in Figure 14 using Eqs. 16 and 17. The moment-rotation relationships can then be converted to moment-curvature by dividing the rotation by L_{def} as in Fig. 13(b) which can then be used to derive the variation in the flexural rigidity EI with moment as in Fig. 13(c). These results can then be used to analyse a member over its full length (Oehlers et al 2012b) that is not only in the softening region *a-c* in Fig. 11 but also in the rest of the member such as along *c-d* in Fig. 11.

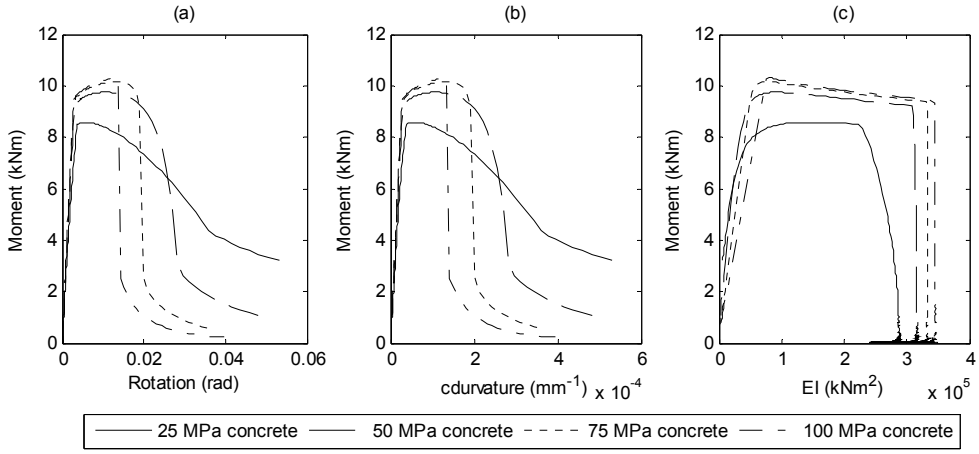

Fig. 13 Outputs from deformation analysis

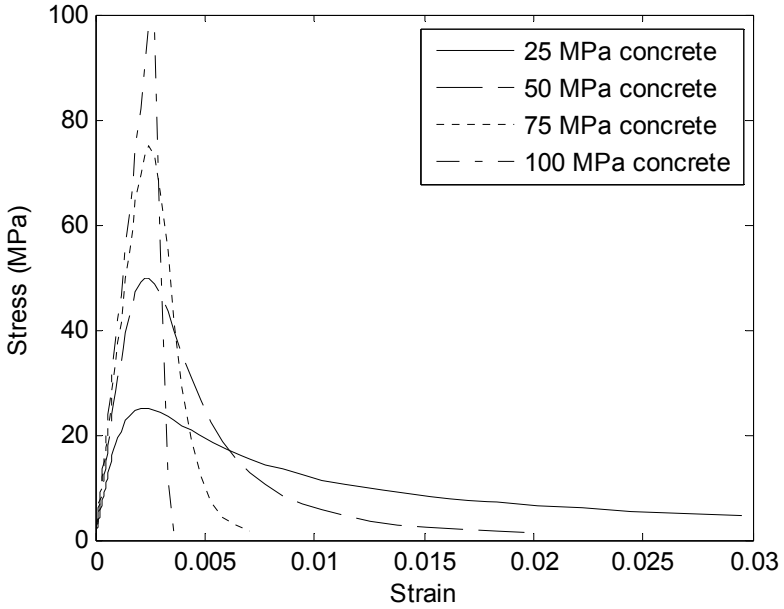

Figure 14 Stress strain relationships for deformation analysis

The method of deformation in the concrete compression zone of depth h_{na} in Fig. 10 can be visualised as follows. As the rotation θ is increased in Fig. 10, the concrete in compression follows the path *a*-*b* in Fig. 2. Over this region *a*-*b*, the deformation of the concrete is governed purely by its material properties so that the results of the analyses in Fig. 13 are size independent, that is the variation in both curvature and flexural rigidity are independent of the chosen L_{def}.

Let us now increase the rotation in Fig. 12(b) so that parts of the concrete in compression follows the path *b*-*d*-*e* in Fig. 2. If the concrete in compression with stresses greater than that at *b* remains elastic so that the concrete material properties follow the path *b*-*c*, then all of the deformation between *b*-*c* and *b*-*d*-*e* is due to micro-cracking during the formation of the wedge. In this case, the results of the analyses in Fig. 13 would be size-dependent, that is dependent of the chosen L_{def}. In contrast, if the concrete material properties followed the path *b*-*d*-*e* in Fig. 2, that is if the strain-gauges in Fig. 1 followed the path *a*-*b*-*d*-*e* in Fig. 2, then there is no difference between the total deformation and that due to the material, so that the curvatures and flexural rigidities in Figs. Fig. 13 are independent of L_{def}. On further application of rotation θ, the compressive concrete follows the path *e*-*f* in Fig. 2 where major sliding of the wedges occur and in which the results in Fig. 13 are certainly size-dependent that is dependent on L_{def}.

The moment-rotation (M/θ) results in Fig. 13(a) are always size dependent but whilst the compressive concrete is governed purely by its material properties the conversion of the moment-rotation to moment-curvature and consequently moment-flexural rigidity is size independent (Visintin et al. 2012b). Any softening, whether in the ascending or descending branches, will make the results size dependent. In analyses, it is convenient to have results that

are size-independent as they can be used at any position of a member particularly whilst the concrete follows the ascending branch in Fig. 2. The non-linearity *b-d-e* in Fig. 2 has been exaggerated to illustrate the size-dependent conversion. In reality, the non-linearity in the ascending branch is an order of magnitude smaller than that in the descending branch as can be seen in Figs. 3-5. Hence, the effect is relatively minor compared with that of the descending branch and it may be more convenient in the analyses just to assume that the non-linearity *b-d-e* in Fig. 2 is purely due to material properties. It is felt that further experimental research similar to that of Kotsovos (1983), Van Mier (1986a) and Jansen et al (1995) is required to determine how much of the non-linearity *b-d-e* in Fig. 2 is due to material non-linearity, that is as measured by strain gauges at discrete positions and well away from the sliding zones as in Fig. 1, and how much is due to softening due to wedge formation to further refine the inputs into this theoretical model.

SUMMARY

Under compression, concrete contracts under material straining ε_{mat} and also contracts due to the shear-friction mechanism of wedge sliding which produces an effective strain ε_{wdg}. The effective strain ε_{wdg} is both size and shape dependent; that is the effective strain varies if the shape L_{pr}/d_{pr} is fixed and L_{pr} is varied and vice versa. To quantify ε_{wdg} through the material testing of prisms, it is necessary to measure the total contraction ε_{axgl} in prisms in which L_{pr}/d_{pr} is greater than or equal to 2 to ensure that the natural formation of the wedge in the prism is the same as that in an RC member. From this approach, the size-dependent stress-strain relationship can be derived: from tests on prisms of one length; and also from published stress-strain curves. These size-dependent stress-strain relationships can be used in a size-dependent moment-rotation analysis to quantify the variation in curvature and flexural-rigidity at all levels of loading for the analysis of RC flexural members.

Allowing for both size and shape, 855 published test results were reanalysed to obtain the relationship between ε_{co} and f_{co}. It was found that allowing for both shape and size substantially reduced the scatter. However it is felt that a further reduction in scatter could be achieved if the parameters that affect the shear-friction behaviour, such as the aggregate size and strength, were also catered for. It is also suggested that further experimental research is required in quantifying softening in the ascending branch.

The major outcome of this research is the ability to develop the size-dependent stress-strain relationships from one size of prism test. This should help in refining existing stress-strain models as well as reduce the cost of deriving stress-strain models for new types of concrete such as steel or polymer fibre concrete or concretes that do not use stone based aggregates such as the use of oil palm kernel. Furthermore, the ability to use these size-dependent stress-strain relationships in size-dependent deformation based analyses should speed up the development of simple design rules for both flexural strength and ductility.

NOTATION

D_{ax}	axial deformation of a prism
d_{pr}	width of prism or cylinder
Exp.	experimental
E_c	concrete modulus; secant modulus when non-linear
EI	flexural rigidity; secant stiffness of M/ χ
F	force profile
f_{co}	peak stress; concrete strength
h_{cr}	widening of shear-friction sliding plane
H_{wdg}	axial component of Δ_{wdg}
h_{na}	depth of neutral axis
L_{def}	deformation length in M/ θ analysis; $L_{seg}/2$
L_{pr}	length of prism or cylinder
L_{pr-1}	length of prism 1; length of standard prism
L_{pr-2}	length of prism 2; length of non-standard prism
L_{seg}	segment length in deformation based analysis
L_{wdg}	axial length of wedge
M	moment
M/ θ	moment rotation analysis; deformation based analysis
M/ χ	moment curvature analysis; strain based analysis
No.	number of tests in a group from which mean values determined
P	axial load
S_{cr}	crack spacing
Theo.	theoretical
α	angle of wedge sliding plane to the axis
α_{nat}	natural angle of α; α when wedge unrestricted by end restraints; about 26^o
δ	deformation profile; axial deformation
δ_t	δ at top surface
Δ_{cr}	slip along the shear-friction sliding plane
Δ_{wdg}	slip along the wedge interface that is Δ_{cr}
ε	strain profile
ε_{axgl}	global axial strain; total strain due to material contraction and wedge sliding

$[(\varepsilon_{axgl-1})_n]_{des}$ ε_{axgl} in descending branch of prism 1 at n^{th} stress level

$[(\varepsilon_{axgl-1})_n]_{asc}$ ε_{axgl} in ascending branch of prism 1 at n^{th} stress level

$(\varepsilon_{ax)pop}$ axial strain in Popovics' expression

ε_{axlc} local axial strain; local strains as measured by strain gauges

ε_{co} strain at f_{co}

ε_{mat} material strain; strain due to material contraction

$(\varepsilon_{mat})_n$ ε_{mat} at n_{th} stress level

$(\varepsilon_{mat})_x$ ε_{mat} at stress level *x*

ε_{wdg} effective strain due to wedge sliding; $2H_{wdg}/L_{pr}$

η ratio of prism or cylinder lengths; L_{pr-1}/L_{pr-2}

θ rotation

μ slenderness ratio; L_{pr}/d_{pr}; prism slenderness

σ stress profile

σ_{ax} axial stress; longitudinal stress

$(\sigma_{ax})_n$ n^{th} level of axial stress

$(\sigma_{ax})_x$ axial stress *x*

σ_{cr} normal stress to shear-friction sliding plane

τ_{cr} shear stress along shear-friction sliding plane

χ curvature

ACKNOWLEDGEMENTS

The authors would like to acknowledge the support of both the Australian Research Council ARC Discovery Project DP0985828 'A unified reinforced concrete model for flexure and shear', and the University of Malaya, Malaysia, Ministry of Higher Education High Impact Research Grant UM.C/HIR/MOHE/ENG/36 'Strengthening Structural Elements For Load and Fatigue using Advanced Techniques'.

REFERENCES

ACI Committee 363 (1992), "State of the art report on high strength concrete", ACI Publication 363R-92, American Concrete Institute, Detroit.

Ahmad, S. H., and Shah, S. P. (1982). "Stress-strain curves of concrete confined by spiral reinforcement". ACI Journal, Title no. 79-46, 484-490.

Ahmad, S. H., and Shah, S. P. (1985). “Behavior of hoop confined concrete under high strain rate”. ACI Journal, Title no. 82-55, 634-647.

Ansari, F., and Li, Q. (1998). “High-strength concrete subjected to triaxial compression”. ACI Materials Journal, Vol. 95, No. 6, 747-755.

Attard, M., and Setunge, S. (1996). “Stress-strain relationship of confined and unconfined concrete”, ACI Mater. J., 95(6), 747-755.

Assa, B., Nishiyama, M., and Watanabe, F. (2001). “New approach for modeling confined concrete. I: Circular columns.” J. Struct. Eng., 127, 743–750.

Bachman, H. (1970). “Influence of shear and bond on rotational capacity of reinforced concrete beams.” Publications, IABSE, Zurich, Vol.30, Part II, pp11-28.

Bazant, Z. P. (1989). “Identification of strain softening constitutive relation from uniaxial tests by series coupling model for localization”. Cement and Concrete Research, 19, 937-977.

Bazant, Z. P., Ozbolt, J. and Eligehausen, R. (1994). “Fracture size effect: review of evidence for concrete structures”. Journal of Structural Engineering, Vol.120, No. 8, 2377-2398.

Bellotti, P. R. (1991). “Cylinder tests: experimental technique and results”. Materials and Structures, Vol. 24, 45-51.

Benzaid, R., Mesbah, H., and Chikh, N. E. (2010). “FRP confined concrete cylinders: Axial compression experiments and strength model”. Vol. 29, No. 16, 2469-2488.

Berthet, J. F., Ferrier, E., and Hamelin, P. (2005). “Compressive behavior of concrete externally confined by composite jackets. Part A: experimental study”. Construction and Building Materials, 19, 223–232.

Bischoff, P. H., and Perry, S. H. (1991). “Compressive behaviour of concrete at high strain rates”. Materials and Structures, 24(144), 425-450.

Bischoff, P. H., and Perry, S. H. (1995). “Impact behaviour of plain concrete loaded in uniaxial compression”. Journal of Engineering Mechanics, Vol. 121, No. 6, 685-693.

British Standards Institution (1996) DD ENV:1992-1-2 Eurocode 2: Design of Concrete Structures.

Candappa, D.P., Setunge, S., and Sanjayan, J.G. (1999), “Stress versus strain relationship of high strength concrete under high lateral confinement”, Cement and Concrete Research 29, 1977–1982.

Candappa, D.P., Sanjayan, J.G., and Setunge, S. (2001), “Complete Triaxial Stress-strain Curves of High-strength Concrete”, Journal of Materials in Civil Engineering, Vol. 13, No. 3, 209-215.

Carrasquillo, R. L., Nilson, A. H., and Slate, F. O. (1981). “Properties of high strength concrete subject to short term load”. ACI Journal, Title no. 78-14, 171-177.

Carreira, D.J., and Chu, K.H. (1985). “Stress-strain relationship for plain concrete in compression”, ACI J. 82, pp. 797-804.

CEB-FIP (1990). “Model Code for the Design of Concrete Structures”. Thomas Telford, London.

Choi, S., Thienel, K. C., and Shah, S. P. (1996). “Strain softening of concrete in compression under different end constraint”. Mag. Concrete Res., London, England, 48(75), 103-115.

Corley, W. G. (1966). “Rotational capacity of reinforced concrete beams”. J. Struct. Div. Proc of ASCE, ST5, 121-146.

Cusson, D., and Paultre, P. (1995). “Stress strain model for confined high-strength concrete”. Journal of Structural Engineering, Vol. 121, No.3, 468-477.

De Nicolo, B., Pani, L., and Pozzo, E. (1994). “Strain of concrete at peak compressive stress for a wide range of strengths”. Materials and Structures, 27, 206-210.

Desayi, P., Iyengar, K. T. S. R., and Reddy, T. S. (1979). “Equation for stress-strain curve of concrete confined in circular steel spiral”. Material and constructions, Vol. 11, No. 65, 339-345.

Dilger, W. H., Koch, R., and Kowalczyk, R. (1984). “Ductility of plain and confined concrete under different strain rates”. ACI Journal, Title no. 81-11, 73-81.

Domone, P. L. J. and Illston, J. M. (2001). “Construction Materials Their Nature and Behaviour”. Third edition by Spon Press.

Fantilli, A.P., Iori, I., and Vallini, P.. (2007). “Size effect of compressed concrete in four point bending RC beams”. Engineering Fracture Mechanics, 74, 97-108.

Gardner, N. J. (1969). “Triaxial behaviour of concrete”. ACI Journal, Title no. 66-15, 136-146.

Gobbi, M. E. and Ferrara, G. (1995). “Strain softening of concrete under compression”. ENEL-CRIS, Milano.

Harmon, M. I., and Neeley, B. D. (1993). “Triaxial characterization of high-strength portland cement concrete”. Transportation research record, 1328, Transportation Research Board, Washington, D. C., 73-77.

Harmon, T.G., Ramakrishnan, S. and Wang, E.H. (1998), “Confined concrete subjected to uniaxial monotonic loading”, Journal of Engineering Mechanics, Vol. 124, No.12, 1303-1309.

Haskett, M., Oehlers, D.J., Mohamed Ali, M.S., and Wu, C., (2009a) “Rigid body moment-rotation mechanism for reinforced concrete beam hinges” Engineering Structures, 31, 1032-1041.

Haskett, M., Oehlers, D.J., Mohamed Ali and Wu, C. (2009b) “Yield penetration hinge rotation in reinforced concrete beams”. ASCE Structural Journal, Vol. 135, Issue 2, Feb., 130-138.

Haskett, M., Mohamed Ali M.S., Oehlers D.J., and Wu, C., (2009c) “Influence of bond on the hinge rotation of FRP plated beams”, special edition of Advances in Structural Engineering, Vol. 12, No. 6, pp 833-843.

Haskett, M., Oehlers, D.J., Mohamed Ali M.S., and Sharma, S. K.. (2010) “The shear friction aggregate interlock resistance across sliding planes in concrete”. Magazine of Concrete Research, Vol. 62, Issue 12, December, pp 907-924.

Haskett, M., Oehlers, D.J., Mohamed Ali, M.S., and Sharma, S.K., (2011) “Evaluating the shear-friction resistance across sliding planes in concrete”. Engineering Structures, 33, pp 1357-1364.

Hillerborg, A. (1989). “The compression stress-strain curve for design of reinforced concrete beam”. Fracture mechanics: application to concrete, American Concrete Institute, Detroit, Mich., 281-294.

Hillerborg, A. (1990). “Fracture mechanics concepts applied to moment capacity and rotational capacity of reinforced concrete beams”. Engineering Fracture Mechanics 35(1-3), 233-240.

Hognested, E. (1951), “A study of combined bending and axial load in reinforced concrete members” Bulletin No399, Engineering Experiment Station, University of Illinois.

Hsu, L. S., and Hsu, C. T. (1994). “Stress-strain behaviour of steel fiber high strength concrete under compression”. ACI Structural Journal, Title no. 91-S44, 448-457.

Hudson, J. A., Crouch, S. L., and Fairhurst, C. (1972). “Soft, stiff and servo-controlled testing machines: a review with reference to rock failure”. Engrg. Geol., 6(3), 155-189.

Imran, I., and Pantazopoulou, S. J. (1996). “Experimental Study of Plain Concrete under Triaxial Stress”. ACI Materials Journal, Vol. 93, No. 6, 589-601.

Jansen, D. C., Shah, S. P., and Rossow, E. C. (1995). “Stress-strain results of concrete from circumferential strain feedback control testing”. ACI Materials Journal, Vol. 92, No. 4, 419-428.

Jansen, D. C., and Shah, S. P. (1997). “Effect of length on compressive strain softening of concrete”. Journal of Engineering Mechanics, Vol. 123, No. 1, 25-35.

Jiang, T., Teng, J. G. (2007). “Analysis-oriented stress-strain models for FRP confined concrete”. Engineering Structures, 29, 2968-2986.

Karabinis, A. I., and Rousakis, T. C. (2002). “Concrete confined by FRP material: A plasticity approach”. Eng. Struct., 24, 923–932.

Kent, D. C., and Park, R. (1971), “Flexural members with confined concrete.” J. Struct. Div. ASCE, 97(7), 1969–1990.

Konig, G., Simsch, G. and Ulmer, M. (1994). “Strain softening of concrete”. Technical University of Darmstadt, 67pp.

Kotsovos, M. D. (1983). “Effect of testing techniques on the post-ultimate behaviour of concrete in compression”. RILEM Materials and Structures, 16, 3-12.

Kshirsagar, S., Lopez-Anido, R. A., and Gupta, R. K. (2000). “Environmental Aging of Fiber-Reinforced Polymer-Wrapped Concrete Cylinders”. ACI Materials Journal, Vol. 97, No. 6, 703-712.

Lahlou, K., Aitcin, P. C. and Chaallal, O. (1992). “Behaviour of high-strength concrete under confined stresses”. Cement and Concrete Composites, 14, 185-193.

Lam, L., Teng, J. G., Cheung, C. H., and Xiao, Y. (2006). “FRP confined concrete under cyclic axial compression”. Cem. Concr. compos., 28(10), 948-958.

Lee, Y. H., William, K. and Kang, H. D. (1995). “Experimental observation of concrete behaviour under uniaxial compression”. Fracture Mechanics of concrete structures, FRAMCOS-2 Conf. Aedificatio Publishers, Freiburg, Germany, pp. 397-414.

Lu, X. B., and Hsu, C. T. (2006). “Behavior of high strength concrete with and without steel fiber reinforcement in triaxial compression”. Cement and Concrete Research, 36, 1679-1685.

Mander, J. B., Priestley, M. J. N., and Park, R. (1988). “Theoretical stress-strain model for confined concrete”. J. Struct. Eng., 114(8), 1804-1826.

Markeset, G. (1994). “Comments on size dependence and brittleness of high strength concrete”. SINTEF Report, STF F94104.

Markeset, G., and Hillerborg, A. (1995). “Softening of concrete in compression localization and size effects”. Cement and Concrete Research, Vol 25, No. 4, pp. 702-708.

Matthys, S., Toutanji, H., Audenaert, K., and Taerwe, L. (2005). “Axial Load Behavior of Large-Scale Columns Confined with Fiber-Reinforced Polymer Composites”. ACI Structural Journal, V. 102, No. 2, 258-267.

Mattock, A.H. (1974), “Shear transfer in concrete having reinforcement at an angle to the shear plane”. ACI Special publication, 42(2), 17-42.

Mendis, P., Pendyala, R., and Setunge, S. (2000). “Stress-strain model to predict the full-range moment curvature behavior of high-strength concrete sections”. Mag. Concrete Res., 52(4), 227–234.

Mills, L. L., and Zimmerman, R. M. (1970). “Compressive strength of plain concrete under multiaxial loading conditions”. ACI Journal, Title No. 67-47, 802-807.

Mohamed Ali, M.S., Oehlers, D.J., and Griffith, M.C. (2010) “The residual strength of confined concrete”, Advances in Structural Engineering,. Vol. 13, No. 4, pp603-618.

Mohamed Ali M.S., Oehlers, D.J., Haskett, M., and Griffith, M.C.. (2012) “The discrete rotation in reinforced concrete beams”. ASCE Journal of Engineering Mechanics, Accepted 24/3/12.

Montoya, E., Vecchio, F. J., and Sheikh, S. A. (2006). “Compression field modeling of confined concrete constitutive models”. JOURNAL OF MATERIALS IN CIVIL ENGINEERING, Vol. 18, No. 4, 510-517.

Nanni, A., and Bradford, N. M. (1995). “FRP jacketed concrete under uniaxial compression.” Constr. Build. Mater., 9(2), 115–124.

Oehlers, D.J., (2010) “The hunt for the elusive concept”. Len Hollaway’s special edition of Advances in Structural Engineering. Vol. 13, No. 5, September, pp755-772.

Oehlers, D.J., Mohamed Ali M.S., Haskett, M., Lucas, W., Muhamad, R., and Visintin, P., (2011a) “FRP reinforced concrete beams – a unified approach based on IC theory”. ASCE Composites for Construction , May/June, Vol. 15, No. 3, pp293-303.

Oehlers, D.J, Haskett, M., Mohamed Ali M.S., Lucas, W., and Muhamad, R., (2011b) “Our obsession with curvature in reinforced concrete modelling”. Advances in Structural Engineering, Vol. 14, No. 3, pp 399-412.

Oehlers, D.J., Mohamed Ali M.S., Griffith, M.C., Haskett, M., and Lucas, W., (2012a) “A generic unified reinforced concrete model”, Proc. ICE , Structures and Buildings, Vol. 165, Issue SB1, February, pp 27-49.

Oehlers, D.J., Visintin, P. And Haskett, M., (2012b) “The ideal bond characteristics for reinforced concrete members”. Bond in Concrete Conference, Brescia, Italy. 18/6/12 – 20/6/12.

Park, R., Priestley, M. J. N., and Gill, W. D. (1982). “Ductility of squareconfined concrete columns.” J. Struct. Div. ASCE, 108(4), 929–950.

Pessiki, S., Graybeal B., and Mudlock, M. (2001) “Proposed design of high-strength spiral reinforcement in compression members”. ACI Structural Journal, Vol. 98, No. 6, 799-810.

Popovics, S. (1970). “A review of stress-strain relationships for concrete”. ACI Journal, Title no. 67-14, 243-248.

Popovics, S. (1973), “A numerical approach to the complete stress–strain curve of concrete.” Cem. Concr. Res., 3(5), 583–599.

Ramesh, K., Seshu, D. R., and Prabhakar, M. (2003). “Constitutive behaviour of confined fibre reinforced concrete under axial compression”. Cement & Concrete Composites 25, 343–350.

Richart, F. E., Brandtzaeg, A., and Brown, R. L. (1928). “Study of the Failure of Concrete under Combined Compressive Stresses,” Bulletin 185, University of Illinois Engineering Station, Urbana.

Richart, F. E., Brantzaeg, A., and Brown, R. L. (1929). “The failure of plain and spirally reinforced concrete in compression”. Bulletin No. 185, Engineering Experiment Station, University of Illinois, Urbana.

Ros, M. (1950), “Material-technological foundation and problems of reinforced concrete”, Bericht No.162, Zurich, Switzerland.

Rokugo, K., and Koyanagi, W. (1992). “Role of compressive fracture energy of concrete on the failure behaviour of reinforced concrete beam”. Application of fracture mechanics to reinforced concrete. Elsevier Applied Science, New York, 437-464.

Rutland, C.A., Wang, M.L. (1997), “The effects of confinement on the failure orientation in cementitious materials experimental observations”, Cement and concrete composites Vol. 19, 149-160.

Saatcioglu, M., and Razvi, S. R. (1992). “Strength and ductility of confined concrete.” J. Struct. Eng., 118(6), 1590–1607.

Sangha, C. M. and Dhir, R. K. (1972). “Strength and complete stress strain relationships for concrete tested in uniaxial compression under different test conditions”. RILEM, 5, 361-370.

Sargin, M., Ghosh, S. K., and Handa, V. K. (1971). “Effects of lateral reinforcement upon the strength and deformation properties of concrete.” Mag. Concrete Res., 23, 99–110.

Scott, B. D., Park, R., and Priestley, M. J. N. (1982). “Stress-Strain Behavior of Concrete Confined by Overlapping Hoops at Low and High Strain Rates”. ACI Journal, Title no. 79-2, 13-27.

Setunge, S., Attard, M. M., and Darvall, P. (1993). “ultimate strength of confined very high strength concrete”. ACI, Structure Journal, 90(6), 632-641.

Shah, S. P. and Ahmad, S.H. (1985), “Structural properties of high strength concrete and its implication for precast prestressed concrete”, Portland Cement Inst. J. 30, No.6, pp92-119.

Shah, S. P., and Sankar, R. (1987). “Internal cracking and strain softening response of concrete under uniaxial compression”. ACI Mat. J., 84(3), 200-212.

Shahawy, M., Mirmiran, A., and Beitelmann, T. (2000). “Tests and modelling of carbon-wrapped concrete columns.” Composites, Part B, 31, 471–480.

Shehata, I. A. E. M., Carneiro, L. A. V. and Shehata, L. C. D. (2002). “Strength of short concrete columns confined with CFRP sheets”. Materials and Structures, Vol. 35, 55-58.

Sfer, D., Carol, I., Gettu, R. and Etse, G. (2002). “Study of the behaviour of concrete under triaxial compression”. Journal of Engineering Mechanics, Vol. 128, No.2, 156-163.

Silva, M. A. G., and Rodrigues, C. C. (2006). “Size and Relative Stiffness Effects on Compressive Failure of Concrete Columns Wrapped with Glass FRP”. Journal of Materials in Civil Engineering, Vol. 18, No. 3, 334-342.

Smith, G. M., and Young, L. E. (1956). “Ultimate Flexural Analysis Based on Stress-Strain Curves of Cylinders”. ACI Journal, Title No. 53-32, 597-609.

Smith, S. S., William, K. J., Gerstle, K. H., and Sture, S. (1989). “Concrete over the top, or is there life after peak?”. ACI Materials Journal, Vol. 86, No. 5, 491-497.

Tadros, G. S. (1970), “Plastic rotation of reinforced concrete members subjected to bending, axial load and shear”, PhD Thesis, University of Calgary.

Tasdemir, M. A., Tasdemir, C., Akyuz, S., Jefferson, A.D., Lydon, F.D., and Barr, B.I.G. (1998), “Evaluation of strains at peak stress in concrete:a three phase composite model approach”, Cement and concrete composites Vol. 20, 301-318.

Torrenti, J. M., Benaija, E. H., and Boulay, C. (1993). “Influence of boundary conditions on strain softening in concrete compression test”. J. Engrg. Mech., ASCE, 119(12), 2369-2384.

Toutanji, H. (1999). “Stress-strain characteristics of concrete columns externally confined with advanced fiber composite sheets.” ACI Mater. J., 96(3), 397–404.

Van Geel, H. J. G. M. (1984). “Uniaxial strain softening of concrete influence of specimen size and boundary shear”. Report BKO 94.09, Eindhoven Uni. of Tech., The Netherlands.

Van Mier, J. G. M. (1984). “Strain softening of concrete under multiaxial loading conditions”. PhD thesis, Eindhoven Uni. of Tech., The Netherlands.

Van Mier, J. G. M. (1986a). “Multiaxial strain-softening of concrete Part one: Fracture”. Materials and Structures, vol. 19, No. 111, pp 179-190.

Van Mier, J. G. M. (1986b). “Multiaxial strain-softening of concrete Part two: load-histories”. Materials and Structures, vol. 19, No. 111, pp 190-200.

Van Mier, J. G. M. et al. (1997), “Strain-softening of concrete in uniaxial compression”, Materials and Structures, vol. 30, pp 195-209.

Van Vliet, M. R. A., and Van Mier, J. G. M. (1996). “Experimental investigation of concrete fracture under uniaxial compression”. Mechanics of Cohesive-frictional Materials, 1, 115-127.

Visintin, P., Oehlers, D.J., Wu, C., and Haskett, M., (2012a) “A mechanics solution for hinges in RC beams with multiple cracks”. Engineering Structures, Vol. 36, pp 61-69.

Visintin, P., Oehlers, D.J., Wu, C., Haskett, M., (2012b) “A mechanics based hinge analysis for reinforced concrete columns”. ASCE Journal of Structural Engineering 20/6/11. Editor requires minor changes 29/8/12.

Visintin, P., Oehlers, D.J., Wu, C., and Griffith, M.C. (2012c) “The Cyclic Behaviour of Reinforced Concrete Beam Hinges”, Earthquake Engineering and Structural Dynamics Vol. 41 Issue 12, pp 1591-1608.

Vonk, R. (1992). “Softening of concrete loaded in compression”. PhD thesis, Eindhoven Uni. of Tech., The Netherlands.

Walraven, J. C. & Reinhardt, H. W. (1981), “Theory and Experiments on Mechanical Behaviour of Cracks in Plain and Reinforced Concrete Subjected to Shear Loading”, Heron, 26(1A), pp. 1-68.

Wang, P. T., Shah, S. P., and Naaman, A. E. (1978). “Stress-strain curves of normal and lightweight concrete in compression”. ACI Journal, Title no. 75-62, 603-611.

Watstein, D. (1953). “Effect of straining rate on the cpmpressive strength and elastic properties of concrete”. ACI Journal, Vol. 24, No. 8, 729-744.

Wee, T. H., Chin, M. S. and Mansur, M. A. (1996), “Strength-strain relationship of high strength concrete in compression”, Journal of Materials in Civil Engineering, 8(2), 70-76.

Weena, P. L., Sanjayan, J. G., and Sujeeva, S. (2005), “Stress–Strain Model for Laterally Confined Concrete”, Journal of Materials in Civil Engineering, ASCE pp 607-616.

Xiao, Y., and Wu, H. (2000). “Compressive behavior of concrete confined by carbon fiber composite jackets.” J. Mater. Civ. Eng., 12(2), 139–146.

Xiao, Q. G., Teng, J. G., and Yu, T. (2010), “Behavior and Modeling of Confined High-strength Concrete”, Journal of Composites for Construction, Vol. 14, No. 3, pp 249-259.

Xie, J., Elwi, A. E., And MacGregor, J. G. (1995). “Mechanical properties of three high-strength concretes containing silica fume”. ACI Materials Journal, Vol. 92, No. 2, 135-143.

Youssef, M. N., Feng, M. Q., and Mosallam, A. S. (2006). “Stress–strain model for concrete confined by FRP composites”. Composites: Part B, 38, 614–628.

Zhang, M. H. and Gjorv, O. E. (1991). “Mechanical properties of high-strength lightweight concrete”. ACI Materials Journal, Vol. 88, No. 3, 240-247.

APPENDIX: TEST DATA

Table 1. Prism tests with $\mu \geq 2$

Ref.	No.	d_{pr} (mm)	L_{pr} (mm)	μ	f_{co} (MPa)	ε_{co} (%)	E_c (GPa)	$\varepsilon_{co\text{-}200}$ (%)
Lahlou et al (1992)	2	100	200	2	46	0.27	25	0.27
	2				78	0.32	34	0.32
	2				113	0.31	43	0.31
Jansen et al (1995)	3	100	200	2	38.3	0.184	30.2	0.184
	3				39.4	0.18	30.2	0.18
	3				40.5	0.18	30.2	0.18
	5				59	0.222	34.1	0.222
	3				61	0.224	34.1	0.224
	3				64	0.226	34.1	0.226
	3				93.8	0.295	35.7	0.295
	5				96.7	0.298	35.7	0.298
	3				99.6	0.302	35.7	0.302
	3	76.2	152.4	2	34.5	0.177	29.4	0.163
	3	152.4	304.8		34.5	0.158	29.8	0.180
	3	76.2	152.4		62	0.224	33	0.215
	2	152.4	304.8		62	0.191	36	0.201
	5	76.2	152.4		103.4	0.299	35.3	0.298
	4	152.4	304.8		103.4	0.232	39.8	0.22
Jansen and Shah (1997)	1	100	200	2	42.8	0.216	27.5	0.216
	1		200	2	55.6	0.248	29.4	0.248
	1		250	2.5	44.1	0.221	28	0.237
	1		250	2.5	55.4	0.247	29.9	0.262
	1		300	3	50.1	0.226	29.6	0.254
	1		300	3	45.7	0.217	28.8	0.246
	1		350	3.5	51.4	0.223	29.7	0.260
	1		350	3.5	43.1	0.196	29.8	0.235
	1		400	4	46.8	0.199	30.3	0.244
	1		450	4.5	46.7	0.199	30.9	0.259
	1		450	4.5	47.7	0.209	30.4	0.274
	1		550	5.5	45.8	0.192	31.1	0.270
	1		550	5.5	45.4	0.19	30.9	0.265
	1		200	2	90.9	0.286	36.8	0.286
	1		200	2	93.1	0.297	35.7	0.297
	1		250	2.5	88.5	0.274	37.3	0.283
	1		250	2.5	88.1	0.269	37.5	0.278
	1		300	3	93.2	0.284	37.5	0.302
	1		300	3	90.8	0.281	37.6	0.301
	1		350	3.5	90.1	0.268	38.7	0.294
	1		350	3.5	92.6	0.277	38.9	0.306
	1		400	4	88.2	0.259	38.9	0.291
	1		450	4.5	88.6	0.268	38.3	0.314
	1		450	4.5	91	0.266	39.6	0.311
	1		550	5.5	90	0.262	39.5	0.322
	1		550	5.5	90.1	0.263	39.7	0.326
Amir (1996)	1	152	304	2	30.8	0.205	25.3*	0.249
	1				32.7	0.246	25.9*	0.308

Table 1. Prism tests with μ ≥ 2 continued

Ref.	No.	d_{pr} (mm)	L_{pr} (mm)	μ	f_{co} (MPa)	ε_{co} (%)	E_c (GPa)	$\varepsilon_{co\text{-}200}$ (%)
Ahmad and Shah (1982)	3	76.2	304.8	4	20.7	0.21	22*	0.268
	4		152.4	2	26.2	0.21	23.9*	0.185
	4				31.6	0.27	27.3*	0.200
	4				37.9	0.22	30.8*	0.230
	4				39.6	0.30	33.8*	0.273
	3				51.7	0.25	30.9*	0.230
	4				52.2	0.25	27.8*	0.260
	3				65.5	0.30	25.6*	0.233
Sangha and Dhir (1972)	6	50.8	101.6	2	41.5	0.341	28.3*	0.245
	6		127	2.5	41.4	0.345	28.3*	0.273
	6		152.4	3	41	0.343	28.2*	0.296
Sfer et al (2002)	1	150	300	2	32.8	0.18	27.3	0.207
	1				38.8	0.21	28.6	0.245
Xie et al (1995)	3	100	200	2	60.2	0.29	32.7*	0.29
	3				92.21	0.3	38.9*	0.3
	3				119	0.36	43.2*	0.36
Candappa et al (1999/2001)	2	100	200	2	40	0.24	28.2*	0.24
	2				60	0.24	32.8*	0.24
	2				74	0.25	35.4*	0.25
	2				101	0.27	40.7*	0.27
Gardener (1969)	1	76.2	152.4	2	40.2	0.36	28.0*	0.306
	1				36.8	0.36	27.0*	0.310
	1				36	0.37	26.8*	0.313
Attard and Setunge (1996)	1	100	200	2	120	0.3	55.7	0.3
	1				120	0.28	52.8	0.28
	1				110	0.28	55.4	0.28
	1				100	0.27	52.9	0.27
	1				132	0.34	49.3	0.34
	1				126	0.34	49.4	0.34
	1				118	0.28	57.8	0.28
	1				110	0.28	58.7	0.28
	1				100	0.26	54.6	0.26
	1				96	0.28	55.8	0.28
	1				60	0.21	45.1	0.21
Ahmad and Shah (1985)	4	76.2	152.4	2	48.13	0.26	30.0*	0.236
	4	76.2	152.4		52.54	0.29	31.0*	0.261
	3	76.2	152.4		37.3	0.23	27.2*	0.208
	2	152.4	304.8		29.65	0.18	25.0*	0.212
	3	76.2	152.4		37.92	0.23	27.3*	0.208
	3	76.2	152.4		43.1	0.25	28.7*	0.226
	3	76.2	152.4		43.8	0.28	28.9*	0.249
	4	76.2	152.4		39.58	0.31	27.8*	0.226
	4	76.2	152.4		51.71	0.35	30.8*	0.307
	3	76.2	152.4		31.65	0.27	25.6*	0.235
	2	152.4	304.8		29.79	0.24	25.0*	0.303
	3	76.2	152.4		37.23	0.27	27.2*	0.238
	3	76.2	152.4		36.96	0.29	27.1*	0.253
	3	76.2	152.4		36.54	0.32	27.0*	0.276

Table 1. Prism tests with μ ≥ 2 continued

Ref.	No.	d_{pr} (mm)	L_{pr} (mm)	μ	f_{co} (MPa)	ε_{co} (%)	E_c (GPa)	$\varepsilon_{co\text{-}200}$ (%)
	12				42.7	0.212	37.6	0.212
	5				63.2	0.216	41.8	0.216
	5				70.2	0.21	43	0.21
	5				65.1	0.216	41.5	0.216
	3				70.5	0.206	40.4	0.206
	5				69.7	0.212	41.5	0.212
	3				71.5	0.213	41.4	0.213
	5				63.6	0.228	42.6	0.228
	5				85.9	0.226	45	0.226
	5				90.2	0.243	44.4	0.243
	5				78.3	0.232	44.3	0.232
	5				85.9	0.231	44.3	0.231
	5				81.2	0.224	43.9	0.224
	3				88.1	0.227	44.5	0.227
	5				81.6	0.211	43.8	0.211
	3				82.6	0.216	44.2	0.216
	5				84.8	0.252	47.2	0.252
	5				85.6	0.232	45.6	0.232
	5				96.2	0.237	46.6	0.237
Wee et al (1996)	2	d=100	200	2	46.4	0.25	35.2	0.25
	2				65.8	0.237	40.8	0.237
	2				73.9	0.243	41.6	0.243
	2				87.6	0.243	44.5	0.243
	2				93.1	0.244	45.4	0.244
	2				95.3	0.242	45.2	0.242
	2				100.6	0.258	45.8	0.258
	2				102.1	0.256	46.1	0.256
	7				102.8	0.247	46.7	0.247
	2				106.3	0.251	48.4	0.251
	5				104.2	0.249	46.3	0.249
	5				92.8	0.242	45.8	0.242
	3				94.6	0.228	47.3	0.228
	5				94.4	0.229	46.3	0.229
	3				96.6	0.232	46.5	0.232
	5				91.5	0.228	45.9	0.228
	3				93.6	0.219	47.1	0.219
	5				91.7	0.266	46	0.266
	5				119.9	0.275	49.1	0.275
	5				125.6	0.273	50.9	0.273
	1				21	0.27	22.1*	0.232
	1				41	0.29	28.2*	0.256
	1				51	0.3	30.6*	0.268
	1				74	0.35	35.5*	0.317
Wang et al (1978)	1	76.2	152.4	2	24	0.29	23.2*	0.242
	1				31	0.31	25.4*	0.267
	1				38.5	0.32	27.5*	0.282
	1				55	0.38	31.5*	0.332

* estimated

Statement of Authorship

Size dependent axial and lateral stress strain relationships for actively confined concrete. Accepted for publication by Advances in Structural Engineering on 05/06/2014.

Visintin, P

Supervised and contributed to research

I hereby certify that the statement of contribution is accurate and I give permission for the inclusion of the paper in this thesis

Signed……..Date……

Chen, Y (Candidate)

Performed analyses and developed model

I hereby certify that the statement of contribution is accurate and I give permission for the inclusion of the paper in this thesis

Signed……Date……

Oehlers, DJ

Supervised and contributed to research

I hereby certify that the statement of contribution is accurate and I give permission for the inclusion of the paper in this thesis

Signed……..Date……

Visintin, P., Chen. Y. & Oehlers, D.J. (2015) Size dependent axial and lateral stress strain relationships for actively confined concrete
Advances in Structural Engineering, v. 18 (1), pp. 1-20

Chapter 3: Extracting Shear Friction Properties from Cylinder Tests

Introduction

The two papers in Chapter 2 have only used shear friction mechanism, furthermore the paper of this Chapter, “Concrete shear-friction material properties: derivation from actively confined compression cylinder tests” shows how to quantify the shear-friction material properties across potential sliding planes, that is the relationship between the shear stress, normal stress, crack widening and interface slip across an initially uncracked concrete sliding plane, from those relatively readily available and inexpensive compression tests. The shear-friction material properties are then presented in a generic form that is directly applicable for the papers in Chapter 4. The importance and application of the proposed shear-friction expressions are also illustrated.

List of manuscripts

Chen, Y., Visintin, P., and Oehlers, D.J. (2014). “Concrete shear-friction material properties: derivation from actively confined compression cylinder tests.” Submitted to Advances in Structural Engineering on 26/03/2014.

Statement of Authorship

Concrete shear-friction material properties: derivation from actively confined compression cylinder tests. Submitted to Advances in Structural Engineering on 26/03/2014.

Chen, Y (Candidate)

Performed analyses and developed model

I hereby certify that the statement of contribution is accurate and I give permission for the inclusion of the paper in this thesis

Signed……..Date……

Visintin, P

Supervised and contributed to research

I hereby certify that the statement of contribution is accurate and I give permission for the inclusion of the paper in this thesis

Signed……Date……

Oehlers, DJ

Supervised and contributed to research

I hereby certify that the statement of contribution is accurate and I give permission for the inclusion of the paper in this thesis

Signed……Date……

Chen. Y., Visintin, P. & Oehlers, D.J. (2015) Concrete Shear-Friction Material Properties: Derivation from Actively Confined Compression Cylinder Tests *Advances in Structural Engineering, v. 18 (8), pp. 1173-1185*

Chapter 4: Applications of Shear Friction Properties

Introduction

Chapter 4 consists of three papers that show the applications of shear friction properties proposed in Chapter 3. The first paper shows how these shear-friction material properties can be used directly to quantify the shear-sliding capacity and also how these shear-friction material properties can also be used to analyse standard shear-sliding tests in order to extract more accurate shear-sliding capacities. It is then shown how these shear-sliding capacities can be used as the failure criteria to quantify the shear capacities of reinforced concrete beams. The main aim of the first paper is to show that the use of mechanics and shear-friction material properties can not only quantify apparently diverse behaviours such as the shear capacity and flexural ductility but also reduce the cost of developing new RC products and in developing more accurate and less conservative design rules. In the second paper, two distinct cylinder failure modes have been examined: that of the circumferential wedge that is common in standard cylinders with aspect ratios of 2:1; and that of the single sliding plane that occurs at higher aspect ratios. Importantly, from this is shown that although each mechanism is defined by the same shear friction material properties different stress strain relationships result and this may explain some of the scatter of test results. In the third paper, mechanics solutions have been developed to show the influence of specimen size, that is both diameter and height, on the stress-strain relationship of axially loaded FRP confined concrete cylindrical specimens using shear friction theory. Due to the capacities of the testing machines, it is often quite difficult to test large or full-scale FRP wrapped specimens under pure compression in order to extract their axial-stress/axial-strain relationships. The third paper shows that through the mechanics of shear friction, how small scale FRP wrapped specimens suitable for compression testing can be designed so that the stress/strain relationship of the full scale member under pure compression can be extracted from those of the small test specimen.

List of manuscripts

Chen, Y., Zhang, T., Visintin, P., and Oehlers, D.J. (2014). “Concrete shear-friction material properties: application to shear capacity of RC beams of all sizes.” Submitted to Advances in Structural Engineering on 26/03/2014.

Visintin, P., Chen, Y., and Oehlers, D. (2014). “Simulating the behaviour of FRP confined cylinders using the shear friction mechanism.” Submitted to ASCE Composites for Construction on 10/10/2014.

Chen, Y., Visintin, P., Oehlers, D.J. (2014). “Extracting size dependent stress/strain relationships from FRP confined concrete cylinders for varying diameters and heights.” To be submitted to Composite Structures.

Statement of Authorship

Concrete shear-friction material properties: application to shear capacity of RC beams of all sizes. Submitted to Advances in Structural Engineering on 26/03/2014.

Chen, Y (Candidate)

Performed analyses and developed model

I hereby certify that the statement of contribution is accurate and I give permission for the inclusion of the paper in this thesis

Signed……..Date……

Zhang, T.

Performed analyses related to shear capacity of RC beams

I hereby certify that the statement of contribution is accurate and I give permission for the inclusion of the paper in this thesis

Signed……..Date……

Visintin, P

Supervised and contributed to research

I hereby certify that the statement of contribution is accurate and I give permission for the inclusion of the paper in this thesis

Signed……Date……

Oehlers, DJ

Supervised and contributed to research

I hereby certify that the statement of contribution is accurate and I give permission for the inclusion of the paper in this thesis

Signed……Date……

Chen. Y., Zhang, T., Visintin, P. & Oehlers, D.J. (2015) Concrete Shear-Friction Material Properties: Application to Shear Capacity of RC Beams of all Sizes *Advances in Structural Engineering, v. 18 (8), pp. 1187-1198*

Statement of Authorship

Simulating the behaviour of FRP confined cylinders using the shear friction mechanism. Submitted to ASCE Composites for Construction on 10/10/2014.

Visintin, P

Supervised and contributed to research

I hereby certify that the statement of contribution is accurate and I give permission for the inclusion of the paper in this thesis

Signed……..Date……

Chen, Y (Candidate)

Performed analyses and developed model

I hereby certify that the statement of contribution is accurate and I give permission for the inclusion of the paper in this thesis

Signed…….Date……

Oehlers, DJ

Supervised and contributed to research

I hereby certify that the statement of contribution is accurate and I give permission for the inclusion of the paper in this thesis

Signed……Date……

Simulating the behaviour of FRP confined cylinders using the shear friction mechanism

Visintin, P., Chen, Y., and Oehlers, D.J.

Abstract

The axial compressive behaviour of concrete confined with FRP has received much attention over the past two and a half decades, with over 90 empirical and semi-empirical models developed to predict the compressive stress strain behaviour. While there is no doubt that in general these models show a good correlation to the dataset from which they were derived, when applied to a global dataset, accuracy is reduced. In response to the largely empirical analysis approaches, which should only be applied within the bounds from which they were developed, a new, mechanics based approach for predicting the axial and lateral stress strain relationships of concentrically loaded FRP confined cylinders is presented. The approach uses shear friction theory to simulate the formation and displacement of sliding planes as concrete softens. It is shown that cylinders can fail through two shear friction mechanisms, namely, through either the formation of a circumferential wedge, or, a single sliding plane. Importantly, from this is shown that although each mechanism is defined by the same shear friction material properties different stress strain relationships result and this may explain some of the scatter of test results. In this paper the mechanism of a single sliding plane is derived and compared to that of a circumferential wedge.

Keywords: FRP confinement; shear friction theory; size effect; slenderness effect

Introduction

The axial compressive behaviour of concrete confined with FRP has received much attention over the past two and a half decades, with extensive testing producing approximately 3000 test results and over 90 axial stress strain models, the majority of which are empirical or semi-empirical. Despite this large amount of testing, it has been shown that existing empirical models, when applied to a global dataset, exhibit poor accuracy (Ozbakkaloglu et al. 2013).

In this paper a new, mechanics based, approach for predicting the axial-stress/axial-strain (σ_{ax}-$\varepsilon_{ax\text{-}gbl}$) and axial-stress/lateral-strain (σ_{ax}-$\varepsilon_{lat\text{-}gbl}$) behaviour of FRP confined concentrically loaded cylinders is presented. This approach uses the shear friction mechanism (Haskett et al. 2010, 2011; Chen et al. 2013, 2014b; Chen et al. 2014a; Oehlers et al. 2012; Oehlers et al. 2014a, 2014b; Visintin et al. 2012,2013) to describe the sliding displacement along a concrete to concrete interface. This sliding mechanism is idealised in Figure 1 where τ_{cr} is the shear stress along the sliding plane, Δ_{wdg} is the relative slip between the adjacent concrete elements, σ_{cr} the stress normal to the sliding plane, that is the confinement applied across the sliding plane, and h_{cr} is the relative separation of the adjacent elements due to shear sliding.

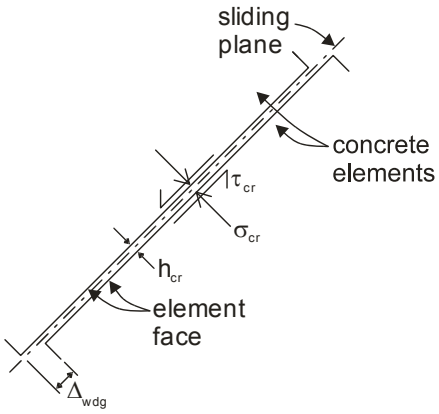

Figure 1 Shear friction mechanism

In the case of FRP confined specimens, the shear friction mechanism is here applied to describe the sliding of concrete wedges which are seen in practice. In this paper two types of concrete wedges, which were observed experimentally, are considered, these are identified as a circumferential wedge in Figure 2(a) and a single sliding plane in Figure 2(b). These two failure modes are strongly correlated to the slenderness of the specimen (Chen et al. 2014a) that is the height to width ratio μ, with the circumferential wedge common when the slenderness ratio μ is approximately 2 and the single sliding plane is common where the slenderness is greater than 2. It must however be emphasised that the single sliding plane is possible at all slendernesses and it will be shown that it represents a lower bounds to the strength of an axially loaded specimen.

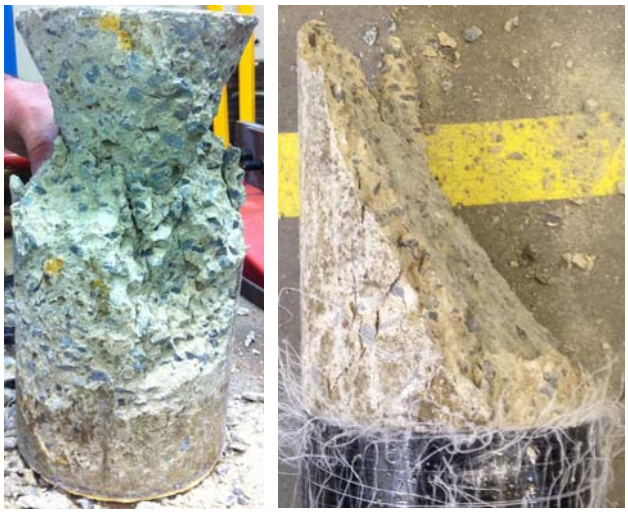

(a) circumferential wedge μ=2 (b) single sliding plane μ=3

Figure 2 circumferential wedge and single sliding plane shear friction mechanisms

The shear friction failure modes shown in Figure 2 are the result of shear sliding along a plane as idealised in Figure 1 which is a function of the shear friction material properties, that is the relationship between τ_{cr}, σ_{cr}, Δ_{wdg} and h_{cr} as illustrated in Figure 3 (Haskett et al

2010, 2011). These shear friction material properties are dependent not only on the concrete compressive strength but also on other parameters such as the aggregate size and strength and mortar properties and are generic such that once known for a specific mix they can be applied to either the circumferential wedge or single sliding plane. That is the shear friction properties in Figure 3 are material properties which control the shear friction sliding mechanism in Figure 1 and which can be applied to any member size and shape such as the cylinders in Figure 2 with different slendernesses and sliding plane configurations.

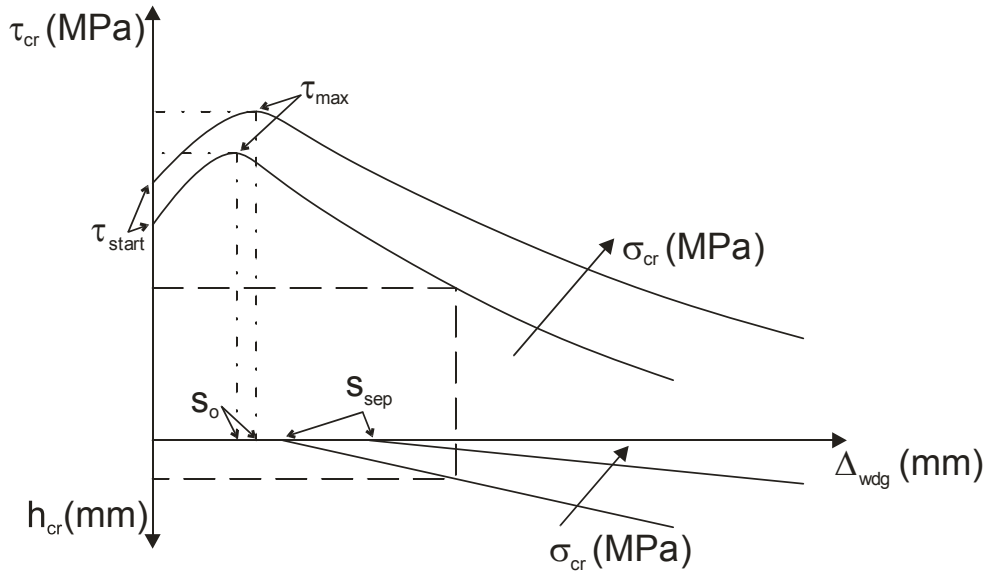

Figure 3: Shear friction material properties

In this paper it will first be shown how the shear friction mechanism in Figure 1 can be used to describe the axial and lateral stress strain behaviour of an actively confined cylinder. The shear friction mechanism of a single sliding plane will then be derived from the conditions of compatibility and equilibrium and compared to that already established for a circumferential wedge (Mohammad Ali et al. 2010; Chen et al. 2014a). The shear friction mechanism will then be applied to predict the axial stress strain relationships of FRP passively confined specimens of different diameters and slendernesses tested as part of this research and it will be shown that the shear friction mechanism can be used to explain some of the scatter seen experimentally.

Mechanics of softening in FRP confined cylinders

Cylinder softening mechanisms

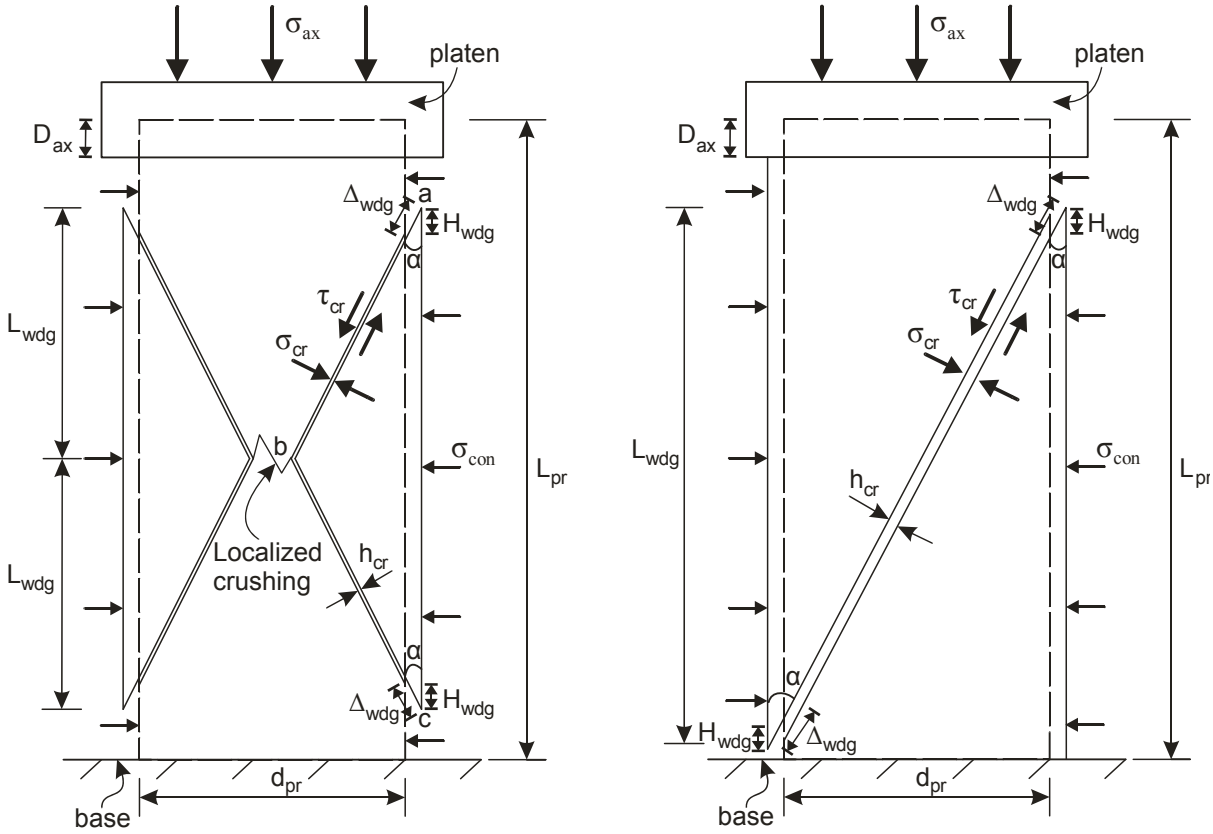

Figure 4: Compression test on a triaxially confined cylinder

Consider the actively confined cylinders in Figure 4 which are of length L_{pr} and diameter d_{pr} and which are subjected to a uniform axial stress of σ_{ax} which results in an axial contraction of D_{ax}. On initial loading D_{ax} is governed wholly by the material strain O-A in Figure 5. At point A corresponding to a stress σ_s concrete softening commences and the total deformation is now a function of the material strain O-A-B and some non-material deformation which takes place along a potential sliding plane at an angle α, where α depends on the Mohr-Coulomb frictional component of the concrete (Balmer et al. 1949; Mattock 1974; Jamet et al 1984; Cusson and Paultre 1995; Rutland and Wang 1997; Harmon et al. 1998; Ansari and Li 1998; Lu and Hsu 2006; Karam and Tabbara 2009; Van Mier and Man 2009; Mohamed Ali M.S. et al 2010; Roddenberry et al 2011; Visintin et al. 2013).

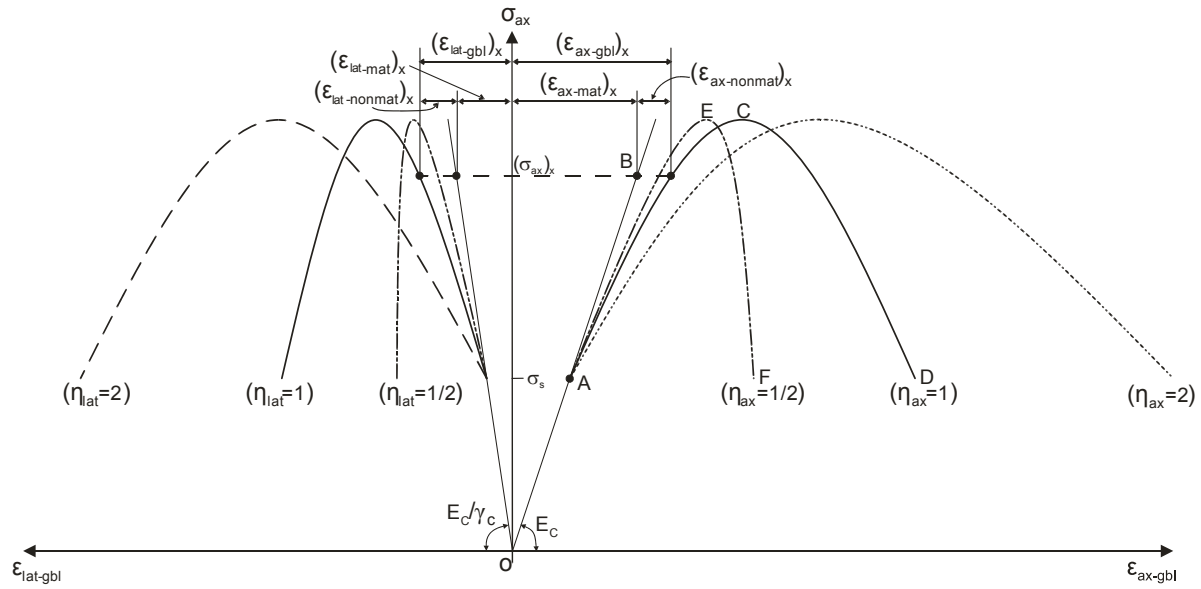

Figure 5: Axial stress global axial strain and global lateral strain relationships

The sliding behaviour of a single or circumferential wedge, that is the contraction due to sliding H_{wdg} in Figures 4(a) and (b), is independent of specimen length and therefore the effective axial strain due to sliding $\varepsilon_{ax\text{-}nonmat}$ is size dependent (Chen et al. 2014a; Visintin et al. 2013). As an example, let us assume that a prism of length L_{pr1} has a single sliding plane as in Figure 4(b) and gives the stress-strain relationship O-A-C-D in Figure 5. The material strain at $(\sigma_{ax})_x$ is $(\varepsilon_{ax\text{-}mat})_x$ as shown and the pseudo-strain due to the contraction due to sliding H_{wdg} in Figure 4(b) is H_{wdg}/L_{pri1} which is shown as $(\varepsilon_{ax\text{-}nonmat})_x$ in Figure 5. Now let us consider a prism of twice the length L_{pri2} such that $L_{pri1}/L_{pri2} = \eta_{ax} = 1/2$. At $(\sigma_{ax})_x$ the material strain will be the same that is $\varepsilon_{mat\text{-}x}$. The contraction due to sliding H_{wdg} will also be the same so that the pseudo strain due to sliding that is H_{wdg}/L_{pri2} will be half of that for the prism of half the length of L_{pri1} that is$(\varepsilon_{ax\text{-}nonmat})_x/2$ in Figure 5. Hence the stress strain relationship will be O-A-E-F. Hence the size dependency. The same argument can be made for lateral dilations due to crack opening and wedge slip $(\varepsilon_{lat\text{-}nonmat})_x$ where, as the ratio of prism diameter is changed $\eta_{lat}=d_{pr1}/d_{pr2}$ the effective strain is varied.

The magnitude of the deformation due to sliding can be derived from the shear friction mechanism and has previously been considered for a circumferential wedge in Chen et al. (2014a). The mechanics of a single sliding plane as in Figure 4(b) will now be considered.

Shear Friction mechanism of a single sliding plane

Through compatibility, the relationship between the global axial strain $\varepsilon_{ax\text{-}gbl}$ and global lateral strain $\varepsilon_{lat\text{-}gbl}$ in Figure 5 and the wedge slip Δ_{wdg} and crack separation h_{cr} in Figure 4(b) can be established. For a given global axial strain $(\varepsilon_{ax\text{-}gbl})_x$ in Figure 5, the proportion of the contraction arising from the material strain $(\varepsilon_{ax\text{-}mat})_x$ is $(\sigma_{ax})_x/E_c$, where E_c is the material modulus. Thus the difference between $\varepsilon_{ax\text{-}gbl}$ and $\varepsilon_{ax\text{-}mat}$ is the effective axial strain due to wedge sliding $\varepsilon_{ax\text{-}nonmat}$. From Figure 4(b), the slip of the wedge in the axial direction is

$$\Delta_{wdg} = \frac{L_{pr}}{\cos\alpha}\left(\varepsilon_{ax-gbl} - \varepsilon_{ax-mat}L_{pr}\right) \quad (1)$$

Similarly, for a given global lateral strain $\varepsilon_{ax\text{-}gbl}$ in Figure 5, the proportion of the total dilation arising from material strain $\varepsilon_{lat\text{-}mat}$ is $(\sigma_{ax})_n/(E_c/\gamma)$ where γ is the material Poisson's ratio. If the section is also considered to be subjected to an active lateral confining stress of σ_{con} as in Figure 4, a contraction of the cross section due to the confining stress is $\varepsilon_{lat\text{-}con} = -\sigma_{con}/E_c$ takes place. Hence the difference between the global lateral strain $\varepsilon_{lat\text{-}gbl}$ and the sum of $\varepsilon_{lat\text{-}mat}$ and $\varepsilon_{lat\text{-}con}$ is the effective lateral strain due to crack separation, h_{cr}, and wedge slip Δ_{wdg} in Figure 4(b) which can be expressed as

$$\varepsilon_{lat-nonmat} = \frac{\left(\Delta_{wdg}\sin\alpha + \frac{h_{cr}}{\cos\alpha}\right)}{d_{pr}} \tag{2}$$

By rearranging Eq. 2, the crack separation is

$$h_{cr} = \left(\varepsilon_{lat-nonmat} d_{pr} - \Delta_{wdg}\sin\alpha\right)\cos\alpha \tag{3}$$

Now consider equilibrium along the sliding plane in Figure 4(b), such that a relationship between the axial stress σ_{ax}, the confining stress σ_{con} and the corresponding shear τ_{cr} and normal σ_{cr} stresses can be determined. For simplicity of the explanation, a free body showing the stresses and forces exerted on the sliding plane is shown in Figure 6.

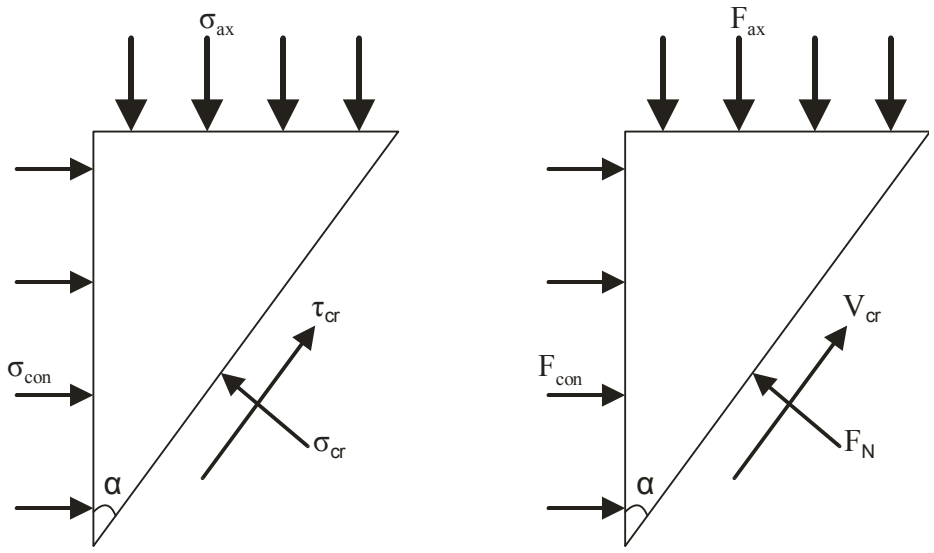

Figure 6: Force equilibrium of a single sliding plane

From horizontal force equilibrium in Figure 6(b)

$$F_{con} + V_{cr}\sin\alpha = F_N\cos\alpha \tag{4}$$

where

$$V_{cr} = \tau_{cr}A_{sld} \tag{5}$$

$$F_N = \sigma_{cr}A_{sld} \tag{6}$$

in which the area of the elliptical sliding plane A_{sld} as illustrated in Figure 7(a) is

$$A_{sld} = \frac{\pi}{4} d_{pr} \frac{d_{pr}}{sin\alpha} \tag{7}$$

and d_{pr} is the width of the cylinder.

From vertical equilibrium in Figure 6(b)

$$F_{ax} = V_{cr} cos\alpha + F_N sin\alpha \tag{8}$$

where the axial force F_{ax} is

$$F_{ax} = \sigma_{ax} \frac{\pi d_{pr}^2}{4} \tag{9}$$

Rearranging Eq. 8 in terms of the normal force across the crack yields

$$F_N = \frac{F_{ax} - V_{cr} cos\alpha}{sin\alpha} \tag{10}$$

Substituting Eq. 10 into Eq. 4 and simplifying gives the shear force across the crack

$$V_{cr} = F_{ax} cos\alpha - F_{con} sin\alpha \tag{11}$$

Further substitution of Eq. 11 into 10 simplifies the expression for the normal force to

$$F_N = F_{ax} sin\alpha + F_{con} cos\alpha \tag{12}$$

In the above equations of equilibrium, the confining force F_{con} in Figure 6(b) can be determined through integration of the lateral stress for cross sections through the depth of the cylindrical wedge. The cylinder wedge, shown in Figure 7(a), is discretised into *n* sections through the depth DE in Figure 7(a), where the cross section for each depth is described by the arc GKH in Figure 7(b).

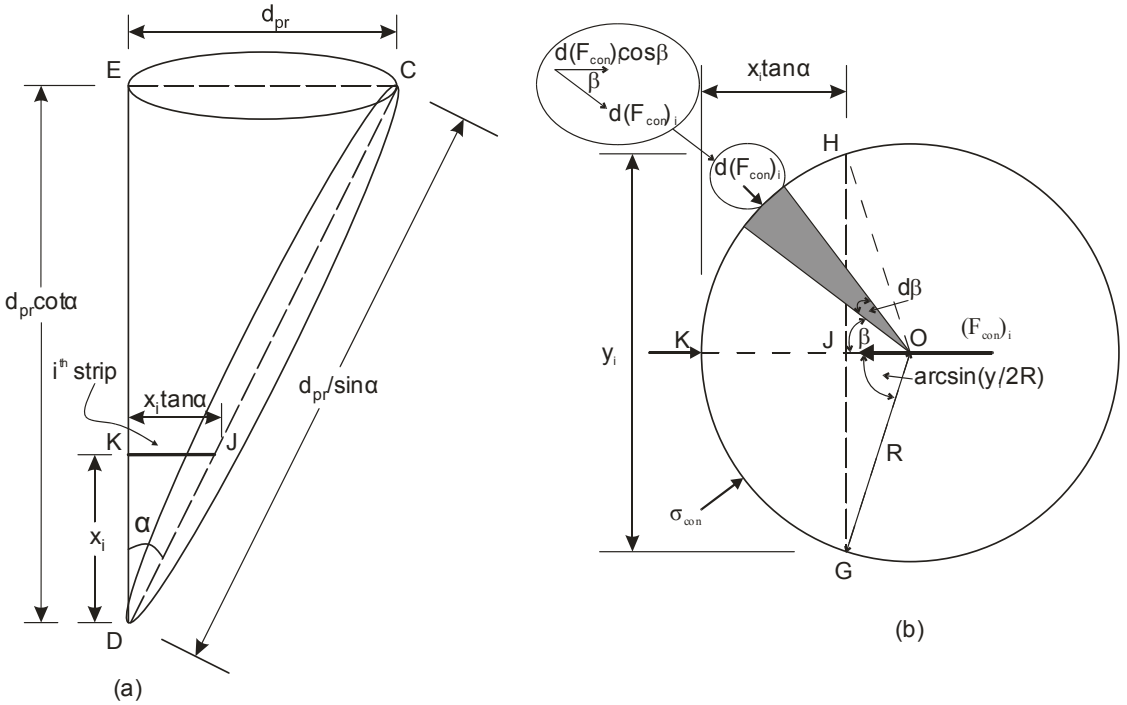

Figure 7 : The confinement force F_{con}

For the purposes of determining the integral of the i^{th} slice, for example slice KJ in Figure 7(a) which is located x_i from the base of the sliding plane, the location x_i is given by

$$x_i = \frac{i}{n} d_{pr} cot\alpha \tag{13}$$

where i/n is the location of the strip as a proportion of the total depth. In Figure 7(b) y_i, which is the length of the chord HG can now be expressed as a function of x_i

$$y_i = 2\left(\sqrt{\left(\frac{d_{pr}}{2}\right)^2 - \left(\frac{d_{pr}}{2} - x_i tan\alpha\right)^2}\right) \tag{14}$$

and substituting Equation 13 into 14, and simplifying gives

$$y_i = 2d_{pr}\left(\sqrt{\frac{i}{n} - \left(\frac{i}{n}\right)^2}\right) \tag{15}$$

Taking line OK in Figure 7(b) as the baseline, the force $d(F_{con})_i$ acting on the shaded element can be determined by integration of the stresses acting between β and β+dβ . Similarly, the total force acing over segment GKH is the integration of stresses between $-\arcsin\left(\frac{y_i}{2R}\right)$ to $\arcsin\left(\frac{y_i}{2R}\right)$ in Figure 7(b), where β is taken as positive for clockwise rotations about baseline OK.

The direction of the confining force of the shaded element $d(F_{con})_i$ in Figure 7(b) acts towards the origin O and by resolution of forces has a horizontal component

$$cos\beta \; d(F_{con})_i = cos\beta \; \sigma_{con} \frac{d_{pr} cot\alpha}{n} R \; d\beta \tag{16}$$

and in Figure 7(b) the total horizontal confining force by integration is

$$(F_{con})_i = \int_{-\arcsin\left(\frac{y_i}{2R}\right)}^{\arcsin\left(\frac{y_i}{2R}\right)} cos\beta \; \sigma_{con} \frac{d_{pr} cot\alpha}{n} R \; d\beta \tag{17}$$

Which is the equivalent confinement force of the i^{th} strip and substituting Equation 15 into 17 and simplifying yields

$$(F_{con})_i = \sigma_{con} \frac{d_{pr} cot\alpha}{n}\left(2d_{pr}\sqrt{\frac{i}{n} - \left(\frac{i}{n}\right)^2}\right) \tag{18}$$

Finally integrating Eq. 18 throughout the depth of the wedge DE in Figure 7(a) gives the total confinement force acing over the single sliding plane DC.

$$F_{con} = \frac{\pi}{4} \sigma_{con} \frac{d_{pr}}{tan\alpha} d_{pr} \tag{19}$$

Now substituting Eqs. 5, 9 and 19 into Eq. 11 and rearranging, the shear stress along the shear sliding is

$$\tau_{cr} = (\sigma_{ax} - \sigma_{con}) \cdot sin\alpha \cdot cos\alpha \tag{20}$$

and substituting Eqs. 6, 9 and 19 into Eq. 12 and rearranging the normal stress along the sliding plane is

$$\sigma_{cr} = \sigma_{ax} \cdot sin^2\alpha + \sigma_{con} \cdot cos^2\alpha \tag{21}$$

Comparison with circumferential wedge mechanism

From the above analyses for a single sliding plane the shear friction properties are given by the following equations in which the coefficient n is equal to 1. From research on the circumferential wedge already developed by Mohammad Ali et al. (2010) and Chen et al. (2014a) for a circumferential wedge the same equations apply but with the coefficient n equal to 2.

$$\Delta_{wdg} = \frac{L_{pr}}{n\cos\alpha}\left(\varepsilon_{ax-gbl} - \varepsilon_{ax-mat}\right) \tag{22}$$

$$h_{cr} = \left(\frac{\varepsilon_{lat-non-mat} d_{pr}}{n} - \Delta_{wdg}\sin\alpha\right)\cos\alpha \tag{23}$$

$$\tau_{cr} = (\sigma_{ax} - n\sigma_{con}) \cdot sin\alpha \cdot cos\alpha \tag{24}$$

$$\sigma_{cr} = \sigma_{ax} \cdot sin^2\alpha + n\sigma_{con} \cdot cos^2\alpha \tag{25}$$

Equations 22 to 25 show that if a specimen failed through a single sliding wedge and was analysed as if it failed through a circumferential wedge then this would give incorrect shear friction properties. Furthermore it will be shown that if two specimens with identical concrete and therefore identical shear friction properties were to fail one through a circumferential wedge and the other through the single sliding plane then different stress-strain relationships would be derived adding to the overall scatter of results.

Simulating passive confinement using the shear friction mechanism

Let us now simulate passive confinement of a cylinder such as that obtained when a specimen is wrapped with FRP, that is let us determine the global axial $\varepsilon_{ax\text{-}gbl}$ and lateral $\varepsilon_{lat\text{-}gbl}$ strains for a given imposed an axial stress σ_{ax}. To simulate an FRP confined cylinder requires first the quantification of the confinement through the circumferential strain ε_{circum} induced in the FRP.

Circumferential strain in FRP confined cylinder test

In order to determine the circumferential strain $\varepsilon_{circum,}$ the final dilated shape of the cylinder needs to be considered. For dilation due to the circumferential wedge in Figure 4(a), the material and non-material expansion occurs uniformly around the circumference of the cylinder. If the lateral dilation of the cylinder is Δd_{pr} then the dilatory strain or lateral global strain $\varepsilon_{lat\text{-}gbl}$ is $\Delta d_{pr}/d_{pr}$. Similarly, the circumferential strain ε_{circum} is $\pi(d_{pr}+\Delta d_{pr})/\pi d_{pr}$ which is it is also equal to $\varepsilon_{lat\text{-}gbl}$. From the geometry of sliding Δ_{wdg} and widening h_{cr} in Figure 4(a) the circumferential strain due to both material dilation and that due to shear friction is given by

$$\varepsilon_{circum} = \varepsilon_{lat-gbl} = \gamma_c \frac{\sigma_{ax}}{E_c} - \frac{\sigma_{con-guess}}{E_c} + \frac{2\left(\Delta_{wdg}\sin\alpha + \frac{h_{cr}}{\cos\alpha}\right)}{d_{pr}} \tag{26}$$

For the case of the single sliding plane in Figure 4(b), the non-material component of the dilation is $(\Delta_{wdg}\sin\alpha + h_{cr}/\cos\alpha)$ which is usually an order of magnitude greater than the material dilation and occurs only along the major axis. Therefore, the cylinder takes an elliptical shape where the minor axis is taken as $d_{pr\text{-}min}$ which is the diameter of a cylinder subjected to only material dilation and confinement, that is,

$$d_{elps-min} = d_{pr}\left[1 + \left(\gamma_c \frac{\sigma_{ax}}{E_c} - \frac{\sigma_{con}}{E_c}\right)\right] \tag{27}$$

and the major axis is taken as the diameter of a cylinder subjected to material and non-material dilation as well as confinement, that is,

$$d_{elps-maj} = d_{pr}\left[1 + \left(\gamma_c \frac{\sigma_{ax}}{E_c} - \frac{\sigma_{con}}{E_c} + \frac{\left(\Delta_{wdg}\sin\alpha + \frac{h_{cr}}{\cos\alpha}\right)}{d_{pr}}\right)\right] \quad (28)$$

The perimeter of the dilated ellipse can then be taken as

$$L_{pr-elps} = \pi\sqrt{\frac{d_{elps-min}^2 + d_{elps-maj}^2}{2}} \quad (29)$$

The change in perimeter gives the circumferential hoop strain and defining the perimeter of a cylinder as $L_{pr\text{-}cir}$

$$\varepsilon_{circum} = \frac{L_{pr-elps} - L_{pr-cir}}{L_{pr-cir}} \quad (30)$$

which is equivalent to

$$\varepsilon_{circum} = \frac{\sqrt{\frac{d_{elps-min}^2 + d_{elps-maj}^2}{2}} - d_{pr}}{d_{pr}} \quad (31)$$

Simulation of FRP confined cylinder test

Having quantified the circumferential strain, the analysis is carried out by guessing a lateral confinement $\sigma_{con\text{-}guess}$ corresponding to the imposed σ_{ax} and then checking if $\sigma_{con\text{-}guess}$ is the same as the confinement σ_{con} arising from the shear sliding mechanism. The analysis can be carried out as follows and can be applied to either of the sliding mechanisms in Figure 4 depending on which is assumed to have occurred.

1. For the given imposed σ_{ax} and guessed $\sigma_{con\text{-}guess}$ in Figure 4, the shear stress τ_{cr} and normal stress σ_{cr} across the potential sliding plane can be determined from the equilibrium Eqns. 24 and 25.
2. For the now known τ_{cr} and σ_{cr} the corresponding slip of the wedge Δ_{wdg} can be determined from the shear friction properties in Figure 3. Which as an example have been connected by a dashed line.
3. Knowing Δ_{wdg} and that the axial material strain $\varepsilon_{ax\text{-}mat} = \sigma_{ax}/E_c$, the global axial strain can be determined from compatibility by rearranging Eq. 22, that is

$$\varepsilon_{ax-gbl} = \frac{n\cos\alpha\Delta_{wdg}}{L_{pr}} + \varepsilon_{ax-mat} \quad (32)$$

4. From the known Δ_{wdg} and σ_{cr} the crack opening h_{cr} in Figure 4 can be determined from the shear friction properties in Figure 3.
5. The confinement is then given by

$$\sigma_{con} = \frac{2\varepsilon_{circum}E_{FRP}t}{d_{pr}} \quad (33)$$

where t is the total thickness of the wrap of modulus E_{FRP}. If σ_{con} does not equal $\sigma_{con\text{-}guess}$ the analysis should be repeated with a new $\sigma_{con\text{-}guess}$ until it does.

Application of the shear friction approach

To demonstrate the ability of the shear friction approach to predict the stress strain behaviour of FRP confined circular sections of different slenderness, a series of tests was

undertaken on concentrically loaded cylinders. The cylinders had a diameter 150mm and heights 300mm, 600mm and 900mm and diameter 100mm and height 600mm, and triplicates of each specimen dimension were tested. The cylinders had an average compressive strength at the time of testing of 36MPa and were each wrapped with 2 layers of CFRP with a single layer thickness of 0.117mm and elastic modulus of 240GPa. All specimens were instrumented with 4 LVDT's to record total axial deformation.

Material properties for analysis

It is important to note here that any material models may be used for the analysis. The purpose of this paper is not to suggest the best material models, but rather, to show the shear friction mechanism for simulating passive confinement. There is no doubt that a better fit with test results could be achieved over time with further research to improve material models.

For analysis it is firstly required that the angle at which sliding plane forms in Figure 4 be known and according to Chen et al. (2013)

$$\alpha = 26^o + \frac{\sigma_{con}}{f_{co}} \times 20^o \tag{34}$$

Also required for the analysis are the shear friction properties in Figure 3. As shown by Chen et al. (2014b), these can be extracted from any standard confined cylinder test or from material models which predict the confined stress strain relationship of a cylinder. For analysis, here generic shear friction properties which are only a function of the concrete strength f_c are applied as follows. It should be noted that in order to produce these generic shear friction models, the stress strain relationship of Popovic (1973) was assumed as well as the compressive-axial-stress/lateral-strain ($\sigma_{ax}/\varepsilon_{latgl}$) relationship Teng et al. (2007).

The wedge-slip/shear-stress (Δ_{wdg}/τ_{cr}) relationship is given by:

$$\frac{\tau_{cr}-\tau_{start}}{\tau_{max}-\tau_{start}} = \frac{\left(\frac{\Delta_{wdg}}{s_o}\right)r^*}{r^*-1+(\frac{\Delta_{wdg}}{s_o})r^*} \tag{35}$$

where τ_{max} is the peak shear stress along sliding plane, as shown in Figure 3 and for a given normal stress and is given by

$$\frac{\tau_{max}}{f_{co}} = -0.6502\left(\frac{\sigma_{cr}}{f_{co}}\right)^2 + 1.104\left(\frac{\sigma_{cr}}{f_{co}}\right) + 0.1659 \tag{36}$$

and where τ_{start} in Figure 3 is the shear stress at the start sliding for a given normal stress and can be given by

$$\frac{\tau_{start}}{f_{co}} = -0.4429\left(\frac{\sigma_{cr}}{f_{co}}\right)^2 + 0.8653\left(\frac{\sigma_{cr}}{f_{co}}\right) + 0.1554 \tag{37}$$

and s_o in Figure 3 is the sliding displacement at τ_{max} and is determined by

$$s_o = 0.429\left(\frac{\sigma_{cr}}{f_{co}}\right)^2 + 0.529\left(\frac{\sigma_{cr}}{f_{co}}\right) + 0.013 \tag{38}$$

furthermore r^* is

$$r^* = \frac{E_c}{E_c - \frac{f_{cc}}{\varepsilon_{cc}}} \times \frac{2+\frac{f_{co}}{f_{cc}}}{3} \tag{39}$$

The wedge-slip - crack separation relationship is given by

$$h_{cr} = \begin{cases} 0 & 0 \leq \Delta < s_{sep} \\ k\left(\Delta_{wdg} - s_{sep}\right) & \Delta \geq s_{sep} \end{cases} \quad (40)$$

where s_{sep} as in Figure 3 is the sliding displacement at which crack widening begins and is given by

$$\frac{s_{sep}}{s_o} = 1 + 10\left(\frac{\sigma_{cr}}{f_{co}}\right)^2 \quad (41)$$

And *k* is a factor which controls the opening rate of concrete and is given by

$$k = -0.563\left(\frac{\sigma_{cr}}{f_{co}}\right) + 0.683 \quad (42)$$

Analysis of test results

A comparison of the experimental and predicted test results is shown in Figure 8. The analysis has been performed in all cases assuming either a single sliding plane or a circumferential wedge as in Figure 4 and it can be seen in Figure 8 that a significant variation in the predicted stress strain relationship results. This difference arising due to the shear friction mechanisms can therefore help to explain some of the variation seen in experimental tests. As the circumferential wedge is only likely to form in specimens with an aspect ratio of approximately 2 it is also suggested that if further empirical research to define the stress strain relationship of concentrically loaded FRP specimens is required then it should be performed on larger specimens such that the failure mechanism of a single sliding plane occurs as this is what is expected in full scale columns.

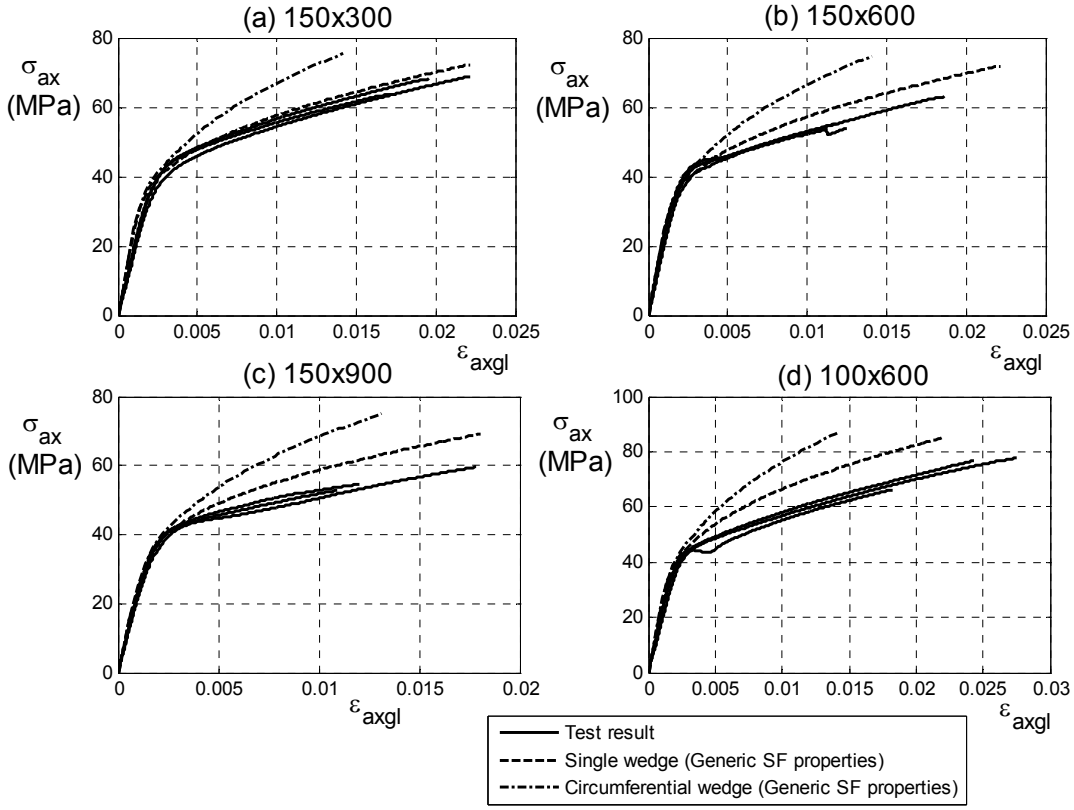

Figure 8: Comparison of experimental and predicted results using generic SF properties

For the analyses in Figure 8, shear friction properties using the relationship between the axial and lateral strains proposed by Teng et al. (2007) have been used. As this value has been estimated and it has been suggested that under some circumstances that it may provide an upper bounds (Xiao et al 2010), the analysis has been repeated in Figure 9 to show the influence of varying ε_{lat} by $\pm$10%. It should be noted that in Figure 9 only the mechanism seen in the test is considered, that is a single sliding plane is considered for all specimens with an aspect ratio greater than 2. Importantly, it can be seen in Figure 9 that a variation of only $\pm$10% in the empirical model of Teng et al. (2007) leads to a significant change in the predicted result. This suggests that the shear friction approach presented here captures the mechanism of confinement which occurs in practice but empirical research is still required to refine material models, most significantly the relationship between the axial and lateral strain.

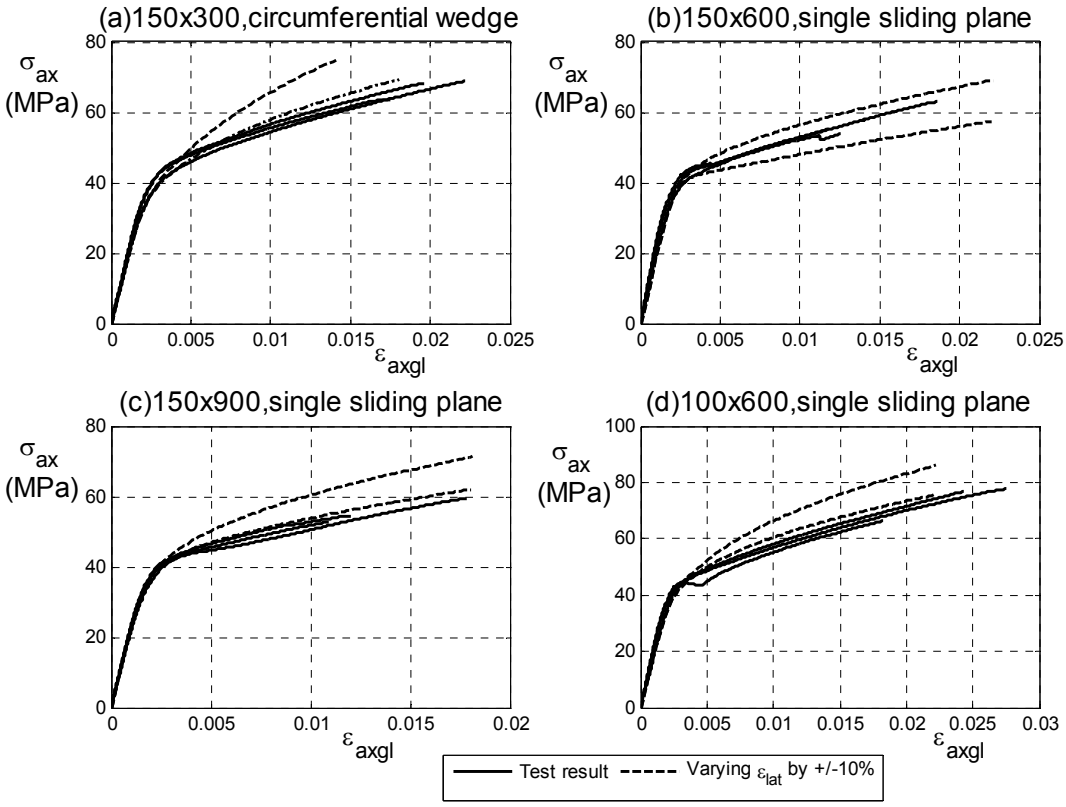

Figure 9: Comparison of experimental and predicted results (Varying ε_{lat} by +/- 10%)

Conclusion

A new mechanics based approach to predicting the axial and lateral stress strain relationships for FRP confined concrete cylinders has been presented. Being mechanics based, the approach is size and slenderness independent in that it copes automatically with changes in size and shape and does not need the inclusion of size factors. The approach can be applied to specimens with any type of concrete or any type of FRP wrap provided the shear friction properties are known. Experiments conducted as part of the model validation

process show that specimens with a slenderness ratio greater than 2 typically fail with the formation of a single sliding plane. The shear friction approach is capable of predicting the response of specimens failing with either a circumferential wedge or a single sliding plane and hence can simulate, through mechanics, the dependency of the passively confined stress strain response on slenderness. It is suggested that as in practice members have a slenderness ratio greater than two there is a need for empirical research to shift focus to experiments on slender specimens and in which the total axial deformation is measured.

Acknowledgements

The authors would like to acknowledge the support of the Australian Research Council ARC Discovery Project DP0985828 'A unified reinforced concrete model for flexure and shear'.

Notation

D_{ax}	axial deformation of a prism
$D_{ax\text{-}mat}$	axial material deformation
D_{lat}	transversal deformation of a prism
d_{pr}	width of prism or cylinder
$d_{pr\text{-}1}$	width of prism 1
$d_{pr\text{-}2}$	width of prism 2
E_c	concrete modulus; secant modulus when non-linear
E_{frp}	elastic modulus of FRP
f_{co}	peak strength of unconfined concrete
f_{cc}	peak strength of confined concrete
$(F_{con})_i$	equivalent confinement force of the i^{th} strip
h_{cr}	crack opening of shear-friction sliding plane
H_{wdg}	axial component of Δ_{wdg}
k	a factor which controls the opening rate of concrete
L_{pr}	length of prism or cylinder
L_{wdg}	axial length of wedge
$L_{pr\text{-}1}$	length of prism 1
$L_{pr\text{-}2}$	length of prism 2
n	number of wedges
r^*	a factor which controls the ductility of the concrete
R	radius of circle
s_o	sliding displacement at τ_{max}
s_{sep}	sliding displacement at just crack widening begins
t	total thickness of FRP
V_{cr}	shear force along the sliding plane

α	angle of wedge sliding plane to the axis
β	integration angle
Δ_{wdg}	slip along shear-friction sliding plane
$\varepsilon_{ax\text{-}gbl}$	global axial strain; total strain due to material contraction and wedge sliding
$\varepsilon_{ax\text{-}mat}$	material strain; local axial strains as measured by strain gauges
$\varepsilon_{lat\text{-}gbl}$	global transversal strain; total lateral strain due to material expansion and wedge sliding
ε_{co}	$\varepsilon_{ax\text{-}gbl}$ at f_{co}
ε_{cc}	$\varepsilon_{ax\text{-}gbl}$ at f_{cc}
$\varepsilon_{ax\text{-}nonmat}$	axial effective strain due to wedge sliding
$\varepsilon_{lat\text{-}mat}$	transverse material strain; lateral strain due to material expansion
$\varepsilon_{lat\text{-}con}$	transverse contraction strain due to confinement
$\varepsilon_{lat\text{-}nonmat}$	transversal effective strain due to wedge sliding;
η_{lat}	lateral size factor; ratio of prism or cylinder width
η_{ax}	axial size factor; ratio of prism or cylinder lengths
γ	material Poisson ratio
μ	slenderness ratio; L_{pr}/d_{pr}; prism slenderness
σ_{ax}	axial stress; longitudinal stress
σ_{con}	active confinement stress
σ_{cr}	normal stress to shear-friction sliding plane
F_N	normal force along the sliding plane
τ_{cr}	shear stress along shear-friction sliding plane
τ_{max}	peak shear stress along sliding plane for a given normal stress

References

Ansari, F., and Li, Q. (1998). “High-strength concrete subjected to triaxial compression.” ACI Materials Journal, 95(6), 747-755.

Balmer, G. G. (1949). “Shear strength of concrete under high triaxial stress – Computation of Mohr’s envelope as a curve.” Structural Research Laboratory Roport No. SP-23, Department of the interior bureau of reclamation, United States.

Chen, Y., Visintin, P., and Oehlers, D.J. (2013). “Size Dependent Stress-Axial Strain and Stress-Lateral Strain Models for Actively Confined Concrete.” School of Civil, Environmental and Mining Engineering Report Departmental Report R-181, The University of Adelaide.

Chen, Y., Visintin, P., Oehlers, D.J., and Alengaram, U. (2014a). "Size Dependent Stress-Strain Model for Unconfined Concrete." ASCE Journal of Structural Engineering, 140(4), 10.1061/(ASCE)ST.1943-541X.0000869.

Chen, Y., Visintin, P., and Oehlers, D.J. (2014b). “Derivation of concrete shear-friction properties from actively confined cylinder tests.” School of Civil, Environmental and Mining Engineering Report Departmental Report R-184, The University of Adelaide.

Cusson, D., and Paultre, P. (1995). “Stress strain model for confined high-strength concrete.” Journal of Structural Engineering, 121(3), 468-477.

Harmon, T.G., Ramakrishnan, S., and Wang, E.H. (1998). “Confined concrete subjected to uniaxial monotonic loading.” Journal of Engineering Mechanics, 124(12), 1303-1309.

Haskett, M., Oehlers, D.J., Mohamed Ali M.S., and Sharma, S. K. (2010). “The shear friction aggregate interlock resistance across sliding planes in concrete.” Magazine of Concrete Research, 62(12), 907-924.

Haskett, M., Oehlers, D.J., Mohamed Ali M.S., and Sharma, S. K. (2011). “Evaluating the shear-friction resistance across sliding planes in concrete.” Engineering Structures, 33(4), 1357-1364.

Jamet, P., Millard, A., and Nanas, G. (1984). “Triaxial behaviour of a Micro-concrete Complete Stress-Strain Curves for Confining Pressures Ranging From 0 to 100 MPa.” GIF SUR YVETTE CEDEX (France), Title no. 91191, 133-140.

Karam, G., and Tabbara, M. (2009). “Hoek–Brown Strength Criterion for Actively Confined Concrete.” Journal of Materials in Civil Engineering, 21(3), 110-118.

Lu, X. B., and Hsu, C. T. (2006). “Behavior of high strength concrete with and without steel fiber reinforcement in triaxial compression.” Cement and Concrete Research, 36(9), 1679-1685.

Mattock, A.H. (1974). “Shear transfer in concrete having reinforcement at an angle to the shear plane.” ACI Special publication, 42(2), 17-42.

Mohamed Ali, M.S., Oehlers, D.J., and Griffith, M.C. (2010). “The residual strength of confined concrete.” Advances in Structural Engineering, 13(4), 603-618.

Oehlers, D.J., Visintin, P., Zhang, T., Chen, Y., and Knight, D (2012). “Flexural rigidity of reinforced concrete members using a deformation based analysis.” Concrete in Australia, 38(4), 50-56.

Oehlers, D.J., Visintin, P., Chen, J.F., and Ibell, T. (2014a). “Simulating RC members Part 1: Partial interaction properties.” Accepted for publication in ICE structures and Buildings 2014.

Oehlers, D.J., Visintin, P., Chen, J.F., and Ibell, T. (2014b). “Simulating RC members Part 2: displacement based analysis.” Accepted for publication in ICE structures and Buildings 2014.

Ozbakkaloglu, T., and Lim, J.C. (2013). “Axial compressive behaviour of FRP-confined concrete: Experimental test database and a new design-orientated model.” Composited: Part B, 55, 607-634.

Ozbakkaloglu, T., Lim, J.C., and Vincent, T. (2013). “FRP-confined concrete in circular sections: Review and assessment of stress-strain models.” Engineering Structures, 49, 1068-1088.

Popovics, S. (1973). “A numerical approach to the complete stress–strain curve of concrete.” Cement and concrete research, 3(5), 583–599.

Roddenberry, M., Kampmann, R., Ansley, M. H., Bouchard, N., and Ping, W. V. (2011). “Failure Behavior of Concrete Cylinders under Different End Conditions.” ACI Material Journal, 108(1), 79-87.

Rutland, C.A., and Wang, M.L. (1997). “The effects of confinement on the failure orientation in cementitious materials experimental observations.” Cement and concrete composites, 19(2), 149-160.

Teng, J. G., Huang, Y. L., Lam, L., and Ye, L.P. (2007). “Theoretical model for fiber-reinforced polymer confined concrete.” Journal of Composites for construction, 11(2), 201-210.

Van Mier, J. G. M. and Man, H. K. (2009). “Some Notes on Microcracking, Softening, Localization, and Size Effects.” International Journal of Damage Mechanics, 18(3), 283-309.

Visintin, P., Oehlers, D.J., Wu, C., and Haskett, M., (2012). “A mechanics solution for hinges in RC beams with multiple cracks.” Engineering Structures, 36, 61-69.

Visintin, P., Oehlers, D.J., Wu, C., and Haskett, M., (2013). “A Mechanics Based Hinge Analysis for Reinforced Concrete Columns.” ASCE Journal of Structural Engineering, posted online ahead of print.

Xiao, Q. G., Teng, J. G., and Yu, T. (2010). “Behavior and Modeling of Confined High-strength Concrete.” Journal of Composites for Construction, 14(3), 249-259.

Statement of Authorship

Extracting size dependent stress/strain relationships from FRP confined concrete cylinders for varying diameters and heights. To be submitted to Composite Structures.

Chen, Y (Candidate)

Performed analyses and developed model

I hereby certify that the statement of contribution is accurate and I give permission for the inclusion of the paper in this thesis

Signed……..Date……

Visintin, P

Supervised and contributed to research

I hereby certify that the statement of contribution is accurate and I give permission for the inclusion of the paper in this thesis

Signed……..Date……

Oehlers, DJ

Supervised and contributed to research

I hereby certify that the statement of contribution is accurate and I give permission for the inclusion of the paper in this thesis

Signed……Date……

Extracting size dependent stress/strain relationships from FRP confined concrete cylinders for varying diameters and heights

Chen, Y., Visintin, P., and Oehlers, D.J.

1. Abstract

Since most of the available data regarding FRP-confined columns has been generated from tests on small-scale cylinders, it is important to ensure that the proposed equations are truly representative of the actual behaviour of full-scale columns. In this paper, mechanics solutions have been developed to show the influence of specimen size, that is both diameter and height, on the stress-strain relationship of axially loaded FRP confined concrete cylindrical specimens using shear friction theory. Two distinct cylinder failure modes have been examined: that of the circumferential wedge that is common in standard cylinders with aspect ratios of 2:1; and that of the single sliding plane that occurs at higher aspect ratios. It is often quite difficult, if not impossible due to the capacities of the testing machines, to test large or full-scale FRP wrapped specimens under pure compression in order to extract their axial-stress/axial-strain relationships. It is shown in this paper through the mechanics of shear friction, how small scale FRP wrapped specimens suitable for compression testing can be designed so that the stress/strain relationship of the full scale member under pure compression can be extracted from those of the small test specimen.

Keywords: FRP; FRP confined concrete; passive confinement; axial-stress/axial-strain relationship; size effect; and shear friction.

2. Introduction

It is widely known (Richart et al 1928 and 1929; Balmer 1949; Gardner 1969; Kotsovos and Newman 1978 and 1979; Jamet et al 1984; Smith et al 1989; Bellotti and Rossi 1991; Lahlou et al 1992; Hammons and Neeley 1993; Setunge et al 1993; Imran 1994; Ansari and Li 1998; Harmon et al 1998; Sfer et al 2002; Lu and Hsu 2006; Xiao et al. 2010) that the stress-strain properties of concrete can be improved through confinement. The ultimate compressive strength (Xie et al 1995; Karbhari and Gao 1997; Candappa et al 2001; Saiidi et al. 2005; Wu et al. 2009; Yu and Teng 2011) and the ductility (Attard and Setunge 1996; Imran and Pantazopoulou 1996 and 2001; Saafi et al. 1999; Xiao and Wu 2000; Teng et al. 2009) of concrete can be improved through active or through passive confinement such as through confinement with fiber-reinforced polymer (FRP) jackets. Typically, the material properties of passively confined concrete are determined experimentally on small scale 2:1 aspect ratio specimens for varying levels of confinement and researchers use these experimental results to develop empirical or semi-empirical equations for the influence of concrete confinement

(Samaan et al. 1998; Toutanji 1999; Moran and Pantelides 2002; Xiao and Wu 2003; Binici 2008; Fahmy and Wu 2010). In order for engineers to fully exploit this improved material performance, e.g. in the form of design guidelines for FRP-strengthened concrete columns, it is important to ensure that any equations developed from small scale concrete specimens are truly representative of the actual behaviour of full-scale columns which have aspect ratios markedly different from the 2:1 ratio most commonly tested.

The influence of specimen size on concrete material properties is a well researched topic as far back as the 1920's (e.g. Gonnerman 1925). In the context of passive confinement, the influence of specimen size (dimensions and aspect ratio) on the potential improvement in concrete strength and ductility of FRP confined concrete members is still heavily researched and debated.

For example, Owen (1998), Peng et al. (1998), Jia and Cheng (2003), Lin and Li (2003), Masia et al. (2004), Theriault et al. (2004), Elkadi and van Mier (2006), Tong et al. (2009), and Wang and Wu (2010) consider the effect of specimen size to be considerable and have experimentally confirmed a size effect in FRP confined concrete columns for both circular and square specimens and with a wide range of wrap types. Conversely, Mirmiran et al. (1998), Lorenzis et al. (2002), Carey and Harries (2005), Matthys et al. (2005), Zhu et al. (2005), Gu et al. (2006), Silva and Rodrigues (2006), and Scott et al. (2010) believe that the size effect on the strength or ductility of FRP-confined concrete columns can be ignored. Moreover, current design codes [American Concrete Institute (ACI) 2002; Canadian Standard Association (CSA) 2002] for concrete structures strengthened with FRP materials do not consider the influence of specimen size on the material behaviour of confined concrete, that is the size effect.

From the above literature review, it is clear that there are differing views on the influence of specimen size on the material response of confined concrete and that further investigation is necessary. In this paper, shear friction theory (Chen et al. 2014b, 2014c) is used to investigate the size effect in axially loaded concrete specimens, where a mechanics relationship is ultimately developed to allow the global axial-stress/axial-strain relationship of the large or full-scale Specimen 3 in Figure 1 to be extracted from small scale test specimens such as Specimen 1 with a smaller diameter and height.

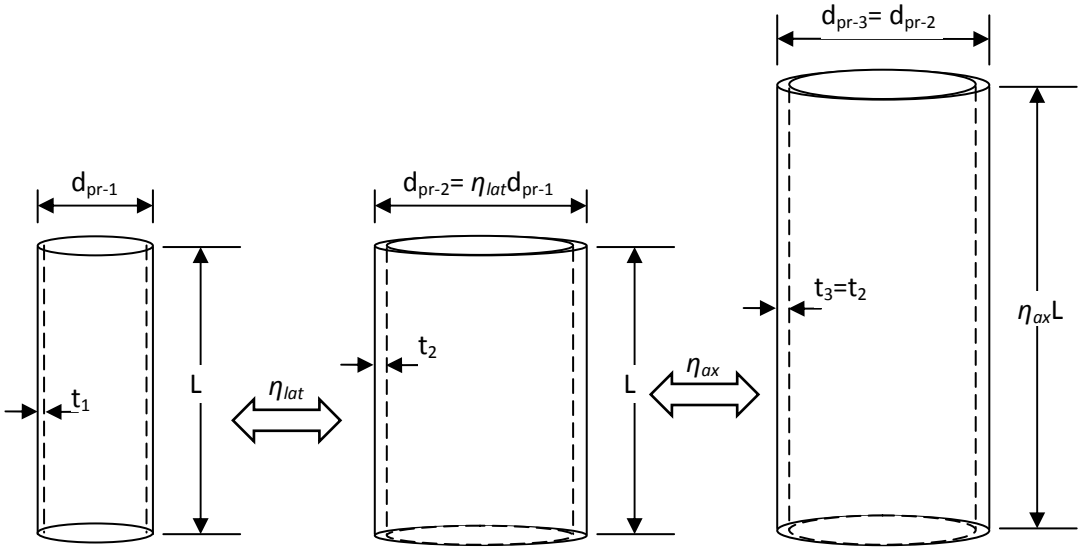

Figure 1: Size relationship of arbitrary-size FRP confined specimens

The global axial-stress/axial-strain relationship of concrete depends on the method of measuring the strain (Chen et al. 2014a, Visintin et al. 2014a); in this paper it will be assumed to be the total axial deformation divided by the height of the cylinder. The global stress/strain relationship also depends on the shape of the cylinder μ, which is defined as the following ratio of the prism length L_{pr} to prism diameter d_{pr}

$$\mu = \frac{L_{pr}}{d_{pr}} \qquad \text{Equation 1}$$

When comparing prisms of differing dimensions in order to quantify the size effect, the ratio of specimen lengths in the axial direction η_{ax}, is defined as the following ratio of the two prism lengths

$$\eta_{ax} = \frac{L_{pr-2}}{L_{pr-1}} \qquad \text{Equation 2}$$

where L_{pr-2} is the height of the taller prism and L_{pr-1} that of the shorter. The lateral size parameter η_{lat} is the ratio of the two prism diameters

$$\eta_{lat} = \frac{d_{pr-2}}{d_{pr-1}} \qquad \text{Equation 3}$$

where d_{pr-1} is the diameter of the narrower cylinder.

This paper quantifies through shear friction mechanics the size effects of Equations 2 and 3 for specimens in which the shape μ in Equation 1 is equal to or greater than 2 as this latter requirement allows the wedge angle α to remain constant.

3. Shear friction mechanism and shear friction properties

Figure 2(a) shows the circumferential wedge model in which a circumferential double wedge *a-b-c* of length $2L_{wdg}$ and at an angle α forms around a cone that depends on the Mohr-Coulomb frictional component of the concrete (Balmer et al. 1949; Mattock 1974; Jamet et al 1984; Cusson and Paultre 1995; Rutland and Wang 1997; Harmon et al. 1998; Ansari and Li 1998; Lu and Hsu 2006; Karam and Tabbara 2009; Van Mier and Man 2009; Mohamed Ali M.S. et al 2010; Roddenberry et al 2011; Visintin et al. 2013). The sliding planes *a-b* and *b-c* are initially uncracked and sliding Δ_{wdg} occurs as shown. Furthermore, for sliding to occur requires localised crushing at the apex *b* of the cones. However, for slender prisms whose aspect ratio μ is bigger than 2, sliding most likely occurs across a diagonal sliding plane as shown in Figure 2(b) which does not require localised crushing. For a fixed angle α in Figure 2, from equilibrium there is a direct relationship between the axial stress σ_{ax}, the normal stress to the sliding plane σ_{cr} and the shear stress along the sliding planes τ_{cr} (Chen et al 2014b). The shear-friction material properties quantify the relationship, across a potential initially uncracked sliding plane, between: the shear stress τ_{cr}; normal stress σ_{cr}; crack width h_{cr}; and sliding along the plane Δ_{wdg}. Hence shear-friction material properties can be used to quantify Δ_{wdg} and consequently the vertical component H_{wdg} and consequently the effective strain ε_{wdg} due to H_{wdg}.

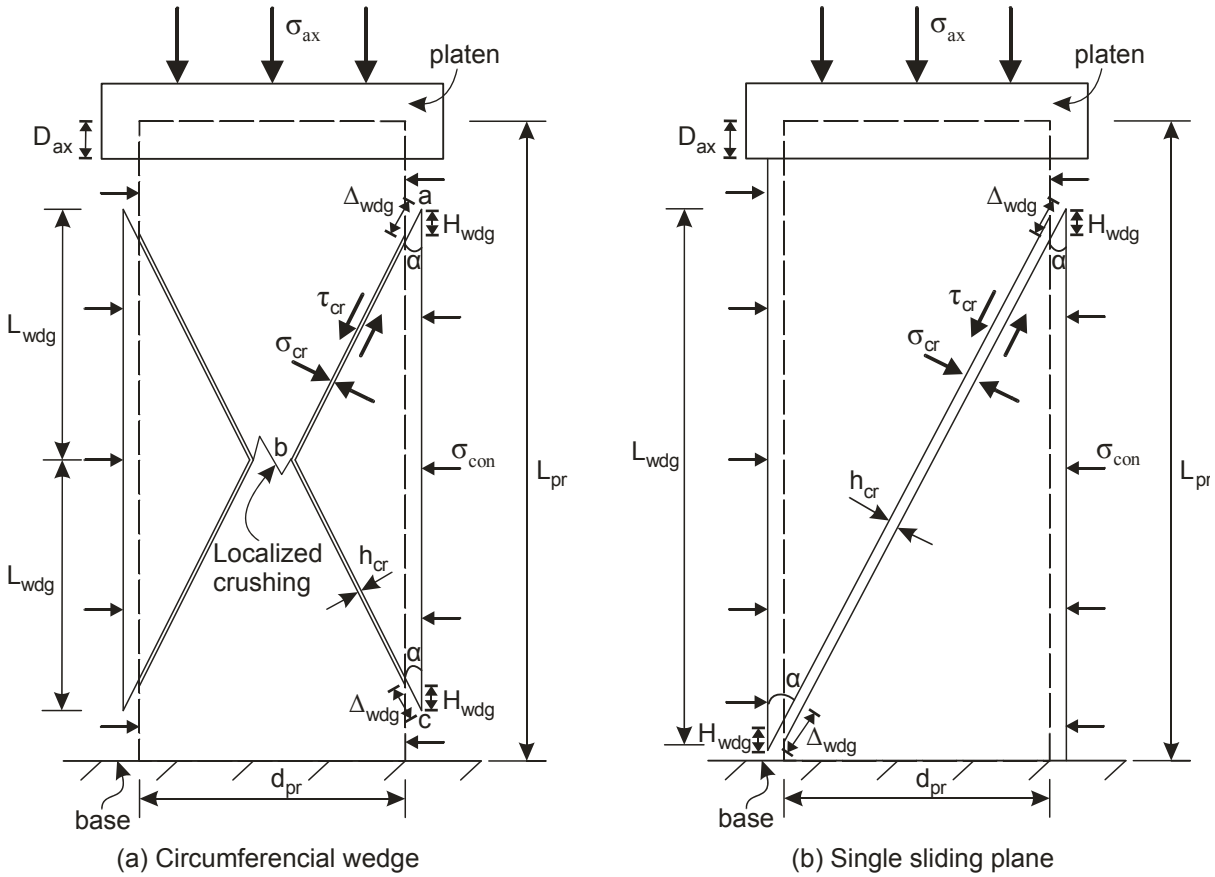

Figure 2: Failure models of a confined cylinder

3.1 General expression for global axial strain

Consider the FRP confined cylinders in Figure 2 which are of length L_{pr} and diameter d_{pr} and which are subjected to a uniform axial stress of σ_{ax} which results in an axial contraction of D_{ax}. The total axial contraction of the prism D_{ax} in Figure 2(a) or 2(b) for the applied axial stress σ_{ax} arises due to both the axial contraction of the material D_{mat} and the axial contraction due to sliding of the wedge D_{wdg} that is

$$D_{ax} = D_{mat} + D_{wdg} \qquad \text{Equation 4}$$

in which the total or global contraction D_{ax} may also be expressed as a function of the global axial strain $\varepsilon_{ax\text{-}gbl}$ as

$$D_{ax} = \varepsilon_{ax-gbl} L_{pr} \qquad \text{Equation 5}$$

where $\varepsilon_{ax\text{-}gbl}$ is a pseudo strain as it consists of both the material contraction and the slip of the wedge.

The material deformation D_{mat} may also be defined as

$$D_{mat} = \varepsilon_{mat} L_{pr} \qquad \text{Equation 6}$$

For convenience, the axial material strain ε_{mat} can be determined as the stress σ_{ax} divided by the concrete modulus E_c. However, it could be taken as nonlinear if the material properties were available. Furthermore,, the contraction due to the sliding of the wedge D_{wdg} in Figure 2(a) or 2(b) is

$$D_{wdg} = \beta H_{wdg} \qquad \text{Equation 7}$$

where β is a coefficient and equals 2 for circumferential wedge model as shown in Figure 2(a) and 1 for single sliding plane model as shown in Figure 2(b). H_{wdg} is the axial component due to sliding along the plane Δ_{wdg} so that it is given by

$$H_{wdg} = \Delta_{wdg} cos\alpha \qquad \text{Equation 8}$$

where α is the angle of the wedge sliding plane to the longitudinal axis and proposed by Visintin et al. (2014a) as

$$\alpha = 26^{o} + \frac{\sigma_{con}}{f_{co}} \times 20^{o} \qquad \text{Equation 9}$$

where f_{co} is the unconfined cylinder strength, and σ_{con} is confinement stress as shown in Figure 2.

Dividing both sides of Equation 7 by L_{pr} results in the effective strain due to wedge sliding as

$$\varepsilon_{wdg} = \frac{\beta \Delta_{wdg} cos\alpha}{L_{pr}} \qquad \text{Equation 10}$$

The global axial strain $\varepsilon_{ax\text{-}gbl}$ is composed of the size independent material strain (σ_{ax}/E_c) and size dependent effective strain ε_{wdg}. Hence, it is size dependent and can be determined from

$$\varepsilon_{ax-gbl} = \frac{\sigma_{ax}}{E_c} + \frac{\beta \Delta_{wdg} cos\alpha}{L_{pr}} \qquad \text{Equation 11}$$

3.2 Quantification of global axial strain

In order to evaluate the slip along the sliding plane Δ_{wdg} in Equation 11, consider the four shear friction components shown in Figure 2. The shear-friction properties are the combinations of the normal stress σ_{cr}, the shear stress τ_{cr}, interface widening h_{cr} and interface sliding Δ_{wdg} as illustrated in Figure 3.

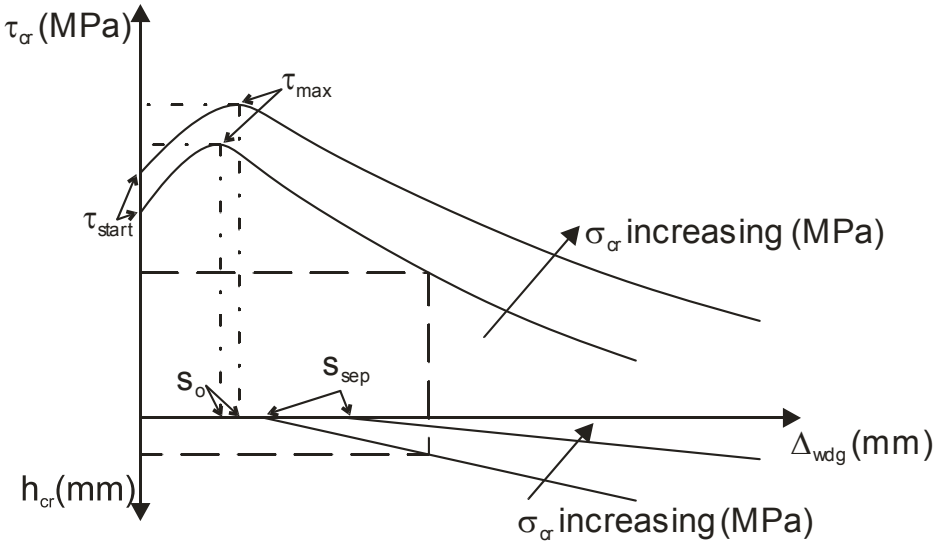

Figure 3: Shear-friction properties

From Mohammad Ali et al. (2010) and Visintin et al. (2014b), the shear stress τ_{cr} and the normal stress σ_{cr} in Figure 2 and required for Figure 3 are determined by

$$\tau_{cr} = (\sigma_{ax} - \beta\sigma_{con}) \cdot sin\alpha \cdot cos\alpha \qquad \text{Equation 12}$$

$$\sigma_{cr} = \sigma_{ax} \cdot sin^2\alpha + \beta\sigma_{con} \cdot cos^2\alpha \qquad \text{Equation 13}$$

that is $\tau_{cr\text{-}1}$ in Figure 3 and $\sigma_{cr\text{-}1}$ can be quantified for a known axial stress $\sigma_{ax\text{-}1}$ and confining stress $\sigma_{con\text{-}1}$. Hence for specific values of $\tau_{cr\text{-}1}$ and $\sigma_{cr\text{-}1}$ as shown in Figure 3, $\Delta_{wdg\text{-}1}$ and $h_{cr\text{-}1}$ can be quantified from the shear friction material relationships as shown.

The shear friction material relationships in Figure 3 can be determined from the following generic expressions (Chen et al. 2014b)

$$\frac{\tau_{cr}}{\tau_{max}} = \frac{2a_1(\Delta_{wdg}+a_2)}{(\Delta_{wdg}+a_2)^2+{a_1}^2} \qquad \text{Equation 14}$$

in which τ_{max}, as in Figure 3, is the maximum shear strength along a sliding plane for a given normal stress σ_{cr} and is given by

$$\frac{\tau_{max}}{f_{co}} = -0.6502\left(\frac{\sigma_{cr}}{f_{co}}\right)^2 + 1.104\left(\frac{\sigma_{cr}}{f_{co}}\right) + 0.1659 \qquad \text{Equation 15}$$

and where the factors a_1 and a_2 control the ductility of shear friction curve as follows

$$a_1 = 4\left(\frac{\sigma_{cr}}{f_{co}}\right) - 0.2 \qquad \text{Equation 16}$$

$$a_2 = 0.1\left(\frac{\sigma_{cr}}{f_{co}}\right) + 0.945 \qquad \text{Equation 17}$$

Furthermore

$$h_{cr} = \begin{cases} 0 & 0 \leq \Delta < s_{sep} \\ k(\Delta_{wdg} - s_{sep}) & \Delta \geq s_{sep} \end{cases} \qquad \text{Equation 18}$$

where s_{sep} in Figure 3 and as follows, is the sliding displacement at the onset of crack widening h_{cr}

$$\frac{s_{sep}}{s_o} = 1 + 10\left(\frac{\sigma_{cr}}{f_{co}}\right)^2 \qquad \text{Equation 19}$$

in which s_o in Figure 3 and as follows, is the sliding displacement at τ_{max}

$$s_o = 0.429\left(\frac{\sigma_{cr}}{f_{co}}\right)^2 + 0.529\left(\frac{\sigma_{cr}}{f_{co}}\right) + 0.013 \qquad \text{Equation 20}$$

and k in Equation 18 is a factor which controls the opening rate of h_{cr} and is given by

$$k = -0.563\left(\frac{\sigma_{cr}}{f_{co}}\right) + 0.683 \qquad \text{Equation 21}$$

In general, the 'Serpentine Curve' of Equation 14 has a good accuracy in the range of $0.8 \leq \Delta_{\mathrm{wdg}} \leq 5\ \mathrm{mm}$. However, it cannot catch both the onset of sliding τ_{start} in Figure 3, nor the ascending branch. For this small range that is $0 \leq \Delta_{\mathrm{wdg}} \leq 0.8$

$$\frac{\tau_{\mathrm{cr}} - \tau_{\mathrm{start}}}{\tau_{\mathrm{max}} - \tau_{\mathrm{start}}} = \frac{\left(\frac{\Delta_{\mathrm{wdg}}}{s_o}\right)a_3}{a_3 - 1 + \left(\frac{\Delta_{\mathrm{wdg}}}{s_o}\right)^{a_3}} \qquad \text{Equation 22}$$

where

$$\frac{\tau_{start}}{f_{co}} = -0.4429\left(\frac{\sigma_{cr}}{f_{co}}\right)^2 + 0.8653\left(\frac{\sigma_{cr}}{f_{co}}\right) + 0.1554 \qquad \text{Equation 23}$$

and a_3 is a factor which controls the ductility of the concrete and is given by

$$a_3 = \frac{E_c}{E_c - \frac{f_{cc}}{\varepsilon_{cc}}} \times \frac{2 + \frac{f_{co}}{f_{cc}}}{3} \qquad \text{Equation 24}$$

in which the confined cylinder strength (Visintin et al. 2014b) is given by

$$f_{cc} = f_{co}\left[1 + 3.65\left(\frac{\sigma_{con}}{f_{co}}\right)^{0.82}\right] \qquad \text{Equation 25}$$

and the strain at the peak strength of confined concrete is given by

$$\varepsilon_{cc} = (4.76 \times 10^{-6} f_{co} + 2.13 \times 10^{-3})\left[1 + 14.74\left(\frac{\sigma_{con}}{f_{co}}\right)^{1.03}\right] \qquad \text{Equation 26}$$

and the concrete modulus (ACI 1992) by

$$E_c = 3320\sqrt{f_{co}} + 6900 \qquad \text{Equation 27}$$

where the unit is in MPa.

4. Effect of two distinct failure models

Previous shear friction research (Visintin et al. 2014b) has indicated that two failure modes can be encountered. That is failure through the formation of a circumferential wedge in Figure 2(a) or through a single sliding plane as shown in Figure 2(b); the failure mode being dependent on the geometry of the specimen (Chen et al. 2014a).

4.1 Effect on factor β

The failure mode factor β first introduced in Equation 7, that equals 2 for the circumferential wedge model in Figure 2(a) and 1 for the single sliding plane model in Figure 2(b), directly affects the axial effective strain due to wedge sliding in Equation 10 and consequently the axial global strain in Equation 11 and, furthermore, the shear friction components in Equations 12 and 13.

4.2 Effect on global lateral strain $\varepsilon_{lat\text{-}gbl}$

For the circumferential wedge model in Figure 2(a), the cross-section of the axial loaded specimen keeps the circular shape as shown in Figure 4(a) and expands uniformly around circumference. Hence, the global lateral strain $\varepsilon_{lat\text{-}gbl}$ is equal about both axes (X and Y directions in Figure 4(a)) and is composed of three components that are: the material dilation strain due to σ_{ax}

$$\varepsilon_{lat-mat} = \gamma_c \frac{\sigma_{ax}}{E_c} \qquad \text{Equation 28}$$

in which γ_c is the material Poisson ratio of the concrete and can be determined by Candappa et al. (2001) as

$$\gamma_c = 8 \times 10^{-6}(f_{co})^2 + 0.0002 f_{co} + 0.138 \qquad \text{Equation 29}$$

where the unit is in MPa; the contracting strain caused by confinement stress σ_{con}

$$\varepsilon_{lat-con} = -\frac{\sigma_{con}}{E_c} \qquad \text{Equation 30}$$

and the expansion strain due to sliding of the wedge (Visintin et al. 2014a, 2014b)

$$\varepsilon_{lat-wdg} = \frac{\beta\left(\Delta_{wdg} \sin\alpha + \frac{h_{cr}}{\cos\alpha}\right)}{d_{pr}} \qquad \text{Equation 31}$$

Hence, the global lateral strain $\varepsilon_{lat\text{-}gbl}$ of the circumferential wedge model is equal to

$$\varepsilon_{lat-gbl} = \varepsilon_{lat-mat} + \varepsilon_{lat-con} + \varepsilon_{lat-wdg} = \varepsilon_{circum-cw} \qquad \text{Equation 32}$$

which will be shown later to be the circumferential strain for the circumferential wedge ε_{circum}. For the single sliding plane failure mode, the cross-section of the axial loaded specimen takes an elliptical shape as shown in Figure 4(b) and the expansion strain due to sliding of the wedge $\varepsilon_{lat\text{-}wdg}$ (Equation 31) occurs only in the direction of sliding direction that is in the X direction in Figure 4(b). Therefore along the major axis, the global lateral strain $\varepsilon_{lat\text{-}gbl\text{-}maj}$ is equal to

$$\varepsilon_{lat-gbl-maj} = \varepsilon_{lat-mat} + \varepsilon_{lat-con} + \varepsilon_{lat-wdg} \qquad \text{Equation 33}$$

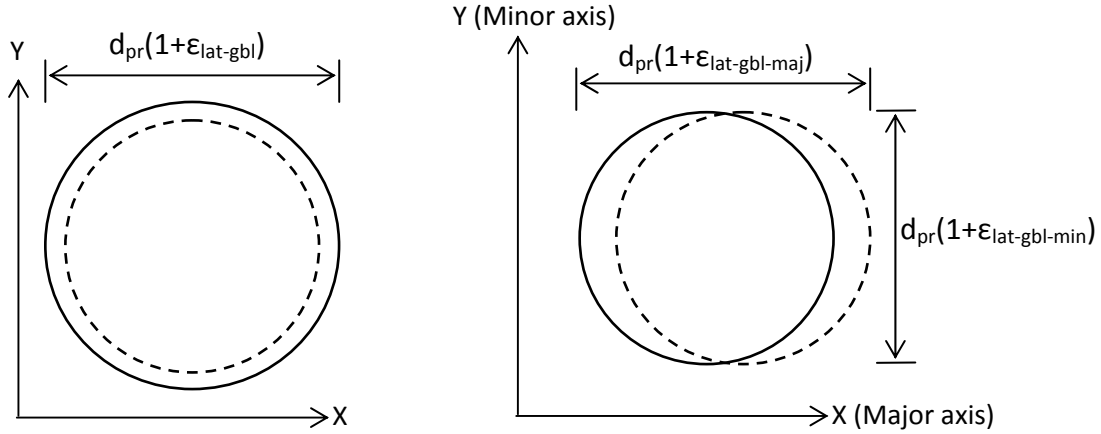

(a) Circumferential wedge (b) Single sliding plane

Figure 4: Cross-section of a confined cylinder for distinctive failure models

However along the minor axis, the global lateral strain $\varepsilon_{lat\text{-}gbl\text{-}min}$ is due only to the material and confinement dilation that is

$$\varepsilon_{lat-gbl-min} = \varepsilon_{lat-mat} + \varepsilon_{lat-con} \qquad \text{Equation 34}$$

4.3 Effect on circumferential strain ε_{circum}

For both failure models in Figure 2, the passive confinement stress of an FRP confined cylinder is always given by

$$\sigma_{con} = \frac{2\varepsilon_{circum} E_{FRP} t}{d_{pr}} \qquad \text{Equation 35}$$

where E_{FRP} is the elastic modulus of the FRP and ε_{circum} is the circumferential strain that depends on the model adopted to simulate the dilation of concrete under axial stress that is either Figures 4(a) or 4(b).

For the circumferential wedge model in Figure 4(a), the cross-section of an axially loaded specimen keeps the circular shape and expands uniformly around the circumference. Meanwhile, the perimeter of the cross-section changes from πd_{pr}, the dashed line shown in Figure 4(a), to $\pi d_{pr}(1+\varepsilon_{lat\text{-}gbl})$, that is the solid line shown in Figure 4(a). Hence, the

circumferential strain $\varepsilon_{circum-cw}$, that is defined as the change in circumference as a proportion of the original length, is $(\pi d_{pr}(1+\varepsilon_{lat-gbl})- \pi d_{pr})/(\pi d_{pr})$ which reduces to the global lateral strain $\varepsilon_{lat-gbl}$ that can be determined from Equation 32.

For the single sliding plane failure mode in Figure 4(b), the cross-section of an axially loaded specimen can be assumed to take an elliptical shape where the minor axis $d_{elps-min}$ is the diameter of a cylinder subjected to only material dilation and confinement as follows.

$$d_{elps-min} = d_{pr}\left(1 + \varepsilon_{lat-gbl-min}\right) \qquad \text{Equation 36}$$

The major axis is taken as the diameter of a cylinder subjected to the material expansion due to σ_{ax}, the contraction caused by confinement stress σ_{con} and the expansion due to sliding of the wedge, that is using Equation 33 it is given by

$$d_{elps-maj} = d_{pr}\left(1 + \varepsilon_{lat-gbl-maj}\right) \qquad \text{Equation 37}$$

As a result, the circumferential strain ε_{circum} of single sliding plane model is governed by

$$\varepsilon_{circum-ss} = \frac{\sqrt{\frac{d_{elps-min}^2+d_{elps-maj}^2}{2}}-d_{pr}}{d_{pr}} \qquad \text{Equation 38}$$

5. Variation in diameter of FRP confined cylinders

In this study, compressive strengths of concrete in the range of 30 to 60 MPa are investigated as this range of concrete compressive strength is consistent with that used to develop the shear friction properties (Chen et al. 2014b) used in this paper. FRP elastic moduli E_{FRP} in the range from 200 to 280 GPa and prism diameters η_{lat} up to a maximum of six times the base prism diameter are adopted.

This study on varying the diameter also assumes the following:

(1) The confined concrete specimens have identical concrete and FRP material properties.

(2) The specimens experience identical failure modes of either the circumferential wedge or single sliding plane failure. The angle of the shear friction sliding plane, α, is equal in all the specimens.

(3) Specimens of varying diameter but which have identical confinement and identical failure modes will have identical axial-stress/axial-strain relationships. This is not an assumption but a product of shear-friction theory and is illustrated in Figure 3 where specimens with the same σ_{cr} will have the same shear-friction properties.

(4) Hence, the material strain ε_{mat} and effective strain due to shear friction properties of two specimens being equal provides the same value of global strain ε_{ax-gbl} (Equation 11);

5.1 Circumferential wedge failure

In following derivations, shear friction properties (Equations 12 to 27) and circumferential strain $\varepsilon_{circum\text{-}cw}$ (Equations 32) are used to investigate the size effect in axially loaded concrete specimens, where a mathematical relationship is ultimately developed to quantify the thickness of FRP wrap t_2 in Figure 1(b) required for a given specimen diameter $d_{pr\text{-}2}$ to provide the same global axial-stress/axial-strain relationship as the concrete cylinder in Figure 1(a) with specimen diameter $d_{pr\text{-}1}$ and FRP wrap thickness t_1.

5.1.1 Mechanics solution

Assuming the specimen fails in a circumferential wedge, and substituting Equation 32 into Equation 35 and simplifying, gives

$$\sigma_{con} = \frac{\gamma_c \frac{\sigma_{ax}}{E_c} + \frac{2\left(\Delta_{wdg}\sin\alpha + \frac{h_{cr}}{\cos\alpha}\right)}{d_{pr}}}{\frac{d_{pr}}{2E_{FRP}t} + \frac{1}{E_c}} \qquad \text{Equation 39}$$

For the case where E_c, γ_c and E_{FRP} and α are independent of specimen geometry that is they are the same, for Specimen 1 in Figure 1(a)

$$\sigma_{con} = \frac{\gamma_c \frac{\sigma_{ax}}{E_c} + \frac{2\left(\Delta_{wdg-1}\sin\alpha + \frac{h_{cr-1}}{\cos\alpha}\right)}{d_{pr-1}}}{\frac{d_{pr-1}}{2E_{FRP}t_1} + \frac{1}{E_c}} \qquad \text{Equation 40}$$

and for Specimen 2 in Figure 1(b)

$$\sigma_{con} = \frac{\gamma_c \frac{\sigma_{ax}}{E_c} + \frac{2\left(\Delta_{wdg-2}\sin\alpha + \frac{h_{cr-2}}{\cos\alpha}\right)}{d_{pr-2}}}{\frac{d_{pr-2}}{2E_{FRP}t_2} + \frac{1}{E_c}} \qquad \text{Equation 41}$$

Equating Equations 40 and 41, and simplifying yields

$$t_2 = \frac{\left(\gamma_c \frac{\sigma_{ax}}{E_c} + \frac{2\left(\Delta_{wdg-1}\sin\alpha + \frac{h_{cr-1}}{\cos\alpha}\right)}{d_{pr-1}}\right)\frac{d_{pr-2}}{2E_{FRP}}}{\gamma_c \frac{\sigma_{ax}}{E_c}\frac{d_{pr-1}}{2E_{FRP}t_1} + \left(\frac{d_{pr-1}^2}{2E_{FRP}t_1 d_{pr-2}} + \frac{d_{pr-1}}{d_{pr-2}}\frac{1}{E_c} - \frac{1}{E_c}\right)\frac{2\left(\Delta_{wdg-1}\sin\alpha + \frac{h_{cr-1}}{\cos\alpha}\right)}{d_{pr-1}}} \qquad \text{Equation 42}$$

Equation 42 above is a mechanics solution for the influence of specimen diameter for circumferential wedge failure. That is, for Specimen 1 with prism diameter $d_{pr\text{-}1}$ and thickness of wrap t_1, Specimen 2 with prism diameter $d_{pr\text{-}2}$ requires an FRP wrap thickness of t_2, where t_2 from Equation 42 provides the same global axial-stress/axial-strain relationship as Specimen 1. However, Equation 42 includes the shear friction properties Δ_{wdg} and h_{cr} that vary according to the magnitude of the applied load. Therefore from Equation 42, the thickness of the FRP wrap must be varied during the loading process in order to get exactly the same global axial-stress/axial-strain curve for two different sized FRP wrapped specimens. The following simplifications can be used to get a practical expression.

5.1.2 Simplification One - Ignoring shear friction properties

Let us first ignore the effect of shear sliding; This is achieved by making all the terms with the shear friction material components $\Delta_{wdg\text{-}1}$ and $h_{cr\text{-}1}$ in Equation 42 equal to zero. Hence the only terms included are the stress-strain material properties. In this case Equation 42 simplifies to

$$t_2 = \eta_{lat} t_1 \qquad \text{Equation 43}$$

where η_{lat} is the ratio of the prism diameters from Equation 3. Equation 43 which has been derived through mechanics is proposed by various researchers (e.g. Theriault et al. 2004, Wang and Wu 2011, Akogbe et al. 2011) and is correct when based purely on material stress-strain properties that is the shear-friction mechanism is ignored.

Accuracy of Simplification One

If the simplified size effect expression Equation 43 is accurate, the global axial-stress/axial-strain relationship of Specimen 1 in Figure 1 with prism diameter $d_{pr\text{-}1}$ and thickness of wrap t_1 will be the same as that of Specimen 2 with prism diameter $d_{pr\text{-}2}$ and a FRP wrap thickness of t_2, where t_2 is from Equation 43.

Prior to calculating the global axial strain $\varepsilon_{ax\text{-}gbl}$ for a given imposed σ_{ax}, the confinement stress σ_{con} is required. The following analysis is carried out by guessing a lateral confinement $\sigma_{con\text{-}guess}$ corresponding to the imposed σ_{ax} and then checking if $\sigma_{con\text{-}guess}$ is the same as the confinement σ_{con} arising from the shear sliding mechanism that is Equation 35. The material and specimen properties adopted in the following examples and which are used throughout the remainder of this paper are: f_{co}=40 MPa, E_{FRP}=240GPa, an FRP rupture strain of $\varepsilon_{frp,rup}$=0.01, t_1=0.176 mm, $d_{pr\text{-}1}$=100 mm.

The analysis is carried out as follows:

(1) For the given imposed σ_{ax} and guessed $\sigma_{con\text{-}guess}$ in Figure 2, the shear stress τ_{cr} and normal stress σ_{cr} across the potential sliding plane can be determined from the equilibrium Equations 12 and 13.

(2) For the now known τ_{cr} and σ_{cr} the corresponding slip of the wedge Δ_{wdg} and crack separation h_{cr} can be determined from Equations 14 and 18.

(3) Knowing shear friction properties (Δ_{wdg}, h_{cr}), the circumferential strain $\varepsilon_{circum\text{-}cc}$ can be determined by Equation 32.

(4) Substituting the known $\varepsilon_{circum\text{-}cc}$ into Equation 35 gives the confinement σ_{con} that has arisen from the shear sliding mechanism. If σ_{con} does not equal $\sigma_{con\text{-}guess}$ then the analysis is repeated with a new $\sigma_{con\text{-}guess}$ until it does.

(5) Knowing the right confinement σ_{con}, Δ_{wdg} can be calculated from Equations 14 as τ_{cr} depends on σ_{con}, and then the global axial strain $\varepsilon_{ax\text{-}gbl}$ can be determined by Equation 11. This gives one point on the global axial-stress/axial-strain curve such as point A in Figure 5.

(6) Varying the given imposed σ_{ax} gives the whole global axial-stress/axial-strain curve as the solid line shown in Figure 5 that is for d_{pr-1}=100 mm.

Varying the cylinder diameter to d_{pr-2}=200 mm, and using Equation 43 to calculate the corresponding thickness t_2, the global axial-stress/axial-strain curve for a 200 mm diameter cylinder can be determined by repeating the above analysis as shown in Figure 5. Similarly, the results for a 300 mm diameter cylinder are also shown. It can be seen that Equation 43 which is based on the mechanics of the material stress-strain properties underestimates the FRP plate thickness required to achieve the same global concrete stress-strain relationship with increasing diameter. Hence the use of Equation 43 in converting the results of small diameter cylinder tests for larger diameter columns is slightly unconservative.

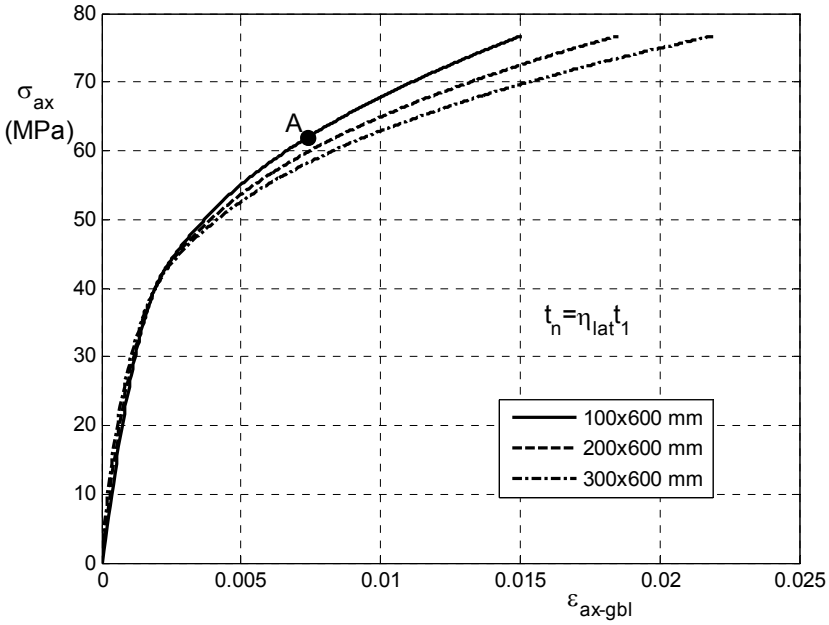

Figure 5 - Global axial-stress/axial-strain relationship using Equation 43

Figure 5 highlights the applicability of the derived expression (Equation 43) to simulate the behaviour of FRP wrapped concrete specimens of varying diameter. It is worth noting that the above analysis can be applied to either of the sliding mechanisms in Figure 2 depending on which is assumed to have occurred.

5.1.3 Simplification Two – ignoring material stress-strain properties

Let us consider again the circumferential strain $\varepsilon_{circum-cc}$ of Equation 32 which is composed of three components: the material dilation strain $\varepsilon_{lat-mat}$ (Equation 28); contracting strain caused by the confinement stress $\varepsilon_{lat-con}$ (Equation 30); and expansion strain due to sliding of the wedge $\varepsilon_{lat-wdg}$ (Equation 31). Consider only the most dominant component of the shear friction properties Δ_{wdg} in Equation 31 and ignore the effect of crack separation h_{cr}, material Poisson ratio γ_c and contraction due to confinement σ_{con}, then Equation 32 simplifies to

$$\varepsilon_{circum-cc} = \frac{2\Delta_{wdg}\sin\alpha}{d_{pr}} \qquad \text{Equation 44}$$

Substituting Equation 44 into Equation 35 yields

$$\sigma_{con} = 4E_{FRP} \cdot \Delta_{wdg} \sin\alpha \cdot \frac{t}{{d_{pr}}^2} \qquad \text{Equation 45}$$

Applying Equation 45 to Specimens 1 and 2 in Figures 1(a) and 1(b), then equating the confinements gives

$$t_2 = {\eta_{lat}}^2 t_1 \qquad \text{Equation 46}$$

Using the same analysis as described in *Section 5.1.2* for Equation 43, the applicability of Equation 46 to simulate the behaviour of FRP wrapped concrete specimens of varying diameter is shown in Figure 6. It can be seen that in this case, which is based purely on the mechanics of the shear friction component of sliding, the use of Equation 46 overestimates the plate thickness required to achieve the same confinement for larger diameter specimens. Hence this is a conservative approach compared with that of Equation 43 which is slightly unconservative. It would appear from Equations 43 and 46 that the exponent in Equation 46 should lie between 1 and 2.

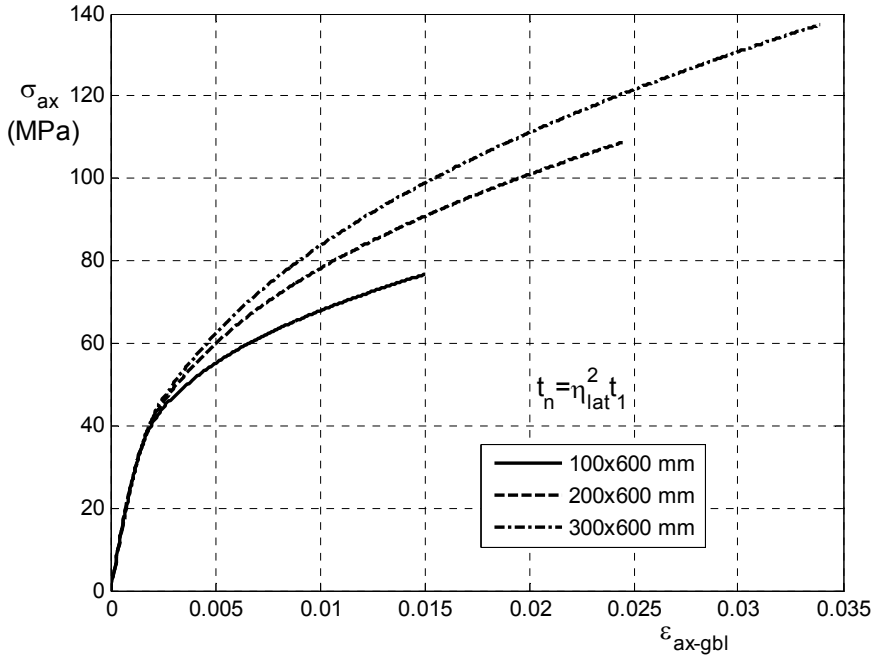

Figure 6 - Global axial-stress/axial-strain relationship using Equation 46

5.1.4 Proposed lateral size expression

Comparing Equations 43 and 46 and from the analyses in Figures 5 and 6, it is clear that the following mathematical expression

$$t_n = {\eta_{lat}}^x t_1 \qquad \text{Equation 47}$$

is a simple and reasonable model to quantify the influence of specimen diameter on the global axial-stress/axial-strain behaviour of an FRP confined concrete specimen.

It has already been shown that it is impossible to get identical stress/strain relationships for specimens with varying diameters. However identical stress/strain responses can be obtained at a point with close correlation elsewhere. Selecting the point of FRP rupture, $\varepsilon_{frp,rup}$ = 0.01, as the "key" point of convergence for the global axial-stress/axial-strain curves, the exponent x in Equation 47 for prism diameter ratios (η_{lat}) of 2, 3 and 6 is 1.17 and 1.23 and 1.29 respectively as shown in Figure 7 below. The first Rupture Point on the left is rupture of the 100 mm cylinder, the next that for the 200 mm cylinder and so on. It can be seen that there is reasonable correlation elsewhere.

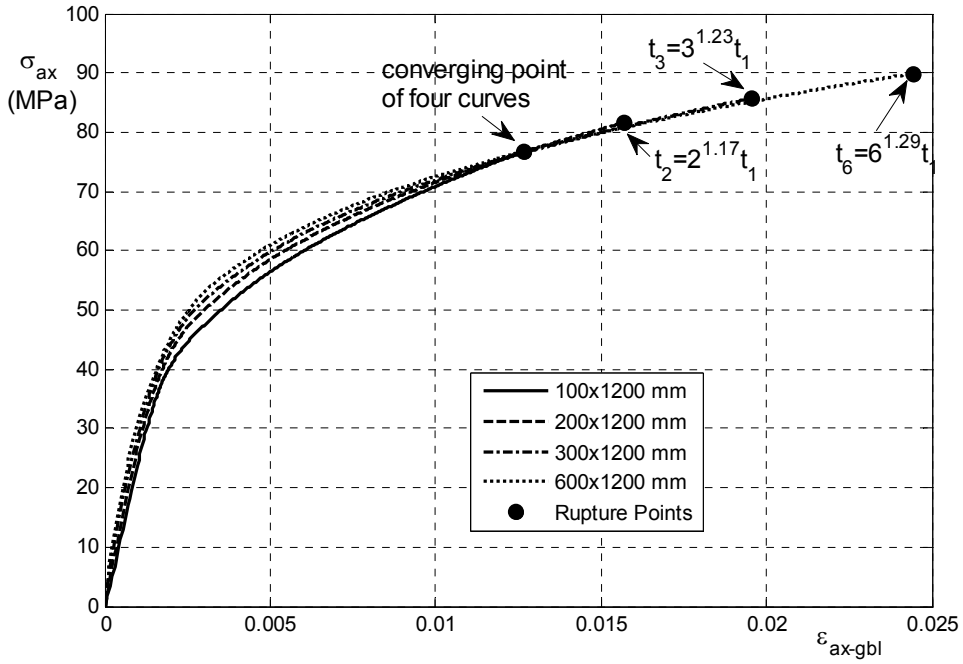

Figure 7 – Convergence for circumferential wedge model

The average of the exponents in Figure 7 is 1.23. A conservative approach would be to use an exponent of 1.29 that is the upper of the range. For example if a 100 mm diameter cylinder had an FRP wrap of 1 mm then a 300 mm diameter cylinder would need a wrap of $3^{1.29}$ to have the same confinement at rupture that is a wrap thickness of 4.12 mm. Conversely to obtain the stress/strain relationship for a 300 mm diameter cylinder with a 4.12 mm FRP wrap would require the testing of a 100 mm diameter cylinder with a 1 mm thick wrap. Bearing in mind that the height of the cylinders must be the same; allowance for variations in the height are quantified later.

5.2 Single sliding plane failure

Similar to the analysis for the circumferential wedge failure mode above, the shear friction properties of Equations 12 to 27 and the circumferential strain $\varepsilon_{circum\text{-}ss}$ of Equations 38 are used to investigate the size effect in axially loaded concrete specimens.

5.2.1 Mathematical solution

Substituting Equation 38 into Equation 35 yields

$$\sigma_{con} = \frac{2E_{FRP}t}{d_{pr}} \frac{\sqrt{\frac{d_{elps-maj}^2 + d_{elps-min}^2}{2}} - d_{pr}}{d_{pr}} \qquad \text{Equation 48}$$

Substituting Equations 36 and 37 into Equation 48 and simplifying results in

$$\sigma_{con} = \frac{2E_{FRP}t}{d_{pr}} \left(\sqrt{\frac{(1+\varepsilon_{lat-gbl-maj})^2 + (1+\varepsilon_{lat-gbl-min})^2}{2}} - 1 \right) \qquad \text{Equation 49}$$

Substituting Equations 33 and 34 into Equation 49 yields

$$\sigma_{con} = \frac{2E_{FRP}t}{d_{pr}} \left(\sqrt{\frac{(1+\varepsilon_{lat-mat}+\varepsilon_{lat-con}+\varepsilon_{lat-wdg})^2 + (1+\varepsilon_{lat-mat}+\varepsilon_{lat-con})^2}{2}} - 1 \right) \qquad \text{Equation 50}$$

Substituting Equations 28, 30 and 31 into Equation 50 and rearranging yields

$$\frac{d_{pr}}{2E_{FRP}t}\sigma_{con} + 1 = \sqrt{\frac{\left[1+\left(\gamma_c \frac{\sigma_{ax}}{E_c} - \frac{\sigma_{con}}{E_c} + \frac{\left(\Delta_{wdg}\sin\alpha + \frac{h_{cr}}{\cos\alpha}\right)}{d_{pr}}\right)\right]^2 + \left[1+\left(\gamma_c \frac{\sigma_{ax}}{E_c} - \frac{\sigma_{con}}{E_c}\right)\right]^2}{2}} \qquad \text{Equation 51}$$

Squaring both sides of Equation 51 and expressing it as a function of confinement σ_{con} provides

$$A \cdot (\sigma_{con})^2 + B \cdot \sigma_{con} + C = 0 \qquad \text{Equation 52}$$

where

$$A = 2\left(\frac{d_{pr}}{2E_{FRP}t}\right)^2 - 2\left(\frac{1}{E_c}\right)^2 \qquad \text{Equation 53}$$

$$B = 2\frac{d_{pr}}{E_{FRP}t} + 2\left(\gamma_c \frac{\sigma_{ax}}{E_c} + \frac{\left(\Delta_{wdg}\sin\alpha + \frac{h_{cr}}{\cos\alpha}\right)}{d_{pr}} + 2\right)\frac{1}{E_c} + 2\gamma_c \frac{\sigma_{ax}}{E_c}\frac{1}{E_c} \qquad \text{Equation 54}$$

and

$$C = -\left(\gamma_c \frac{\sigma_{ax}}{E_c} + \frac{\left(\Delta_{wdg}\sin\alpha + \frac{h_{cr}}{\cos\alpha}\right)}{d_{pr}}\right)^2 - 2\left(\gamma_c \frac{\sigma_{ax}}{E_c} + \frac{\left(\Delta_{wdg}\sin\alpha + \frac{h_{cr}}{\cos\alpha}\right)}{d_{pr}}\right) - \left(\gamma_c \frac{\sigma_{ax}}{E_c}\right)^2 - 2\left(\gamma_c \frac{\sigma_{ax}}{E_c}\right)$$

Equation 55

Solving for the positive root of Equation 52 gives

$$\sigma_{con} = \frac{\sqrt{B^2 - 4AC} - B}{2A} \qquad \text{Equation 56}$$

Applying Equation 56 to Specimens 1 and 2 in Figure 1 and equating them gives

$$\frac{\sqrt{{B_1}^2 - 4A_1C_1} - B_1}{2A_1} = \frac{\sqrt{{B_2}^2 - 4A_2C_2} - B_2}{2A_2} \qquad \text{Equation 57}$$

where A_1 and A_2 are from Equation 53; B_1 and B_2 from Equation 54; and C_1 and C_2 from Equation 55. Removing the square root of Equation 57, and expressing it in terms of A_2 yields

$$C_1{}^2A_2{}^2 + \left(B_1{}^2C_2 + 2A_1C_2C_1 - C_1B_1B_2 - 4A_1C_1A_2C_2\right)A_2 + \left((A_1C_2)^2 - A_1C_2B_1B_2 + A_1C_1B_2{}^2\right) = 0$$ Equation 58

Equation 58 is the governing equation that includes the relationship of thickness ratio t_2/t_1 and lateral size of the specimen η_{lat}. Substituting Equations 53, 54 and 55 into the positive root of Equation 58 and simplifying results in

$$t_2 = \frac{\eta_{lat} d_{pr-1}}{2E_{FRP}\sqrt{\sqrt{G\left(2\left(\frac{d_{pr-1}}{2E_{FRP}t_1}\right)^2 - 2\left(\frac{1}{E_c}\right)^2\right)\left(2\frac{d_{pr-1}}{E_{FRP}t_1} + \frac{2\varepsilon_{lat-wdg} + 4\varepsilon_{lat-mat} + 4}{E_c}\right)^2} + \frac{(\eta_{lat}+1)\left(\frac{1}{E_c}\right)^2 - \left(\frac{d_{pr-1}}{2E_{FRP}t_1}\right)^2}{\eta_{lat}}}}$$

Equation 59

in which G is a parameter equal to

$$G = \frac{\eta_{lat} - 1}{4\eta_{lat}}\left(\left(\varepsilon_{lat-wdg}\right)^2 + 2\varepsilon_{lat-wdg} + 2(\varepsilon_{lat-mat})^2 + 4\varepsilon_{lat-mat} + 2\varepsilon_{lat-wdg}\varepsilon_{lat-mat}\right)$$

Equation 60

Equation 59 is a mechanics expression for the influence of specimen diameter for a single sliding plane failure. This expression is equivalent to Equation 42 for the influence of specimen for circumferential wedge failure. Equation 59 does not lend itself to practical application due to its complexity. If shear friction properties are ignored, as for the circumferential wedge model in Sections *5.1.2*, the simplified expression of Equation 59 is still dependent on the axial stress σ_{ax} and consequently not suitable for practical application. Similarly, when only considering the most dominant component of shear friction properties Δ_{wdg}, the simplified expression of Equation 59 is still dependent on shear friction properties and not applicable at all.

5.2.2 Proposed lateral size expression

Repeating the same approach as for the circumferential wedge failure mode earlier, and adopting FRP rupture as the "key" convergence point, the exponent x in Equation 47 is 1.16 and 1.21 and 1.26 respectively for η_{lat} 2, 3 and 6 respectively as shown in Figure 8. Hence this exponent only varies slightly from that derived from the circumferential wedge and a safe design would be to use the upper end of the range which for the circumferential wedge was 1.29.

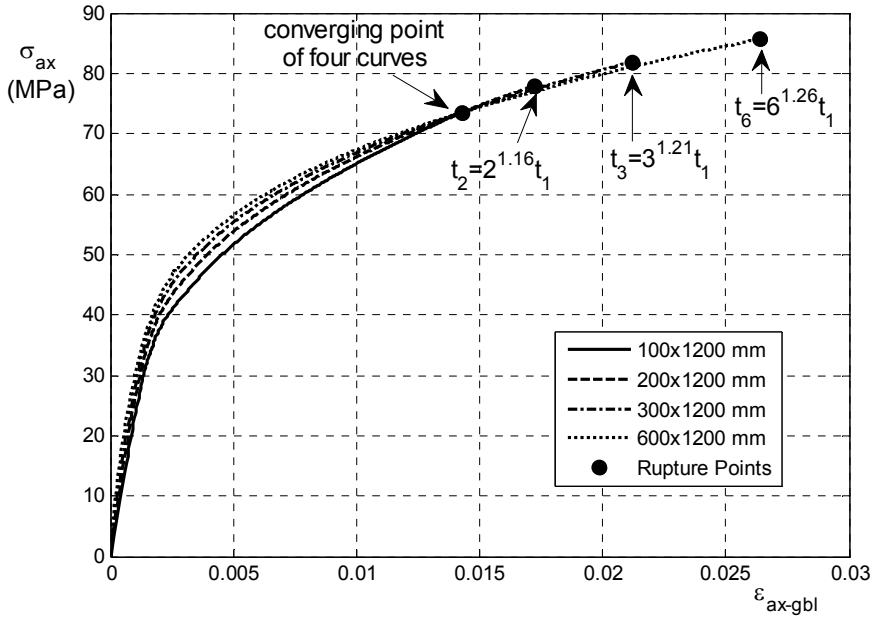

Figure 8: Convergence for single sliding plane model

5.3 Comparison of lateral size effect

The exponent of Equation 47 for both the circumferential wedge and single sliding plane for various cylinder diameter ratios η_{lat} are shown in Figure 9. It can be seen that there is not a large variation between failure modes nor a large change and, hence, using the upper bound value of 1.29 as derived previously will not give an overly conservative design. Hence it is suggested that to ensure the same confinement

$$t_n = {\eta_{lat}}^{1.29} t_1 \qquad \text{Equation 61}$$

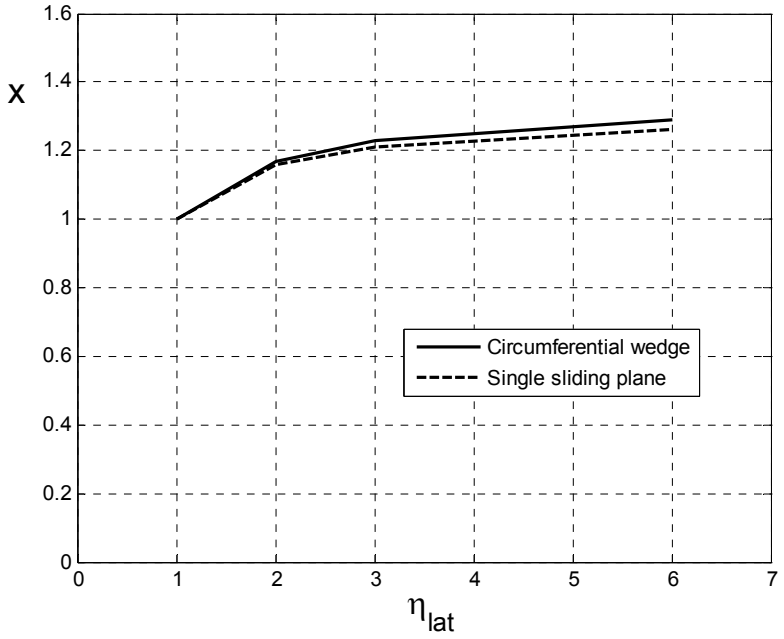

Figure 9: The relationship between lateral size of the specimen η_{lat} and power of size effect expression x

6. Variation in height of FRP confined cylinder

Section 5 has been concerned with the size effect of varying the diameter of a cylinder. It was shown that for Specimen 2 in Figure 1 to have the same confinement as Specimen 1 the FRP plate thickness would have to be increased according to Equation 61 in which the exponent is 1.29. This would ensure that the confinement in both specimens are close so that the global axial-stress/axial-strain relationship would also be close. It is also worth noting that this research assumed that the angle of wedge α remained constant which requires that the shape factor μ in Equation 1 is always greater than or equal to two.

The global axial-stress/axial-strain relationship also depends on height. For specimens with the same diameter and FRP wrap, the variation in confinement with axial stress is identical so that the wedge deformation D_{wdg} is identical. Hence if one specimen has a material deformation D_{mat-1} and wedge deformation D_{wdg-1} in Equation 4, then when the height is doubled, as an example, the wedge deformation stays the same that is D_{wdg-1} but the material deformation doubles to $2D_{mat-1}$ according to Equation 6. Based on this shear-friction mechanism, research on cylinders without FRP wraps has shown (Chen et al. 2014a, Visintin et al. 2014a) that the global axial-stress/axial-strain relationship of say Specimen 3 in Figure 1 can be obtained from that of Specimen 2 using the following expression when $\mu \geq 2$.

$$\varepsilon_{ax-gbl-3} = \left(\varepsilon_{ax-gbl-2} - \varepsilon_{mat}\right)\frac{1}{\eta_{ax}} + \varepsilon_{mat} \qquad \text{Equation 62}$$

where $\varepsilon_{ax\text{-}gbl\text{-}2}$ and $\varepsilon_{ax\text{-}gbl\text{-}3}$ are the global axial strains of Specimens 2 and 3 in Figure 1 respectively and are determined by Equation 5.

Equation 62 is not only applicable to specimens without FRP confinement but also applicable to specimens with the same confinement (Chen et al. 2014a, Visintin et al. 2014a) as this ensures that for a given axial stress the shear friction components are identical. When Specimens 2 and 3 in Figure 1 have the same diameter and FRP plate thickness then for a given axial load they have the same confinement. Consequently Equation 62 can be used to extract the global axial-stress/axial-strain relation of one specimen from the other. Hence if Specimen 3 with a plate thickness t_2 is tested to obtain the concrete global axial-stress/axial-strain relationship then from this global axial-stress/axial-strain relationship can be obtained the global axial-stress/axial-strain relationship for the shorter Specimen 2 using Equation 62. Furthermore, the global axial-stress/axial-strain relationship of Specimen 2 applies to Specimen 1 if the plate thickness t_2 is reduced to t_1 according to Equation 61 The converse is also applicable such that a small size specimen such as Specimen 1 in Figure 1 can be designed such that the global axial-stress/axial-strain relationship for the larger Specimen 3 can be extracted from that of the smaller specimen.

As an example, the solid line shown in Figure 10 is the test global axial-stress/axial-strain relationship of small size specimen (equivalent to Specimen 1 in Figure 1) which is a 100X200 mm cylinder wrapped with 0.5 mm thick FRP. Hence, the global axial-stress/axial-strain relationship for a 100X600 mm specimen wrapped with 0.5 mm thick FRP can be derived from the 100x200 cylinder results using Equation 62 and this is shown as the dash-dot line in Figure 10. It can be seen from Figure 10 that tripling the length of the specimen from 200 to 600 mm has no effect on the axial material strain ε_{mat}, however, the effective strain due to wedge ε_{wdg} decreases to one-third. Furthermore, for a 300X600 mm specimen wrapped with t_2 thickness FRP, where t_2 is from Equation 61 and equals $3^{1.29}$ X0.5=2.06 mm, provides the same global axial-stress/axial-strain relationship as that of the above 100X600 mm specimen. From a numerical analysis in Chen et al. (2014b and 2014c) and shown in Figures 5 to 8, significant shear sliding does not occur until the axial stress σ_{ax} reaches about the compressive strength of unconfined concrete f_{co}. Hence, neither the size nor the thickness of FRP has any effect on the diverging stress σ_{di} in Figure 10 which is appropriately constant at f_{co}.

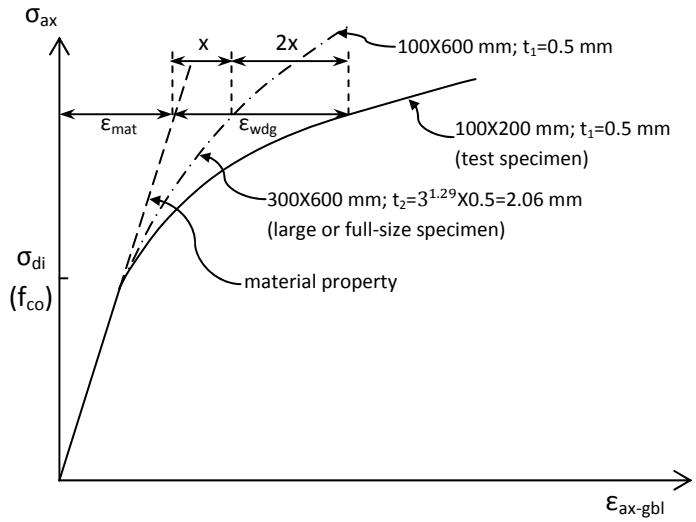

Figure 10: Extracting full-size properties from test specimen

7. Conclusion

Based on the mechanics of shear-friction, it has been shown that the global axial-stress/axial-strain relationship of a large or full-scale symmetrically or uniformly loaded FRP confined cylindrical specimen can be extracted from mechanically designed small scale FRP wrapped test specimens. This design approach allows for the size effects due to variations in cylinder diameter, height and FRP wrap thickness through the mechanics of shear friction.

A numerical shear friction approach has been developed for simulating FRP confined concrete cylinders. Two distinct failure modes have been examined, and mechanics relationships show that for varying concrete prism diameter the FRP wrap thickness must vary with applied axial load to provide identical stress-strain relationships for differing prism dimensions. Hence, it is not possible to get identical stress-strain curves for two different sized FRP wrapped concrete cylinders as the FRP wrap thickness is unable to be varied during loading. However, simplified expressions are proposed that give good accuracy for a wide range of cylindrical specimen widths and heights.

This research should enhance the value or usefulness of testing FRP confined cylinders as in theory the results from a single test can be adapted to apply to a wide range of shapes and sizes.

Acknowledgements

The authors would like to acknowledge the support of the Australian Research Council ARC Discovery Project DP0985828 ‘A unified reinforced concrete model for flexure and shear’.

References

ACI Committee 363 (1992). “State of the art report on high strength concrete”, ACI Publication 363R-92, American Concrete Institute, Detroit.

Ansari, F., and Li, Q. (1998). “High-strength concrete subjected to triaxial compression.” ACI Materials Journal, 95(6), 747-755.

Balmer, G. G. (1949). “Shear strength of concrete under high triaxial stress – Computation of Mohr’s envelope as a curve.” Structural Research Laboratory Roport No. SP-23, Department of the interior bureau of reclamation, United States.

Bazant, Z. P. (1984). “Size effect in blunt fracture: concrete, rock, metal.” Journal of Engineering Mechanics, 110(4), 518-535.

Bellotti, P. R. (1991). “Cylinder tests: experimental technique and results”. Materials and Structures, Vol. 24, 45-51.

Binici, B. (2008). “Design of FRPs in circular bridge column retrofits for ductility enhancement.” Engineering Structures, 30(3), 766-776.

Carey, S. A., and Harries, K. A. (2005). “Axial behavior and modeling of confined small-, medium-, and large-scale circular sections with carbon fiber-reinforced polymer jackets.” ACI Structural Journal, 102(4).

Chen, Y., Visintin, P., Oehlers, D., and Alengaram, U. (2014a). “Size-Dependent Stress-Strain Model for Unconfined Concrete.” Journal of Structural Engineering, 140(4), 04013088.

Chen, Y., Visintin, P., and Oehlers, D.J. (2014b). “Concrete shear-friction material properties: derivation from actively confined compression cylinder tests.” Submitted to Advances in Structural Engineering on 26/03/14.

Chen, Y., Zhang, T., Visintin, P., and Oehlers, D.J. (2014c). “Concrete shear-friction material properties: application to shear capacity of RC beams of all sizes.” Submitted to Advances in Structural Engineering on 26/03/14.

Chen, Y. (2014). “Quantifying the compressive ductility of concrete in RC members through shear friction mechanics.” PhD thesis, Department of Civil, Environment and Mining Engineering,The University of Adelaide, Australia.

De Lorenzis, L., Micelli, F., and La Tegola, A. (2002). “Influence of Specimen Size and Resin Type on the Behaviour of FRP-Confined Concrete Cylinders,” Proceedings of ACIC-2002: Advanced Polymer Composites for Structural Applications in Construction, Southampton, pp. 231-239.

Fahmy, M. F., & Wu, Z. (2010). “Evaluating and proposing models of circular concrete columns confined with different FRP composites.” Composites Part B: Engineering, 41(3), 199-213.

Gardner, N. J. (1969). “Triaxial behaviour of concrete”. ACI Journal, Title no. 66-15, 136-146.

Gonnerman, H. F. (1925). “Effect of size and shape of test specimen on compressive strength of concrete.” Structural materials research laboratory.

Hamdy, M. M. and Radhouane, M. (2010). “Axial load Capacity of Concrete-Filled FRP Tube Columns: Experimental versus Theoretical Predictions,” Journal of Composites for Construction ASCE, Vol. 14, No. 2, 231-243.

Harmon, T.G., Ramakrishnan, S. and Wang, E.H. (1998), “Confined concrete subjected to uniaxial monotonic loading”, Journal of Engineering Mechanics, Vol. 124, No.12, 1303-1309.

Imran, I., and Pantazopoulou, S. J. (1996). “Experimental Study of Plain Concrete under Triaxial Stress”. ACI Materials Journal, Vol. 93, No. 6, 589-601.

Jamet, P., Millard, A., and Nanas, G. (1984). “Triaxial behaviour of a Micro-concrete Complete Stress-Strain Curves for Confining Pressures Ranging From 0 to 100 MPa”. GIF SUR YVETTE CEDEX (France), Title no. 91191, 133-140.

Karbhari, V. M., & Gao, Y. (1997). “Composite jacketed concrete under uniaxial compression-verification of simple design equations.” Journal of materials in civil engineering, 9(4), 185-193.

Kotsovos, M. D. and Newman J. B. (1978). “Generalised stress-strain relations for concrete”. Journal of the Engineering Mechanics Division, ASCE, Vol. 104, No. EM4, pp. 845-856.

Kotsovos, M. D. and Newman J. B. (1979). “A mathematical description of the deformational behaviour of concrete complex loading”. Magazine of Concrete Research, Vol. 31, No. 107, pp. 77-90.

Lahlou, K., Aitcin, P. C. and Chaallal, O. (1992). “Behaviour of high-strength concrete under confined stresses”. Cement and Concrete Composites, 14, 185-193.

Lam, L., & Teng, J. G. (2003). “Design-oriented stress–strain model for FRP-confined concrete.” Construction and Building Materials, 17(6), 471-489.

Lu, X. B., and Hsu, C. T. (2006). “Behavior of high strength concrete with and without steel fiber reinforcement in triaxial compression”. Cement and Concrete Research, 36, 1679-1685.

Moran, D. A., & Pantelides, C. P. (2002). “Variable strain ductility ratio for fiber-reinforced polymer-confined concrete.” Journal of Composites for Construction, 6(4), 224-232.

Richart, F. E., Brandtzaeg, A., and Brown, R. L. (1928). “Study of the Failure of Concrete under Combined Compressive Stresses,” Bulletin 185, University of Illinois Engineering Station, Urbana.

Richart, F. E., Brantzaeg, A., and Brown, R. L. (1929). “The failure of plain and spirally reinforced concrete in compression”. Bulletin No. 185, Engineering Experiment Station, University of Illinois, Urbana.

Saafi, M., Toutanji, H., & Li, Z. (1999). “Behavior of concrete columns confined with fiber reinforced polymer tubes.” ACI Materials Journal, 96(5):500–9.

Saiid Saiidi, M., Sureshkumar, K., & Pulido, C. (2005). “Simple carbon-fiber-reinforced-plastic-confined concrete model for moment-curvature analysis.” Journal of Composites for Construction, 9(1), 101-104.

Samaan, M., Mirmiran, A., & Shahawy, M. (1998). “Model of concrete confined by fiber composites.” Journal of Structural Engineering, 124(9), 1025-1031.

Setunge, S., Attard, M. M., and Darvall, P. (1993). “ultimate strength of confined very high strength concrete”. ACI, Structure Journal, 90(6), 632-641.

Sfer, D., Carol, I., Gettu, R. and Etse, G. (2002). “Study of the behaviour of concrete under triaxial compression”. Journal of Engineering Mechanics, Vol. 128, No.2, 156-163.

Silva, M. A., & Rodrigues, C. C. (2006). “Size and relative stiffness effects on compressive failure of concrete columns wrapped with glass FRP.” Journal of materials in civil engineering, 18(3), 334-342.

Smith, S. S., William, K. J., Gerstle, K. H., and Sture, S. (1989). “Concrete over the top, or is there life after peak?”. ACI Materials Journal, Vol. 86, No. 5, 491-497.

Smith, S. T., Kim, S. J., & Zhang, H. (2010). “Behavior and effectiveness of FRP wrap in the confinement of large concrete cylinders.” Journal of Composites for Construction, 14(5), 573-582.

Teng, J. G., Chen, J. F., and Lam, L. (2002). FRP-strengthened RC structures, Wiley, London.

Teng, J. G., Jiang, T., Lam, L., & Luo, Y. Z. (2009). “Refinement of a design-oriented stress–strain model for FRP-confined concrete.” Journal of Composites for Construction, 13(4), 269-278.

Theriault, M., Neale, K. W., & Claude, S. (2004). “Fiber-reinforced polymer-confined circular concrete columns: investigation of size and slenderness effects.” Journal of composites for Construction, 8(4), 323-331.

Toutanji, H. (1999). “Stress-strain characteristics of concrete columns externally confined with advanced fiber composite sheets.” ACI Materials Journal, 96(3):397–404.

Visintin, P., Chen, Y., and Oehlers, D. (2014a). “Size dependent axial and lateral stress strain relationships for actively confined concrete.” Accepted for publication by Advances in Structural Engineering on 05/06/2014.

Visintin, P., Chen, Y., and Oehlers, D.J. (2014b). “Simulating the behaviour of FRP confined cylinders using the shear friction mechanism.” To be submitted to ASCE Composites for Construction.

Wang, Y. F., and Wu, H. L. (2010). “Size effect of concrete short columns confined with aramid FRP jackets.” Journal of Composites for Construction, 15(4), 535-544.

Wu, H. L., Wang, Y. F., Yu, L., & Li, X. R. (2009). “Experimental and computational studies on high-strength concrete circular columns confined by aramid fiber-reinforced polymer sheets.” Journal of Composites for Construction, 13(2), 125-134.

Wu, Y. F., and Zhou, Y. W. (2010). “Unified Strength Model Based on Hoek-Brown Failure Criterion for Circular and Square Concrete Columns Confined by FRP.” Journal of Composites for Construction ASCE, Vol. 14, No. 2, 175-184.

Xiao, Y., & Wu, H. (2000). “Compressive behavior of concrete confined by carbon fiber composite jackets.” Journal of Materials in Civil Engineering, 12(2), 139-146.

Xiao, Y., & Wu, H. (2003). “Compressive behavior of concrete confined by various types of FRP composite jackets.” Journal of Reinforced Plastics and Composites, 22(13), 1187-1201.

Xiao, Q. G., Teng, J. G., and Yu, T. (2010), “Behavior and Modeling of Confined High-strength Concrete”, Journal of Composites for Construction, Vol. 14, No. 3, pp 249-259.

Youssef, M. N., Feng, M. Q., & Mosallam, A. S. (2007). “Stress–strain model for concrete confined by FRP composites. Composites Part B: Engineering, 38(5), 614-628.

Chapter 5: Tests on Steel Tube Confined Concrete

1. Introduction

It is widely known (Richart et al 1928 and 1929; Balmer 1949; Gardner 1969; Kotsovos and Newman 1978 and 1979; Jamet et al 1984; Smith et al 1989; Bellotti and Rossi 1991; Lahlou et al 1992; Hammons and Neeley 1993; Setunge et al 1993; Imran 1994; Xie et al 1995; Attard and Setunge 1996; Imran and Pantazopoulou 1996 and 2001; Ansari and Li 1998; Harmon et al 1998; Candappa et al 2001; Sfer et al 2002; Lu and Hsu 2006; Xiao et al. 2010) that the stress-strain properties of concrete can be improved through active and passive confinement such as through confinement with steel tubes. Steel tube confined concrete columns (STCC or referred to by other researchers as concrete-filled steel tube columns) have become more and more popular as confined members for structural design purposes.

Due to limitations in the capacity of testing equipment, typical material properties of steel tube confined concrete are determined experimentally on small scale specimens of varying aspect ratios and tube diameter-to-thickness ratios and these experimental results are then used to develop empirical or semi-empirical equations for the influence of concrete confinement (Schneider 1998, Huang et al. 2002, Cai 2003, Sakino et al. 2004, Giakoumelis and Lam 2004, Chen 2005, Han 2007, Hatzigeorgiou 2008). Hence, it is important to ensure that the proposed equations are truly representative of the actual behaviour of full-scale columns. Moreover, current design codes [American Concrete Institute (ACI) 1999; American Institute of Steel Construction (AISC) 1999; Australian Standards: Concrete Structures (AS3600) 1994; Australian Standards: Steel Structures (AS4100) 1998; Chinese Standards: Code for Design of Concrete Structures (GB50010) 2010] for concrete structures strengthened with steel tube materials do not consider the influence of specimen size on the material behaviour of confined concrete that is the size effect. Contrary to the view of ignoring size effect, some researchers (Sakino et al. 2004) have proposed expressions of scale effects on the compressive strength and axial-stress/axial-strain curve that were regressed from their experimental tests.

It has been introduced in Chapter 2 that the axial-stress/axial-strain relationship depends on the shape of the prism μ, which is defined as the ratio of the length to diameter,

$$\mu = \frac{L_{pr}}{d_{pr}} \qquad \text{Equation 1}$$

the axial size of the specimen η_{ax}, which is defined as the ratio of the prism lengths, such as lengths of specimens 2 and 3 in Figure 1

$$\eta_{ax} = \frac{L_{pr-3}}{L_{pr-2}} \qquad \text{Equation 2}$$

and the lateral size of the specimen η_{lat}, which is defined as the ratio of the prism diameters, such as diameters of specimens 1 and 2 in Figure 1

$$\eta_{lat} = \frac{d_{pr-2}}{d_{pr-1}}$$ Equation 3

Theoretical analyses (e.g. Chen et al. 2014a, Visintin et al. 2014 in Chapter 2) have investigated and explained the size effect for specimens with a constant diameter but varying lengths, such as specimens 2 and 3 in Figure 1. Moreover, the size effect for specimens with a constant length and varying diameters, such as specimens 1 and 2 in Figure 1 has been quantified in Chapter 4.

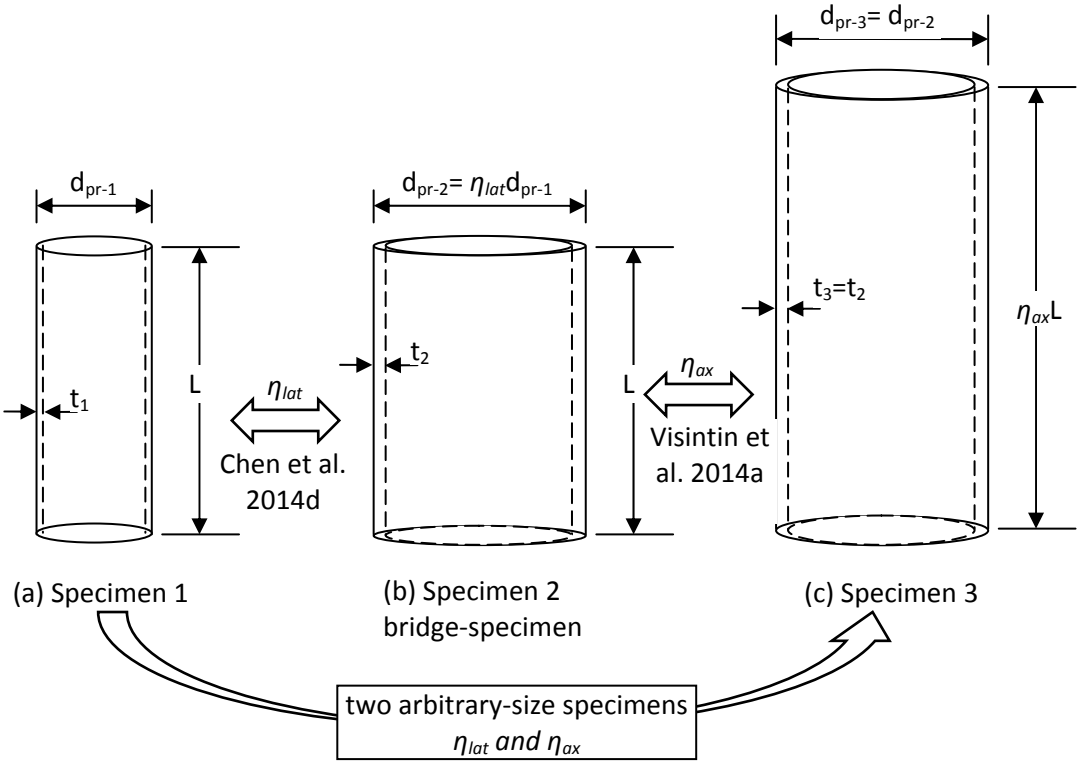

Figure 1: Size relationship of two arbitrary-size specimens

The main aim of this test program is to verify the accuracy of the following axial size effect expression proposed in Chapter 2:

$$\varepsilon_{axgl-3} = \left(\varepsilon_{axgl-2} - \varepsilon_{mat}\right)\frac{1}{\eta_{ax}} + \varepsilon_{mat}$$ Equation 4

where ε_{axgl-2} and ε_{axgl-3} is global axial strain of specimens 2 and 3 as shown in Figure 1 respectively and equals to total axial strain due to material contraction and wedge sliding;

ε_{mat} is material strain due to material contraction that equals the axial stress σ_{ax} divided by the concrete modulus E_c;

and also to verify the following lateral size effect expression proposed in Chapter 4:

$$t_2 = \eta_{lat}{}^{x} t_1 \qquad \text{Equation 5}$$

where t_1 and t_2 is the thickness of the steel tube for specimens 1 and 2 as shown in Figure 1;

x is the exponent of lateral size effect equation which lies between 1 and 1.29 and which depends on the lateral size of the specimen η_{lat} and failure model.

It is worthy to note that Equation 5 was originally derived for FRP-confined concrete but which should be able to predict the behavior of concrete confined with other materials, as long as the equation for the lateral dilation behaviour of concrete is accurate. Hence, once the thickness ratio of smaller specimen to the bridge-specimen (t_1/t_2 in Figure 1) complies with Equation 5, the bridge-specimen, that is specimen 2 in Figure 1, will has a stress-strain curve similar to the smaller specimen, that is specimen 1 in Figure 1. Furthermore, the axial size effect expression Equation 4 can be used to convert the axial-stress/axial-strain relationship of specimen 2 into that of specimen 3, and vice versa.

Once the above axial and lateral size effect expressions have been calibrated and validated, the axial-stress/axial-strain relationship of a full-scale specimen (e.g. specimen 3 in Figure 1) can be derived from that of a tested small-scale specimen like specimen 1 in following steps:

1. The confined concrete specimens 1 to 3 in Figure 1 consist of identical concrete and confining steel tube material properties, and where the thickness of the steel tube, diameter and length are varied as shown in Figure 1;
2. The thickness of the smaller specimen t_1 can be determined from the known t_3 by using the lateral size effect expression (Equation 5) in which the lateral size of the specimen η_{lat} equals $d_{pr\text{-}1}/d_{pr\text{-}3}$;
3. The tested axial-stress/axial-strain relationship of specimen 1 should be the same as that of specimen 2;
4. As specimens 2 and 3 have the same diameter and thickness of steel tube, and where length only varies; using the axial size effect expression (Equation 4) can be used to convert stress-axial train curve of specimen 2 into that of specimen 3;

Besides aiming to verify the axial and lateral size effect expressions of Equations 4 and 5, these tests also aim to confirm following assumptions proposed in Chapter 2, that is:

1. the angle of wedge sliding plane to the longitudinal axis, α proposed in Chapter 2, is given

$$\alpha = 26^{o} + \frac{\sigma_{con}}{f_{co}} \times 20^{o} \qquad \text{Equation 6}$$

where the confinement stress σ_{con} can appropriately treat as constant at

$$\sigma_{con} = \frac{2f_y t}{d_{pr}}$$ Equation 7

once the steel tube has been yielded at f_y.

2. the global lateral strain within the wedge region should be bigger than those out of the wedge region.

2. Design of specimens

The concrete used in this test with an aggregate size of 10 mm, had about a 50MPa compressive strength. In a half day, the concrete was poured, vibrated and left to cure for a minimum of 28 days as specified. A wooden formwork and safety straps with buckles were used to hold the cylinders in place during the pouring and curing process as shown below in Figure 2.

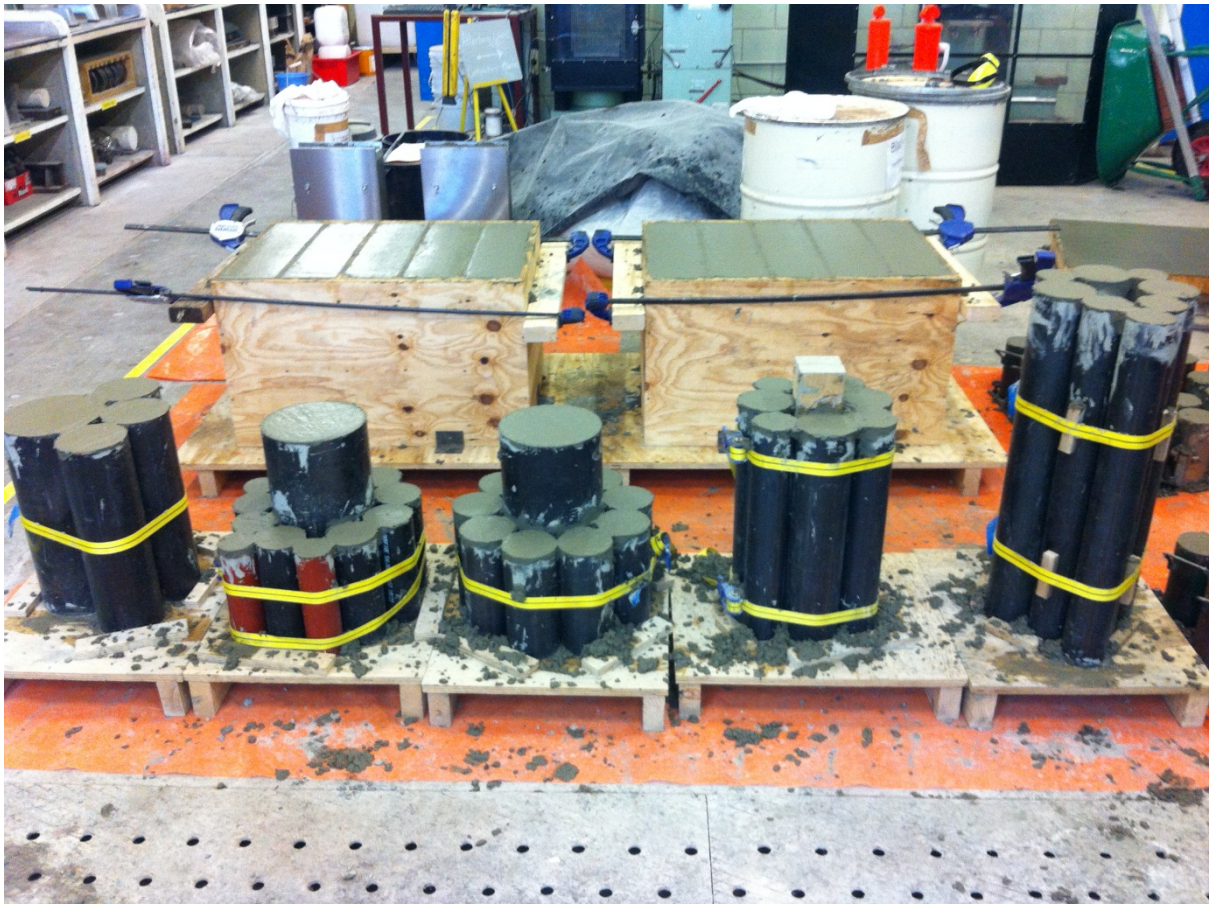

Figure 2: Pouring and curing steel tube confined concrete

The general information for the test steel tube confined concrete is shown below in Table 1 where the thirteen columns show contents as follows in sequence: ① test series number; ② specimen name, in which the first two letters represent the "Group Name" of this specimen, e.g. specimen GA-1A is specimen 1A in Group A; ③ the age of concrete at

testing; ④ the yield stress of steel tube provided by manufacturer; ⑤ the external diameter of steel tube recommended by manufacturer; ⑥ the thickness of steel tube recommended by manufacturer; ⑦the height of steel tube; ⑧the number of lateral strain gauges per height that is at one level; ⑨individual distance between bottom platen and a specific height level of lateral strain gauges; ⑩the number of axial strain gauges at a given height; ⑪individual distance between bottom platen and a specific height level of axial strain gauges; ⑫number of 10mm strain gauges per specimen; ⑬number of LVDTs per specimen.

With the exception of series 3 which had only one repetition, each series comprised three replicate specimens.

Three groups of specimens, whose diameters are the same but lengths are varying, are designed to verify the axial size effect expression, Equation 4, for the axial size of the specimen η_{ax}. Group A in Table 1 is composed of test series 1, 2 and 3 whose diameters are all 76.1 mm, and lengths are 250, 500 and 750 mm. Group B comprises test series 4, 5 and 6 whose diameters are 88.9 mm, and lengths are 250, 500 and 750 mm. Group C includes test series 11, 12 and 13 whose diameters are 114.3 mm, and lengths are 250, 500 and 750 mm. The material properties, such as the compressive strength of concrete f_{co}, the yield stress of steel tube f_y and the thickness of steel tube t, are all constant in each group. Hence, the confinement stress σ_{con} is constant at any given applied axial stress σ_{ax} in each group.

Two groups of test series, whose diameters are varying and lengths are constant, are designed to verify the lateral size effect expression, equation 5, for lateral size of the specimen η_{lat}. Group D is composed by test series 7 and 9 whose lengths are both 250 mm, and diameter is 101.6 and 114.3 mm separately. Group E includes test series 8 and 10 whose size dimensions are equal to test series 7 and 9 separately. The compressive strength of concrete f_{co} is constant in these two groups.

The yield stress of steel tube f_y in Group A, Group C and Group E is 250 MPa, while in Group B and Group D it is 350 MPa.

Table 1 - Description of specimens

Test Series No.	Specimen No.	Age (Days)	f_y (MPa)	External diameter, D (mm)	Thickness of steel tube, t (mm)	Length, L (mm)	Lateral Strain Gauges		Axial Strain Gauges		Total	LVDT
①	②	③	④	⑤	⑥	⑦	⑧	⑨	⑩	⑪	⑫	⑬
1	GA-1A	116	250	76.1	3.6	250	4	50, 100, 150, 200	0	0	16	4
	GA-1B	116	250	76.1	3.6	250	0	0	0	0	0	4
	GA-1C	116	250	76.1	3.6	250	0	0	0	0	0	4
2	GA-2A	118	250	76.1	3.6	500	0	0	0	0	0	4
	GA-2B	118	250	76.1	3.6	500	0	0	0	0	0	4
	GA-2C	118	250	76.1	3.6	500	0	0	0	0	0	4
3	GA-3A	137	250	76.1	3.6	750	0	0	0	0	0	4
	GA-3B	137	250	76.1	3.6	750	0	0	0	0	0	4
4	GB-4A	88	350	88.9	3.2	250	3	50, 125, 200	3	50, 125, 200	18	4
	GB-4B	88	350	88.9	3.2	250	2	50, 125	2	50, 125	8	4
	GB-4C	88	350	88.9	3.2	250	2	50, 125	2	50, 125	8	4
5	GB-5A	140	350	88.9	3.2	500	0	0	0	0	0	4
	GB-5B	140	350	88.9	3.2	500	0	0	0	0	0	4
	GB-5C	140	350	88.9	3.2	500	0	0	0	0	0	4

Table 1 - Description of specimens (continued)

Test Series No.	Specimen No.	Age (Days)	f_y (MPa)	External diameter, D (mm)	Thickness of steel tube, t (mm)	Length, L (mm)	Lateral Strain Gauges		Axial Strain Gauges		Total	LVDT
①	②	③	④	⑤	⑥	⑦	⑧	⑨	⑩	⑪	⑫	⑬
6	GB-6A	137	350	88.9	3.2	750	0	0	0	0	0	4
	GB-6B	137	350	88.9	3.2	750	0	0	0	0	0	4
	GB-6C	137	350	88.9	3.2	750	0	0	0	0	0	4
7	GD-7A	92	350	101.6	3.2	250	4	50, 100, 150, 200	0	0	16	4
	GD-7B	92	350	101.6	3.2	250	0	0	0	0	0	4
	GD-7C	92	350	101.6	3.2	250	0	0	0	0	0	4
8	GE-8A	92	250	101.6	4	250	4	50, 100, 150, 200	0	0	16	4
	GE-8B	92	250	101.6	4	250	0	0	0	0	0	4
	GE-8C	92	250	101.6	4	250	0	0	0	0	0	4
9	GD-9A	126	350	114.3	3.6	250	4	50, 100, 150, 200	0	0	16	4
	GD-9B	126	350	114.3	3.6	250	0	0	0	0	0	4
	GD-9C	126	350	114.3	3.6	250	0	0	0	0	0	4
10	GE-10A	131	250	114.3	4.5	250	4	50, 100, 150, 200	0	0	16	4
	GE-10B	131	250	114.3	4.5	250	0	0	0	0	0	4
	GE-10C	131	250	114.3	4.5	250	0	0	0	0	0	4

Table 1 - Description of specimens (continued)

Test Series No.	Specimen No.	Age (Days)	f_y (MPa)	External diameter, D (mm)	Thickness of steel tube, t (mm)	Length, L (mm)	Lateral Strain Gauges		Axial Strain Gauges		Total	LVDT
①	②	③	④	⑤	⑥	⑦	⑧	⑨	⑩	⑪	⑫	⑬
11	GC-11A	132	250	114.3	5.4	250	4	50, 100, 150, 200	0	0	16	4
	GC-11B	132	250	114.3	5.4	250	0	0	0	0	0	4
	GC-11C	132	250	114.3	5.4	250	0	0	0	0	0	4
12	GC-12A	118	250	114.3	5.4	500	0	0	0	0	0	4
	GC-12B	118	250	114.3	5.4	500	0	0	0	0	0	4
	GC-12C	118	250	114.3	5.4	500	0	0	0	0	0	4
13	GC-13A	139	250	114.3	5.4	750	0	0	0	0	0	4
	GC-13B	139	250	114.3	5.4	750	0	0	0	0	0	4
	GC-13C	139	250	114.3	5.4	750	0	0	0	0	0	4
Total	38	--	--	--	--	--	--	--	--	--	130	--

3. Instrumentation and test rig

The machine used for this concentric compressive load testing is the Amsler, a device capable of applying large compression loads between two plates by using pressurised oil. Metal plates are dental pasted to the top and bottom of each specimen to ensure the specimen has a flat and parallel surface for the platens to apply loading to as seen in Figure 3. The diameter of metal plate is always about 5mm to 10mm smaller than the inner diameter of steel tube as shown in Figure 4, therefore, the testing load is only applied directly to the confined concrete such that possible steel tube buckling can be avoided.

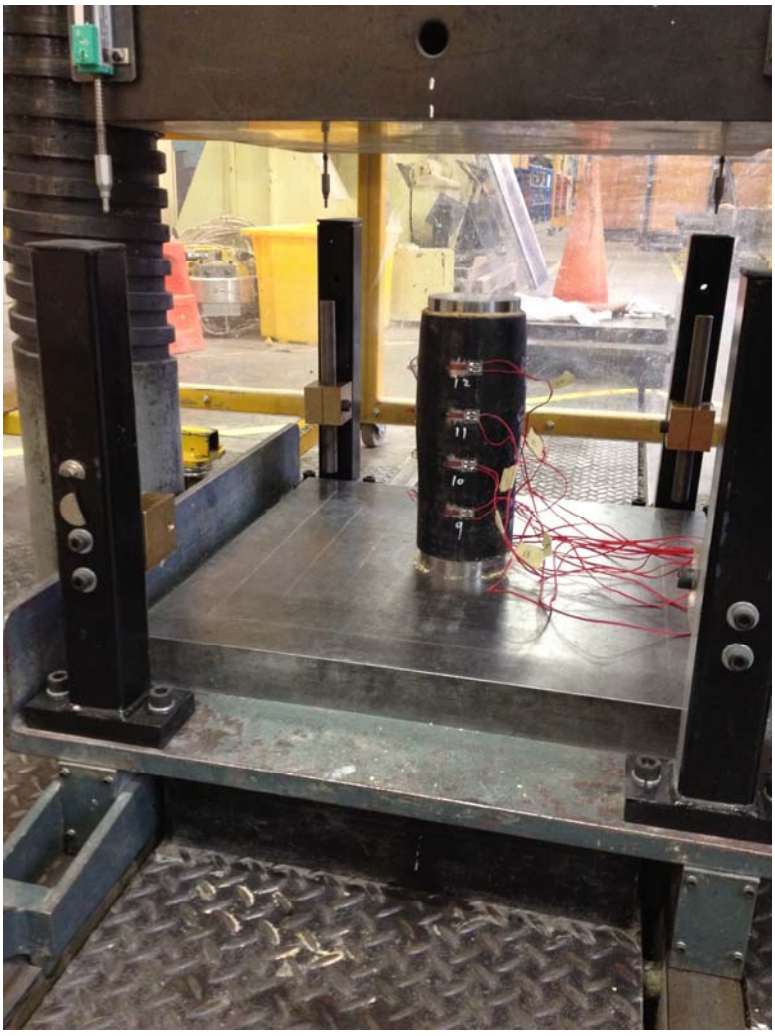

Figure 3: Example of specimen ready to test

The proposed axial size effect expression, Equation 4, is based on the on shear friction mechanism such that the global axial strain is required. Therefore, 4 linear variable differential transformers (LVDTs) are fixed at every corner of the square loading platen of the testing machine as shown in Figure 4 to measure and record the whole deformation over the length of the test which can be used to calculate the global axial strain. Figure 4 shows the front, side and plan views of test rig of which the 4 LVDT are labelled as L-NW, L-SE, L-NE and L-SW separately. The name of “L-NW, L-SE, L-NE and L-SW” means that the

location of LVDT is on the North-West, South-East, North-East and South-West direction of tested specimen as shown in Figure 4(b).

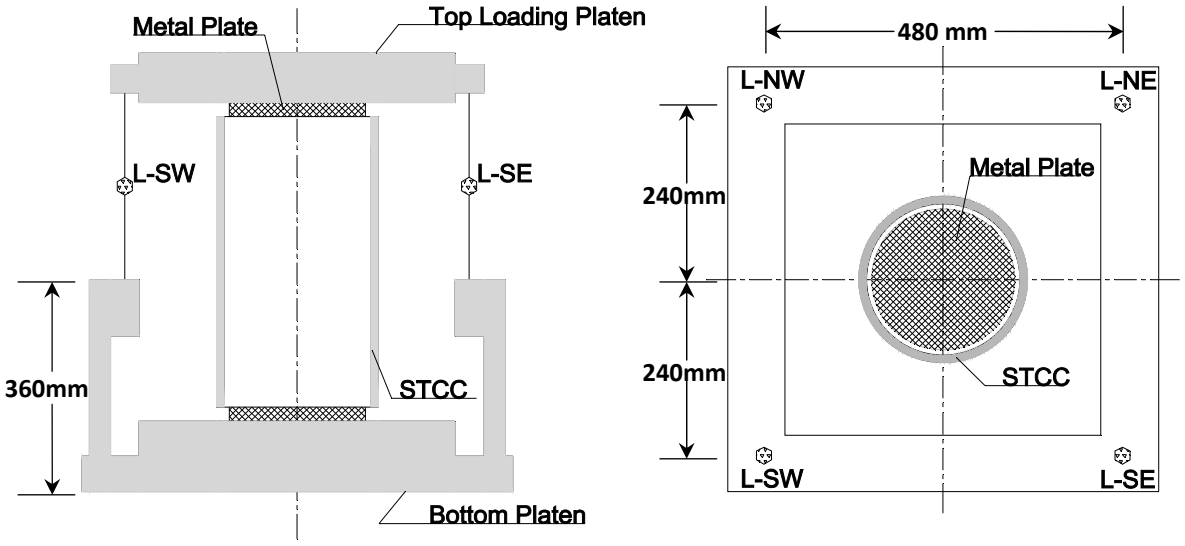

(a) Front/Side View (b) Plan View

Figure 4: Front, side and plan views of test rig

In order to verify the assumption of ignoring the bond between concrete and confinement material that has been adopted by deriving the axial size effect expression, Equation 4 and lateral size effect expression, Equation 5, specimen GB-4A is attached three axial strain gauges 120^{o} equally apart around the circumference at heights of 50, 125 and 200 mm from the bottom separately as shown in Figure 5. Additionally, specimens GB-4B and GB-4C are attached two axial strain gauges 180^{o} around the circumference at heights of 50 and 125 mm from the bottom separately as shown in Figure 6. These axial strain gauges should indicate zero or very small value during loading process if the above assumption is right.

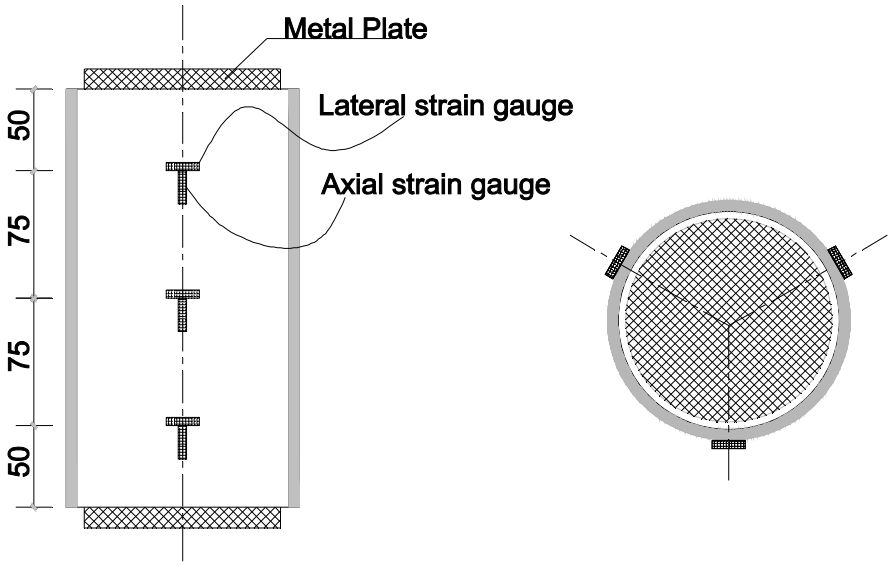

(a) Front View (b) Plan View

Figure 5: Strain gauges of specimen GB-4A

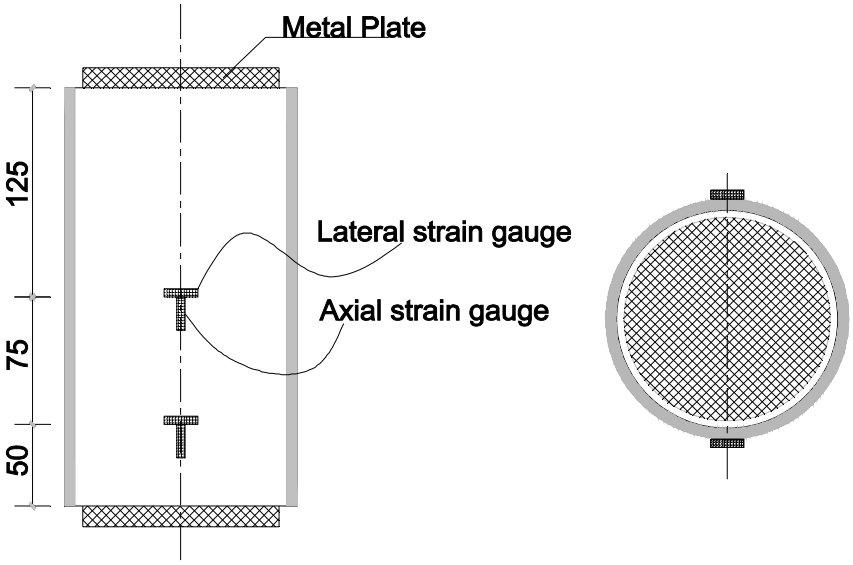

(a) Front View (b) Plan View

Figure 6: Strain gauges of specimen GB-4B and GB-4C

The proposed lateral size effect expression, Equation 5 is based on the shear friction mechanism that requires the measurement of the global lateral strain which can only be caught in the wedge region (Visintin et al. 2014 in Chapter 2). So, specimens GA-1A, GD-7A, GE-8A, GD-9A, GE-10A and GC-11A were instrumented with 4 lateral stain gauges 90° apart around the circumference and every 50mm along the height. As shown in Figure 7, each specimen has a total of 16 lateral strain gauges that is 4 lateral strain gauges at each level to

measure the lateral strain at each level which can be used to calculate the confinement stress at each level.

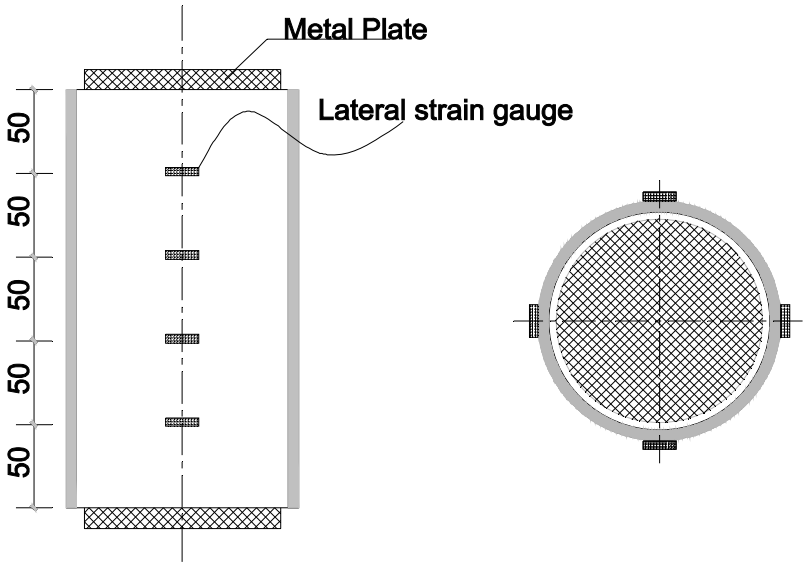

(a) Front View (b) Plan View

Figure 7: Strain gauges of specimens GA-1A, GD-7A, GE-8A, GD-9A, GE-10A and GC-11A

For each specimen the testing process is as follows:

1. By measuring the distance between the edge of the bottom platen and centre of specimen to confirm that the specimen is on the centre of platen to ensure consistent loading;
2. Bring the crosshead (top loading platen) down into position just above the specimen;
3. Set the LVDTs in position allowing enough room for travel during the test;
4. Start recording on the computer the strain gauges, LVDT displacements and load;
5. Open the valve to apply force on the bottom platen which begins to lift;
6. Carefully adjust the load rate via the valve dial as the platen picks up the weight of the load and starts to compress;
7. The load process is controlled by two steps. At beginning, the load rate is 120 KN/min till about 60% proposed peak load (Chen 2005). Then change to displacement control at 0.2 mm/min till the test finishes;
8. Slow and control the test around the peak load and slowly unload the specimen to capture the unloading curve data if applicable;
9. The loading process is stopped once the LVDTs have reached their range or the test specimen has failed which is always accompanied by a muffled noise and when the resisting load will decrease by more than 30% immediately (Chen 2005);
10. Photograph the tested specimen;

11. Cut the steel tube open to check the failure mechanism of the concrete and measure the dimensions of wedge;

The last process step is to verify the proposed angle of the wedge sliding plane relative to the longitudinal axis, Equation 6. It is also worthy noting that using constant load and displacement controls will result in differnent stress application rate for specimens having differnet diameter or strain rates for specimens having different length.

4. Material test results

Twelve control specimens (100x200 concrete cylinders) were tested throughout the testing period and details are shown in Table 2. The nine columns of Table 2 show contents as follows in sequence: ①cylinder number; ②the age of concrete at testing date; ③diameter of cylinder; ④height of cylinder; ⑤weight of cylinder; ⑥density of cylinder; ⑦peak load; ⑧compressive strength; ⑨average compressive strength of this series test. The typical failure model of control specimen is circumferential wedge model as shown in Figure 8.

Figure 8: Typical failure model of control specimen

Table 2 – Summary of control cylinder results

Cylinder No.	Age (Days)	Diameter (mm)	Length (mm)	Weight (g)	Density (Kg/m^3)	Load (KN)	Strength (MPa)	Average (MPa)
①	②	③	④	⑤	⑥	⑦	⑧	⑨
C1a	88	100.2	197.3	3544.6	2279.5	381.3	48.4	50.0
C1b	88	100.6	198.5	3572.6	2265.5	409.5	51.5	
C1c	88	100.4	198.4	3570.1	2274.1	395.5	50.0	
C2a	92	100.2	196.7	3499.3	2257.2	344.5	43.7	46.1
C2b	92	99.8	196.2	3490.0	2275.1	346.0	44.3	
C2c	92	99.3	197.0	3549.6	2327.8	390.2	50.4	
C3a	118	99.8	196.9	3554.6	2308.9	371.3	47.5	49.4
C3b	118	100.1	199.5	3576.6	2279.2	402.5	51.2	
C3c	118	99.5	199.4	3577.1	2308.3	385.5	49.6	
C4a	137	99.9	197.7	3479.3	2246.4	374.5	47.8	49.6
C4b	137	100.6	199.2	3499.0	2211.0	398.0	50.1	
C4c	137	99.7	199.0	3555.6	2289.8	398.2	51.0	

A total of three coupon tests were undertaken for each steel tube member to minimize random error. The general information of the steel coupon tests is shown below in Table 3 where the eight columns show contents as follows in sequence: ①steel coupon number; ②the yield stress of steel tube recommended by manufacturer; ③the ultimate stress of steel tube recommended by manufacturer; ④the thickness of steel tube recommended by manufacturer; ⑤test result of yield stress; ⑥test result of tensile strain at yield stress; ⑦test result of ultimate stress; ⑧test result of tensile strain at ultimate stress. An example of coupon test dimensions has been shown in Figure 9.

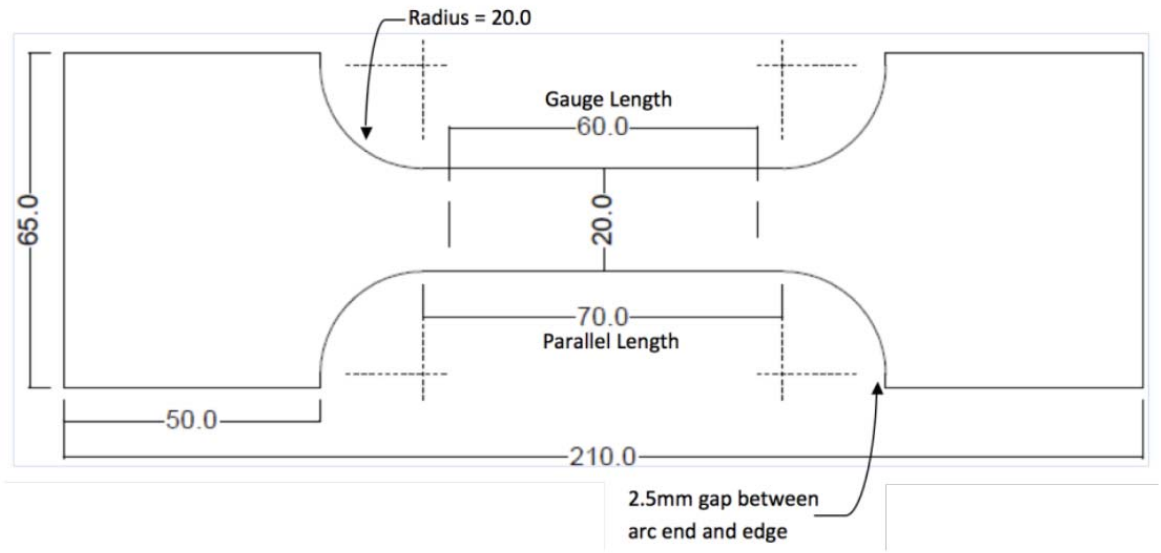

Figure 9: Example of steel coupon test dimension

Table 3 – Summary of steel coupon tests

Steel coupon No.	Recommend value of Manufacturer			Test Results			
	Yield stress f_y (MPa)	Ultimate stress f_u (MPa)	Thickness, t (mm)	Yield stress f_y (MPa)	Strain at f_y, ε_y	Ultimate stress f_u (MPa)	Strain at f_u, ε_u
①	②	③	④	⑤	⑥	⑦	⑧
S1a	250	320	3.6	253	0.221	326	2.74
S1b	250	320	3.6	269	0.251	328	3.58
S1c	250	320	3.6	260	0.252	332	1.69
S2a	250	320	4.5	277	0.253	366	2.57
S2b	250	320	4.5	282	0.324	364	3.26
S2c	250	320	4.5	288	0.322	367	2.49
S3a	350	430	3.2	332	0.218	439	3.56
S3b	350	430	3.2	338	0.297	437	2.89
S3c	350	430	3.2	346	0.265	440	2.21

5. Test results

There are a total of five types of raw and corrected test results for each specimen as labelled in Column 3 in Table 4 that includes:

1) Type one: Load/axial-displacement relationship, in which the legend of *L-NW, L-SE, L-NE and L-SW* is corresponding to the LVDTs in Figure 4;

2) Type two: Load/global-axial-strain relationship, in which the global strain equals the data of the LVDT divided by the length of the specimen and the legend of *NW, SE, NE and SW* is corresponding to the LVDT of *L-NW, L-SE, L-NE and L-SW* in Figure 4;

3) Type three: Load/local-axial-strain relationship, in which the legend *ASG-direction-number* represents the height of the axial strain gauge in mm away from the bottom and on the South, East, North or West faces of the specimen as shown in Figures 5 and 6;

4) Type four: Load/lateral-strain relationship, in which the legend *LSG-direction-number* represents the height of the lateral strain gauge in mm away from the bottom and on the South, East, North or West faces of specimen as shown in Figures 5 to 7;

5) Type five: Load/global and load/local strains relationship, which compares the average of the local axial strains for each layer with the global axial strain;

The nine columns of Table 4 show the contents as follows in sequence: ①specimen name; ②Figure number; ③Figure type; ④content of this figure; ⑤displacement or strain at peak point of the mean curve for this figure; ⑥peak load of the mean curve for this figure in column (2); ⑦displacement or strain at end point of the mean curve for this figure; ⑧end load of the mean curve for this figure; ⑨the stiffness at 40% of peak load for the mean curve, K_{40} that is determined by the secant slope at 40% of peak load; ⑩reason for stopping the test. The units of columns ⑤ to ⑨ in Table 4 refer to corresponding figures and the "*NA*" means that this value is not available or not reliable (e.g. the recorded displacement at peak load for raw test result contains bedding down and other random system error which is required to be corrected first).

The corresponding failure photos and sliding angle α of these specimens are shown in Table 5. The six columns of Table 5 show contents as follows in sequence: ①specimen name; ②the shape of steel tube after test; ③failure model of confined concrete; ④proposed expression for the angle of the principal sliding plane with confinement, α_{Theo} (Equation 6); ⑤the measured angle of the principal sliding plane with confinement, α_{Exp}; ⑥the ratio of α_{Theo} to α_{Exp}.

Table 4 - Raw and corrected test results of individual specimen

Specimen No.	Figure No.	Figure Type	Description of figure	Key points for the mean curve				Stiffness K_{40}	Reason for stopping test
①	②	③	④	⑤	⑥	⑦	⑧	⑨	⑩
GA-1A	10	Type one	Raw data of LVDTs	NA	NA	NA	NA	NA	Specimen fails
	11	Type one	Corrected, Remove bedding down of Figure 10	7.21	521	19.87	486	248	
	12	Type two	Derived from Figure 11	2.89		7.95		621	
	13	Type four	Raw data, lateral strain gauges at 50 mm layer	2420		3624		NA	
	14	Type four	Raw data, lateral strain gauges at 100 mm layer	16516		27929		NA	
	15	Type four	Raw data, lateral strain gauges at 150 mm layer	23459		39941		NA	
	16	Type four	Raw data, lateral strain gauges at 200 mm layer	5690		14905		NA	
	17	Type four	Raw data, average lateral strain result of each layer	12021		21600		NA	
GA-1B	18	Type one	Raw data of LVDTs	NA	NA	NA	NA	NA	Reached LVDT's range
	19	Type one	Corrected, Remove bedding down of Figure 18	5.63	513	21.24	488	156	
	20	Type two	Derived from Figure 19	2.25		8.49		177	
GA-1C	21	Type one	Raw data of LVDTs	NA	NA	NA	NA	NA	Reached LVDT's range
	22	Type one	Corrected, Remove bedding down of Figure 21	4.86	517	16.8	503	227	
	23	Type two	Derived from Figure 22	1.94		6.72		569	

Table 4 - Raw and corrected test results of individual specimen (continued)

Specimen No.	Figure No.	Figure Type	Description of figure	Key points for the mean curve				Stiffness K_{40}	Reason for stopping test
①	②	③	④	⑤	⑥	⑦	⑧	⑨	⑩
GA-2A	24	Type one	Raw data of LVDTs	NA	NA	NA	NA	NA	Reached LVDT's range
	25	Type one	Corrected, Remove bedding down of Figure 24	4.07	485	29.3	427	195	
	26	Type two	Derived from Figure 25	0.81		5.87		974	
GA-2B	27	Type one	Raw data of LVDTs	NA	NA	NA	NA	NA	Reached LVDT's range
	28	Type one	Corrected, Remove bedding down of Figure 27	6.36	497	24.3	431	142	
	29	Type two	Derived from Figure 28	1.27		4.86		708	
GA-2C	30	Type one	Raw data of LVDTs	NA	NA	NA	NA	NA	Reached LVDT's range
	31	Type one	Corrected, Remove bedding down of Figure 30	6.03	511	29.6	351	166	
	32	Type two	Derived from Figure 31	1.21		5.62		829	
GA-3A	33	Type one	Raw data of LVDTs	NA	NA	NA	NA	NA	Specimen fails
	34	Type one	Corrected, Remove bedding down of Figure 33	6.06	485	15.7	347	125	
	35	Type two	Derived from Figure 34	0.81		2.10		935	
GA-3B	36	Type one	Raw data of LVDTs	NA	NA	NA	NA	NA	Reached LVDT's range
	37	Type one	Corrected, Remove bedding down of Figure 36	5.92	474	15.9	334	142	
	38	Type two	Derived from Figure 37	0.79		2.12		1068	

Table 4 - Raw and corrected test results of individual specimen (continued)

Specimen No.	Figure No.	Figure Type	Description of figure	Key points for the mean curve				Stiffness K_{40}	Reason for stopping test
①	②	③	④	⑤	⑥	⑦	⑧	⑨	⑩
GB-4A	39	Type one	Raw data of LVDTs	NA	NA	NA	NA	NA	Reached LVDT's range
	40	Type one	Corrected, Remove bedding down of Figure 39	6.84	665	28.9	633	409	
	41	Type two	Derived from Figure 40	2.74		11.5		1022	
	42	Type three	Raw data, axial strain gauges at 50 mm layer	0.78		1.13		NA	
	43	Type three	Raw data, axial strain gauges at 125 mm layer	1.51		2.02		NA	
	44	Type three	Raw data, axial strain gauges at 200 mm layer	0.87		1.34		NA	
	45	Type five	Compare average result of local axial strain for each layer with global axial strain	NA	NA	NA	NA	NA	
	46	Type four	Raw data, lateral strain gauges at 50 mm layer	9807	665	27633	633	NA	
	47	Type four	Raw data, lateral strain gauges at 125 mm layer	14939		31071		NA	
	48	Type four	Raw data, lateral strain gauges at 200 mm layer	11467		17414		NA	
	49	Type four	Raw data, average lateral strain result of each layer	12071		25372		NA	

Table 4 - Raw and corrected test results of individual specimen (continued)

Specimen No.	Figure No.	Figure Type	Description of figure	Key points for the mean curve				Stiffness K_{40}	Reason for stopping test
①	②	③	④	⑤	⑥	⑦	⑧	⑨	⑩
GB-4B	50	Type one	Raw data of LVDTs	NA	NA	NA	NA	NA	Specimen fails
	51	Type one	Corrected, Remove bedding down of Figure 50	7.15	657	9.34	653	423	
	52	Type two	Derived from Figure 51	2.86		3.74		1056	
	53	Type three	Raw data, axial strain gauges at 50 mm layer	0.4		0.41		NA	
	54	Type three	Raw data, axial strain gauges at 125 mm layer	1.44		1.55		NA	
	55	Type five	Compare average result of local axial strain for each layer with global axial strain	NA	NA	NA	NA	NA	
	56	Type four	Raw data, lateral strain gauges at 50 mm layer	4822	657	4975	653	NA	
	57	Type four	Raw data, lateral strain gauges at 125 mm layer	15384		16890		NA	
	58	Type four	Raw data, average lateral strain result of each layer	10103		10932		NA	

Table 4 - Raw and corrected test results of individual specimen (continued)

Specimen No.	Figure No.	Figure Type	Description of figure	Key points for the mean curve				Stiffness K_{40}	Reason for stopping test
①	②	③	④	⑤	⑥	⑦	⑧	⑨	⑩
GB-4C	59	Type one	Raw data of LVDTs	NA	NA	NA	NA	NA	Specimen fails
	60	Type one	Corrected, Remove bedding down of Figure 59	20.8	670	23.7	629	448	
	61	Type two	Derived from Figure 60	8.35		9.50		1118	
	62	Type three	Raw data, axial strain gauges at 50 mm layer	0.39		0.49		NA	
	63	Type three	Raw data, axial strain gauges at 125 mm layer	1.50		1.67		NA	
	64	Type five	Compare average result of local axial strain for each layer with global axial strain	NA	NA	NA	NA	NA	
	65	Type four	Raw data, lateral strain gauges at 50 mm layer	5216	670	5141	629	NA	
	66	Type four	Raw data, lateral strain gauges at 125 mm layer	1855		1717		NA	
	67	Type four	Raw data, average lateral strain result of each layer	3535		3429		NA	
GB-5A	68	Type one	Raw data of LVDTs	NA	NA	NA	NA	NA	Specimen fails
	69	Type one	Corrected, Remove bedding down of Figure 68	6.71	658	19.8	609	252	
	70	Type two	Derived from Figure 69	1.34		3.96		1262	

Table 4 - Raw and corrected test results of individual specimen (continued)

Specimen No.	Figure No.	Figure Type	Description	Key points for the mean curve				Stiffness K_{40}	Reason for stopping test
①	②	③	④	⑤	⑥	⑦	⑧	⑨	⑩
GB-5B	71	Type one	Raw data of LVDTs	NA	NA	NA	NA	NA	Reached LVDT's range
	72	Type one	Corrected, Remove bedding down of Figure 71	5.32	648	20.4	619	229	
	73	Type two	Derived from Figure 72	1.06		4.07		1144	
GB-5C	74	Type one	Raw data of LVDTs	NA	NA	NA	NA	NA	Reached LVDT's range
	75	Type one	Corrected, Remove bedding down of Figure 74	6.87	633	20.5	612	168	
	76	Type two	Derived from Figure 75	1.37		4.10		839	
GB-6A	77	Type one	Raw data of LVDTs	NA	NA	NA	NA	NA	Specimen fails
	78	Type one	Corrected, Remove bedding down of Figure 77	7.72	648	14.9	584	192	
	79	Type two	Derived from Figure 78	1.03		1.99		1442	
GB-6B	80	Type one	Raw data of LVDTs	NA	NA	NA	NA	NA	Specimen fails
	81	Type one	Corrected, Remove bedding down of Figure 80	7.58	634	17.3	527	180	
	82	Type two	Derived from Figure 81	1.01		2.31		1352	
GB-6C	83	Type one	Raw data of LVDTs	NA	NA	NA	NA	NA	Specimen fails
	84	Type one	Corrected, Remove bedding down of Figure 83	7.30	629	23.1	491	156	
	85	Type two	Derived from Figure 84	0.97		3.08		1166	

Table 4 - Raw and corrected test results of individual specimen (continued)

Specimen No.	Figure No.	Figure Type	Description of figure	Key points for the mean curve				Stiffness K_{40}	Reason for stopping test
①	②	③	④	⑤	⑥	⑦	⑧	⑨	⑩
GD-7A	86	Type one	Raw data of LVDTs	NA	NA	NA	NA	NA	Specimen fails
	87	Type one	Corrected, Remove bedding down of Figure 86	4.93	856	19.8	823	668	
	88	Type two	Derived from Figure 87	1.76		7.92		1670	
	89	Type four	Raw data, lateral strain gauges at 50 mm layer	2408		4117		NA	
	90	Type four	Raw data, lateral strain gauges at 100 mm layer	6026		15753		NA	
	91	Type four	Raw data, lateral strain gauges at 150 mm layer	14189		34611		NA	
	92	Type four	Raw data, lateral strain gauges at 200 mm layer	11140		43214		NA	
	93	Type four	Raw data, average lateral strain result of each layer	8441		24424		NA	
GD-7B	94	Type one	Raw data of LVDTs	NA	NA	NA	NA	NA	Specimen fails
	95	Type one	Corrected, Remove bedding down of Figure 94	4.89	790	19.2	763	574	
	96	Type two	Derived from Figure 95	1.79		7.97		1437	
GD-7C	97	Type one	Raw data of LVDTs	NA	NA	NA	NA	NA	Reached LVDT's range
	98	Type one	Corrected, Remove bedding down of Figure 97	5.24	799	20.4	765	300	
	99	Type two	Derived from Figure 98	2.10		8.18		751	

Table 4 - Raw and corrected test results of individual specimen (continued)

Specimen No.	Figure No.	Figure Type	Description of figure	Key points for the mean curve				Stiffness K_{40}	Reason for stopping test
①	②	③	④	⑤	⑥	⑦	⑧	⑨	⑩
GE-8A	100	Type one	Raw data of LVDTs	NA	NA	NA	NA	NA	Reached LVDT's range
	101	Type one	Corrected, Remove bedding down of Figure 100	3.46	852	19.8	795	543	
	102	Type two	Derived from Figure 101	1.38		7.92		1358	
	103	Type four	Raw data, lateral strain gauges at 50 mm layer	1558		15499		NA	
	104	Type four	Raw data, lateral strain gauges at 100 mm layer	3243		32726		NA	
	105	Type four	Raw data, lateral strain gauges at 150 mm layer	7009		32956		NA	
	106	Type four	Raw data, lateral strain gauges at 200 mm layer	3542		42601		NA	
	107	Type four	Raw data, average lateral strain result of each layer	3838		21665		NA	
GE-8B	108	Type one	Raw data of LVDTs	NA	NA	NA	NA	NA	Reached LVDT's range
	109	Type one	Corrected, Remove bedding down of Figure 108	3.25	836	20.2	787	556	
	110	Type two	Derived from Figure 109	1.30		8.07		1389	
GE-8C	111	Type one	Raw data of LVDTs	NA	NA	NA	NA	NA	Specimen fails
	112	Type one	Corrected, Remove bedding down of Figure 111	3.29	855	19.9	706	524	
	113	Type two	Derived from Figure 112	1.31		7.96		1310	

Table 4 - Raw and corrected test results of individual specimen (continued)

Specimen No.	Figure No.	Figure Type	Description of figure	Key points for the mean curve				Stiffness K_{40}	Reason for stopping test
①	②	③	④	⑤	⑥	⑦	⑧	⑨	⑩
GD-9A	114	Type one	Raw data of LVDTs	NA	NA	NA	NA	NA	Reached LVDT's range
	115	Type one	Corrected, Remove bedding down of Figure 114	5.83	1153	19.3	1079	614	
	116	Type two	Derived from Figure 115	2.33		7.74		1534	
	117	Type four	Raw data, lateral strain gauges at 50 mm layer	4570		10159		NA	
	118	Type four	Raw data, lateral strain gauges at 100 mm layer	5558		18340		NA	
	119	Type four	Raw data, lateral strain gauges at 150 mm layer	6612		19987		NA	
	120	Type four	Raw data, lateral strain gauges at 200 mm layer	10412		25046		NA	
	121	Type four	Raw data, average lateral strain result of each layer	6788		18383		NA	
GD-9B	122	Type one	Raw data of LVDTs	NA	NA	NA	NA	NA	Reached LVDT's range
	123	Type one	Corrected, Remove bedding down of Figure 122	5.75	1154	20.3	1081	540	
	124	Type two	Derived from Figure 123	2.30		8.14		1349	
GD-9C	125	Type one	Raw data of LVDTs	NA	NA	NA	NA	NA	Reached LVDT's range
	126	Type one	Corrected, Remove bedding down of Figure 125	5.81	1151	19.1	1077	646	
	127	Type two	Derived from Figure 126	2.31		7.72		1615	

Table 4 - Raw and corrected test results of individual specimen (continued)

Specimen No.	Figure No.	Figure Type	Description of figure	Key points for the mean curve				Stiffness K_{40}	Reason for stopping test
①	②	③	④	⑤	⑥	⑦	⑧	⑨	⑩
GE-10A	128	Type one	Raw data of LVDTs	NA	NA	NA	NA	NA	Reached LVDT's range
	129	Type one	Corrected, Remove bedding down of Figure 128	3.51	1064	20.4	974	473	
	130	Type two	Derived from Figure 129	1.40		8.16		1183	
	131	Type four	Raw data, lateral strain gauges at 50 mm layer	1299		9932		NA	
	132	Type four	Raw data, lateral strain gauges at 100 mm layer	2164		8761		NA	
	133	Type four	Raw data, lateral strain gauges at 150 mm layer	2962		21745		NA	
	134	Type four	Raw data, lateral strain gauges at 200 mm layer	4364		22095		NA	
	135	Type four	Raw data, average lateral strain result of each layer	2697		15633		NA	
GE-10B	136	Type one	Raw data of LVDTs	NA	NA	NA	NA	NA	Reached LVDT's range
	137	Type one	Corrected, Remove bedding down of Figure 136	3.53	1038	19.8	969	551	
	138	Type two	Derived from Figure 137	1.41		7.94		1377	
GE-10C	139	Type one	Raw data of LVDTs	NA	NA	NA	NA	NA	Reached LVDT's range
	140	Type one	Corrected, Remove bedding down of Figure 139	2.97	1029	17.7	974	646	
	141	Type two	Derived from Figure 140	1.19		7.08		1617	

Table 4 - Raw and corrected test results of individual specimen (continued)

Specimen No.	Figure No.	Figure Type	Description of figure	Key points for the mean curve				Stiffness K_{40}	Reason for stopping test
①	②	③	④	⑤	⑥	⑦	⑧	⑨	⑩
GC-11A	142	Type one	Raw data of LVDTs	NA	NA	NA	NA	NA	Reached LVDT's range
	143	Type one	Corrected, Remove bedding down of Figure 142	7.75	1134	19.2	1097	586	
	144	Type two	Derived from Figure 143	3.10		7.68		1464	
	145	Type four	Raw data, lateral strain gauges at 50 mm layer	3250		16875		NA	
	146	Type four	Raw data, lateral strain gauges at 100 mm layer	7465		29688		NA	
	147	Type four	Raw data, lateral strain gauges at 150 mm layer	19308		32098		NA	
	148	Type four	Raw data, lateral strain gauges at 200 mm layer	14958		39223		NA	
	149	Type four	Raw data, average lateral strain result of each layer	11245		29471		NA	
GC-11B	150	Type one	Raw data of LVDTs	NA	NA	NA	NA	NA	Reached LVDT's range
	151	Type one	Corrected, Remove bedding down of Figure 150	7.66	1168	22.7	1126	462	
	152	Type two	Derived from Figure 151	3.06		9.10		1156	
GC-11C	153	Type one	Raw data of LVDTs	NA	NA	NA	NA	NA	Reached LVDT's range
	154	Type one	Corrected, Remove bedding down of Figure 153	13.6	1129	23.3	1110	653	
	155	Type two	Derived from Figure 154	5.40		9.31		1633	

Table 4 - Raw and corrected test results of individual specimen (continued)

Specimen No.	Figure No.	Figure Type	Description of figure	Key points for the mean curve				Stiffness K_{40}	Reason for stopping test
①	②	③	④	⑤	⑥	⑦	⑧	⑨	⑩
GC-12A	156	Type one	Raw data of LVDTs	NA	NA	NA	NA	NA	Reached LVDT's range
	157	Type one	Corrected, Remove bedding down of Figure 156	(8.02,1120)	1120	(30.4,1058)	1058	312	
	158	Type two	Derived from Figure 157	(3.21,1120)		(12.1,1058)		1558	
GC-12B	159	Type one	Raw data of LVDTs	NA	NA	NA	NA	NA	Reached LVDT's range
	160	Type one	Corrected, Remove bedding down of Figure 159	(9.36,1147)	1147	(29.0,1062)	1062	377	
	161	Type two	Derived from Figure 160	(3.74,1147)		(11.6,1062)		1886	
GC-12C	162	Type one	Raw data of LVDTs	NA	NA	NA	NA	NA	Reached LVDT's range
	163	Type one	Corrected, Remove bedding down of Figure 162	(9.41,1138)	1138	(29.3,1073)	1073	330	
	164	Type two	Derived from Figure 163	(3.77,1138)		(11.7,1073)		1650	
GC-13A	165	Type one	Raw data of LVDTs	NA	NA	NA	NA	NA	Specimen fails
	166	Type one	Corrected, Remove bedding down of Figure 165	(8.67,1119)	1119	(21.7,1000)	1000	376	
	167	Type two	Derived from Figure 166	(3.47,1119)		(8.69,1000)		2820	
GC-13B	168	Type one	Raw data of LVDTs	NA	NA	NA	NA	NA	Reached LVDT's range
	169	Type one	Corrected, Remove bedding down of Figure 168	(11.6,1131)	1131	(16.0,1112)	1112	298	
	170	Type two	Derived from Figure 169	(4.66,1131)		(6.42,1112)		2232	
GC-13C	171	Type one	Raw data of LVDTs	NA	NA	NA	NA	NA	Reached LVDT's range
	172	Type one	Corrected, Remove bedding down of Figure 171	(9.37,1111)	1111	(18.0,1053)	1053	292	
	173	Type two	Derived from Figure 172	(3.75,1111)		(7.22,1053)		2189	

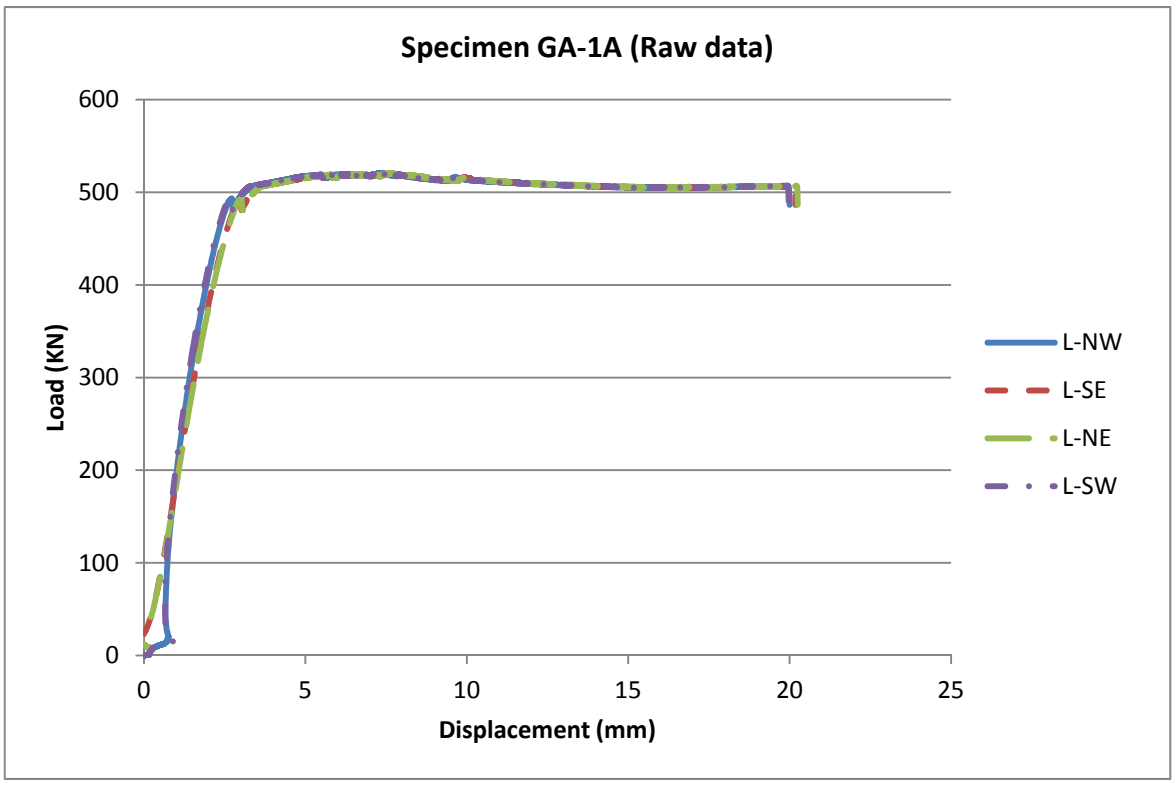

Figure 10: Load/axial-displacement relationship

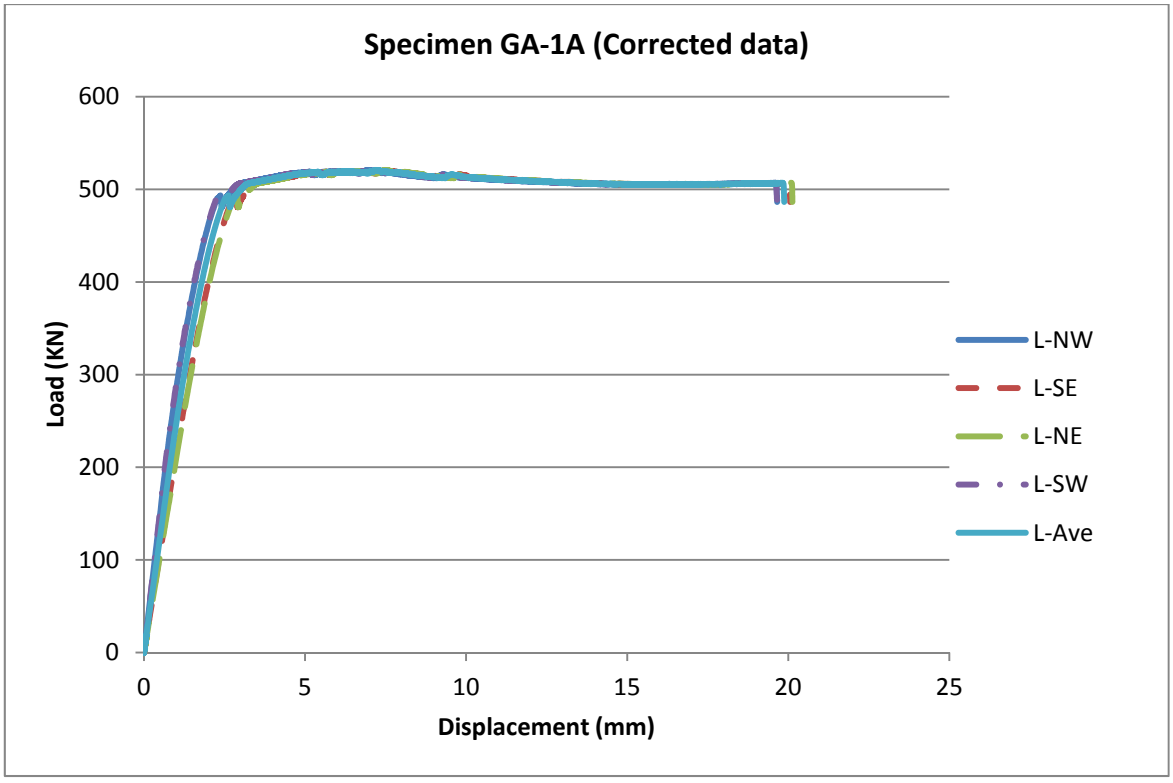

Figure 11: Load/axial-displacement relationship

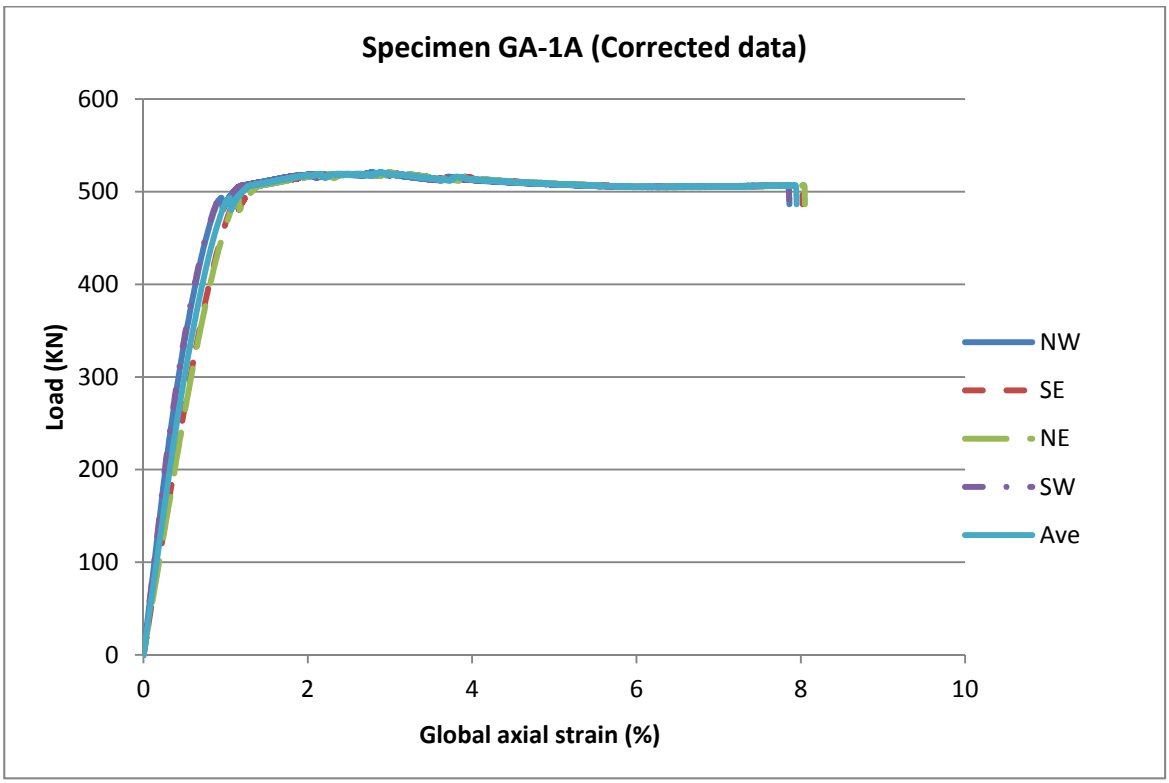

Figure 12: Load/global-axial-strain relationship

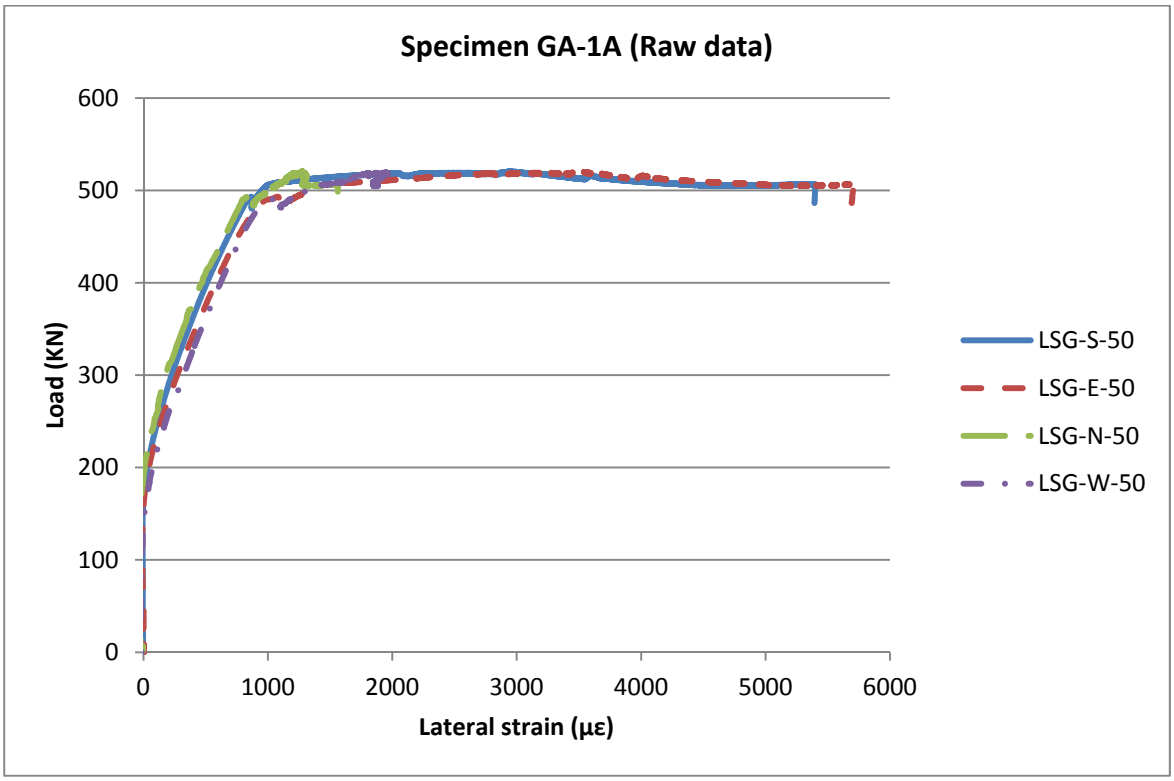

Figure 13: Load/lateral-strain relationship

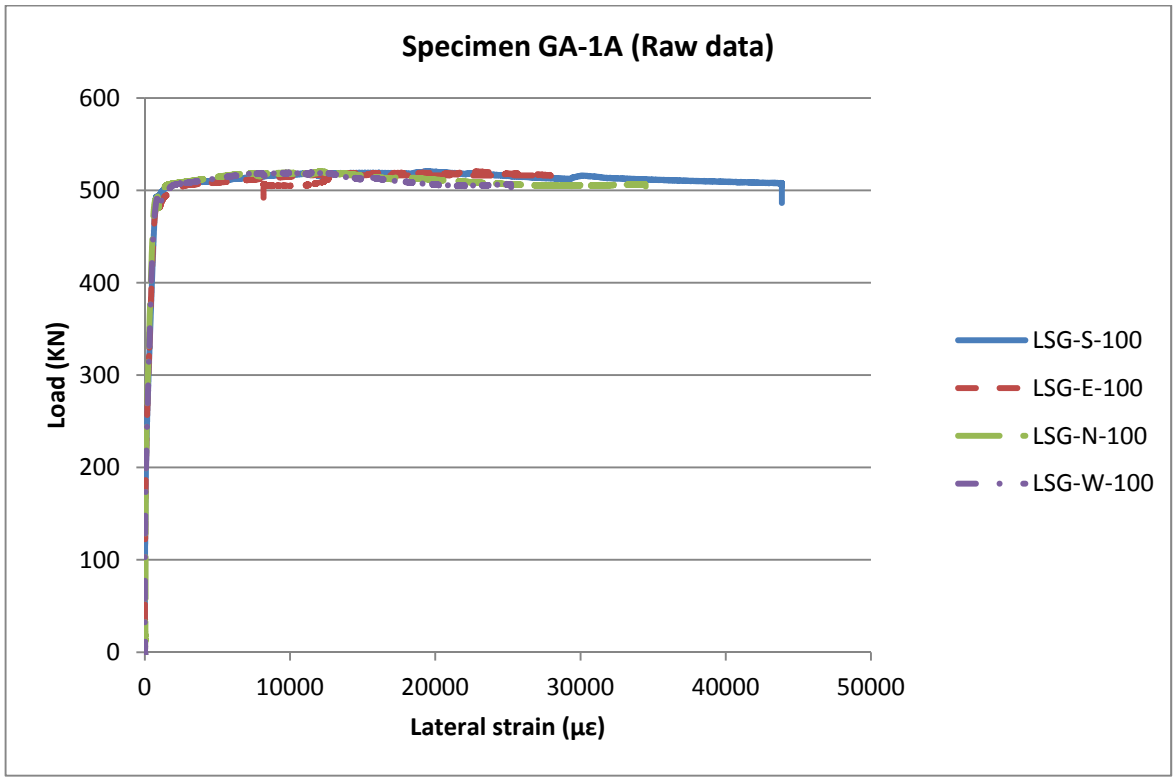

Figure 14: Load/lateral-strain relationship

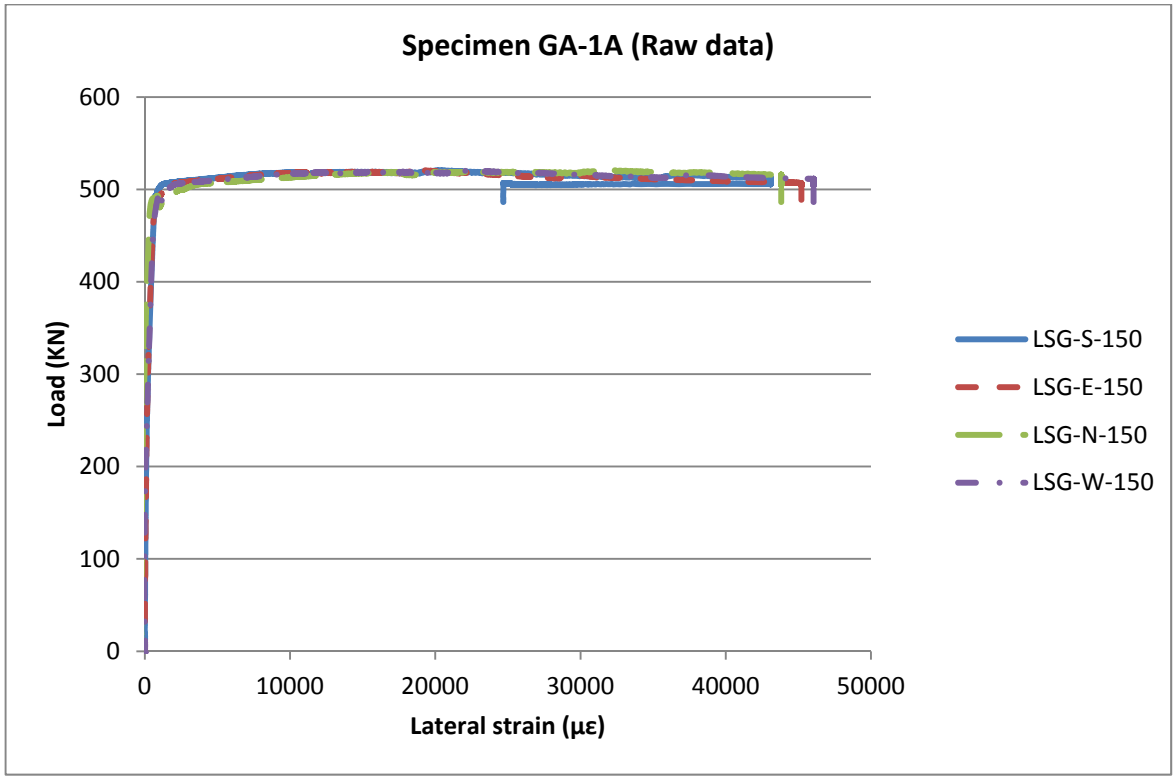

Figure 15: Load/lateral-strain relationship

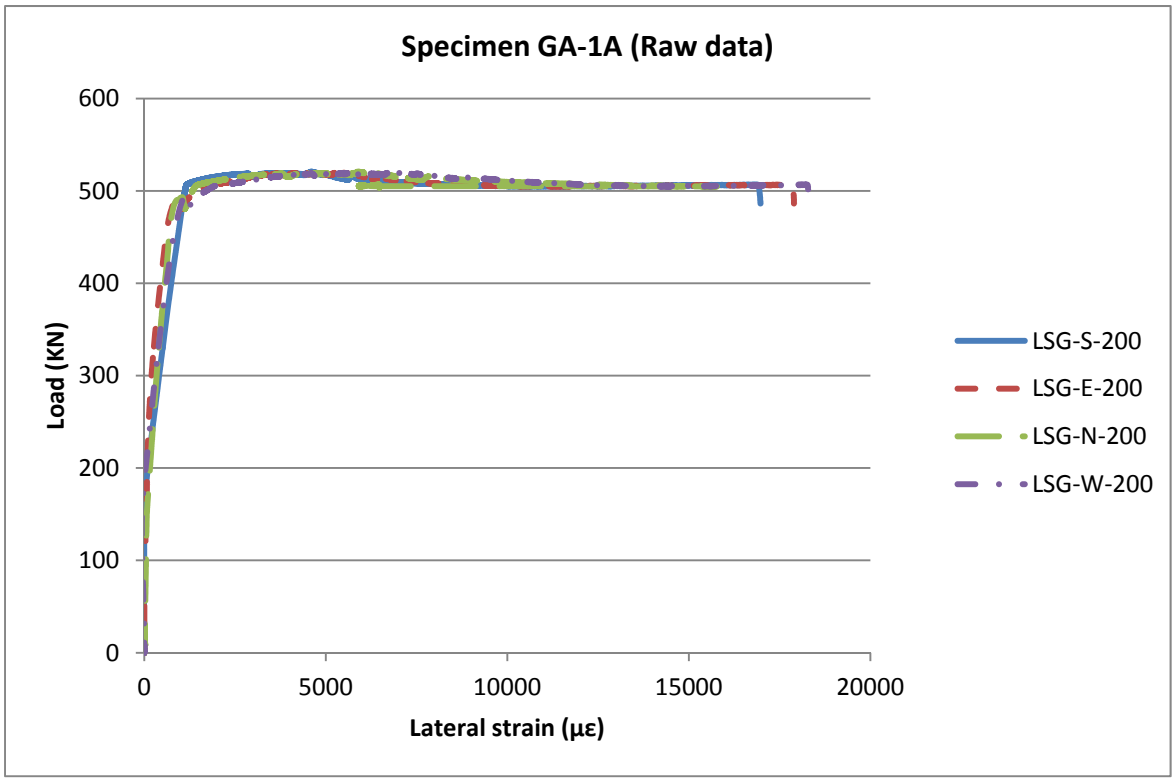

Figure 16: Load/lateral-strain relationship

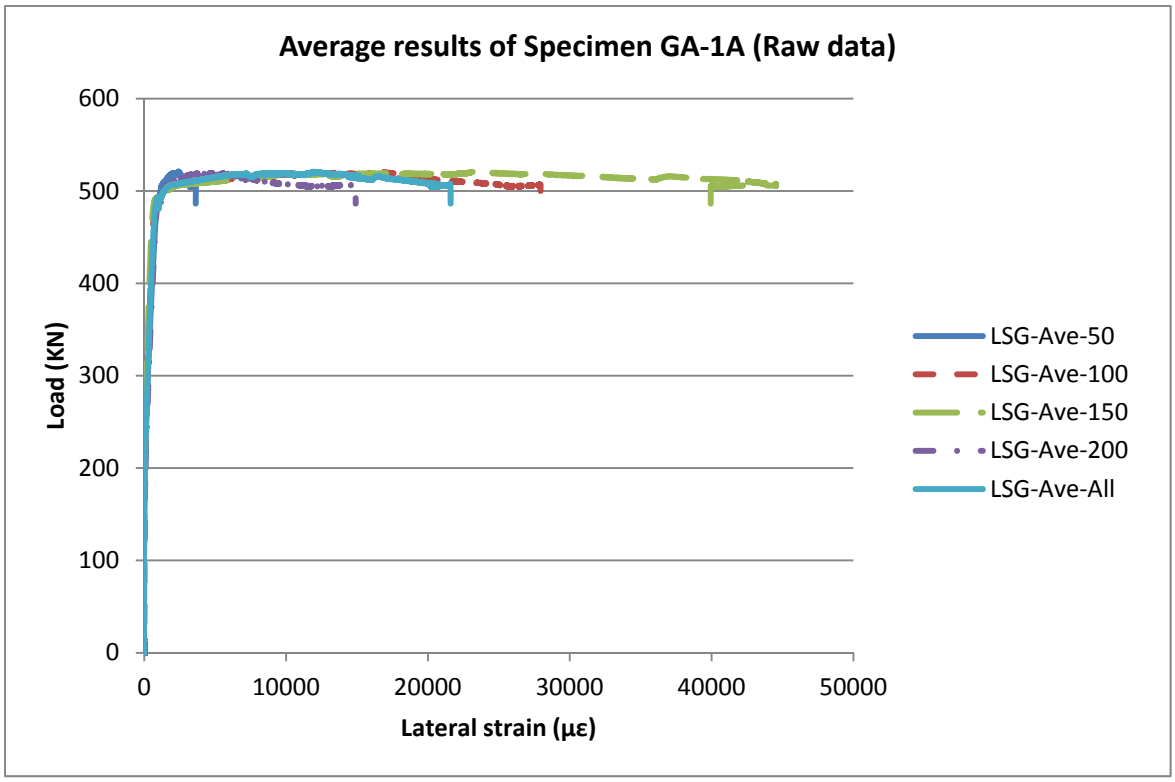

Figure 17: Load/lateral-strain relationship

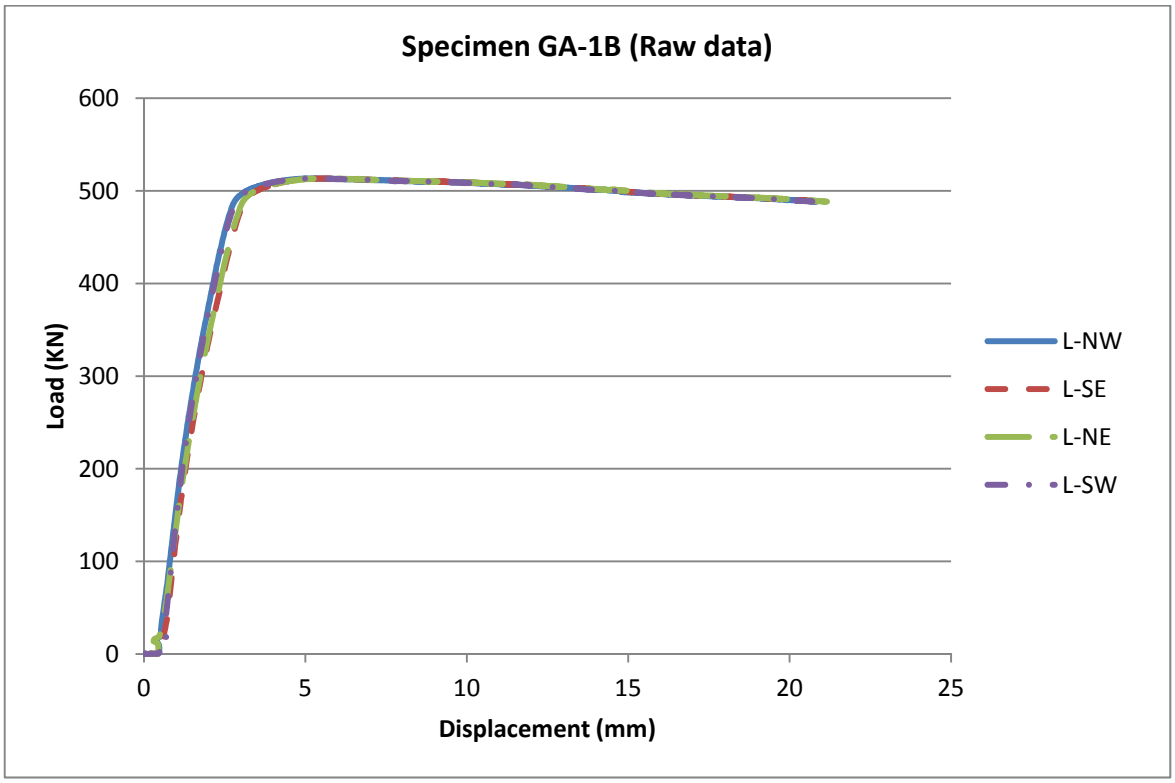

Figure 18: Load/axial-displacement relationship

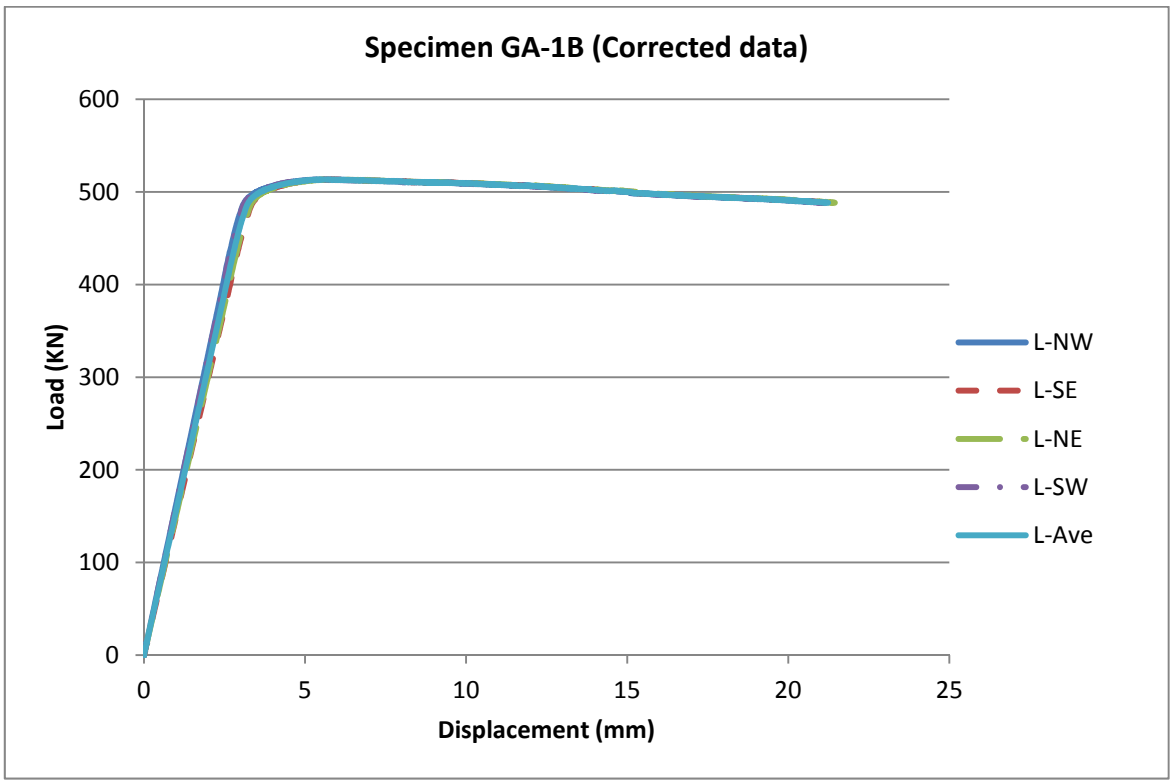

Figure 19: Load/axial-displacement relationship

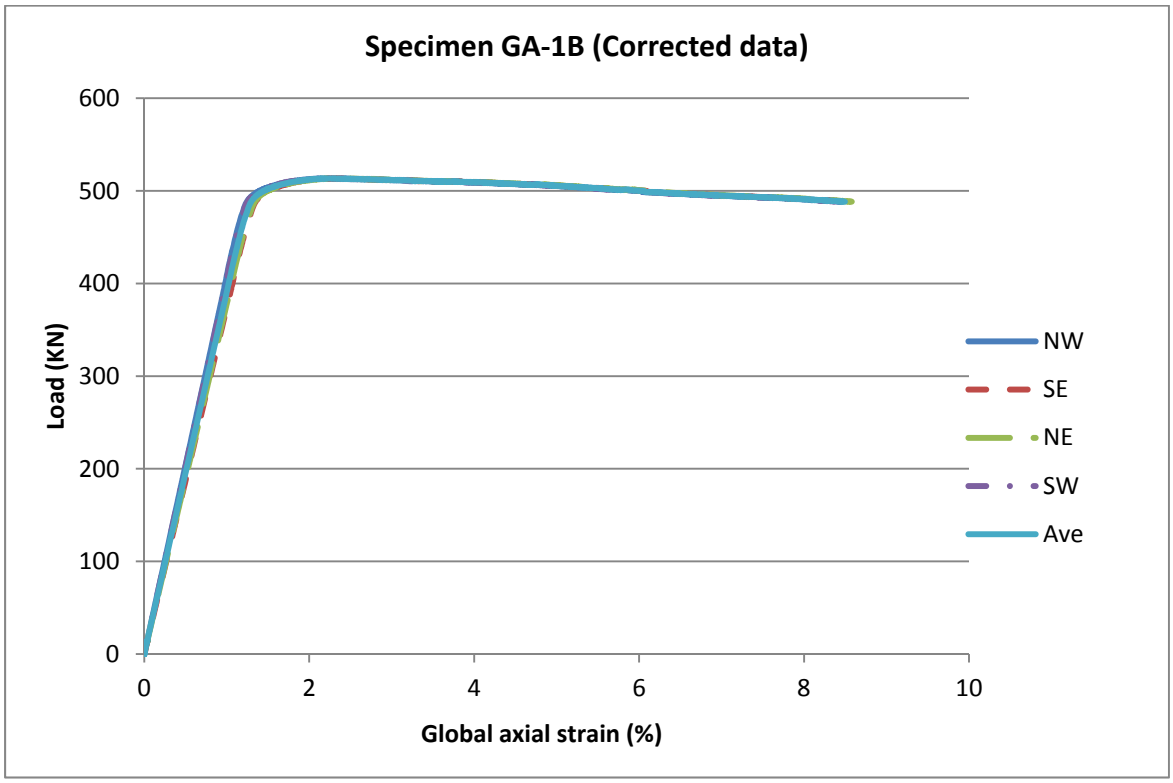

Figure 20: Load/global-axial-strain relationship

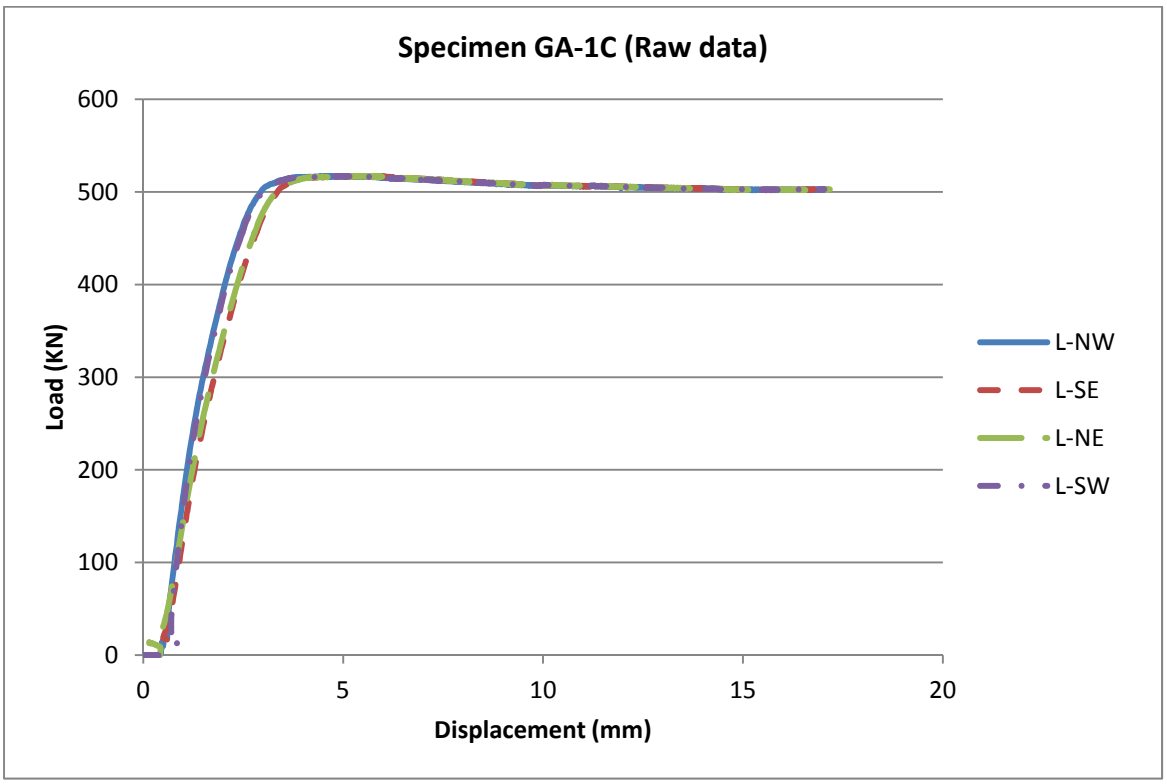

Figure 21: Load/axial-displacement relationship

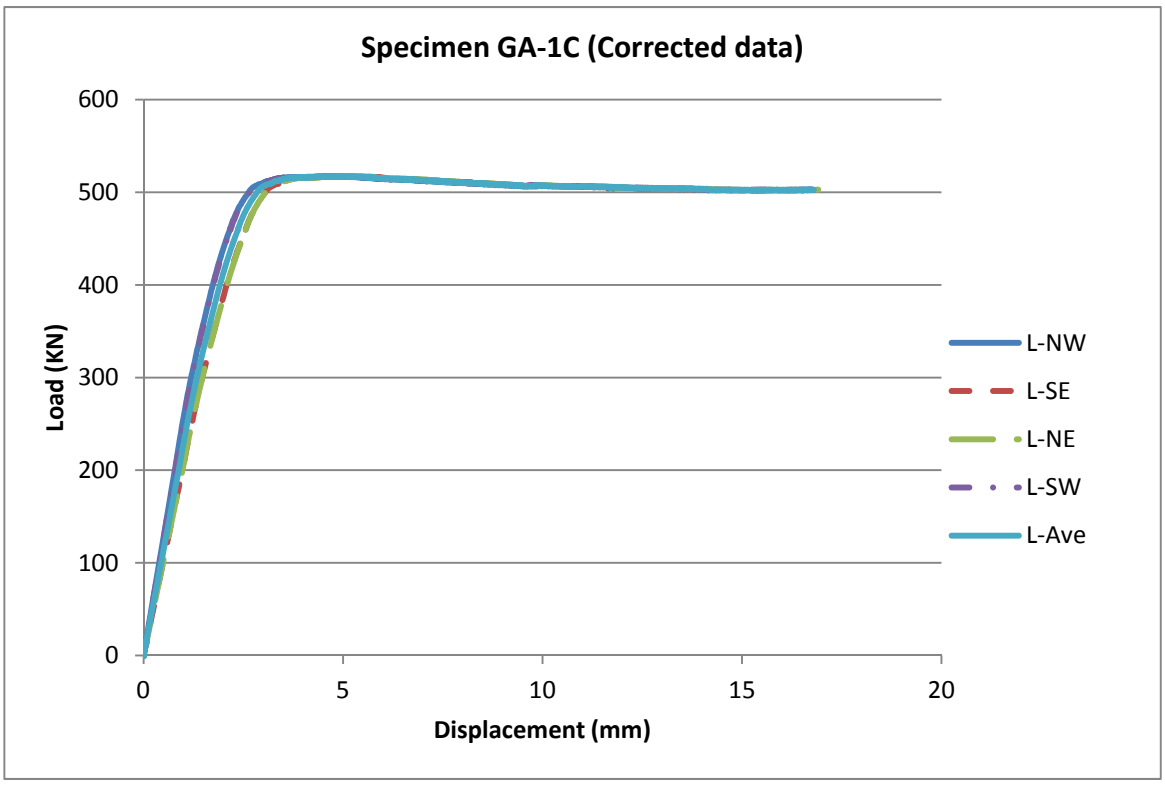

Figure 22: Load/axial-displacement relationship

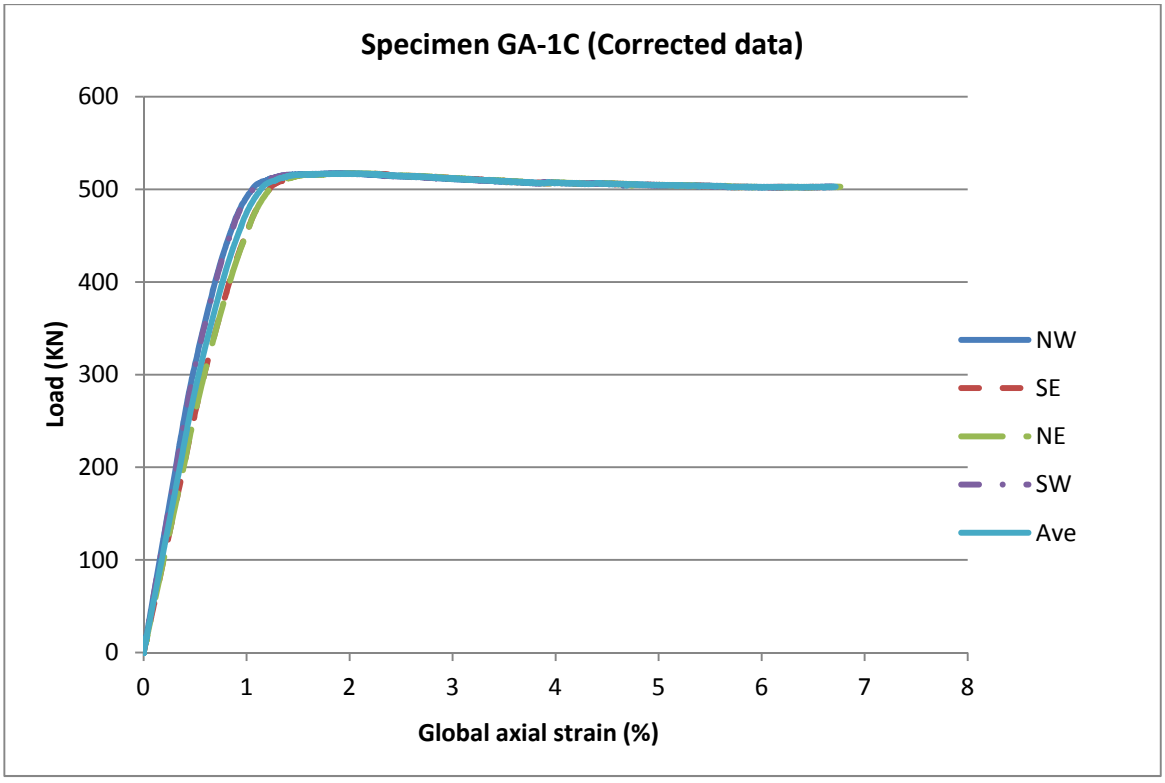

Figure 23: Load/global-axial-strain relationship

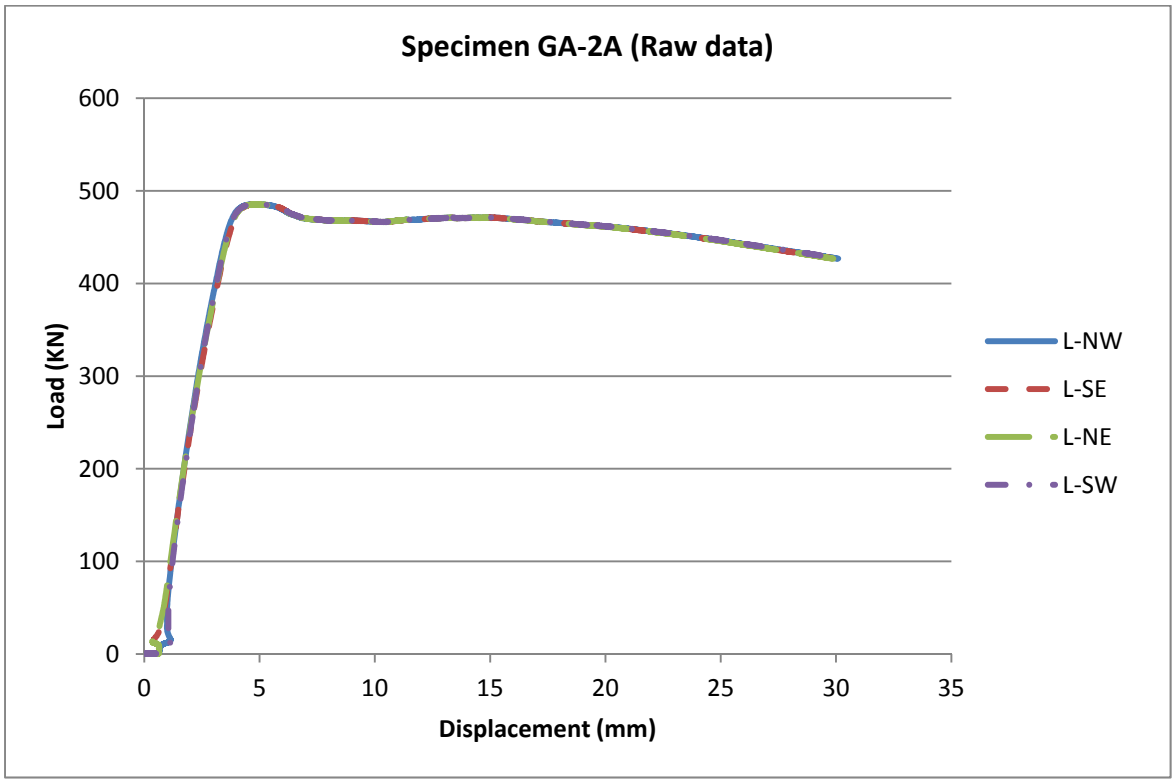

Figure 24: Load/axial-displacement relationship

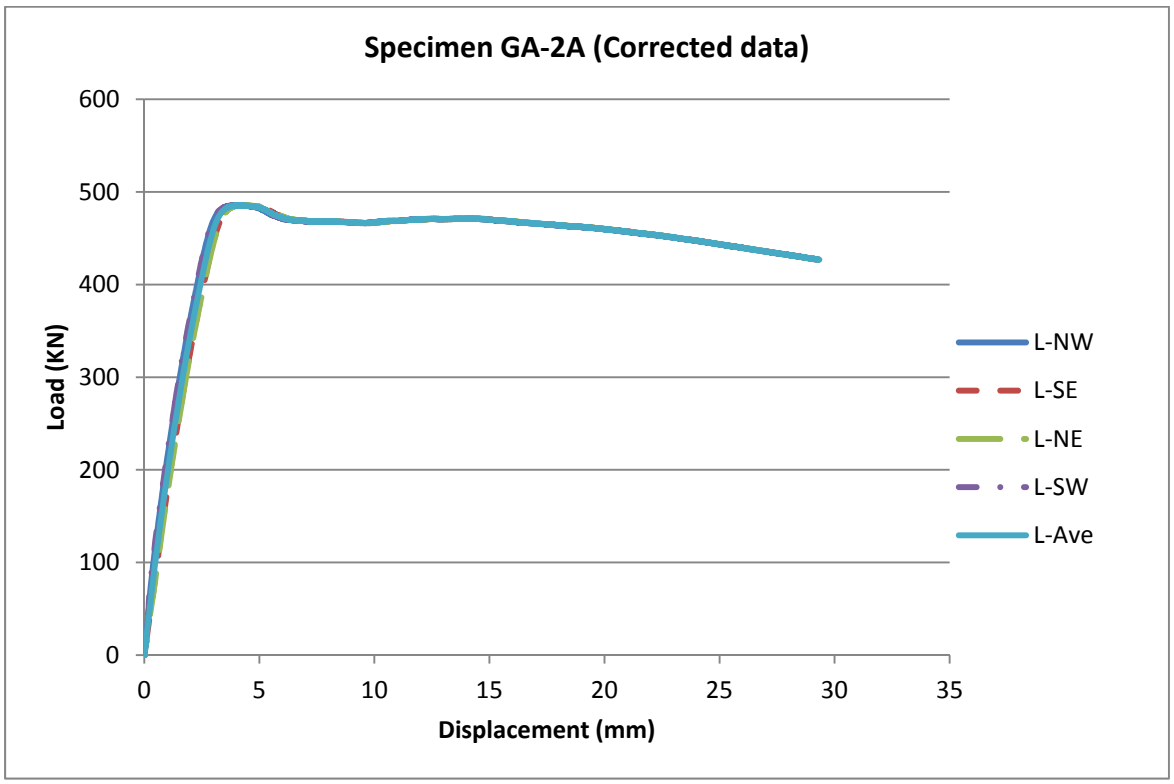

Figure 25: Load/axial-displacement relationship

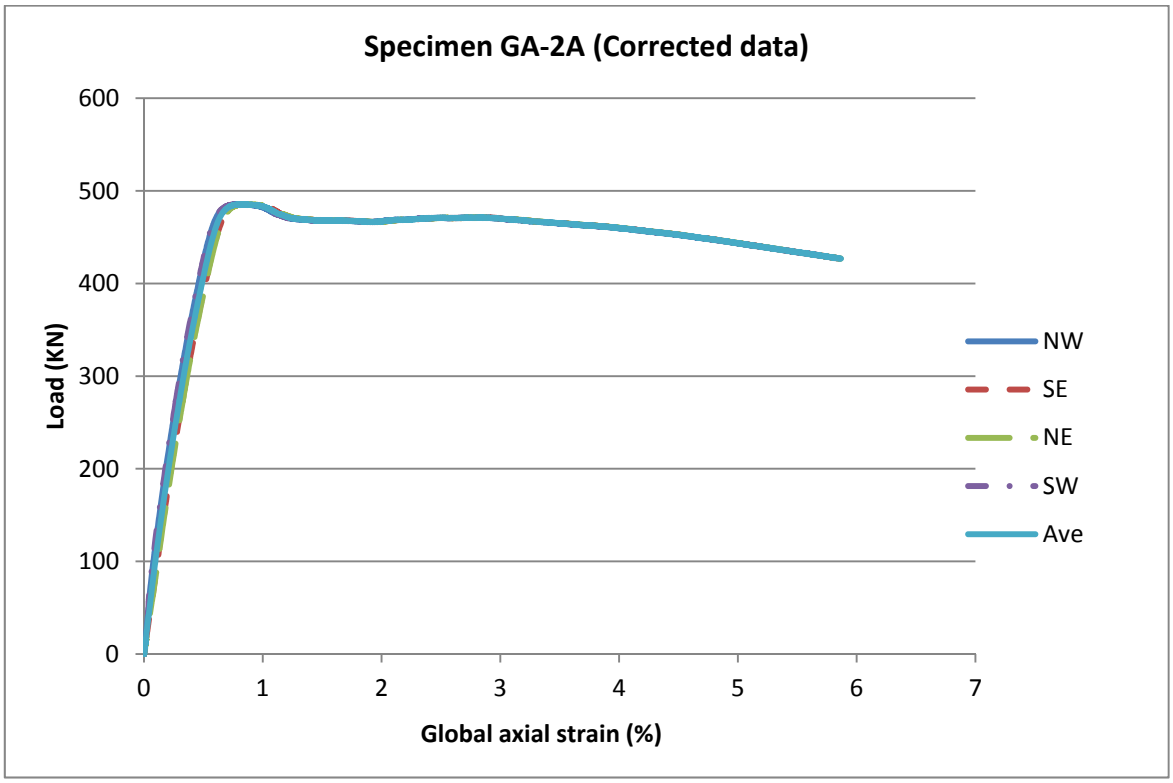

Figure 26: Load/global-axial-strain relationship

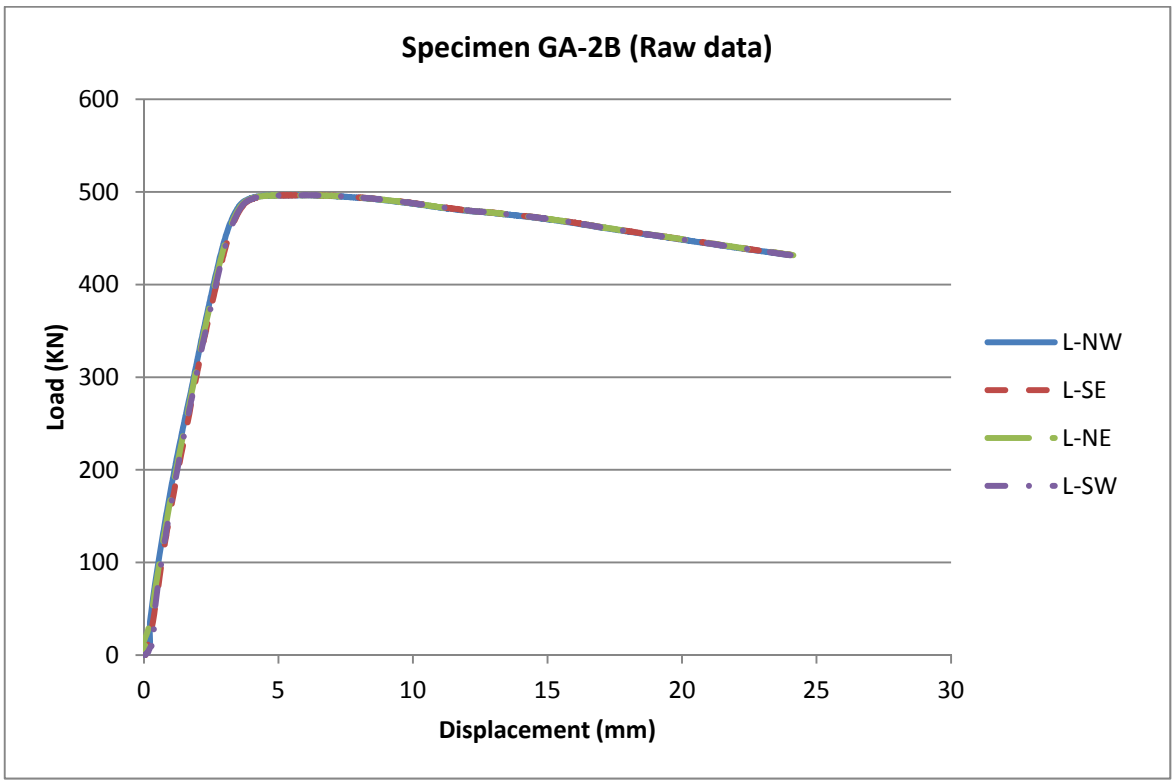

Figure 27: Load/axial-displacement relationship

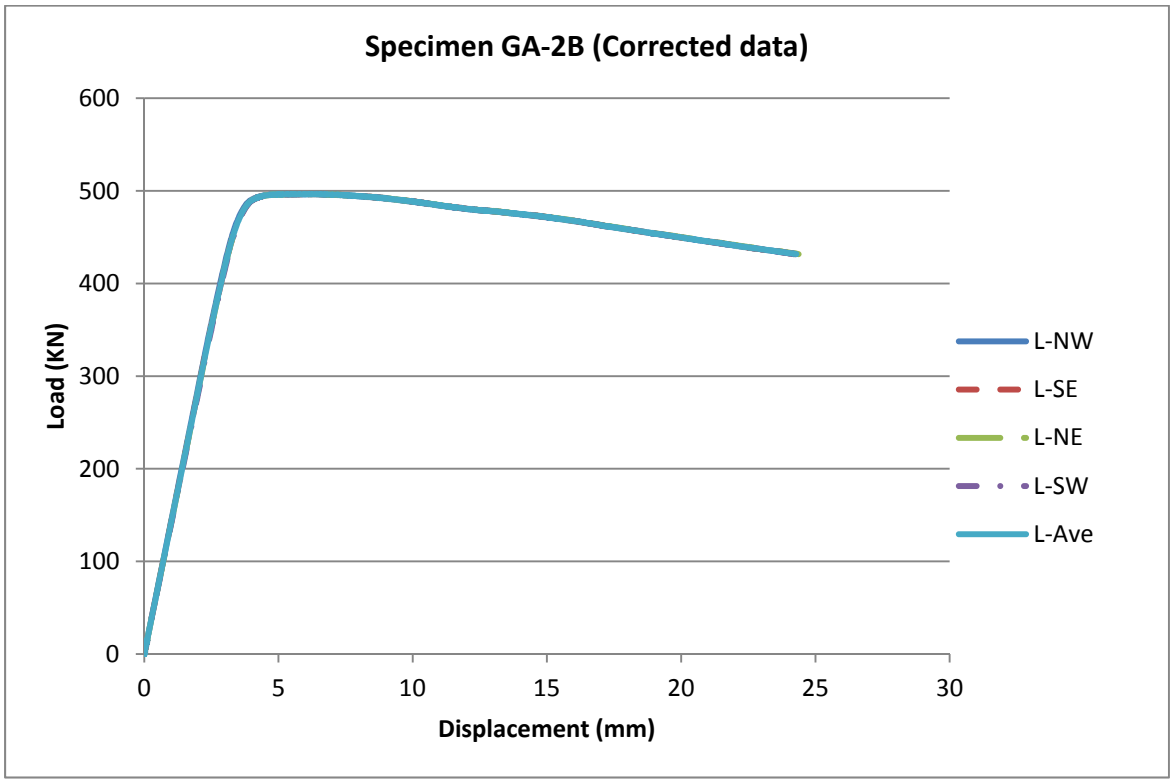

Figure 28: Load/axial-displacement relationship

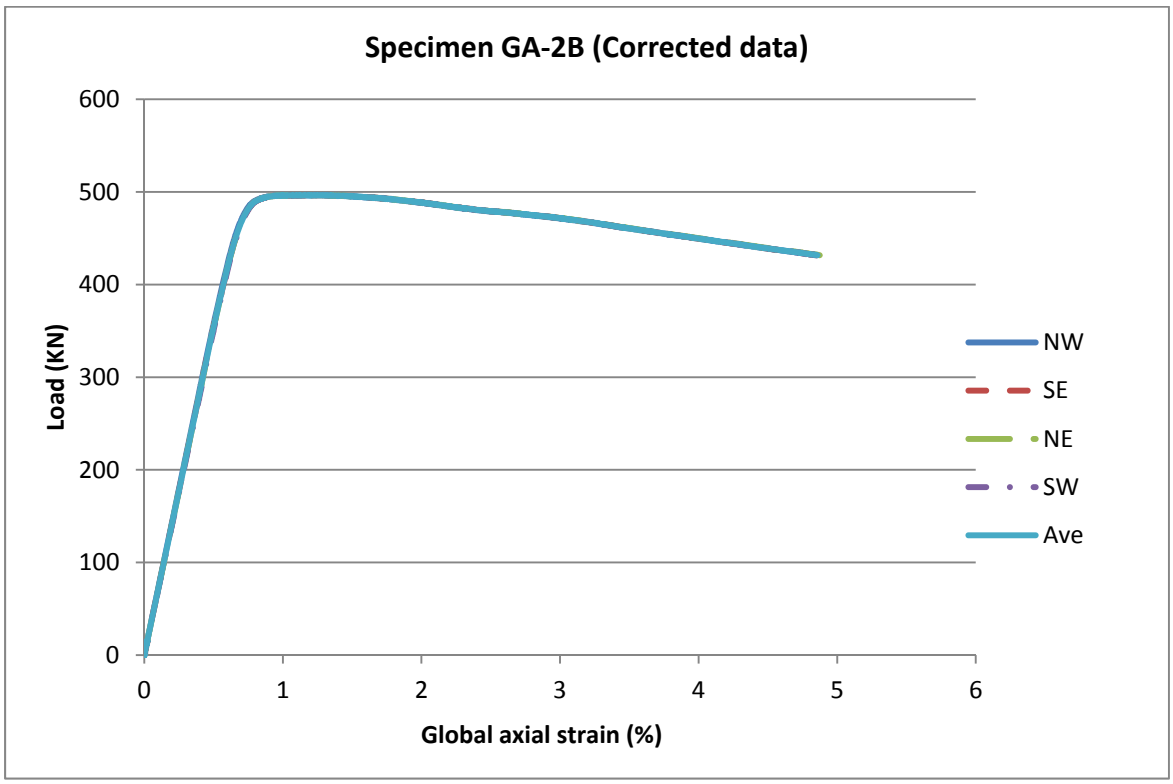

Figure 29: Load/global-axial-strain relationship

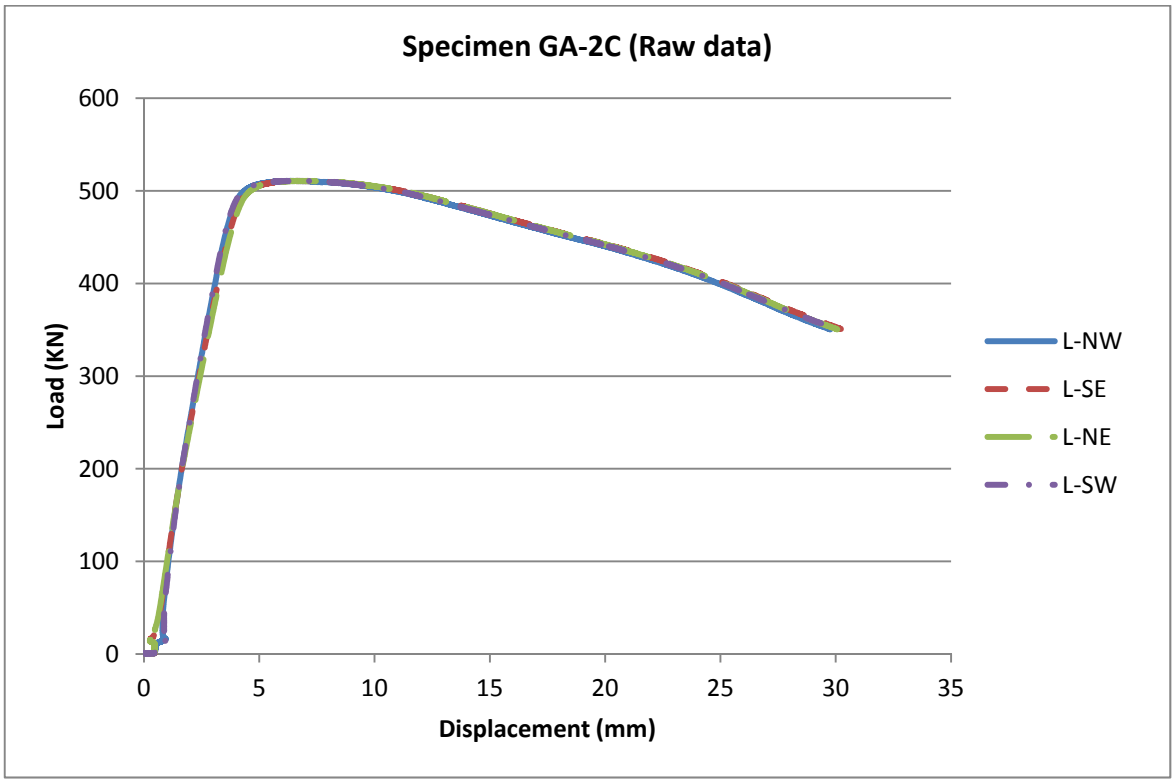

Figure 30: Load/axial-displacement relationship

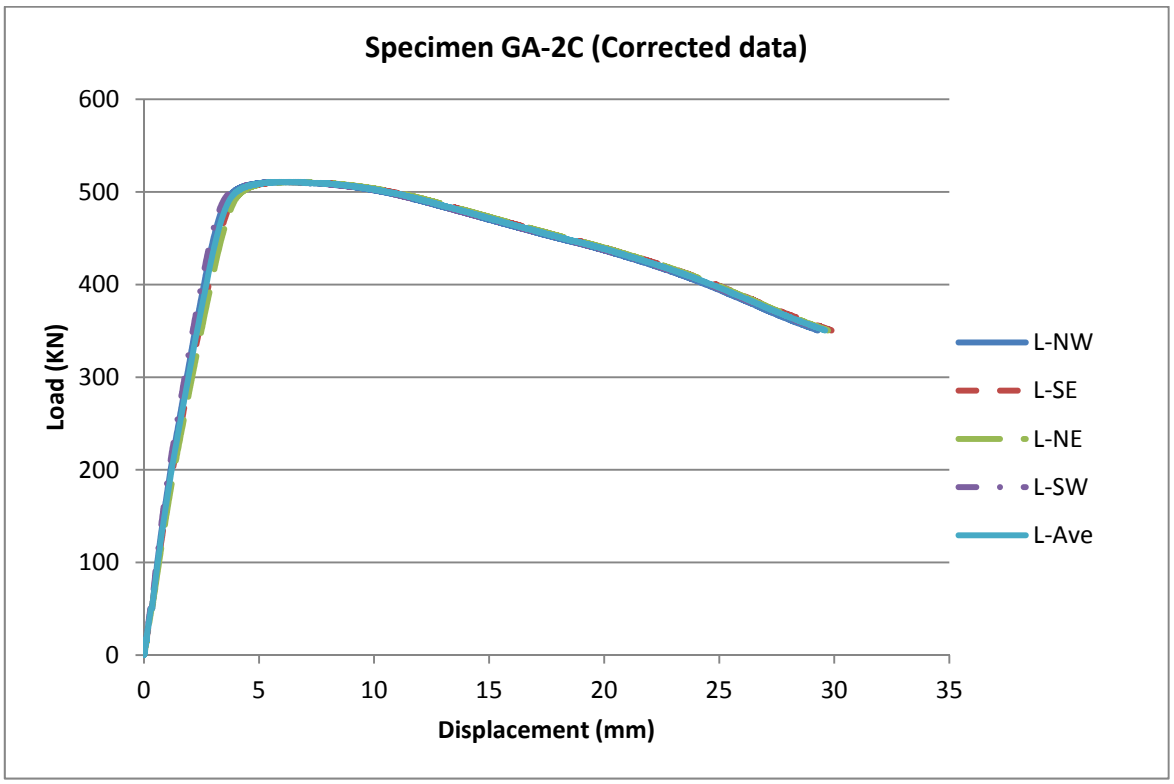

Figure 31: Load/axial-displacement relationship

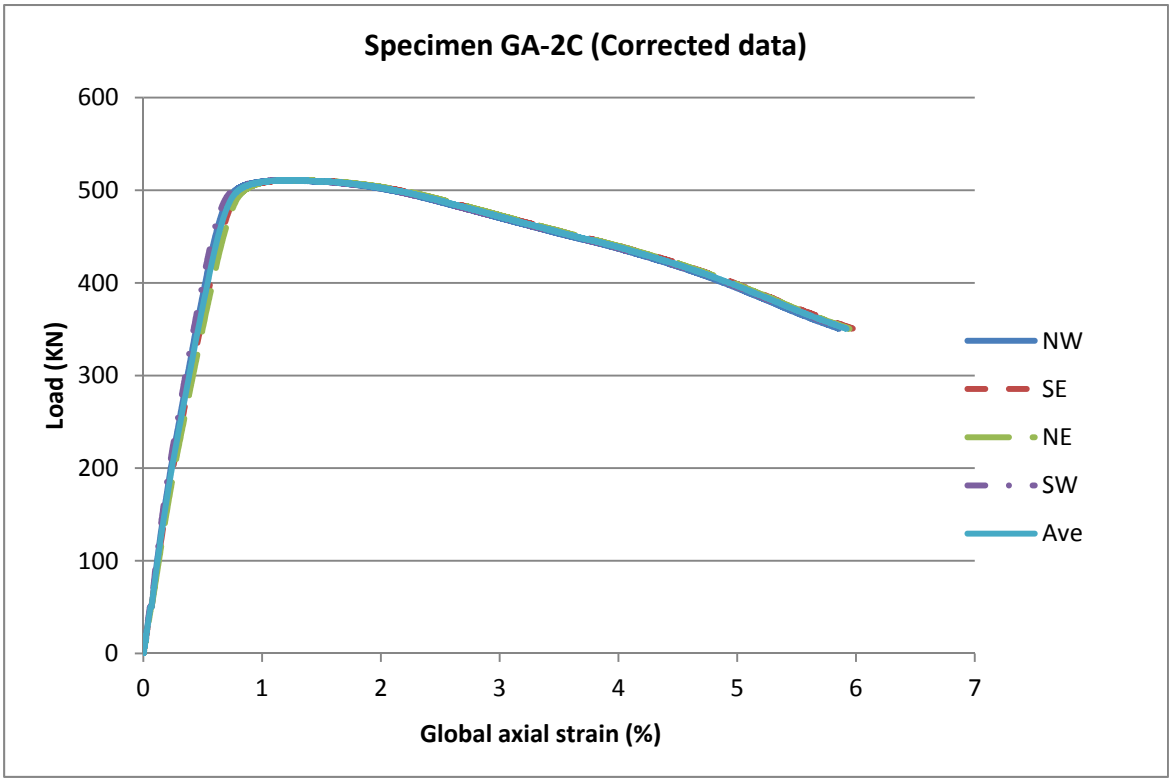

Figure 32: Load/global-axial-strain relationship

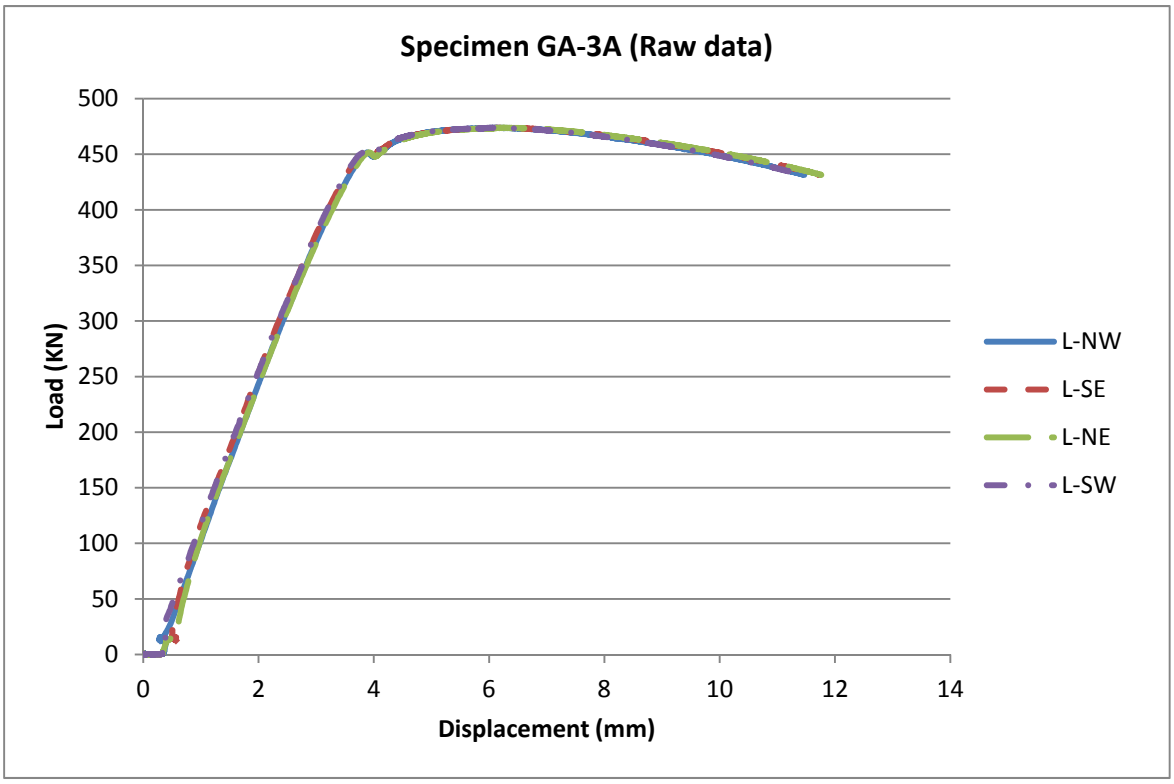

Figure 33: Load/axial-displacement relationship

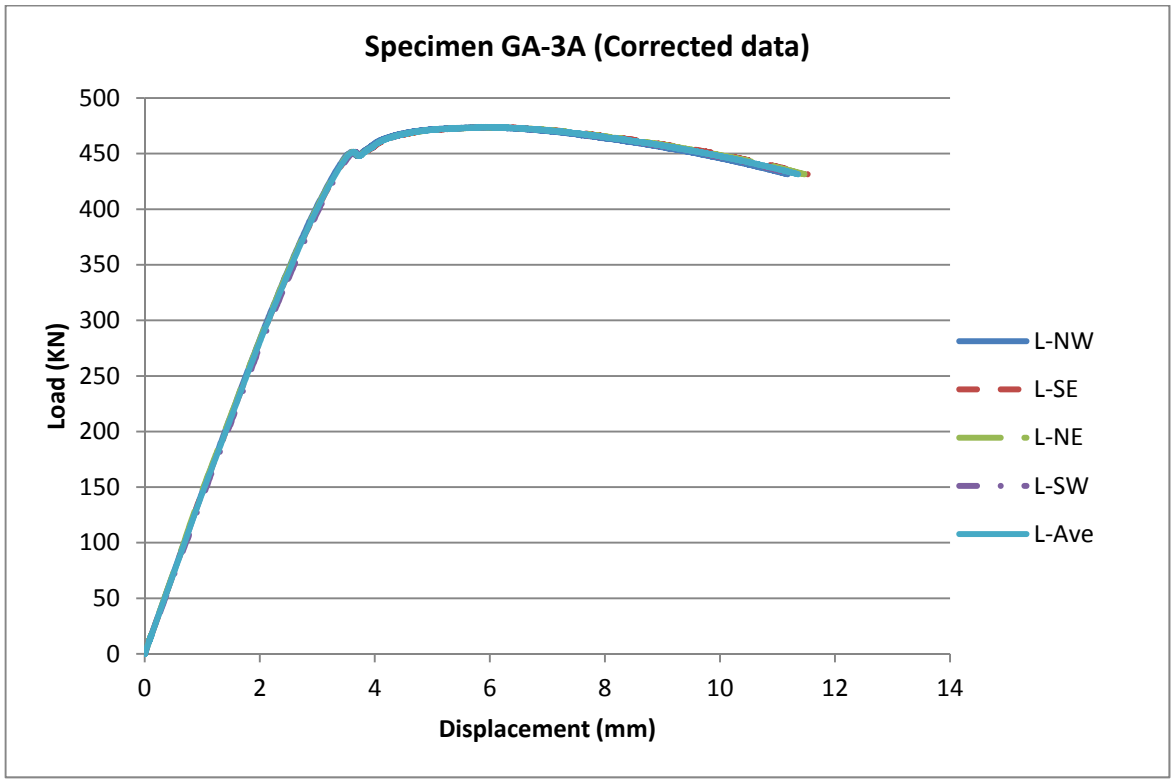

Figure 34: Load/axial-displacement relationship

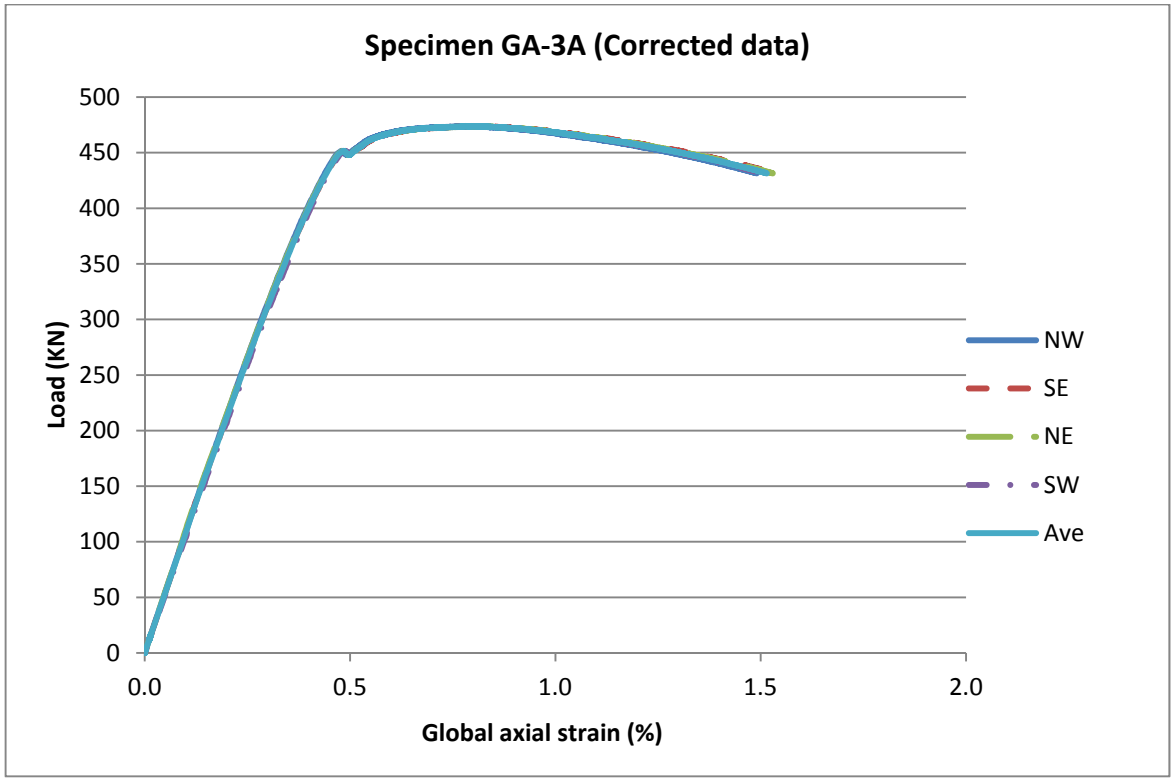

Figure 35: Load/global-axial-strain relationship

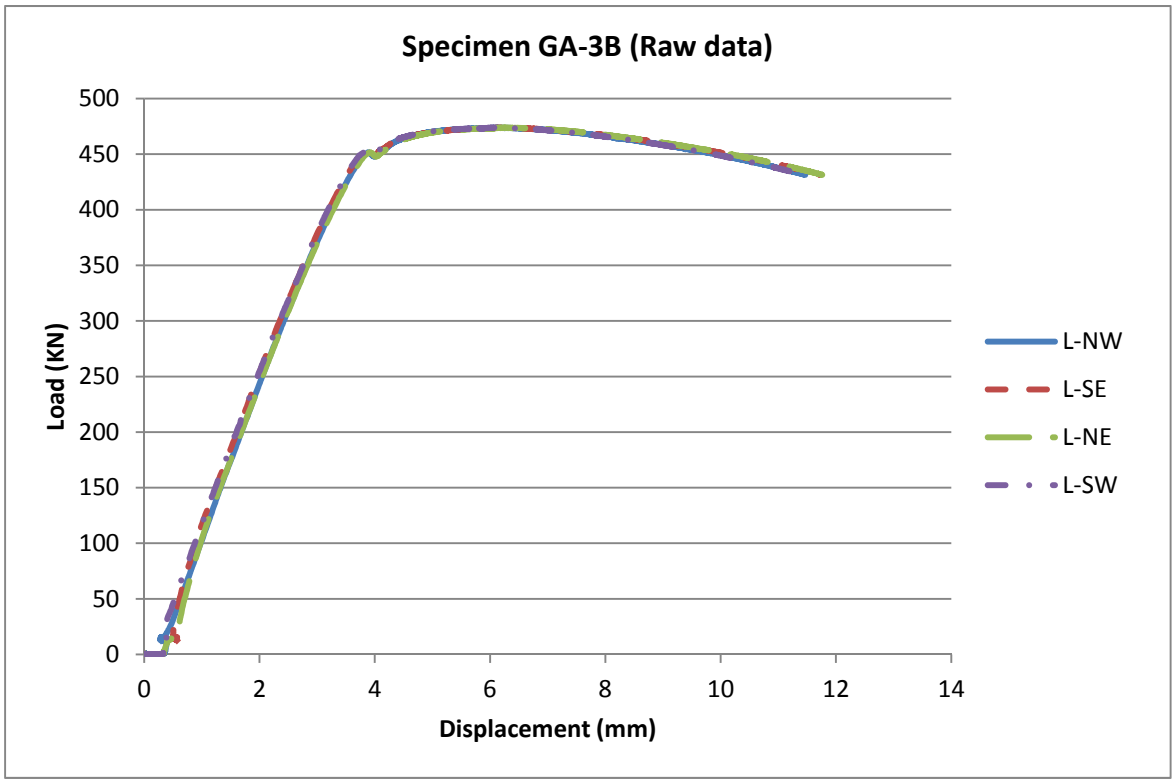

Figure 36: Load/axial-displacement relationship

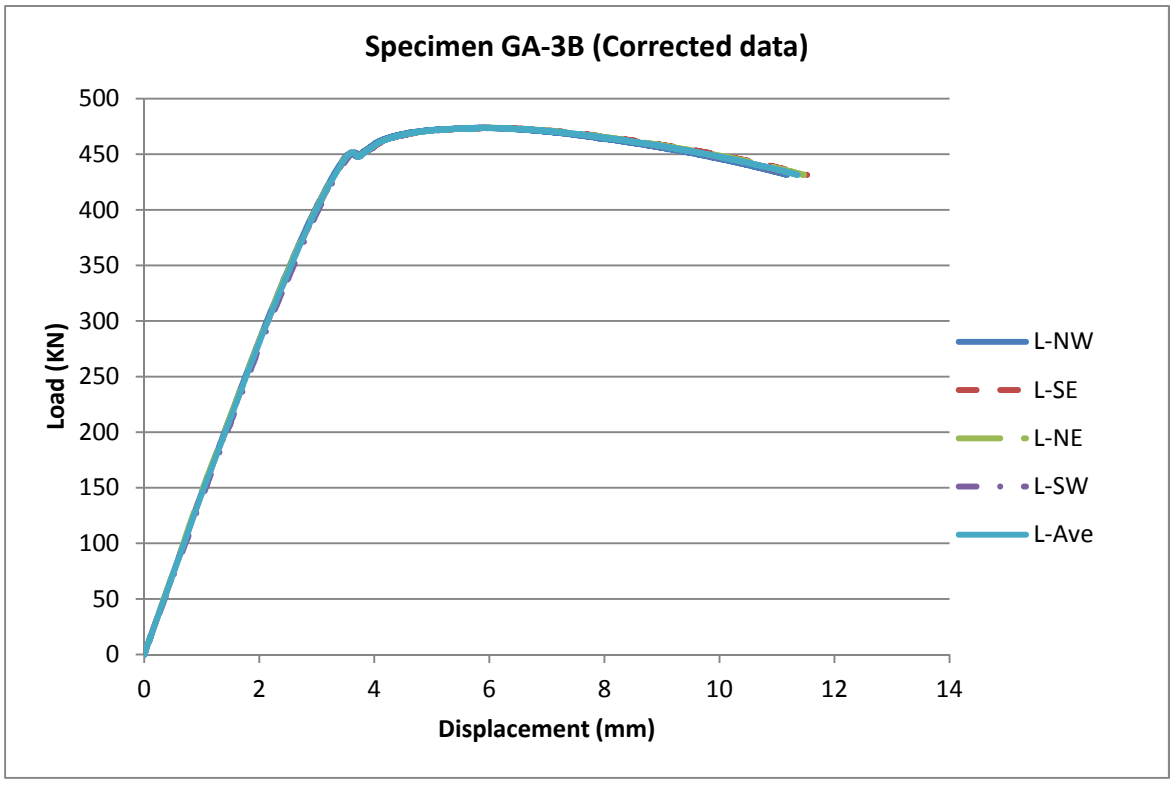

Figure 37: Load/axial-displacement relationship

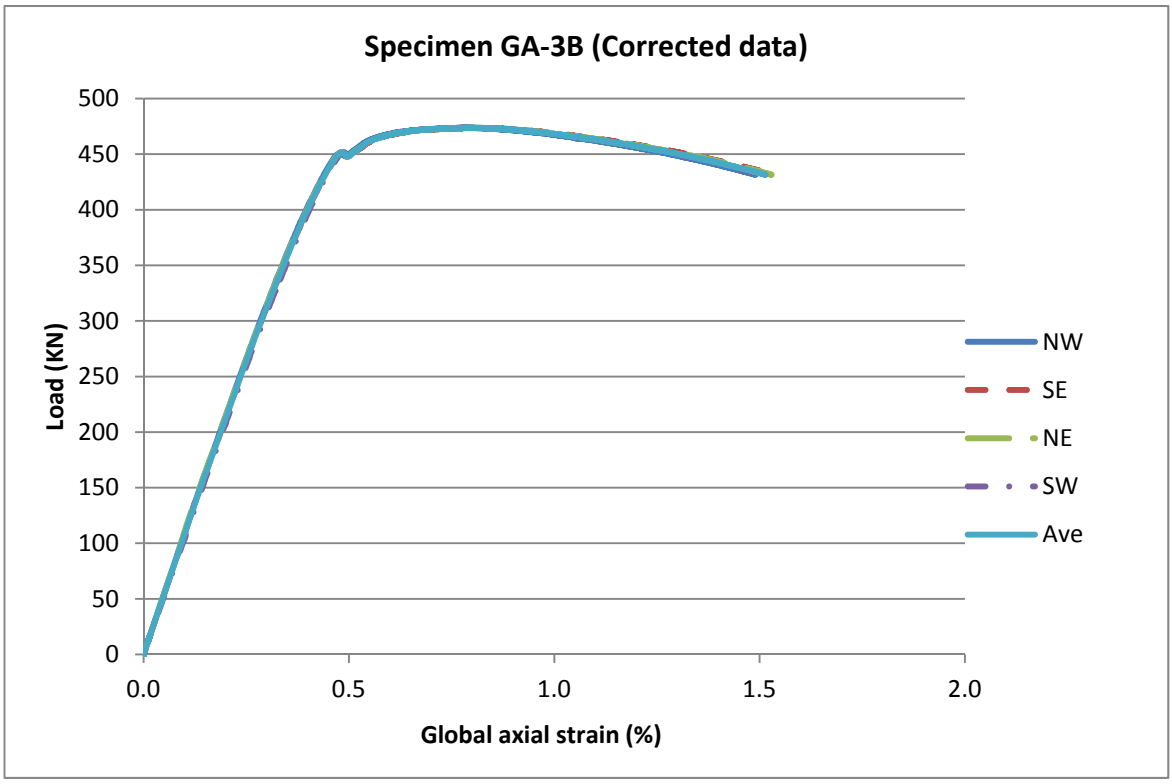

Figure 38: Load/global-axial-strain relationship

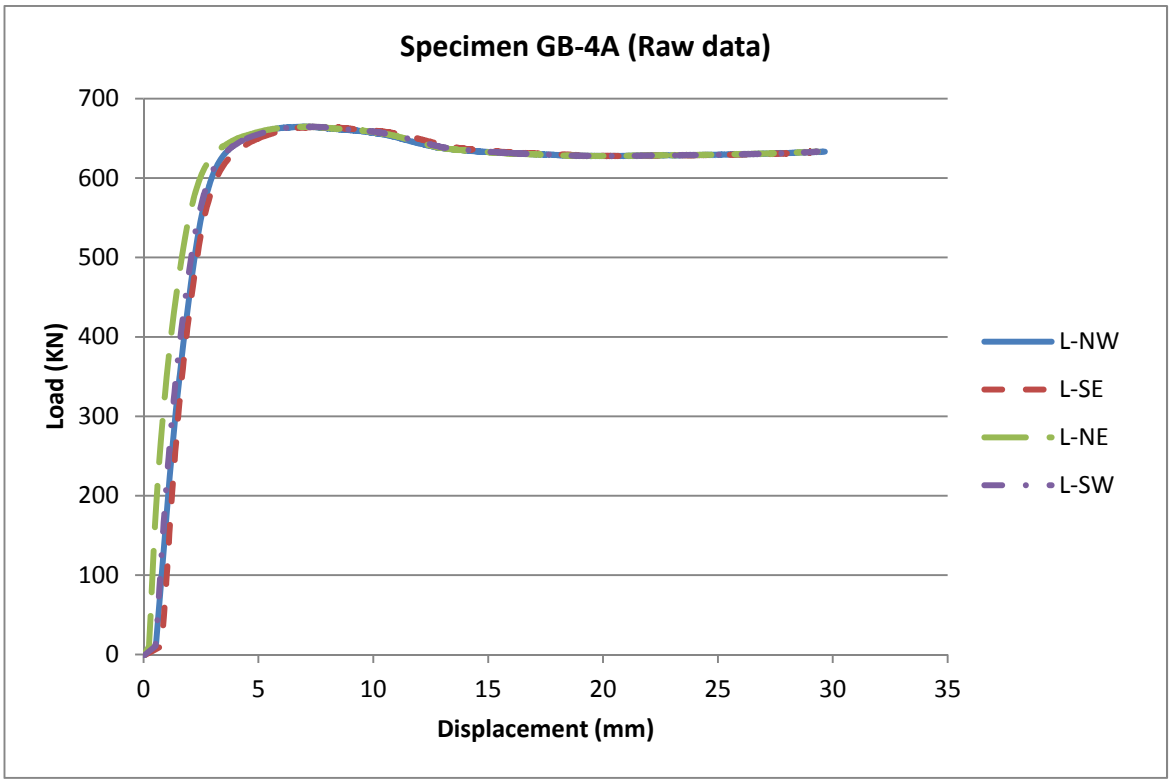

Figure 39: Load/axial-displacement relationship

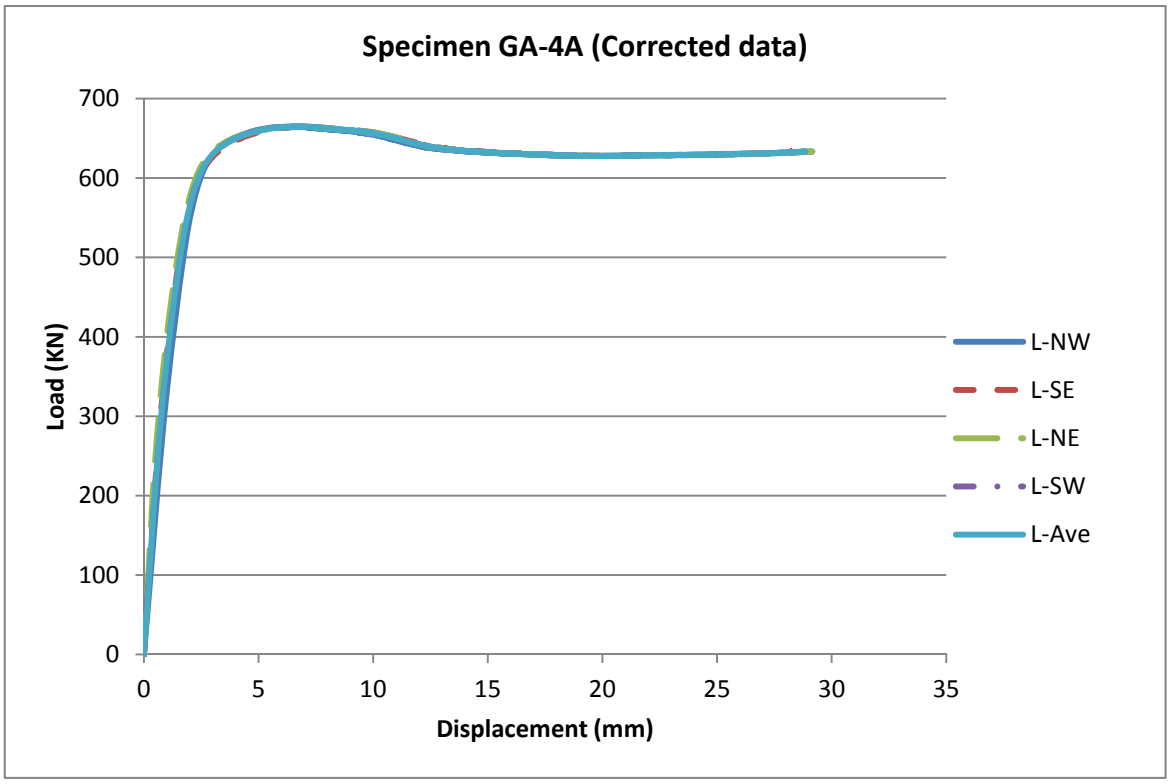

Figure 40: Load/axial-displacement relationship

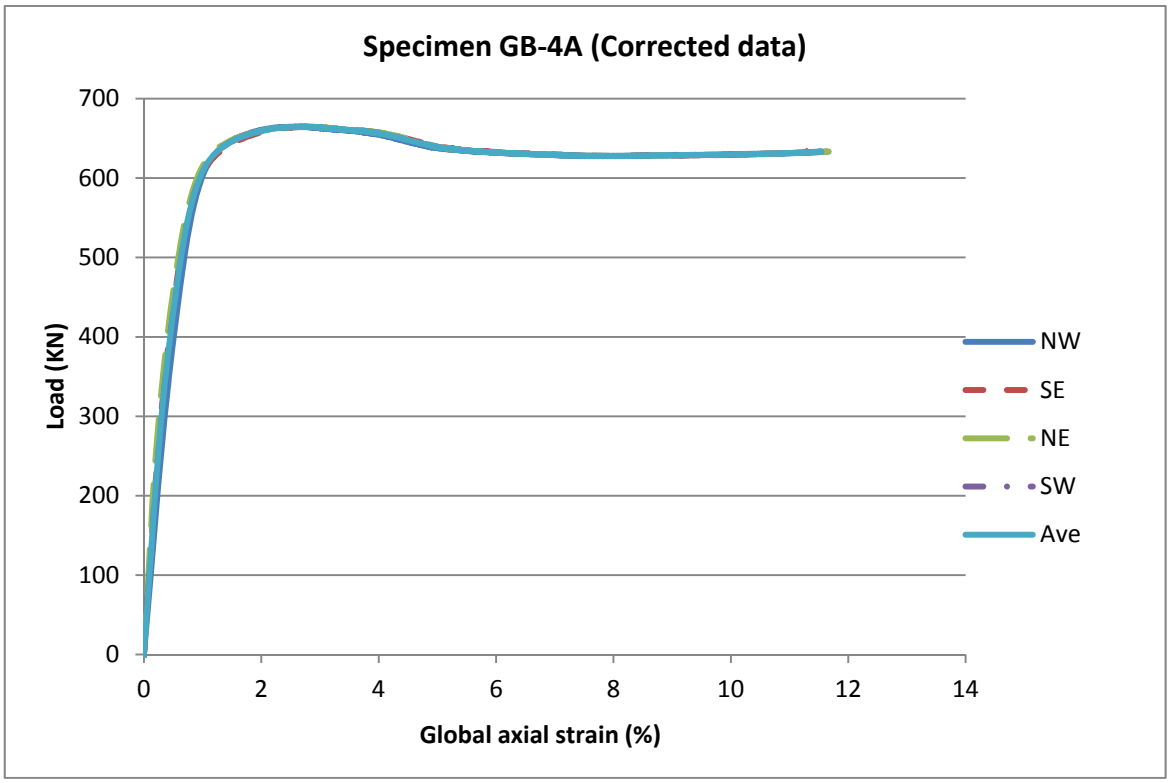

Figure 41: Load/global-axial-strain relationship

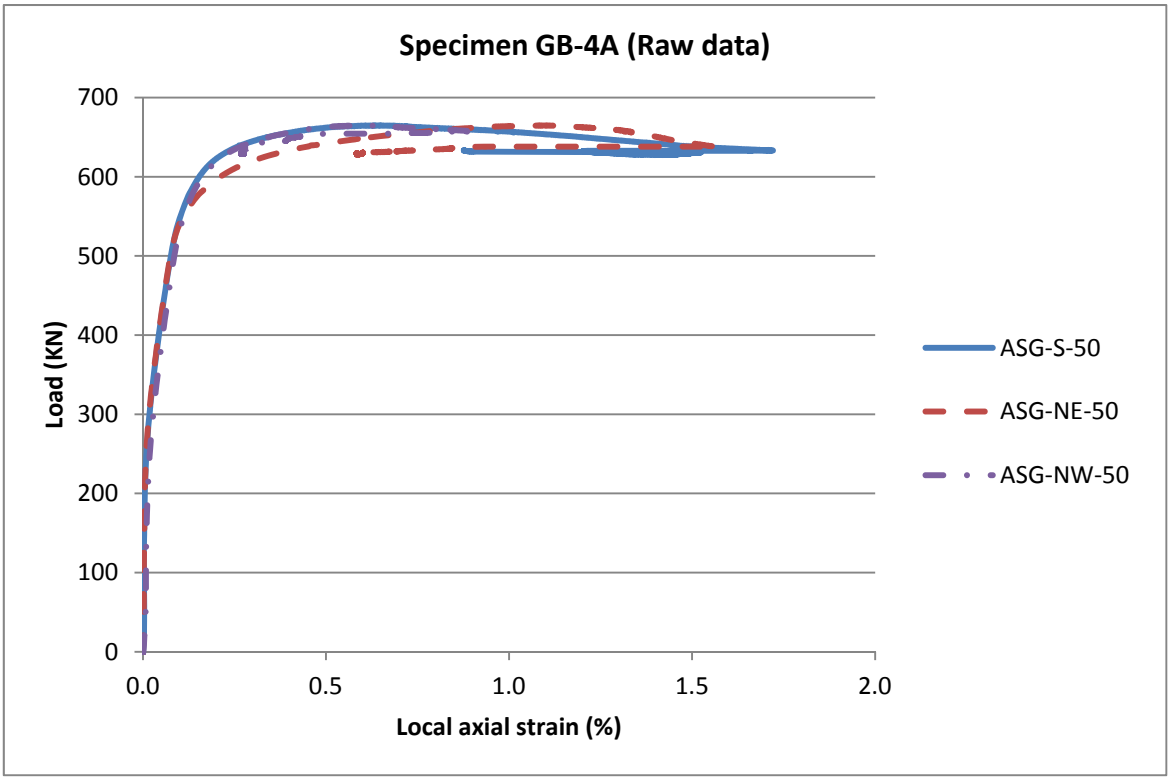

Figure 42: Load/local-axial-strain relationship

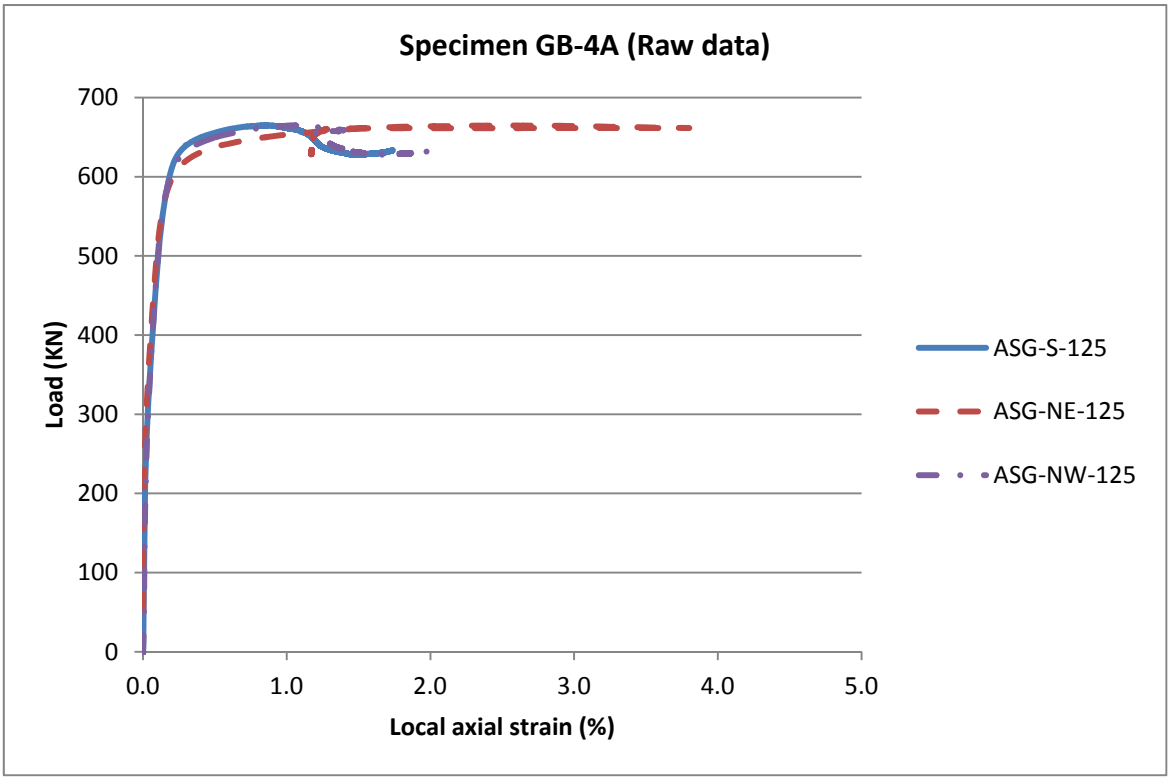

Figure 43: Load/local-axial-strain relationship

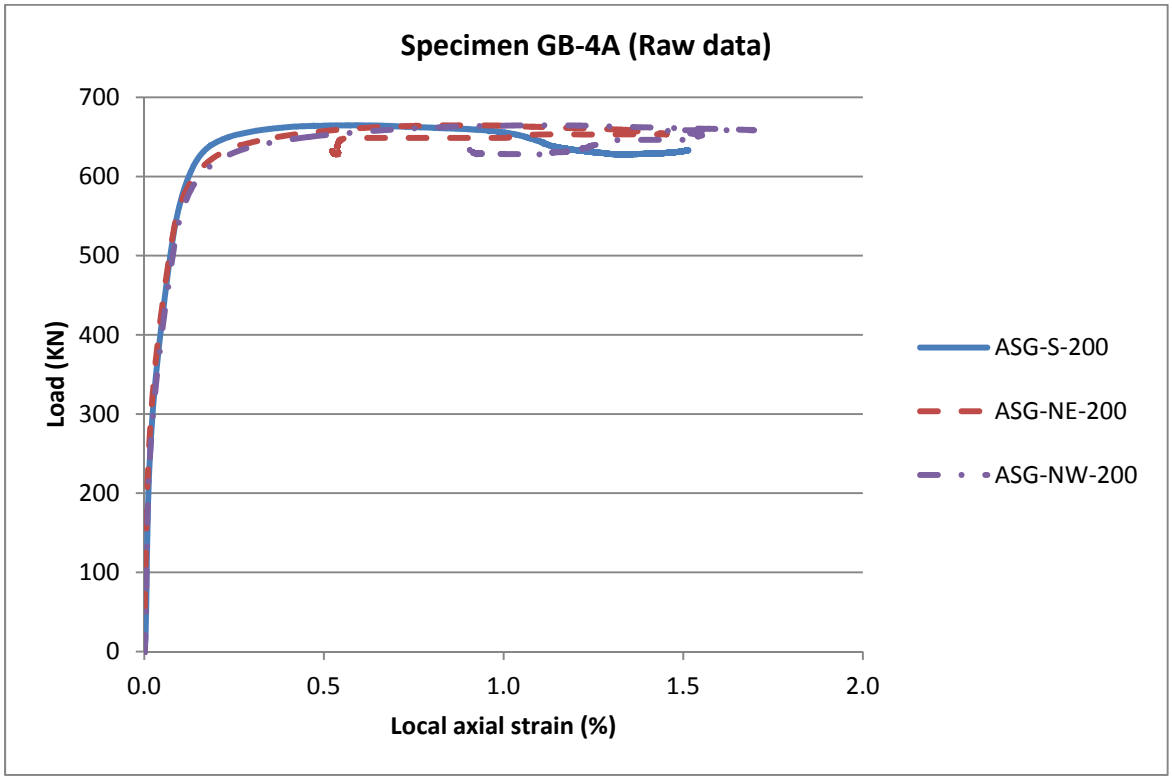

Figure 44: Load/local-axial-strain relationship

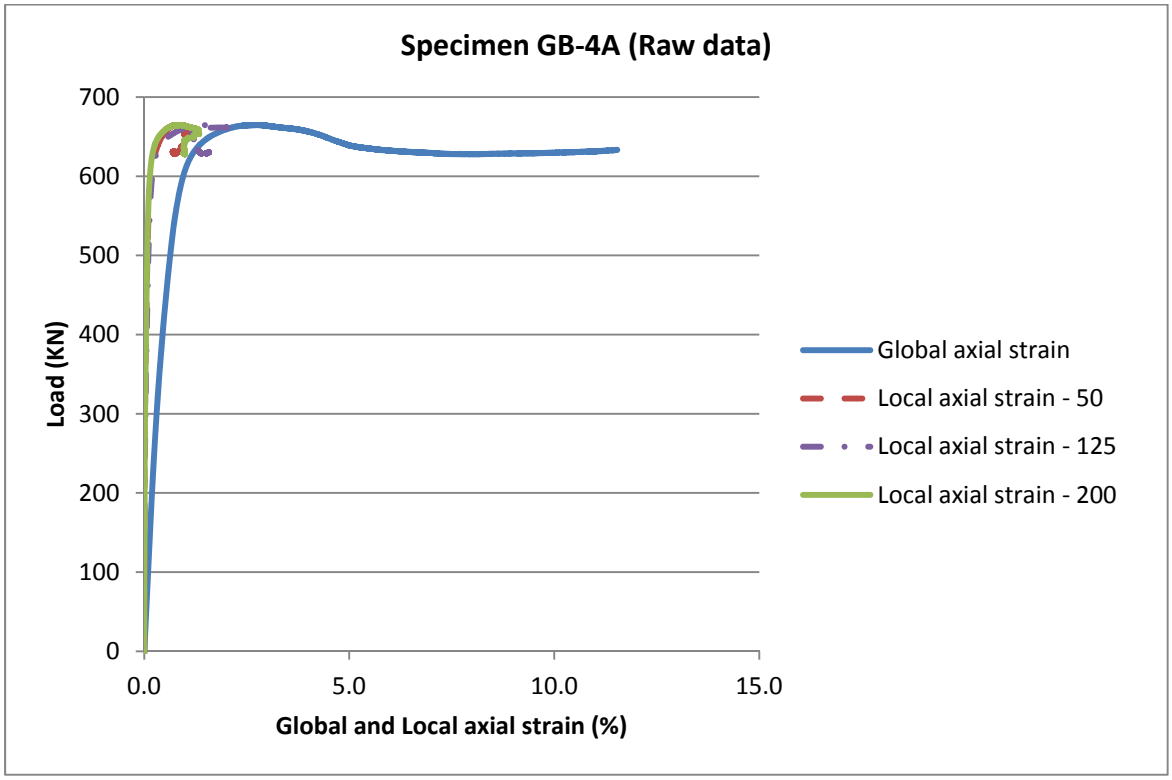

Figure 45: Load/global and load/local strains relationship

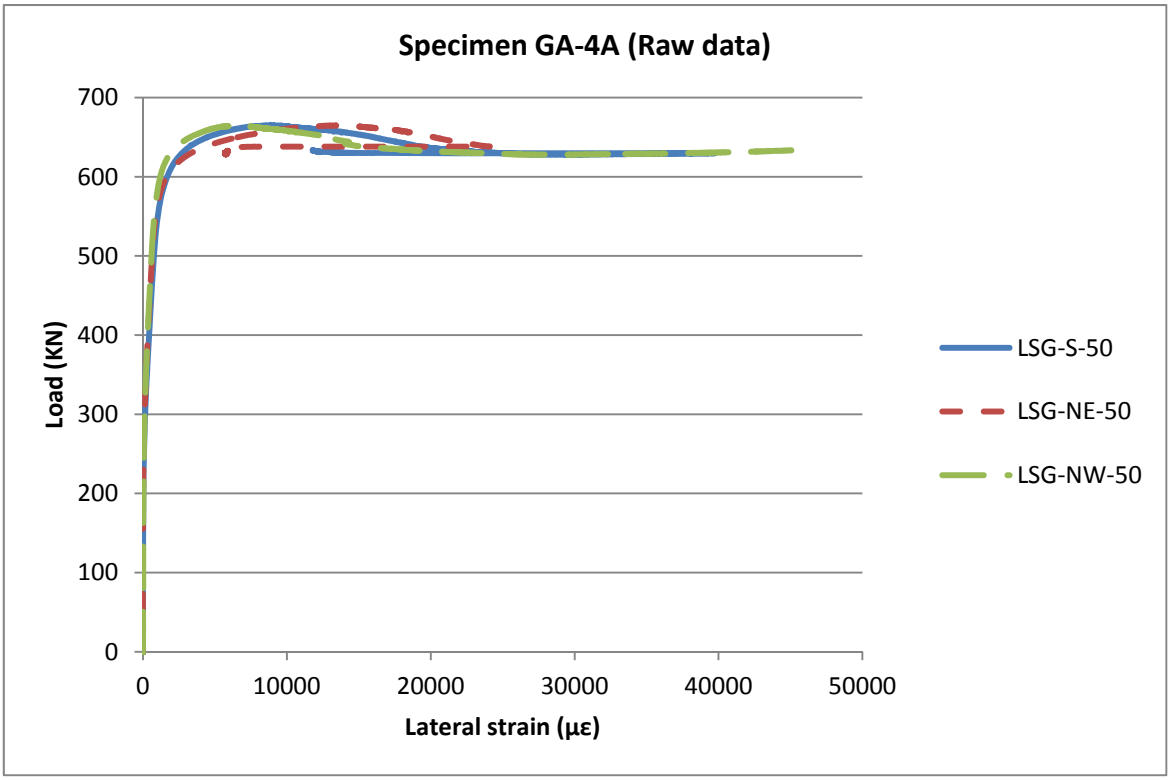

Figure 46: Load/lateral-strain relationship

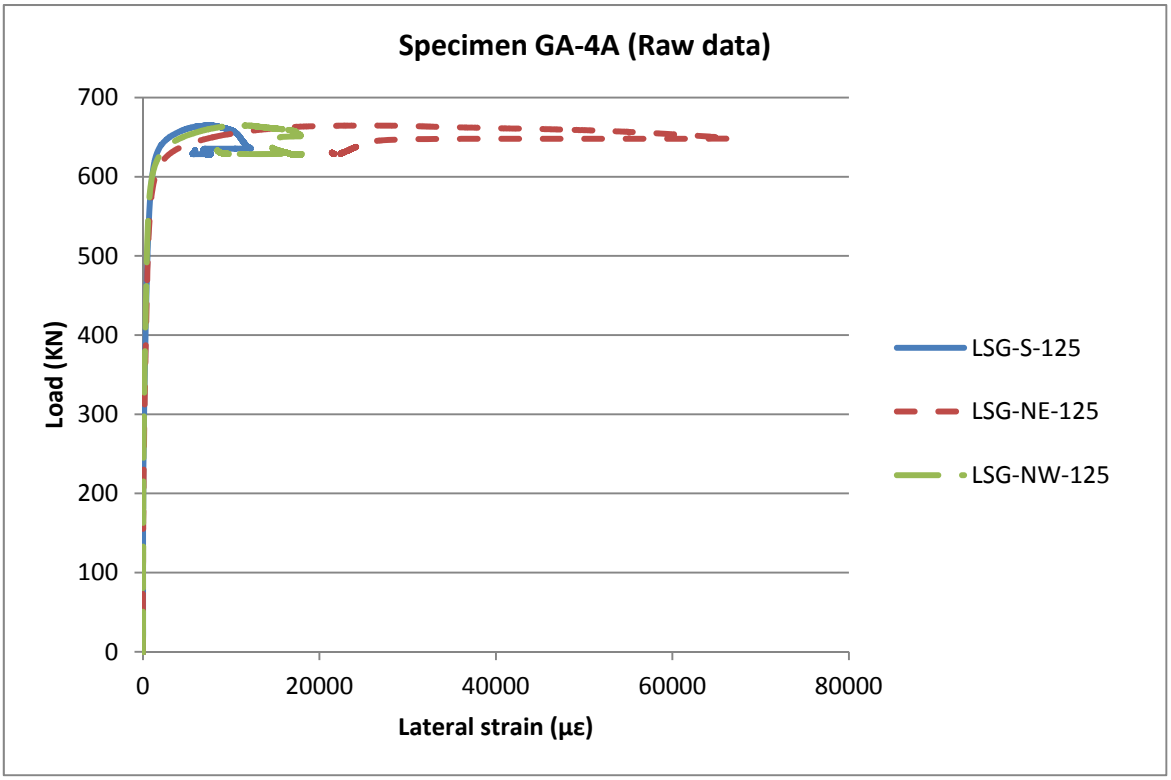

Figure 47: Load/lateral-strain relationship

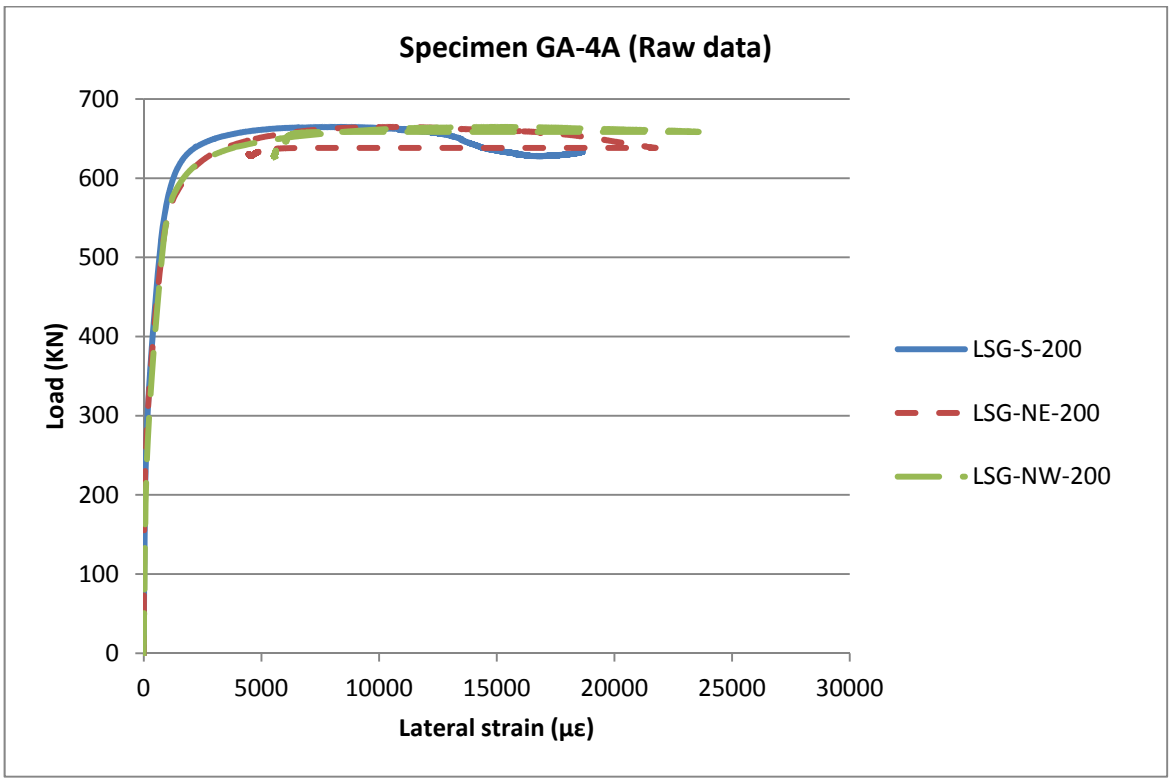

Figure 48: Load/lateral-strain relationship

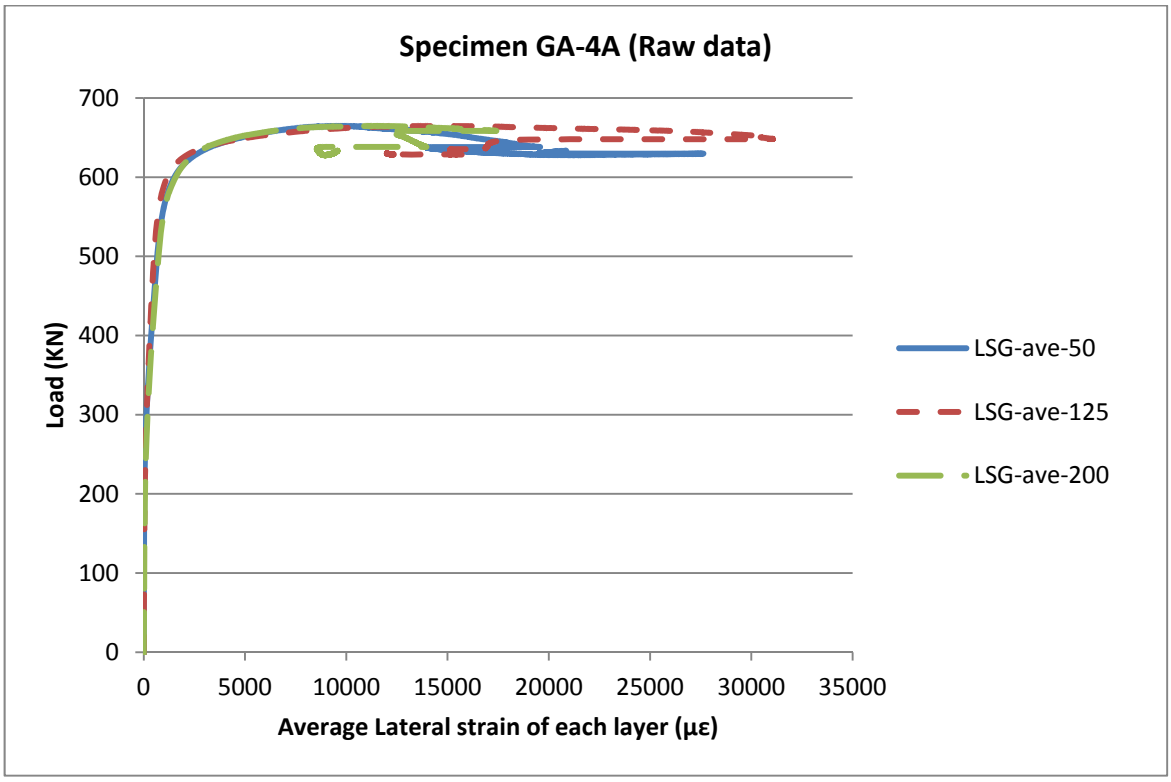

Figure 49: Load/lateral-strain relationship

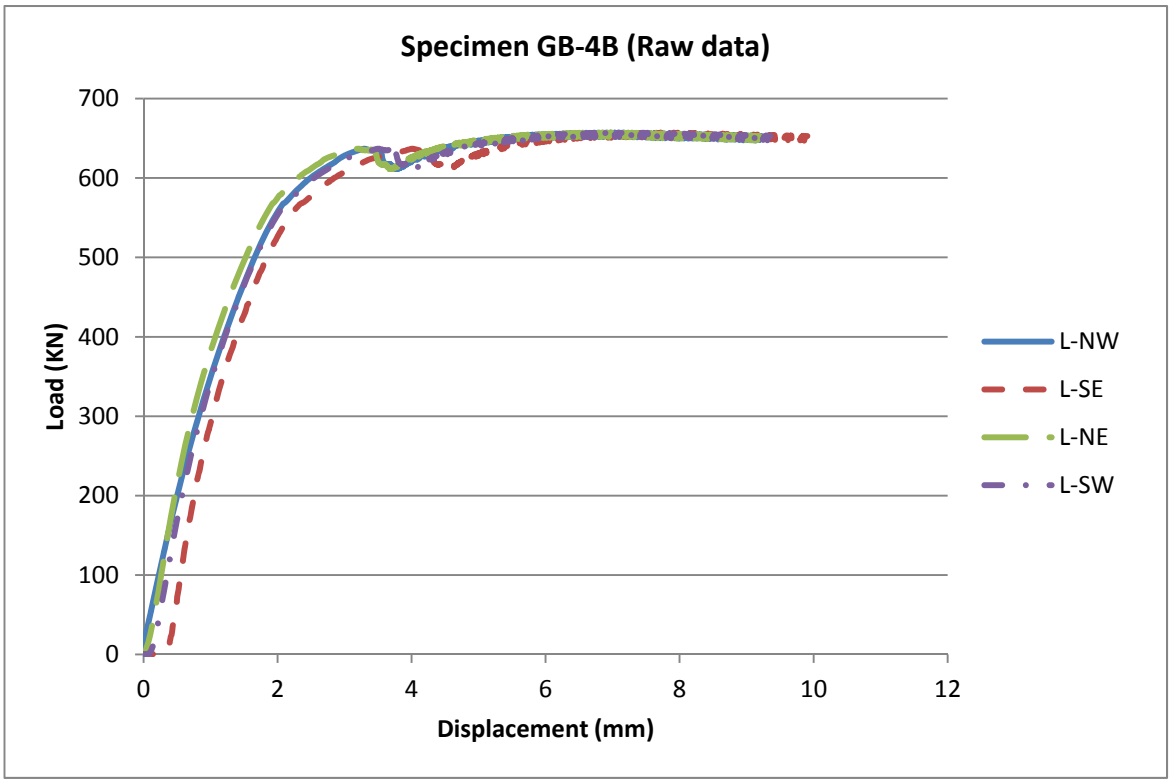

Figure 50: Load/axial-displacement relationship

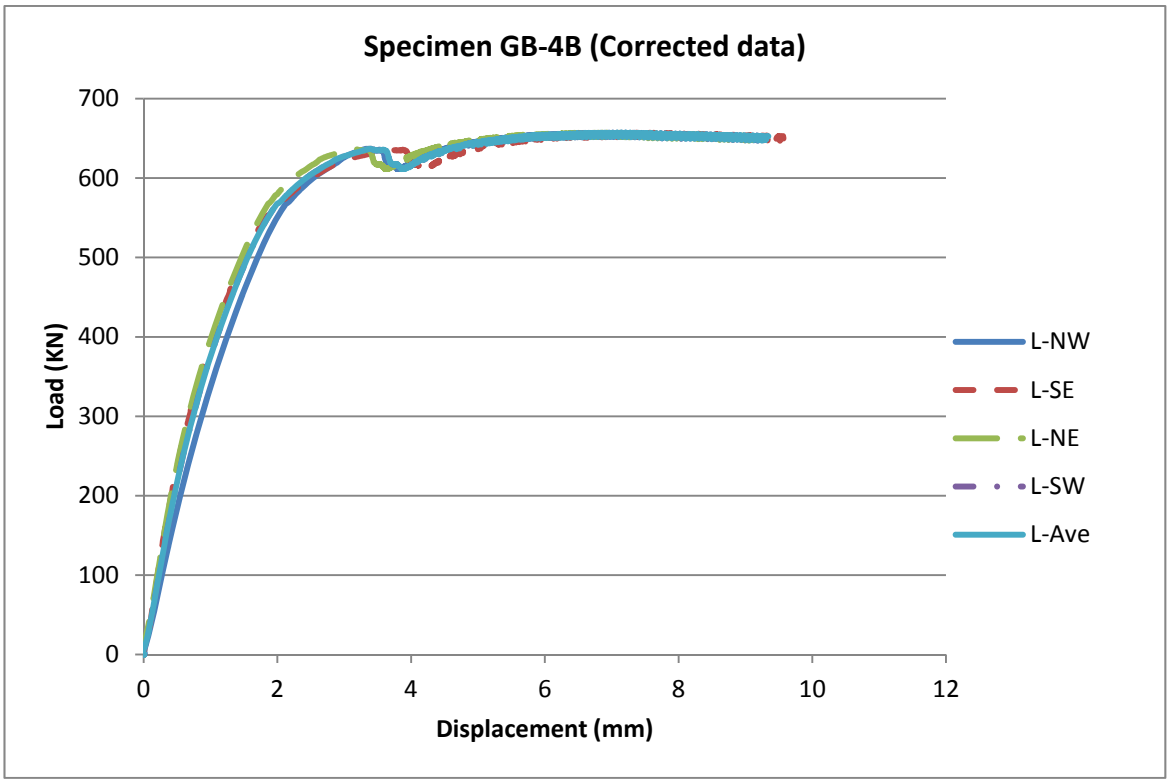

Figure 51: Load/axial-displacement relationship

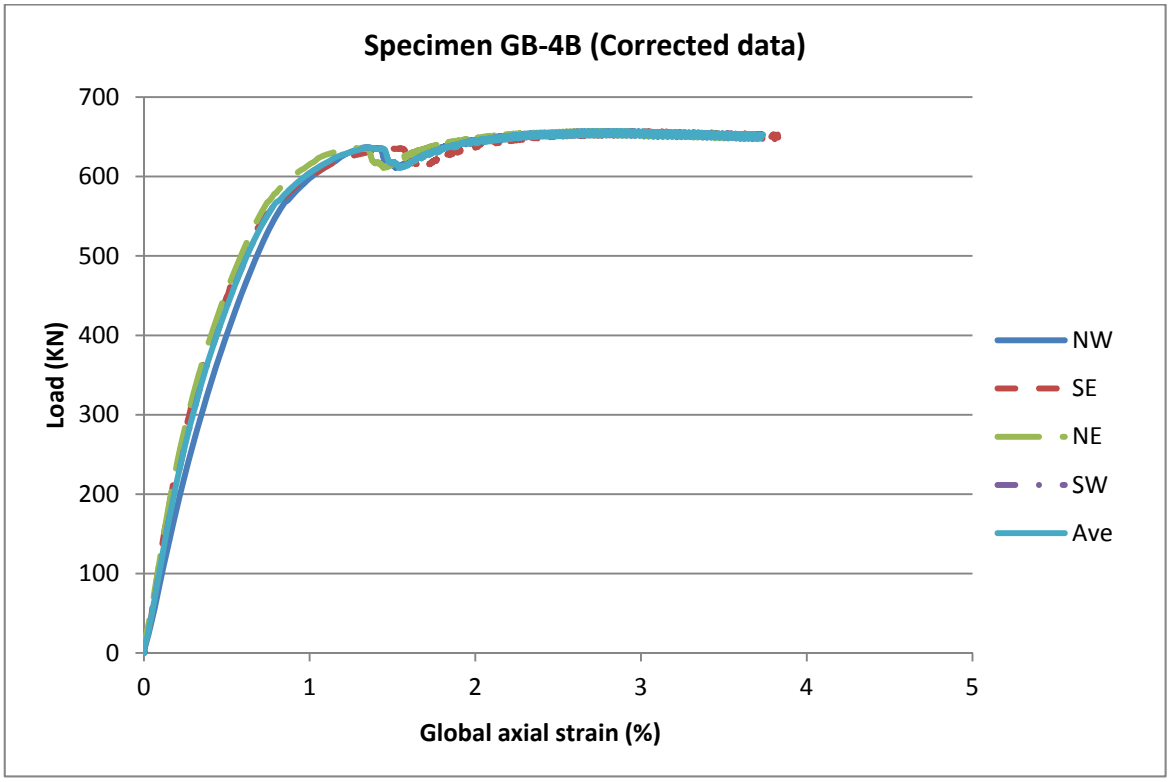

Figure 52: Load/global-axial-strain relationship

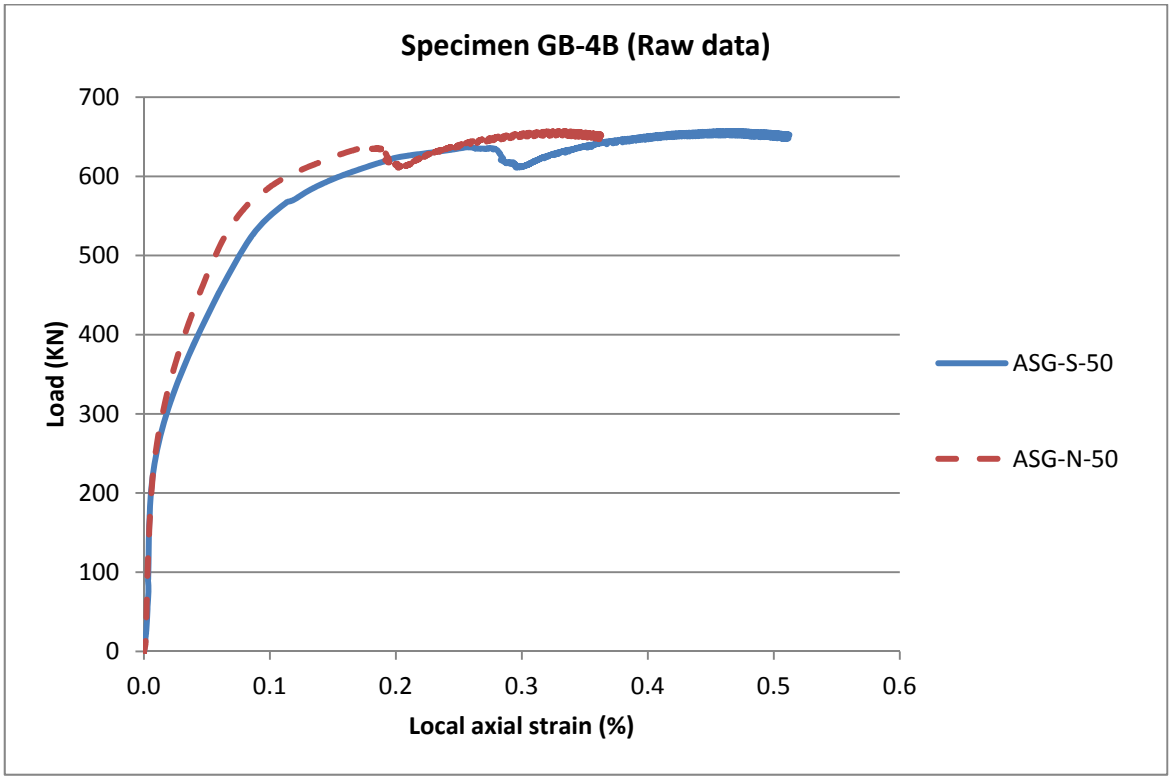

Figure 53: Load/local-axial-strain relationship

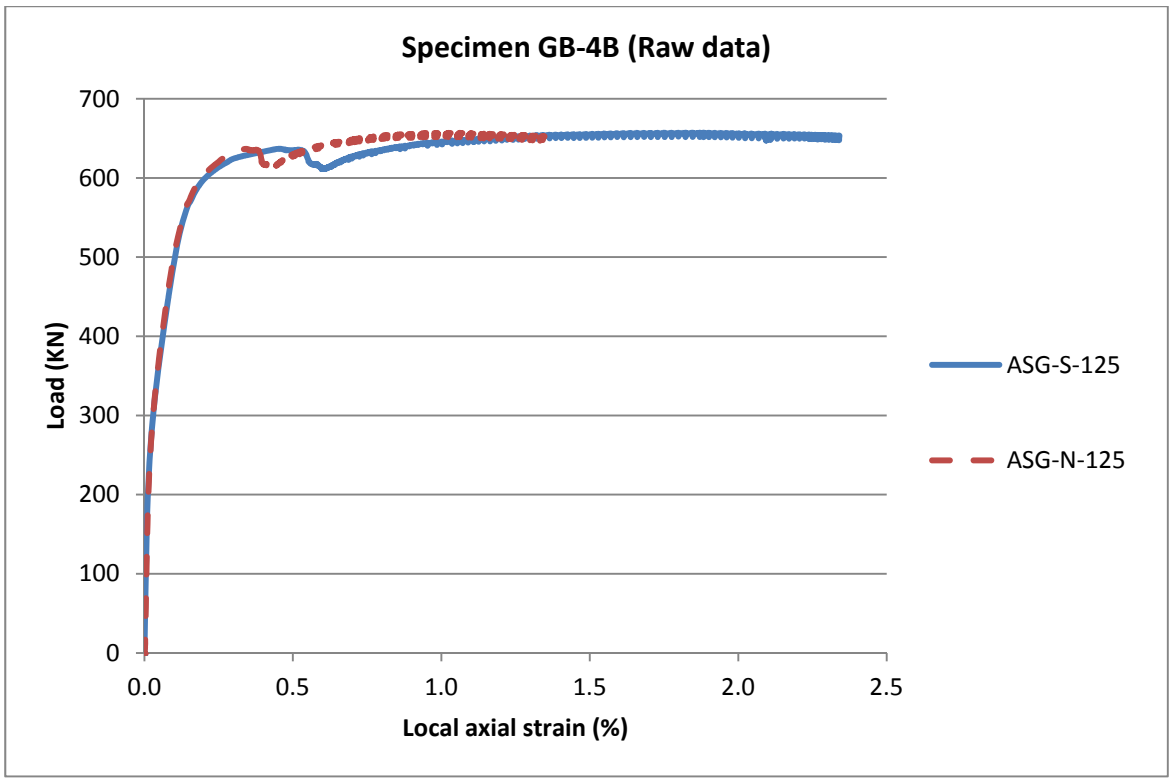

Figure 54: Load/local-axial-strain relationship

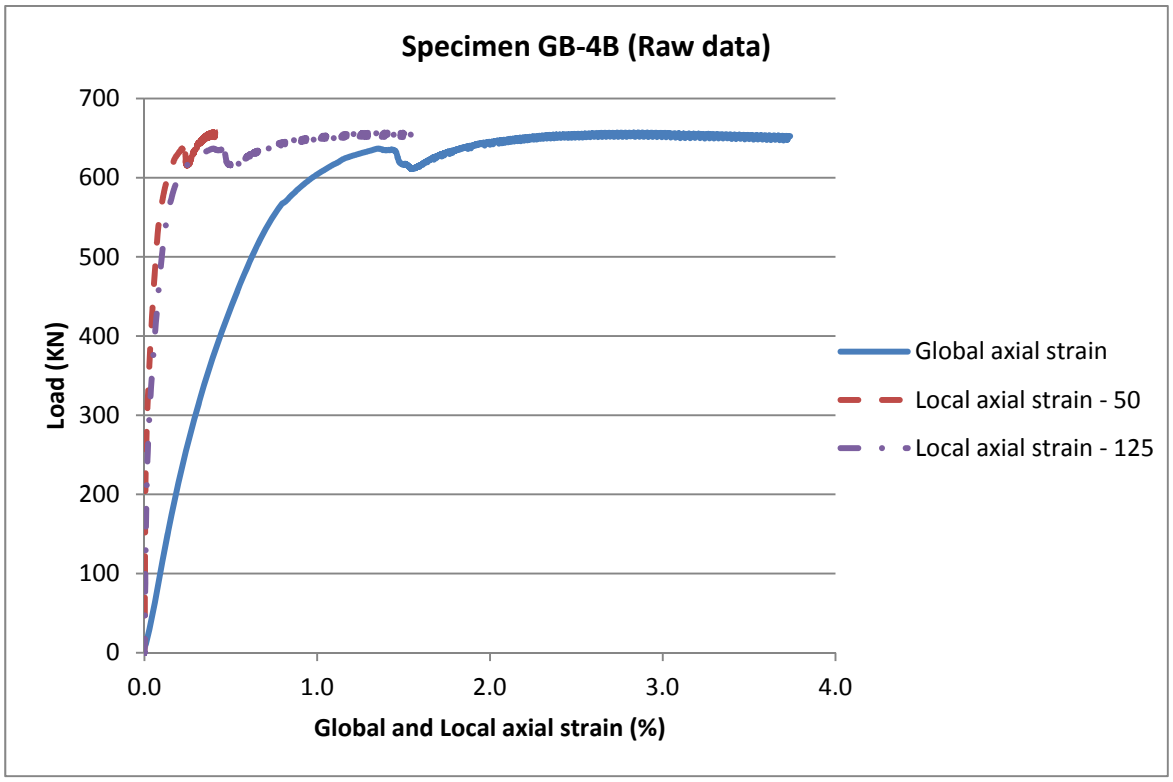

Figure 55: Load/global and load/local strains relationship

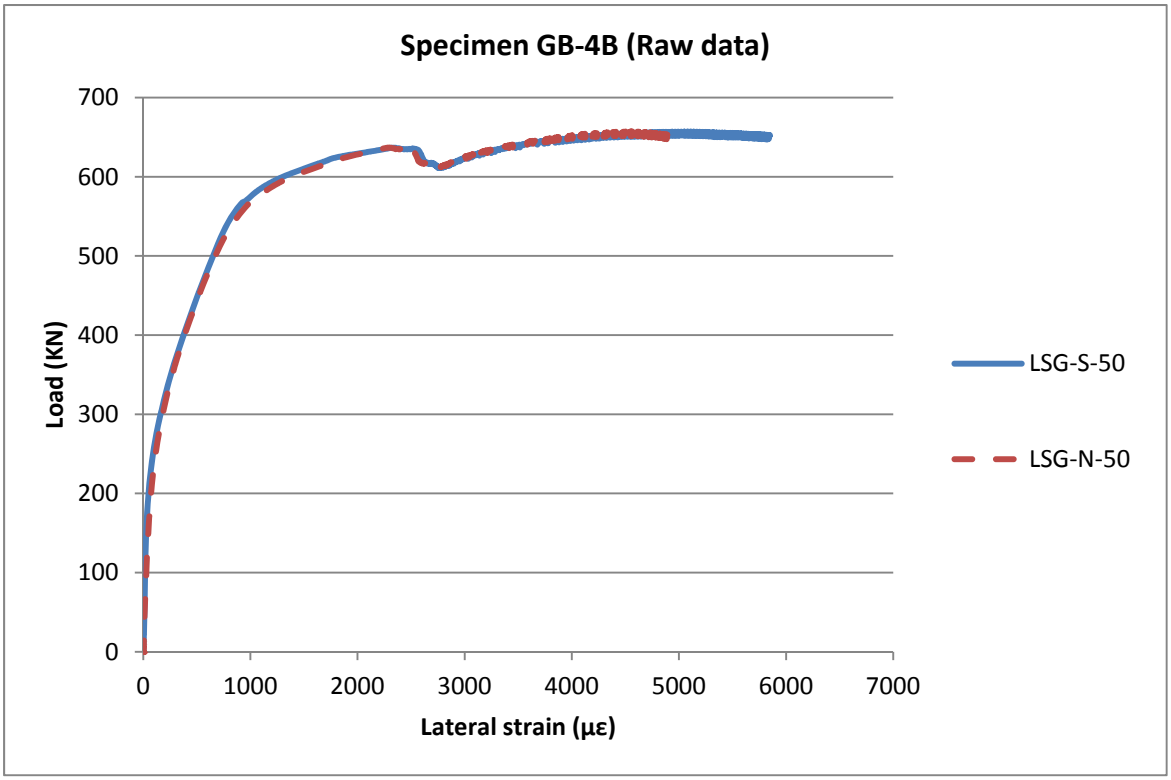

Figure 56: Load/lateral-strain relationship

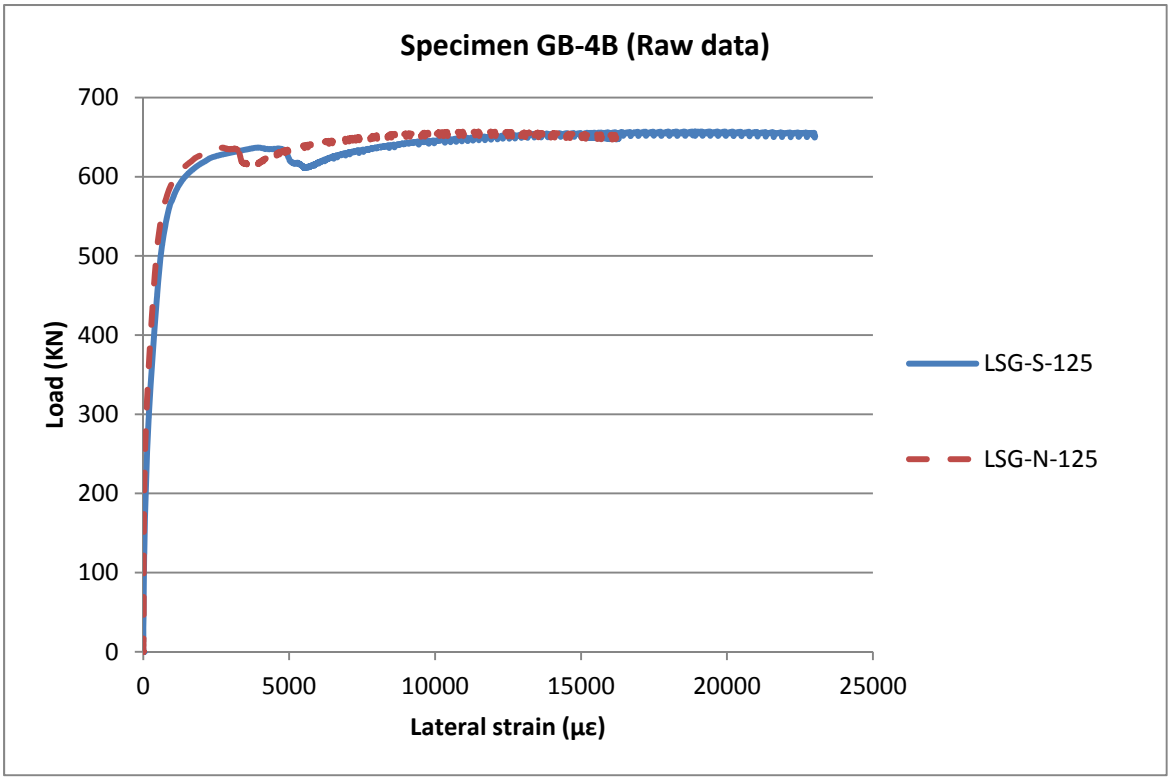

Figure 57: Load/lateral-strain relationship

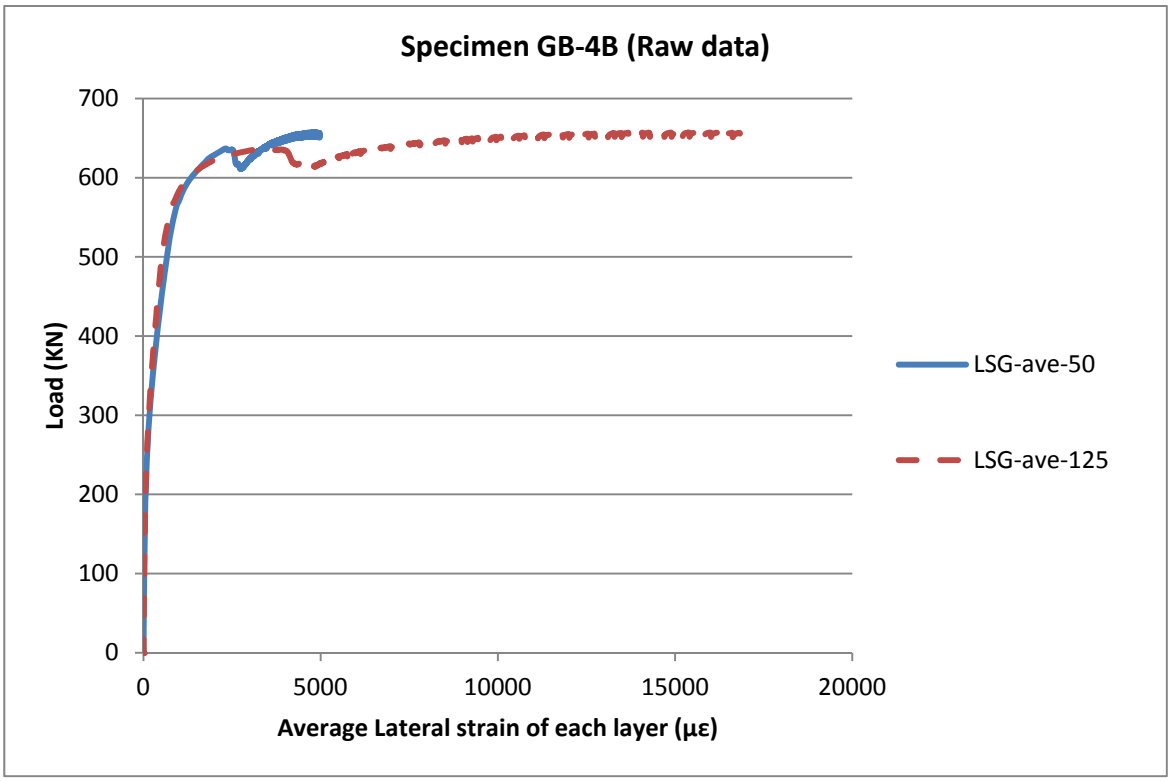

Figure 58: Load/lateral-strain relationship

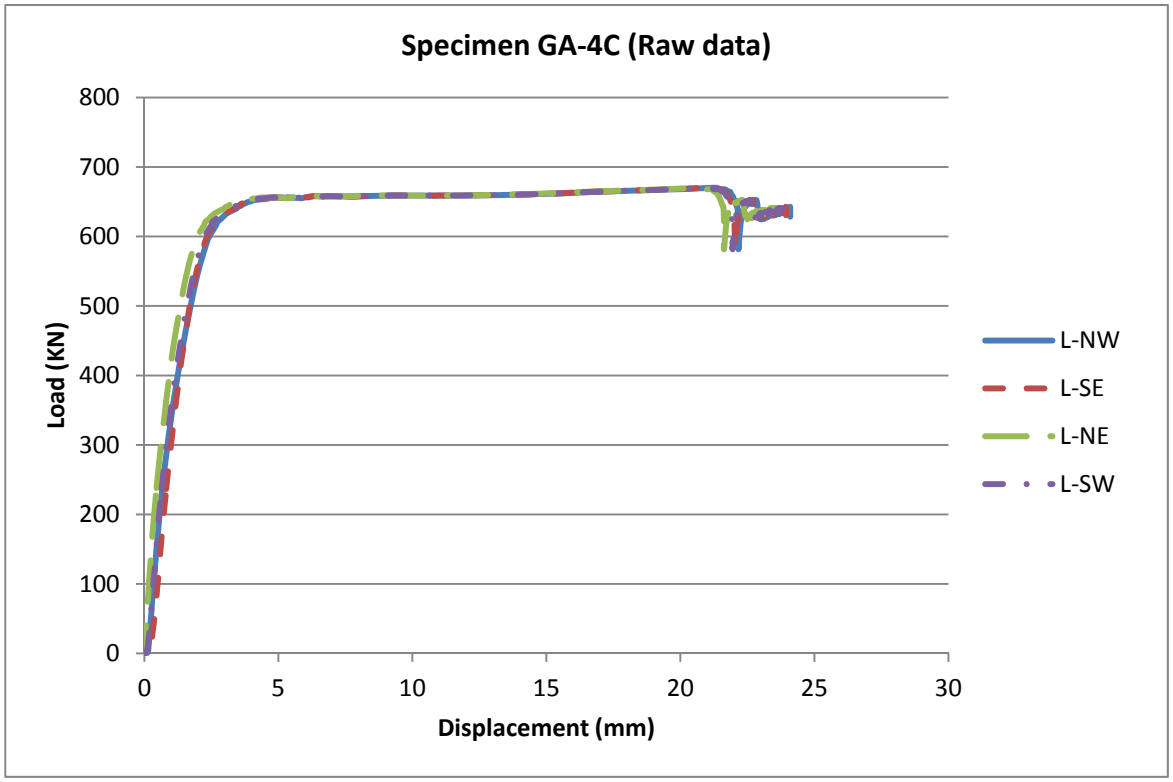

Figure 59: Load/axial-displacement relationship

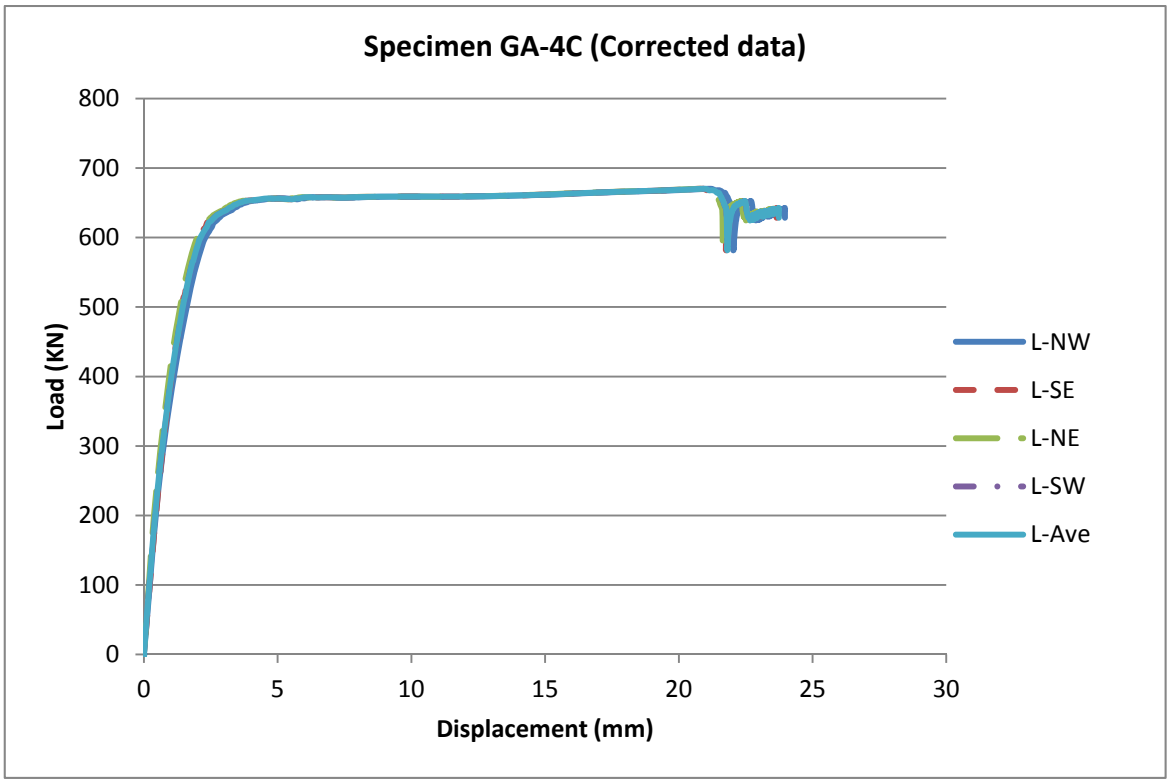

Figure 60: Load/axial-displacement relationship

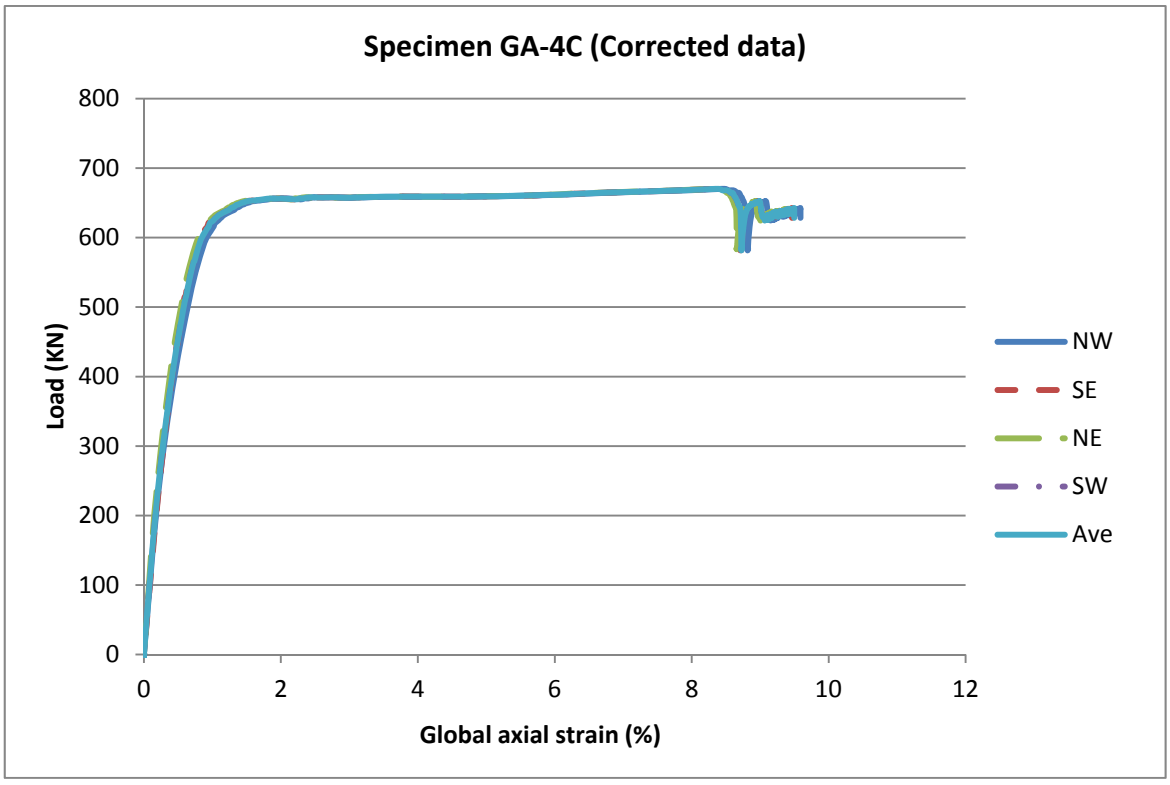

Figure 61: Load/global-axial-strain relationship

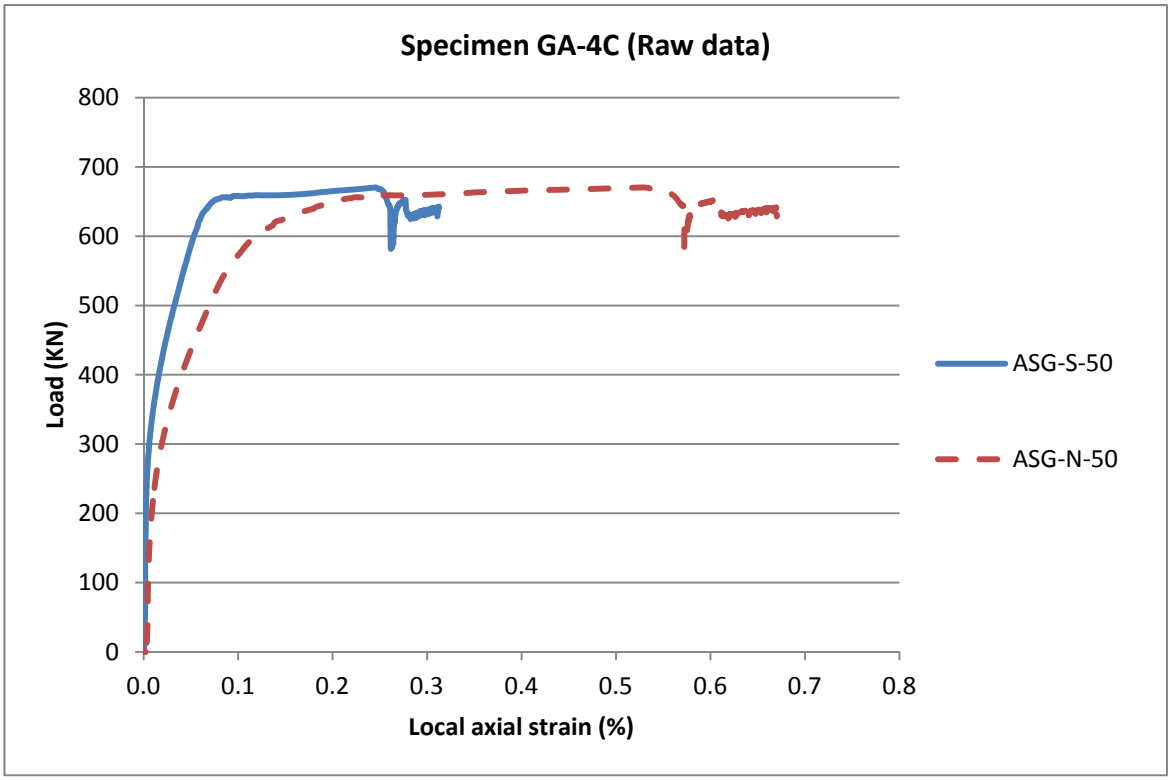

Figure 62: Load/local-axial-strain relationship

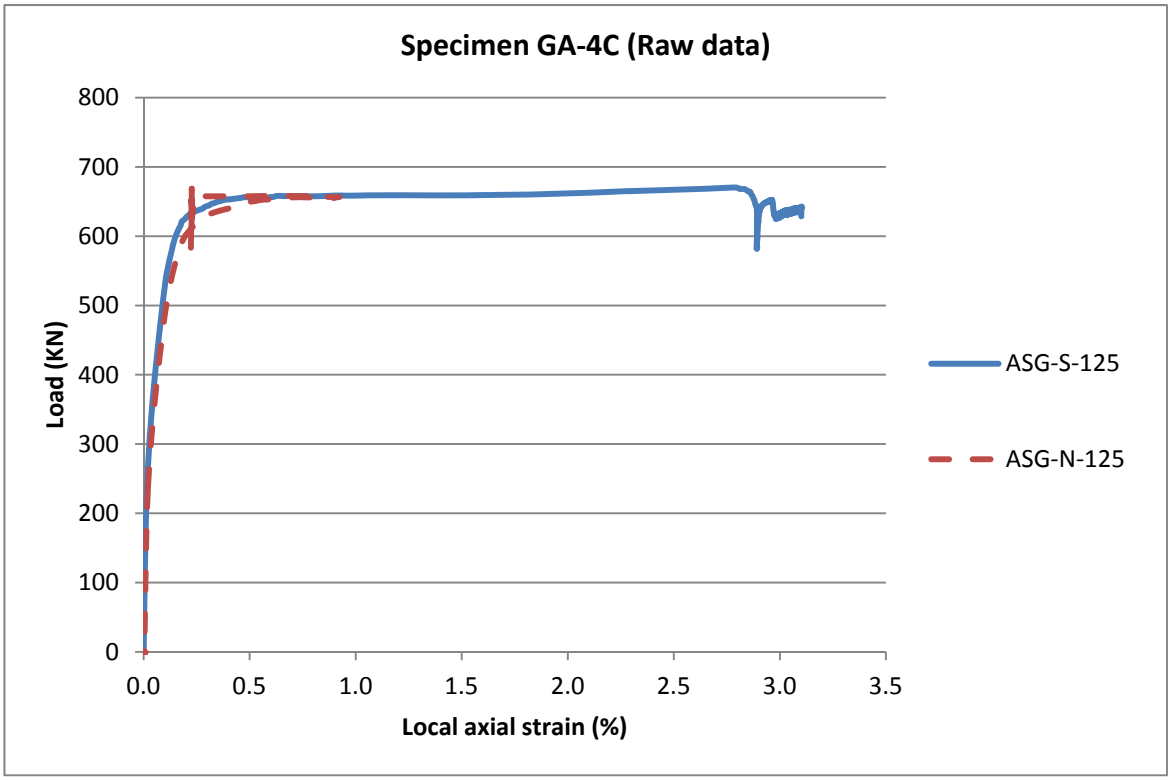

Figure 63: Load/local-axial-strain relationship

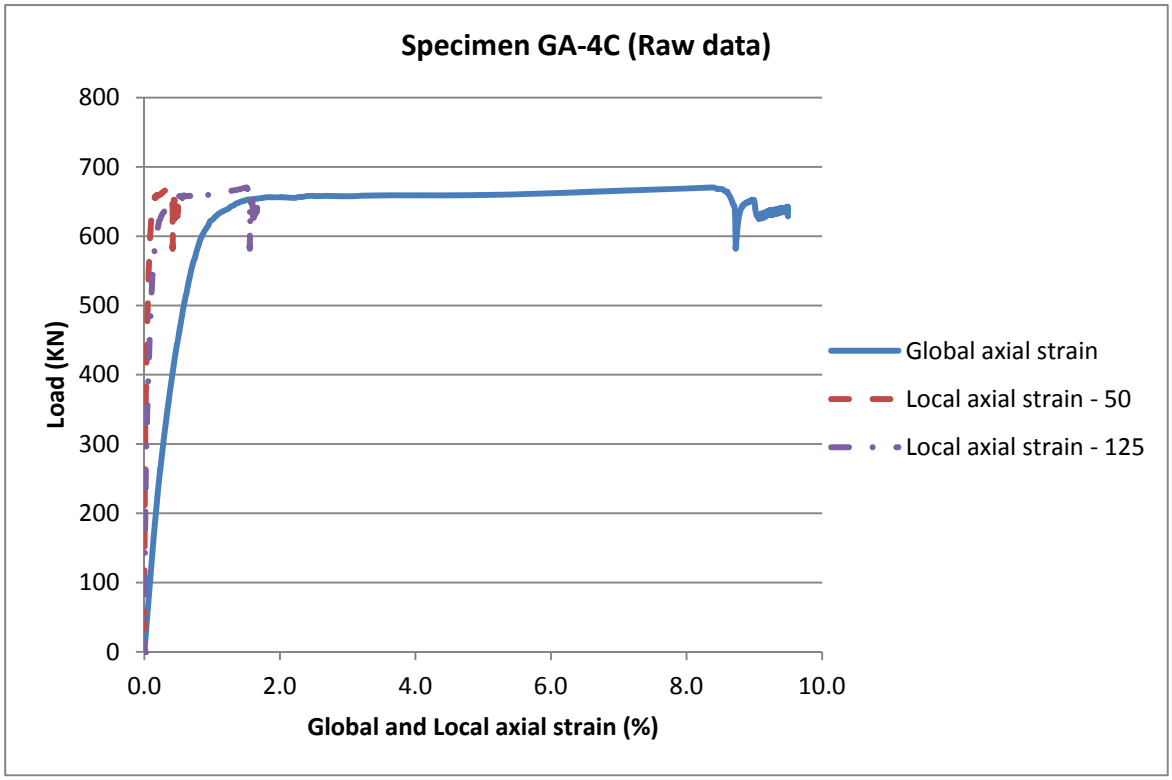

Figure 64: Load/global and load/local strains relationship

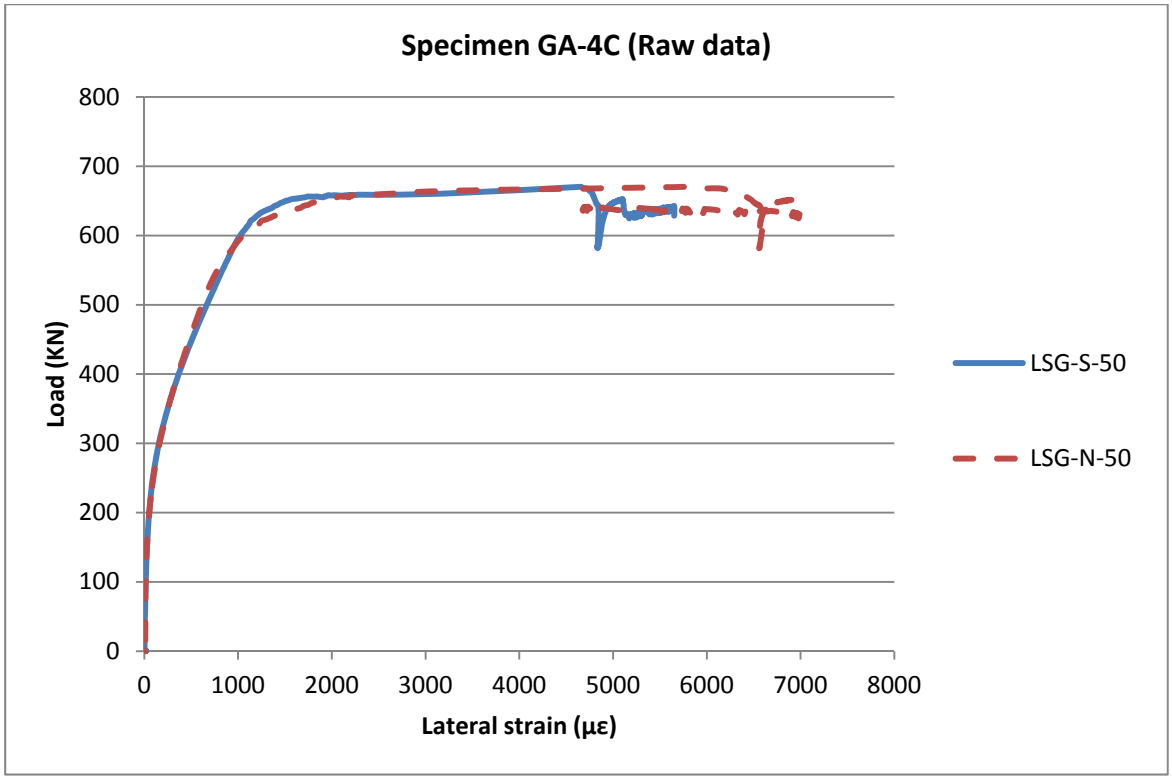

Figure 65: Load/lateral-strain relationship

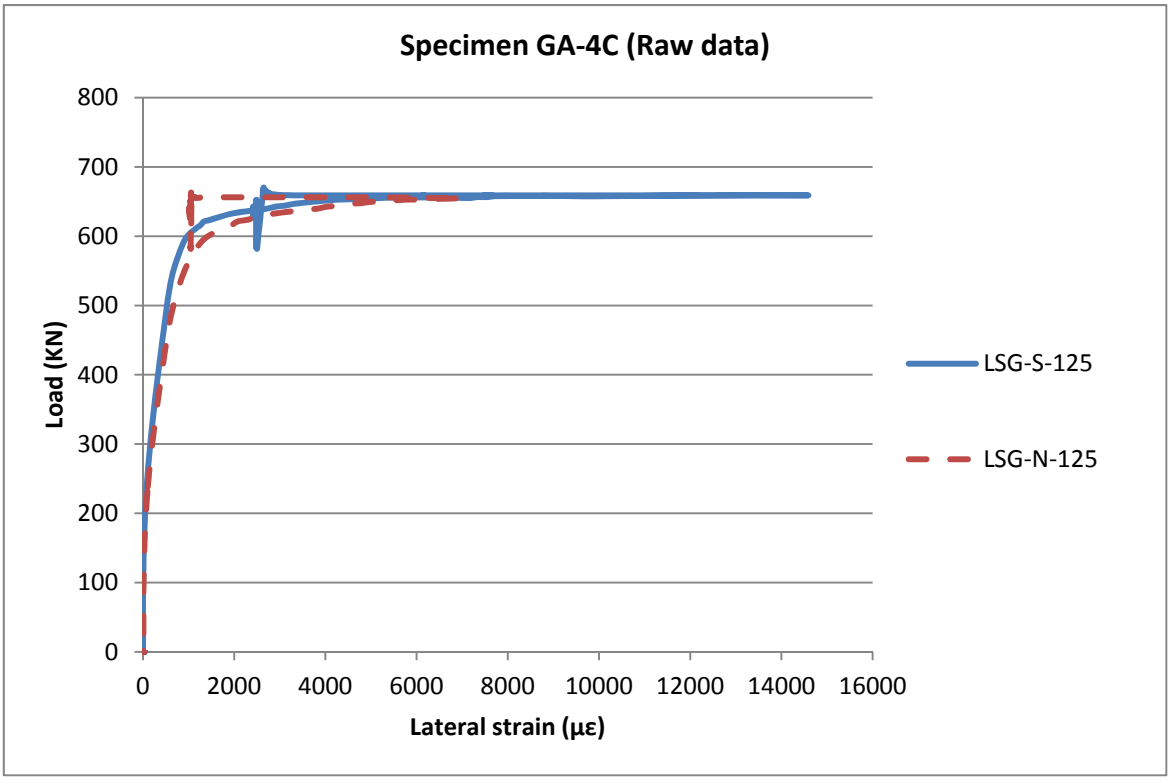

Figure 66: Load/lateral-strain relationship

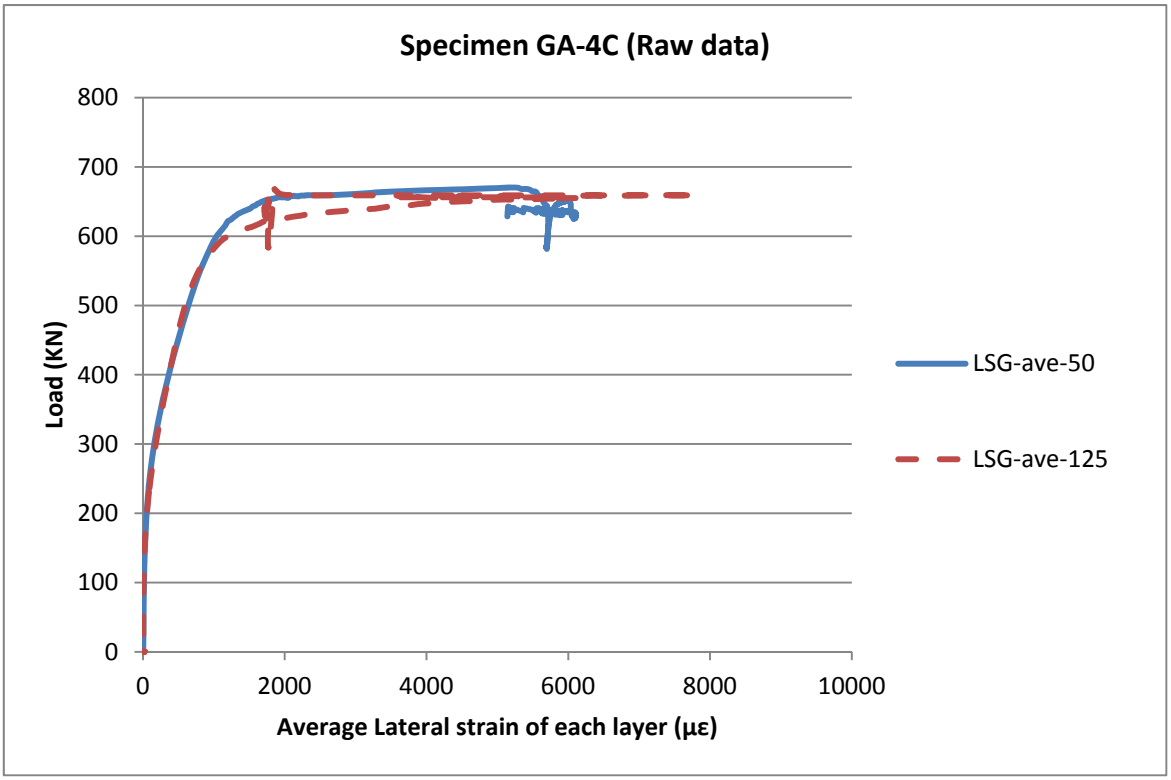

Figure 67: Load/lateral-strain relationship

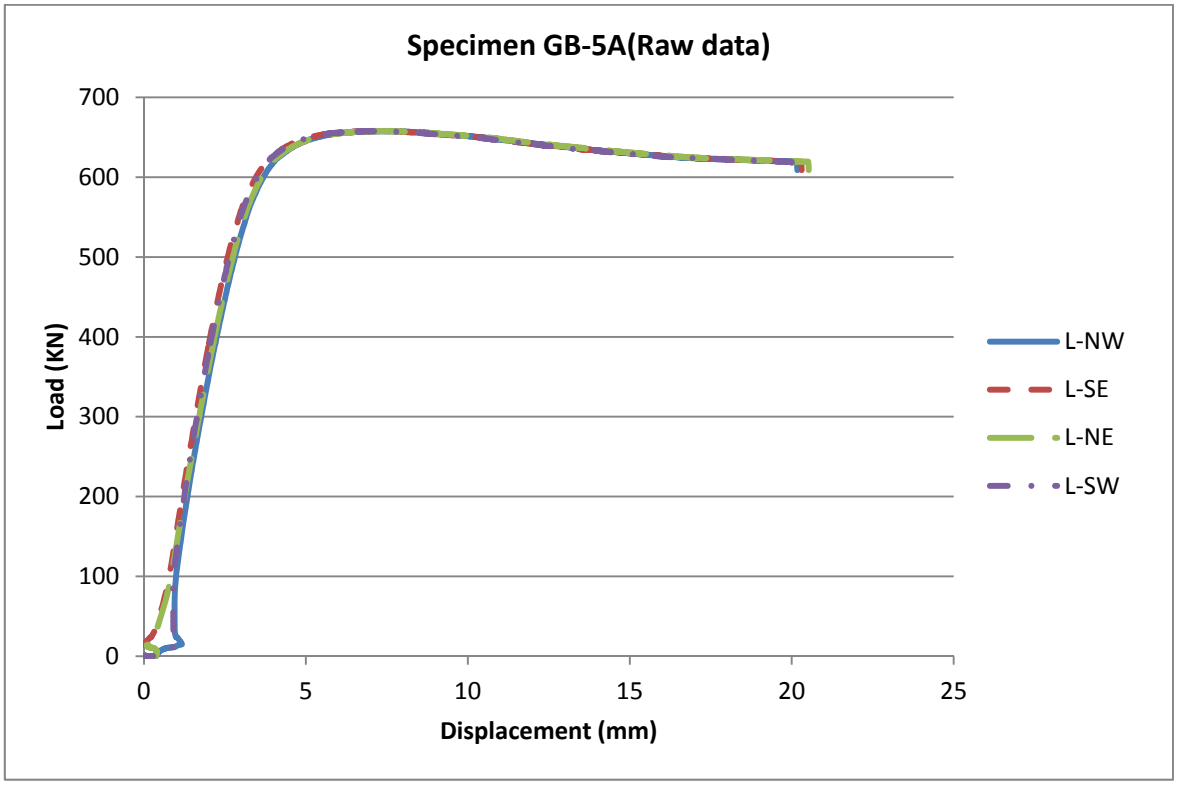

Figure 68: Load/axial-displacement relationship

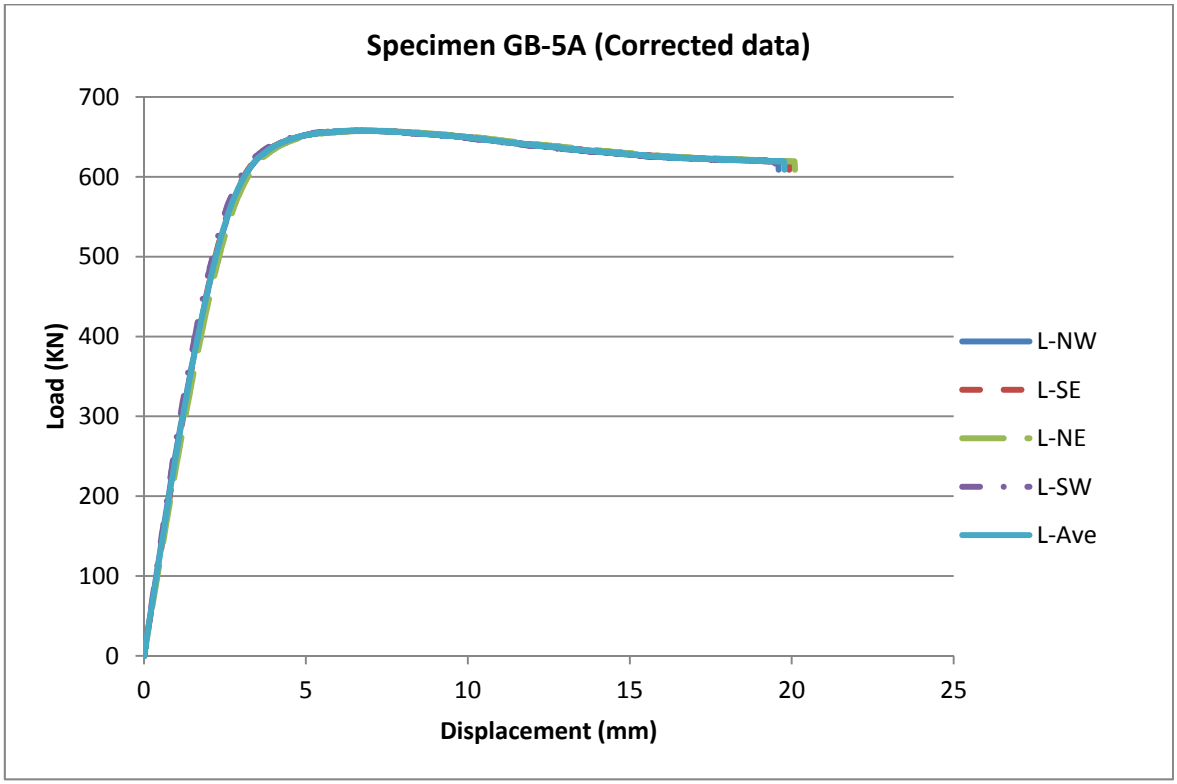

Figure 69: Load/axial-displacement relationship

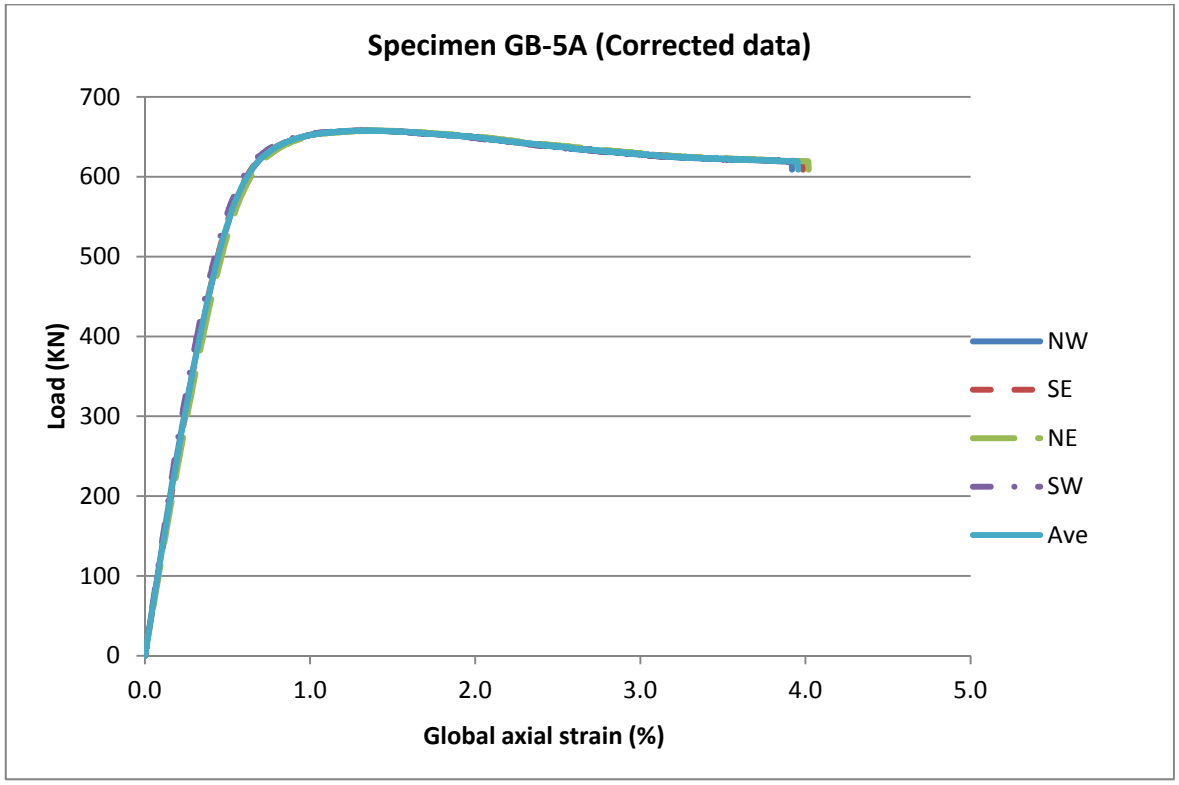

Figure 70: Load/global-axial-strain relationship

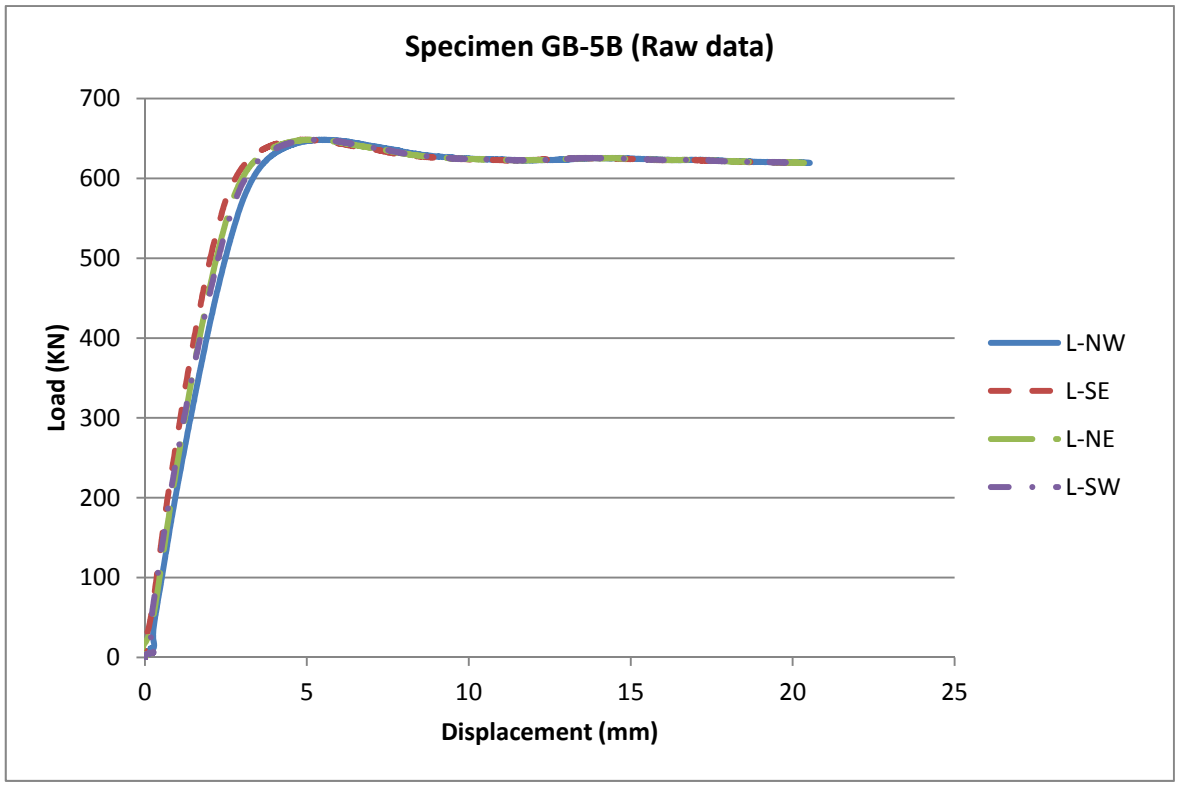

Figure 71: Load/axial-displacement relationship

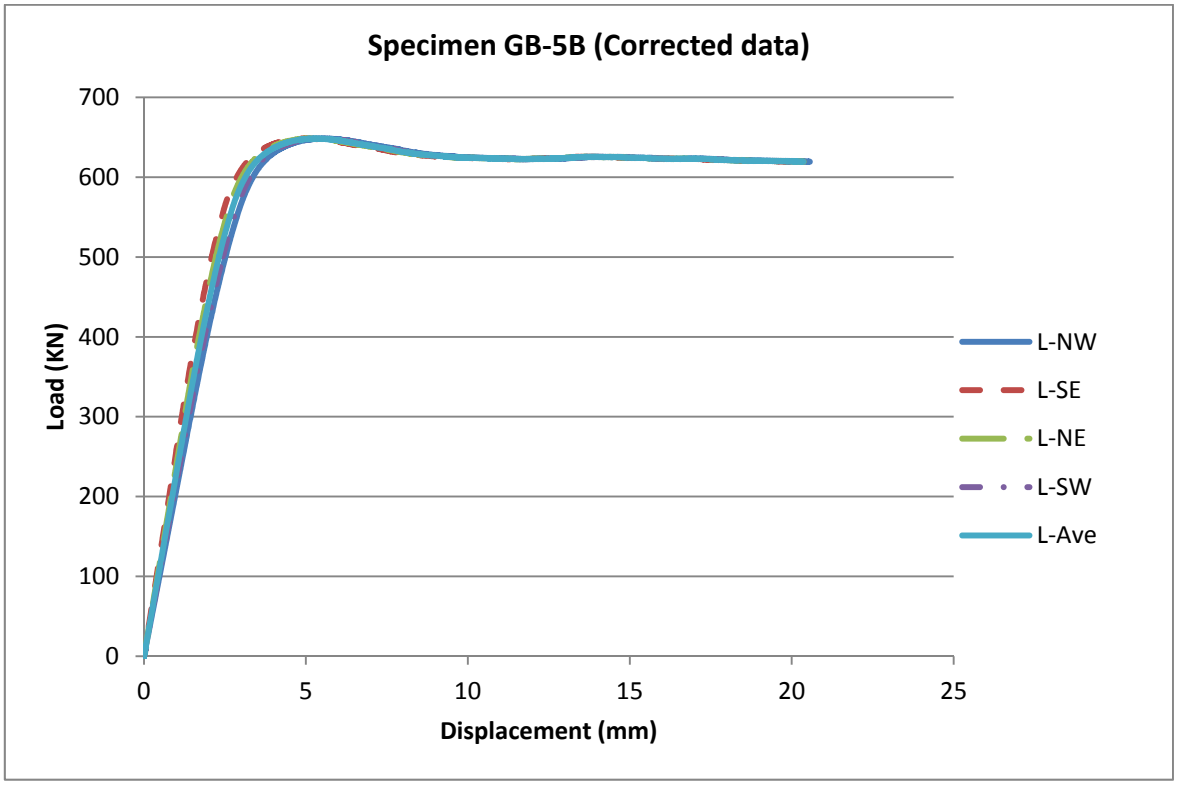

Figure 72: Load/axial-displacement relationship

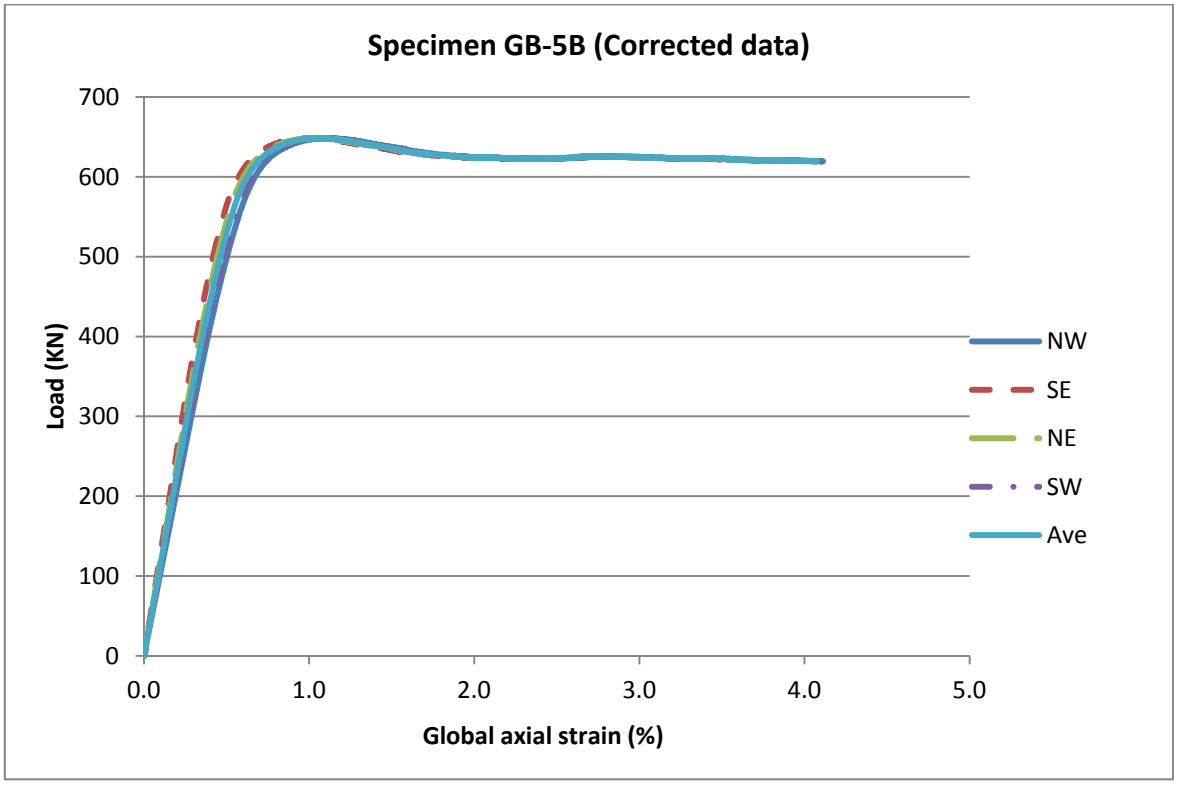

Figure 73: Load/global-axial-strain relationship

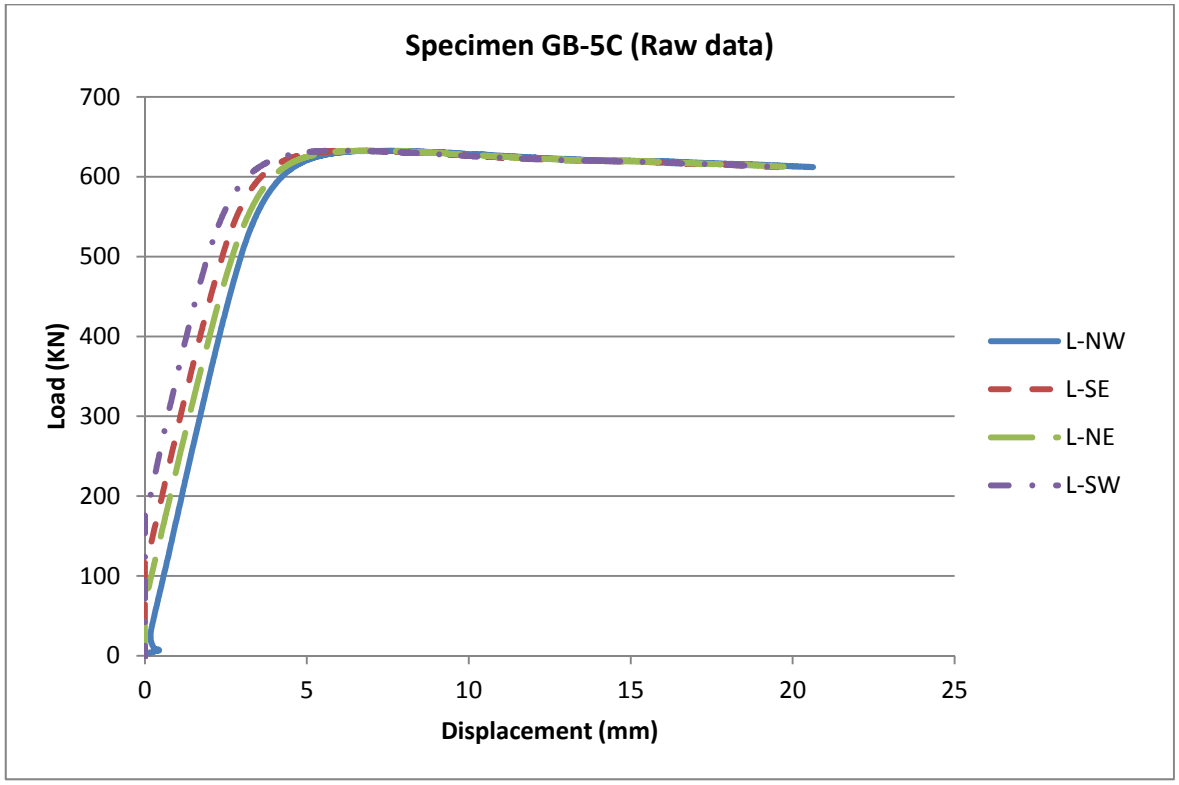

Figure 74: Load/axial-displacement relationship

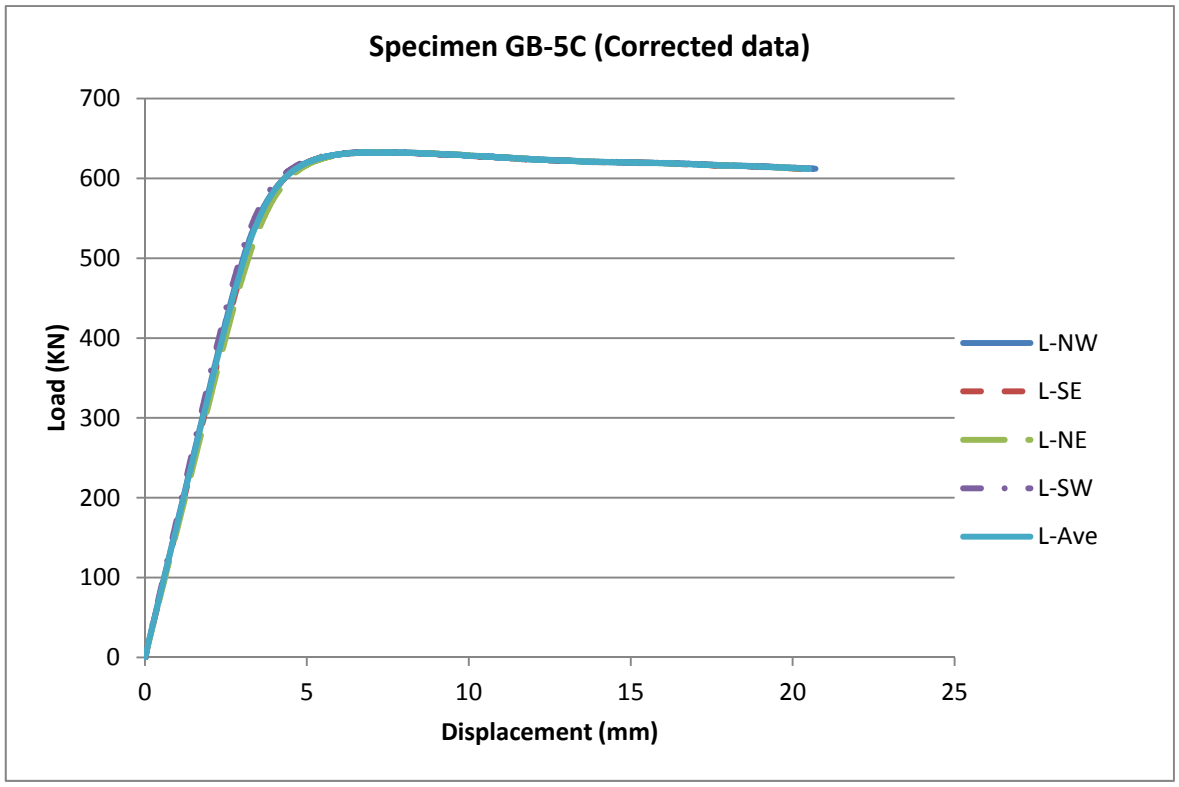

Figure 75: Load/axial-displacement relationship

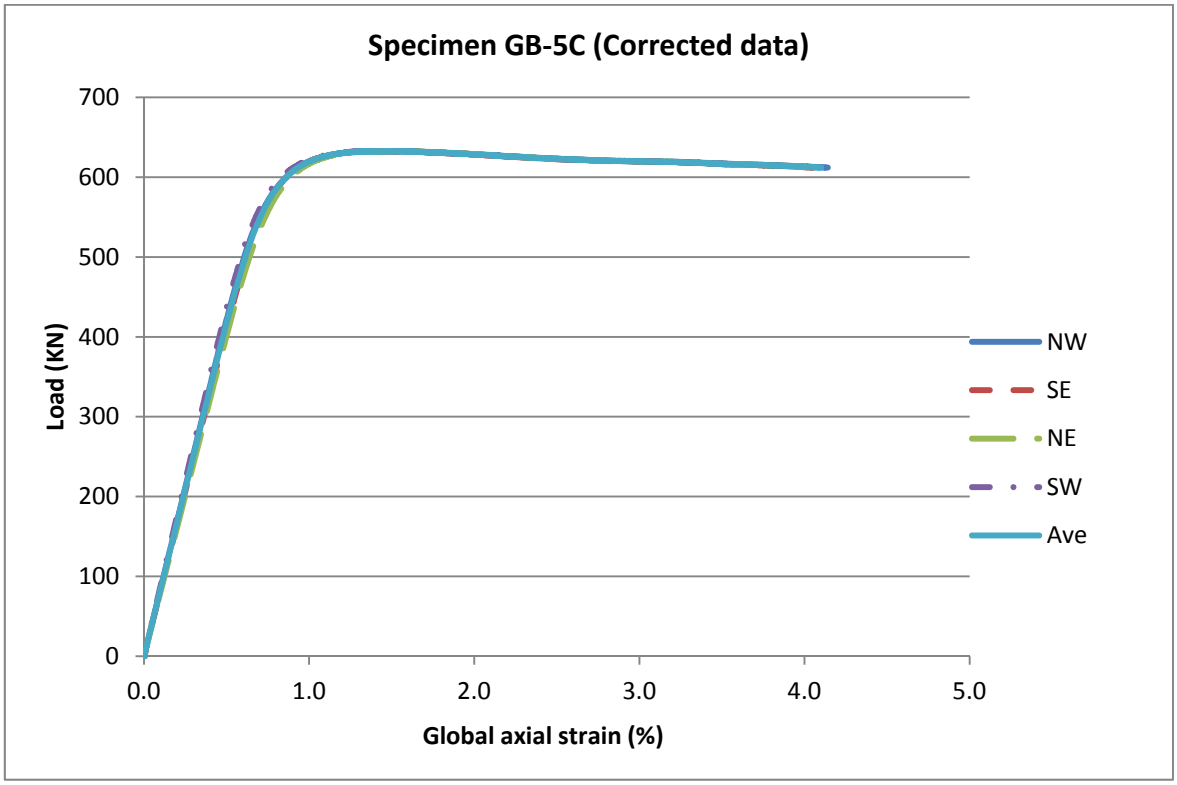

Figure 76: Load/global-axial-strain relationship

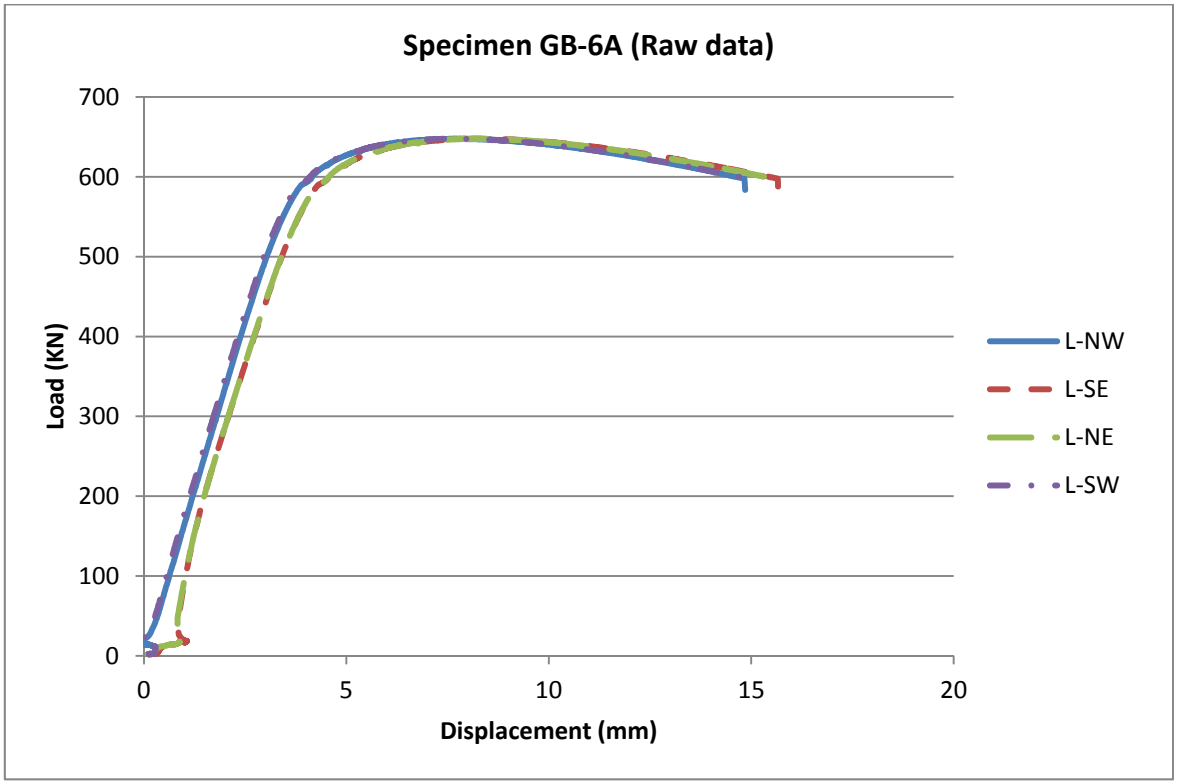

Figure 77: Load/axial-displacement relationship

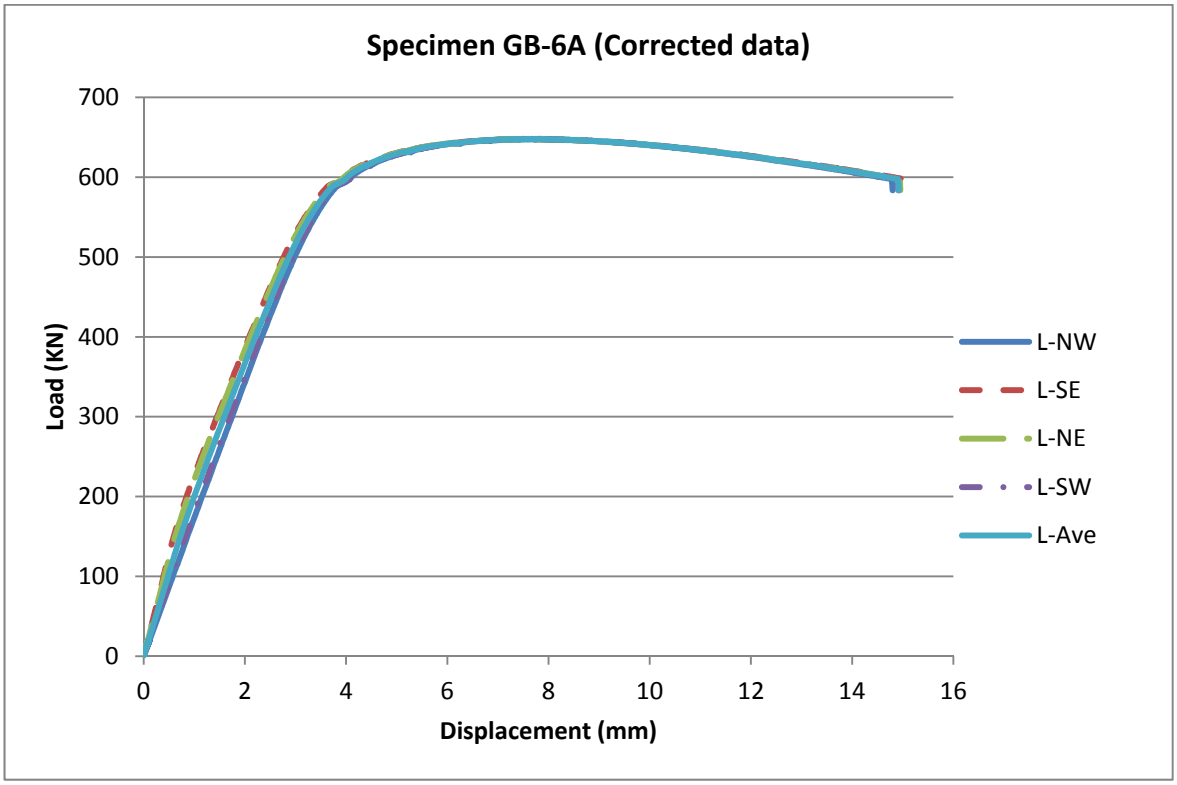

Figure 78: Load/axial-displacement relationship

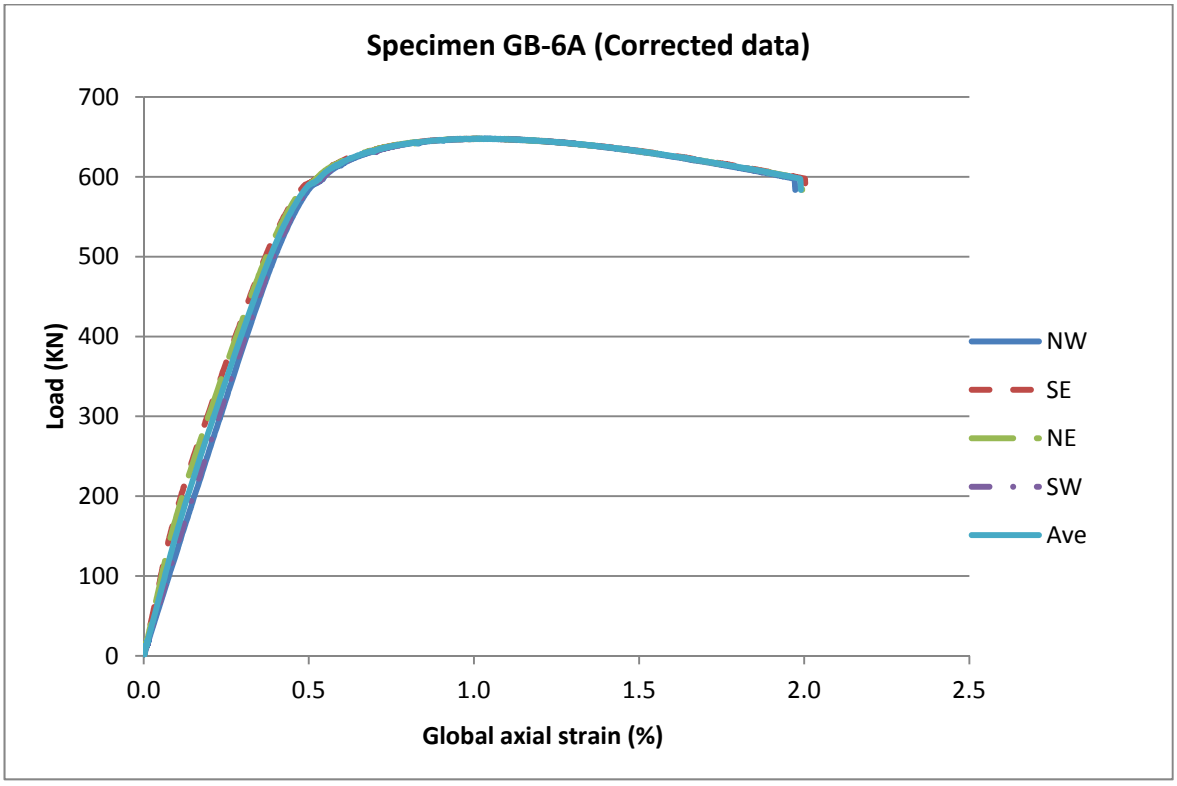

Figure 79: Load/global-axial-strain relationship

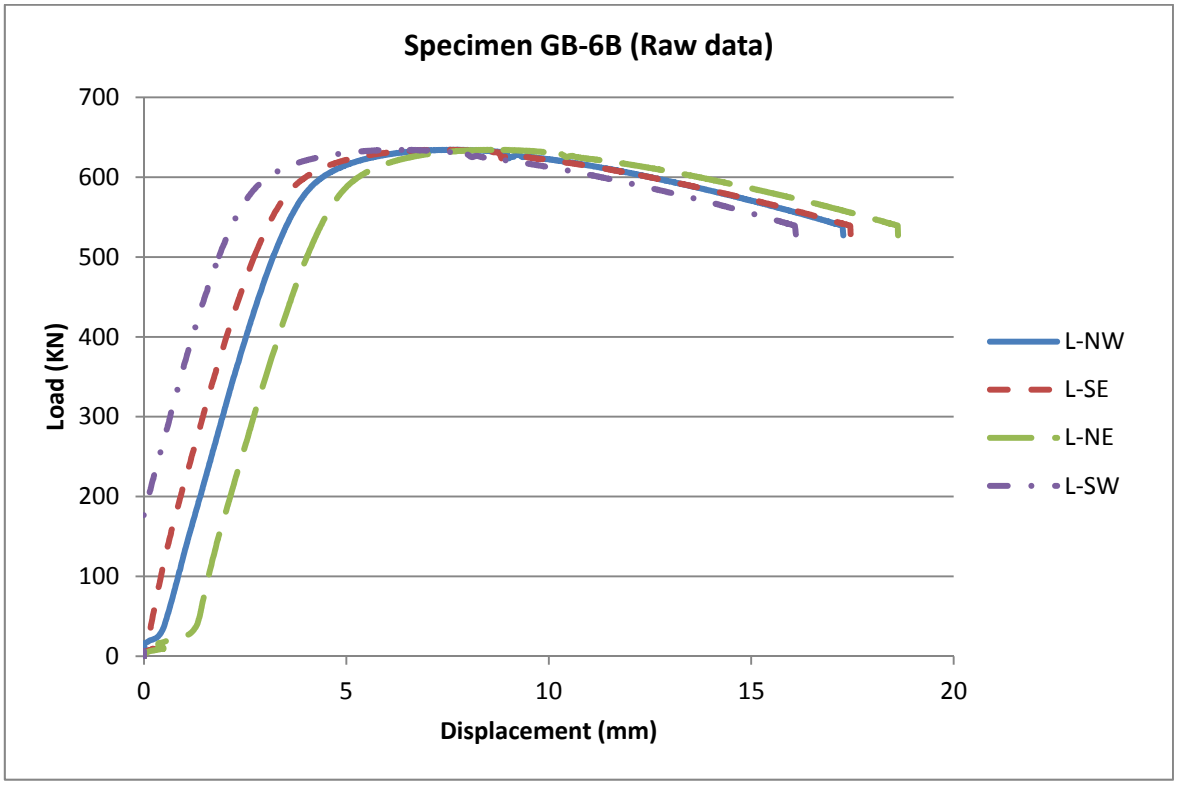

Figure 80: Load/axial-displacement relationship

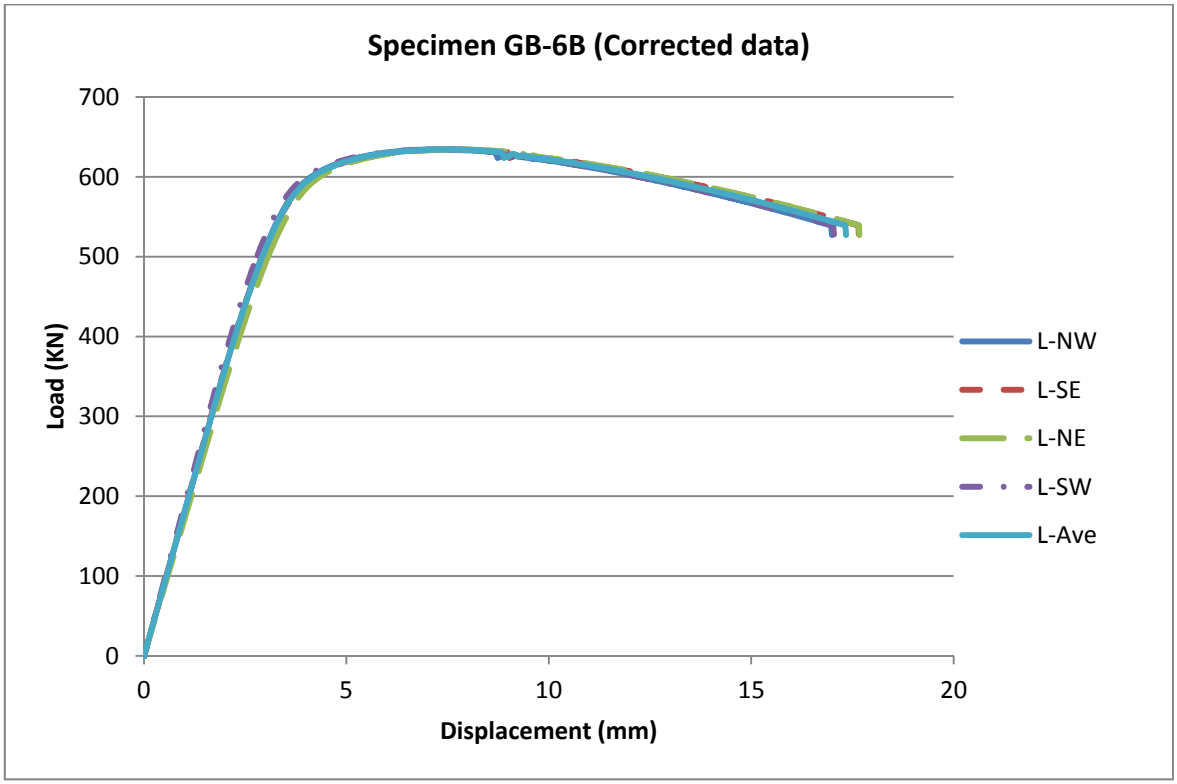

Figure 81: Load/axial-displacement relationship

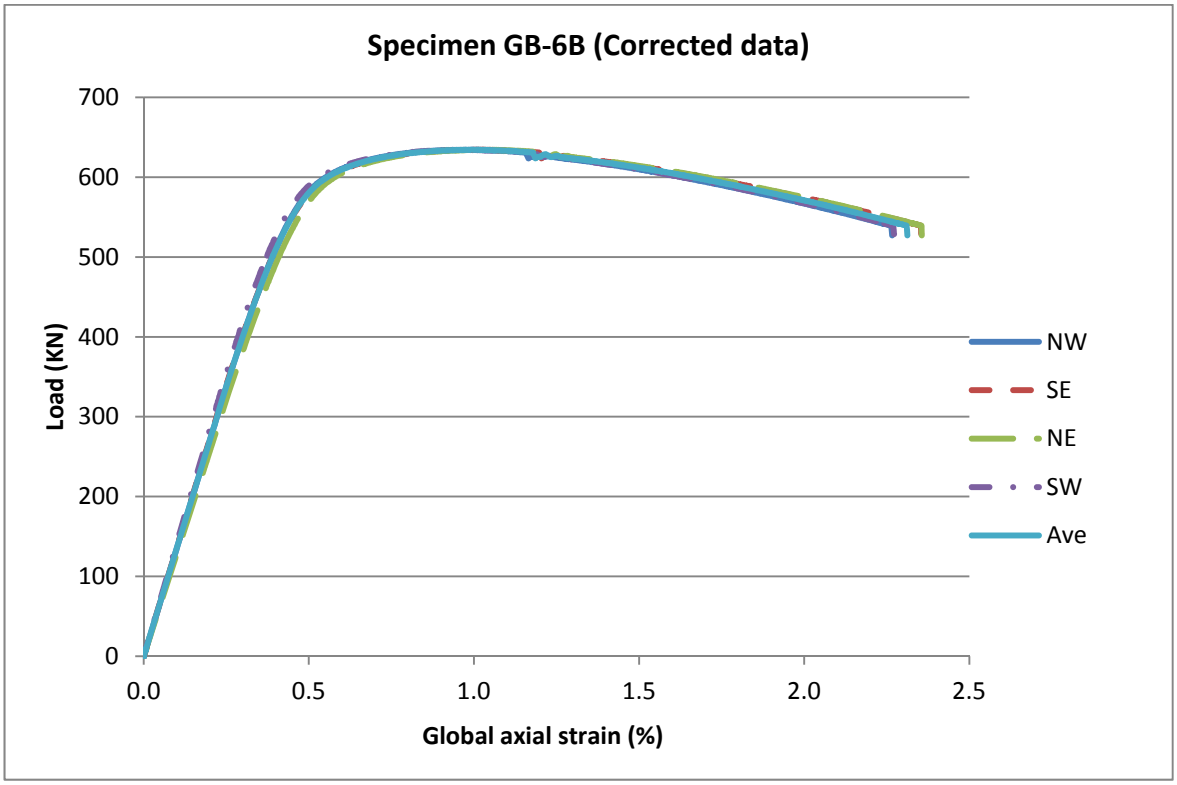

Figure 82: Load/global-axial-strain relationship

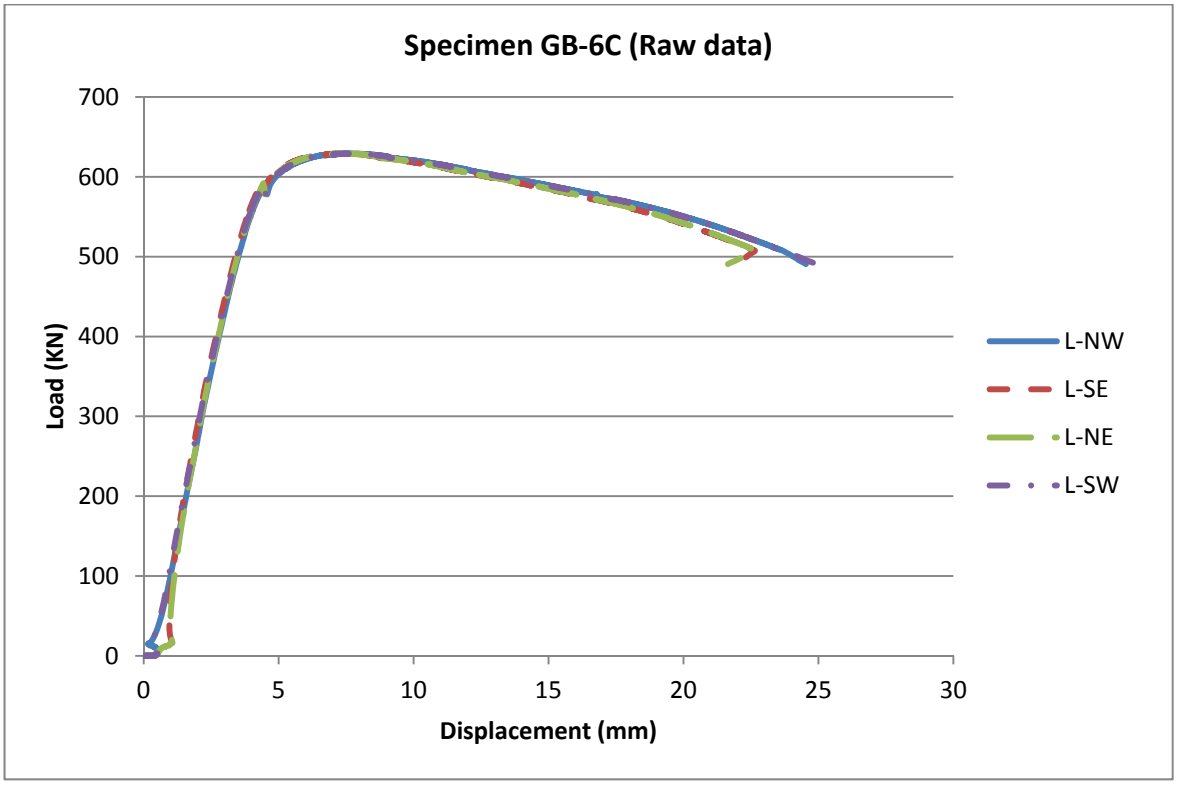

Figure 83: Load/axial-displacement relationship

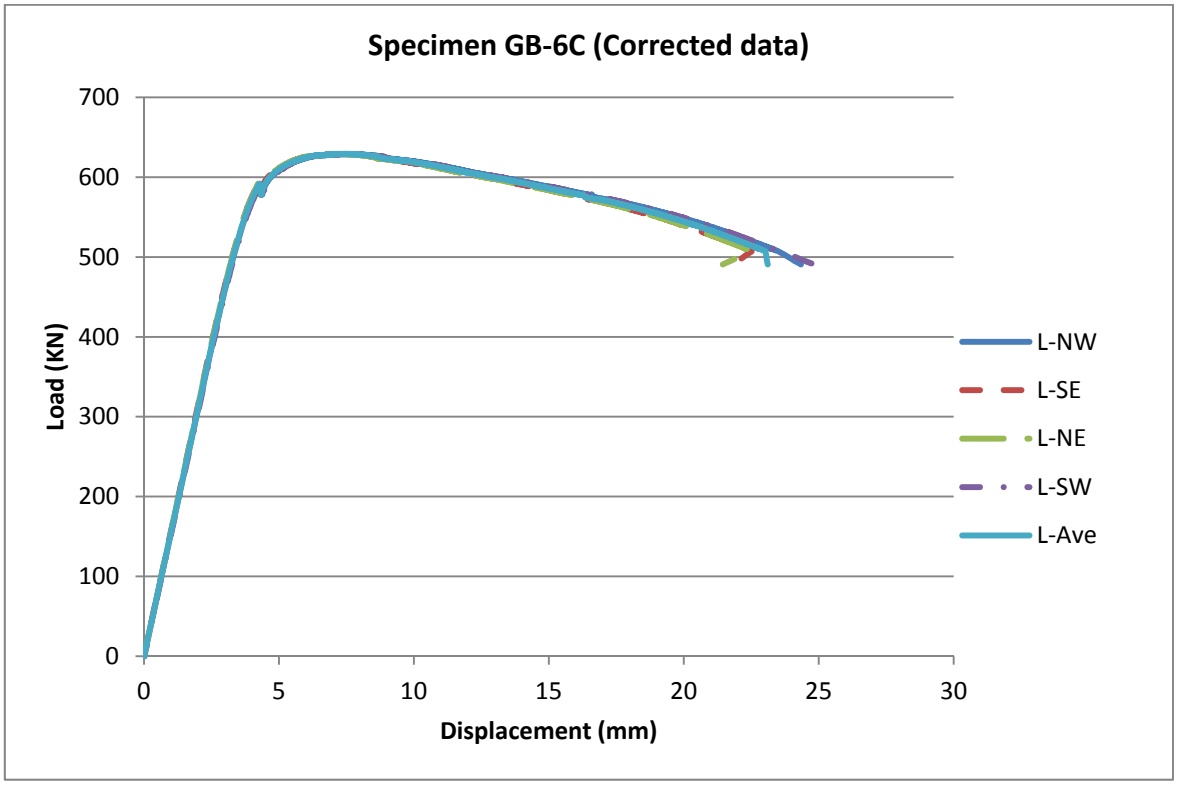

Figure 84: Load/axial-displacement relationship

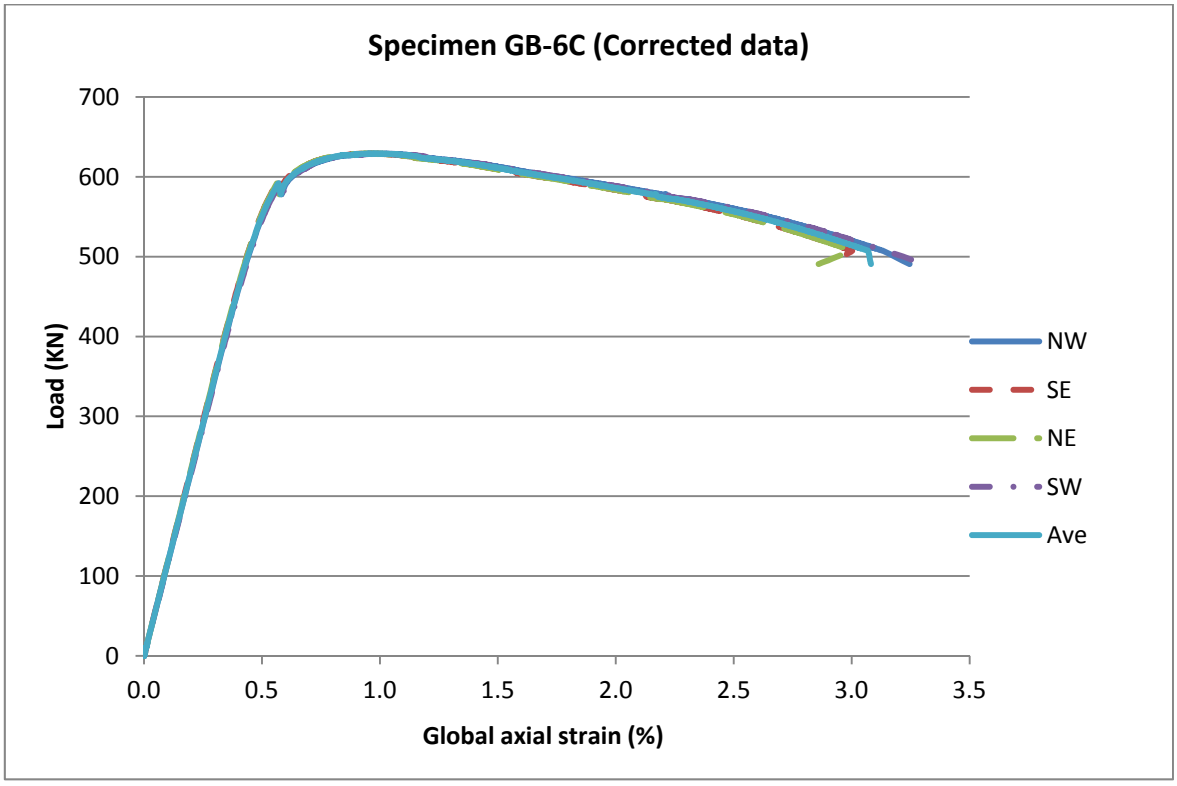

Figure 85: Load/global-axial-strain relationship

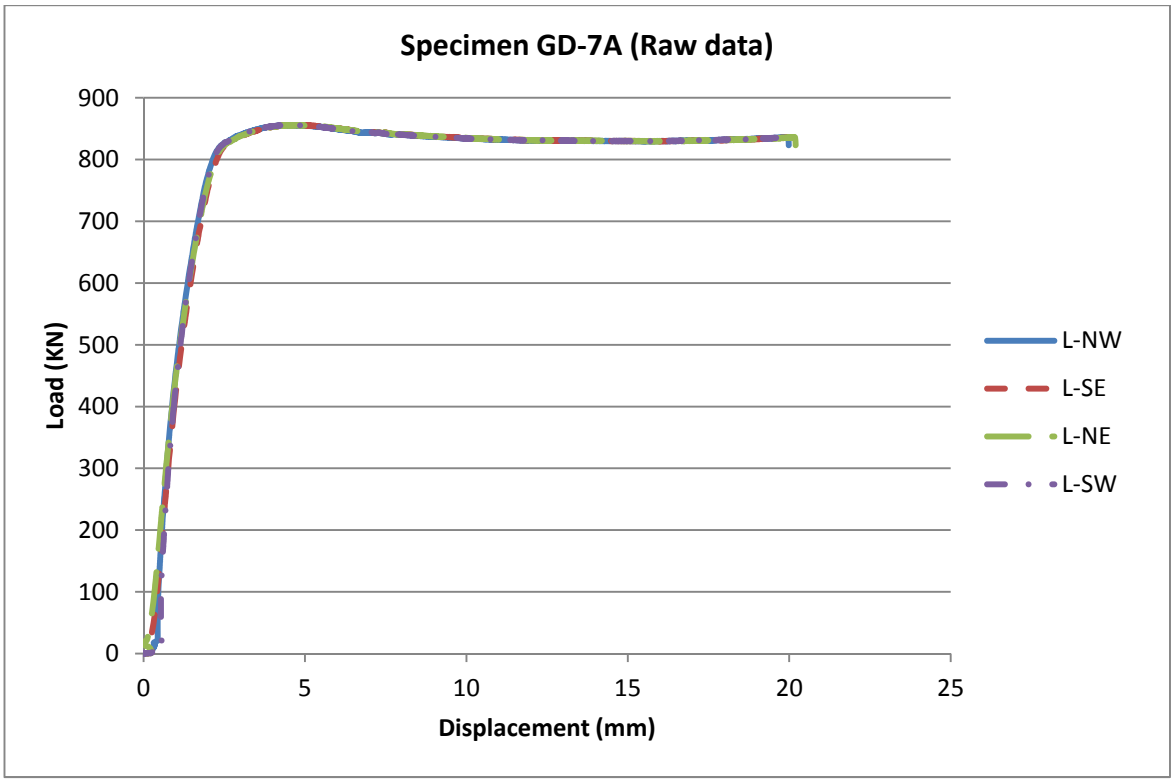

Figure 86: Load/axial-displacement relationship

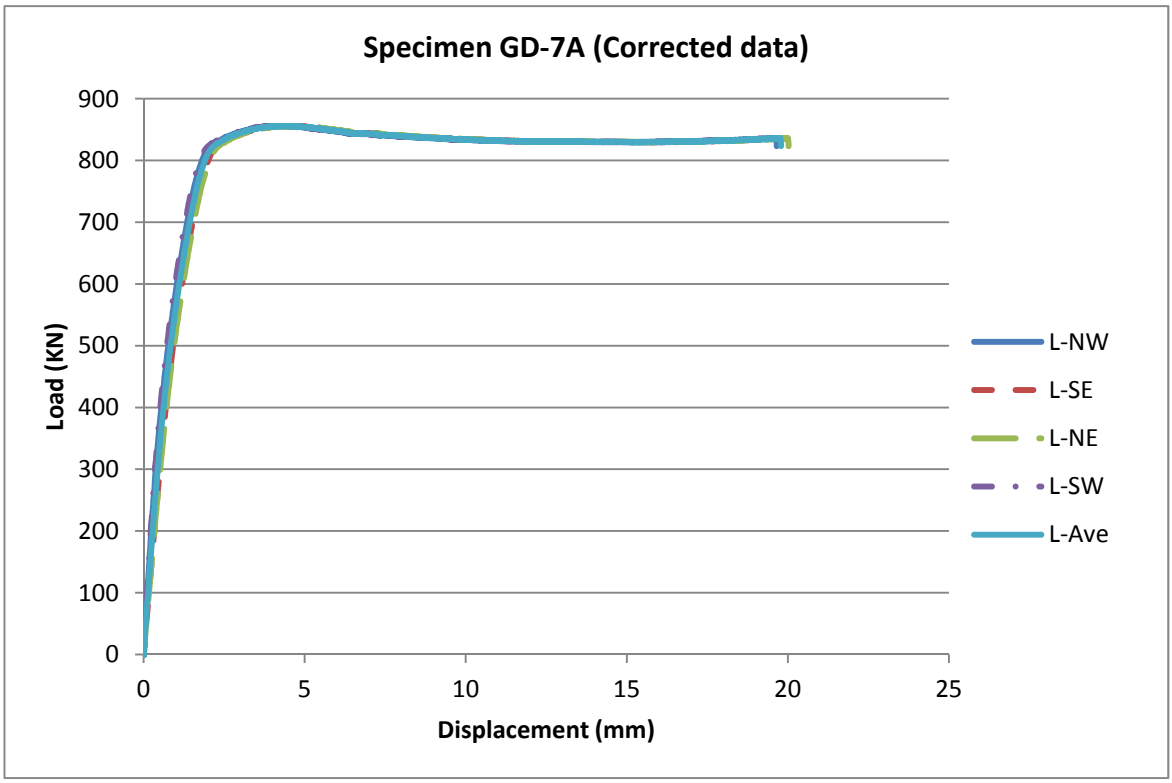

Figure 87: Load/axial-displacement relationship

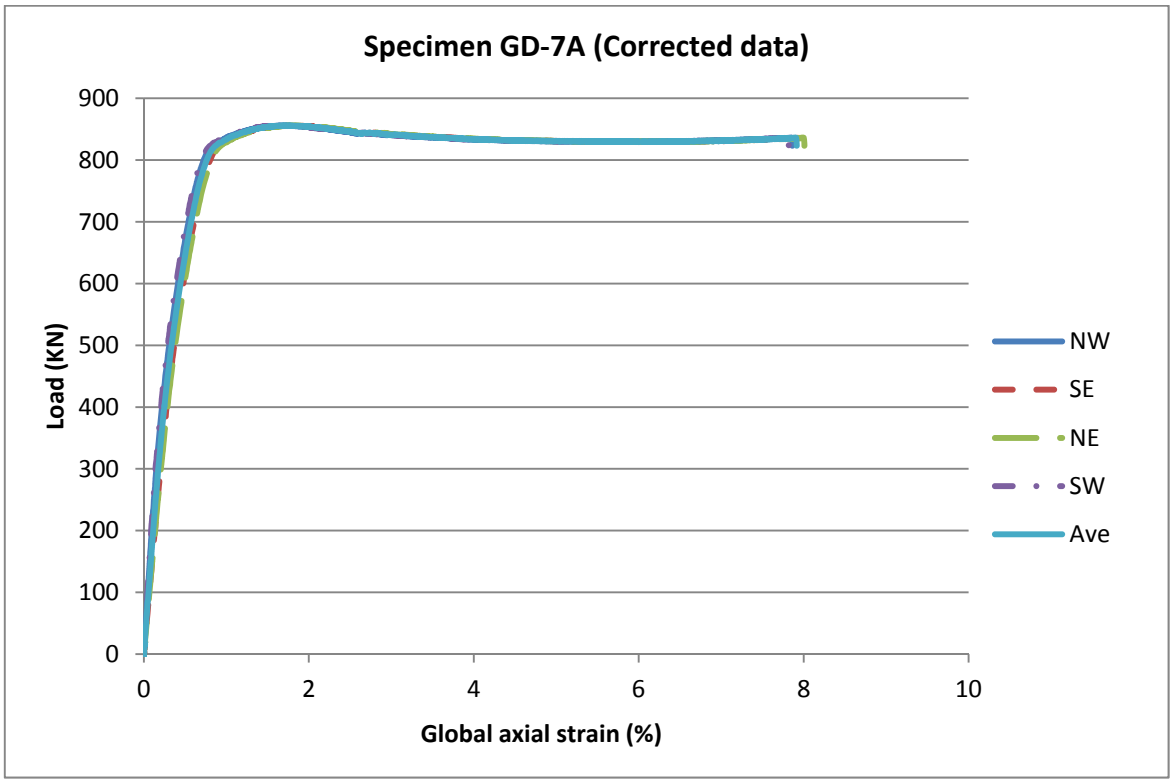

Figure 88: Load/global-axial-strain relationship

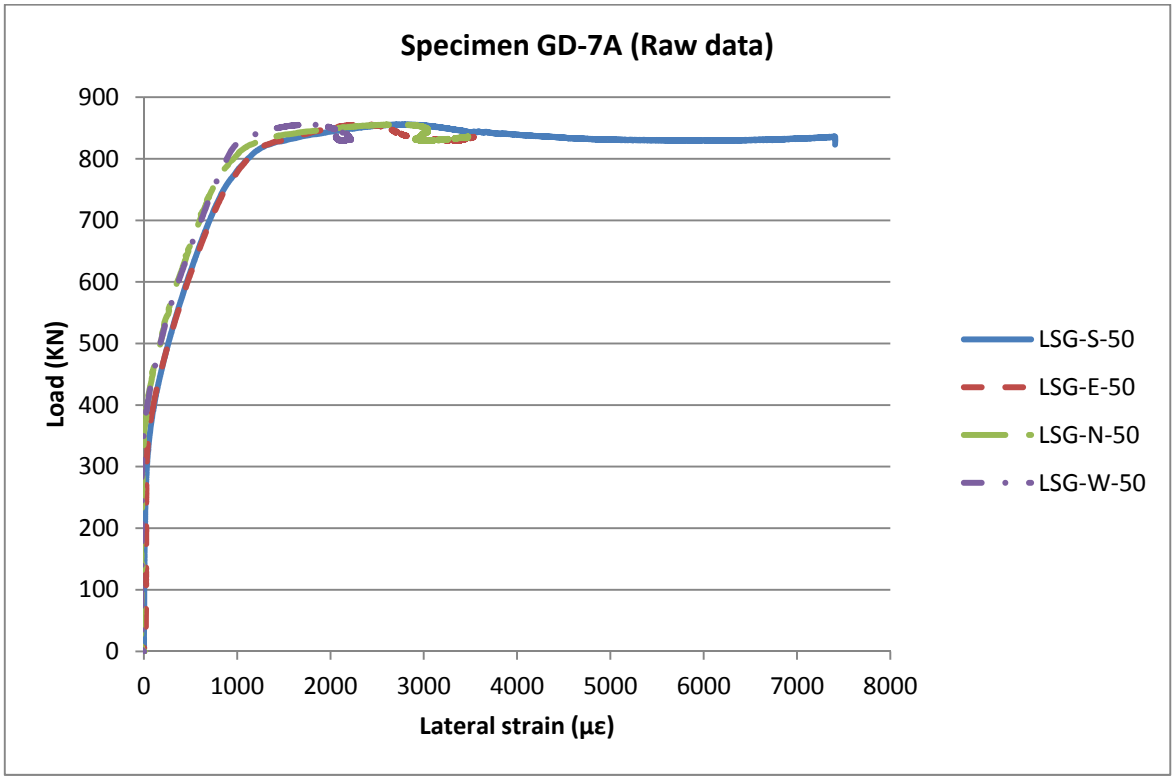

Figure 89: Load/lateral-strain relationship

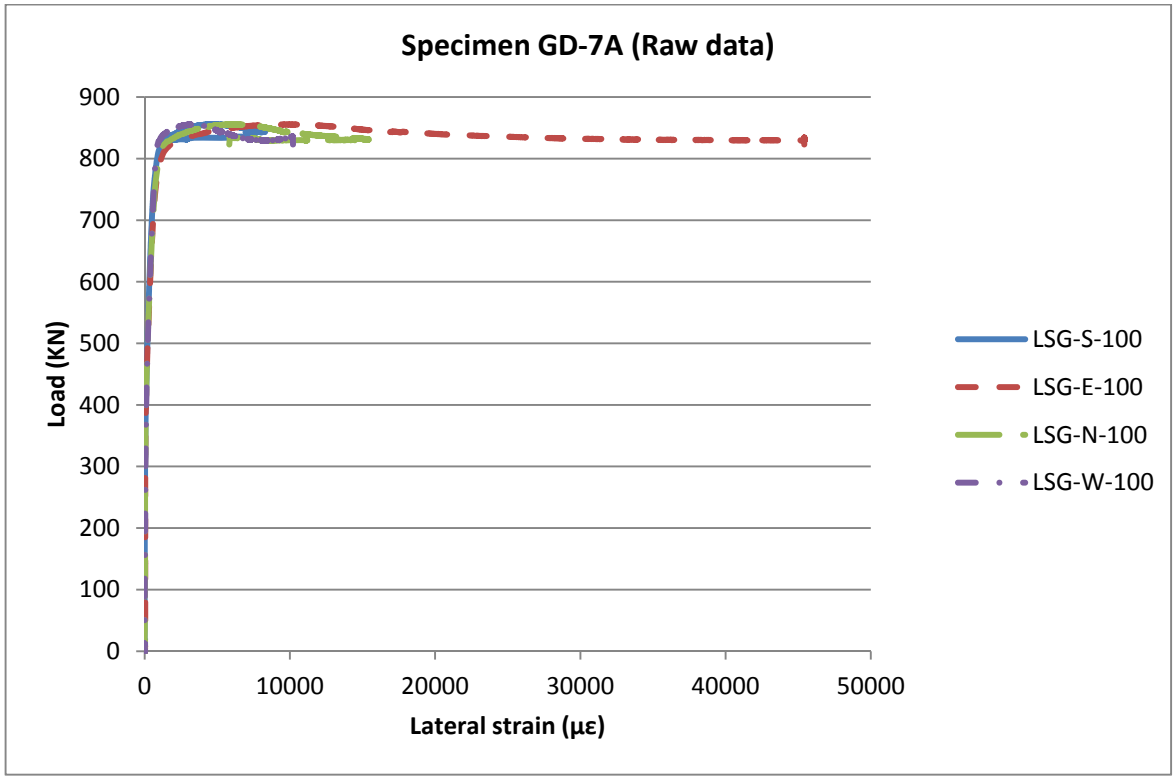

Figure 90: Load/lateral-strain relationship

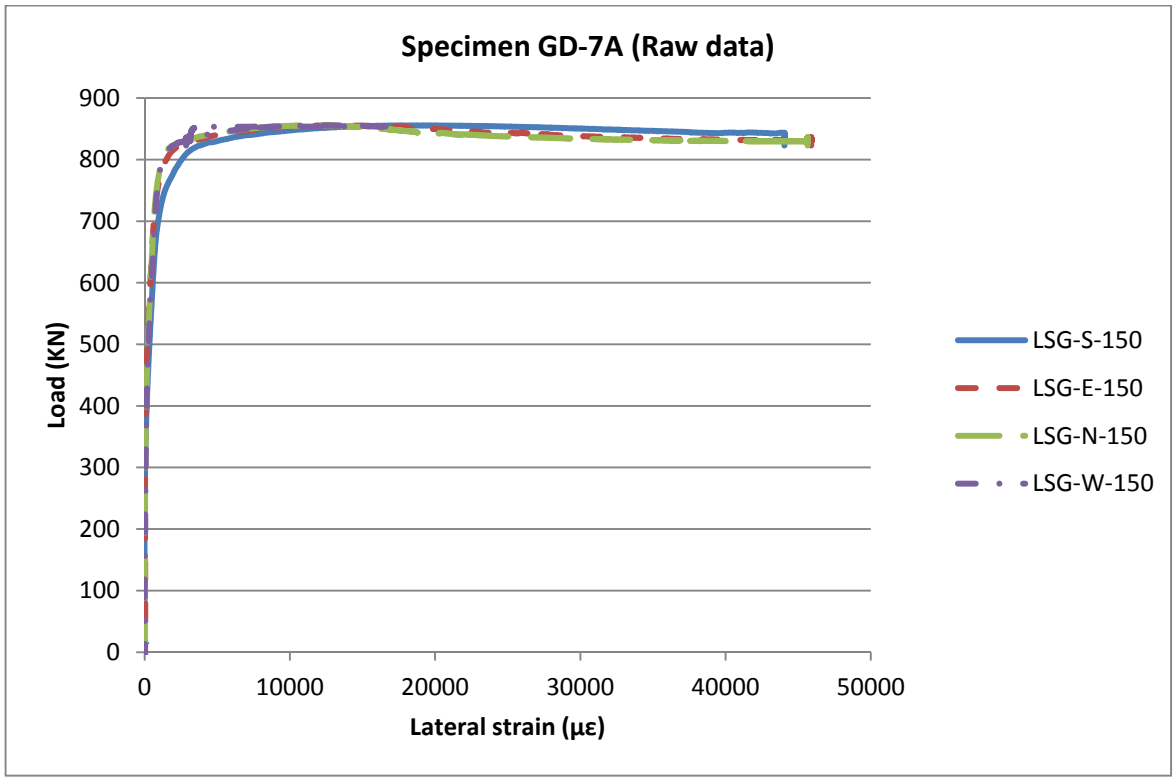

Figure 91: Load/lateral-strain relationship

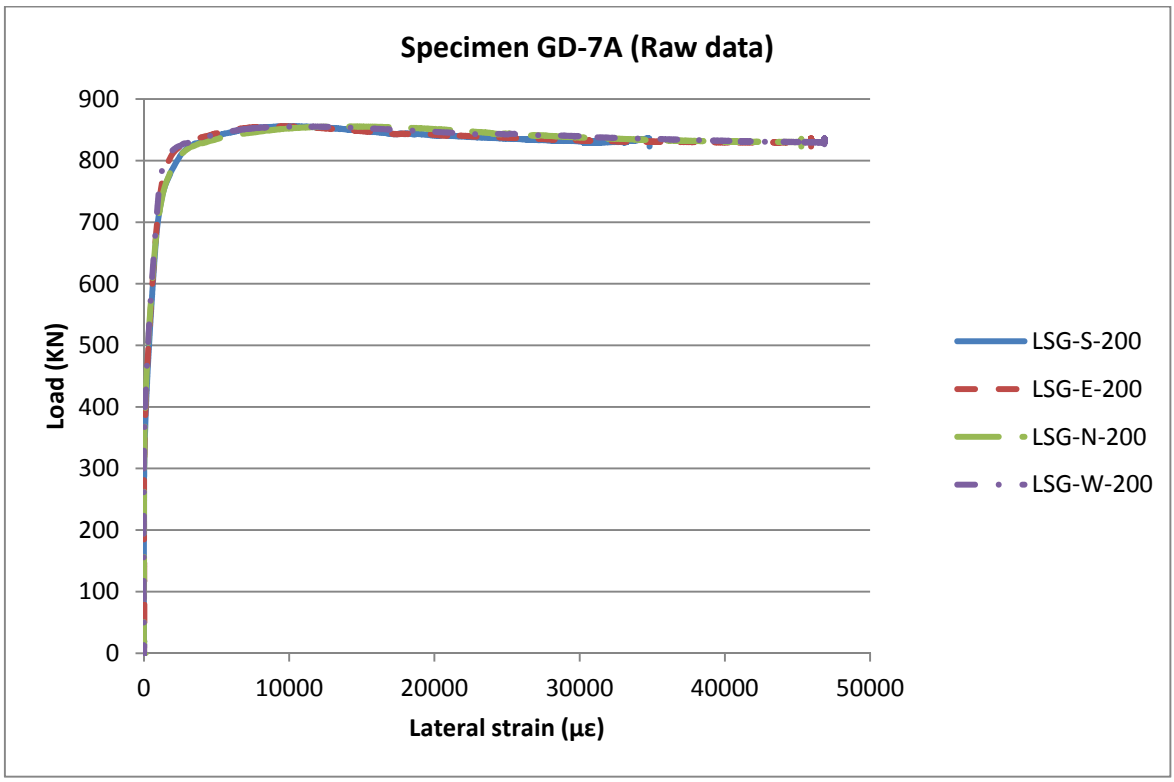

Figure 92: Load/lateral-strain relationship

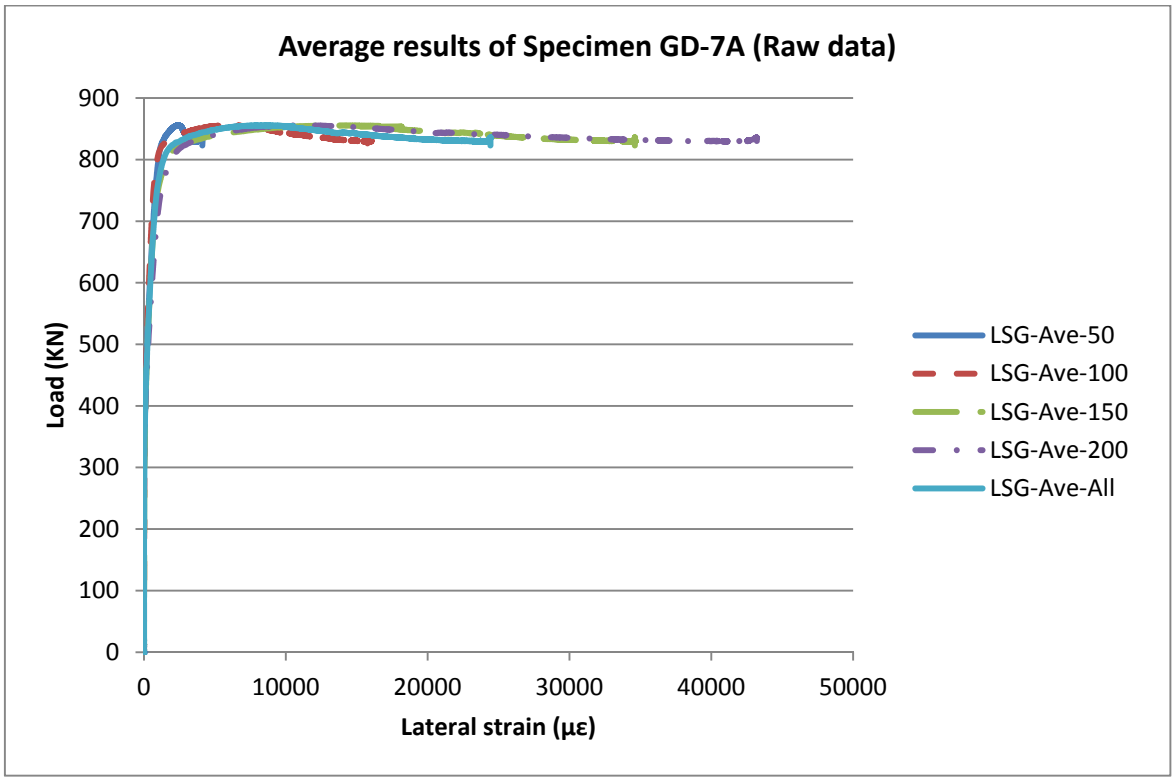

Figure 93: Load/lateral-strain relationship

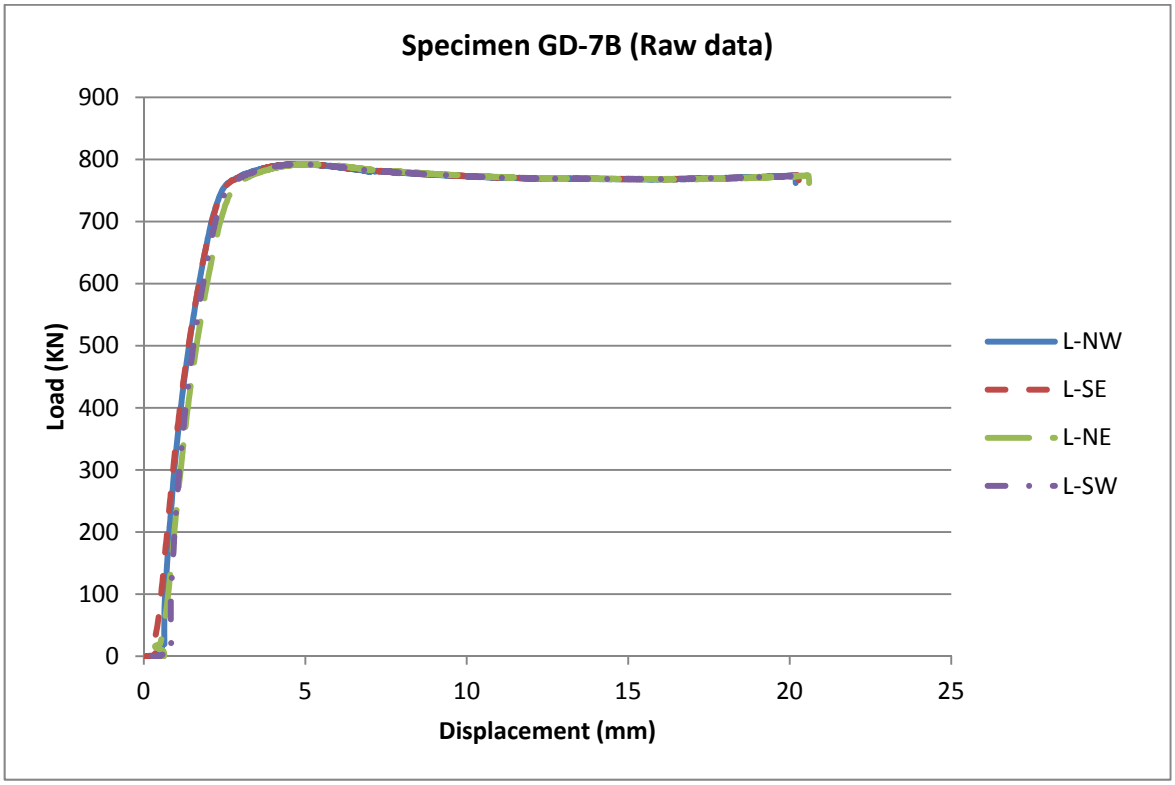

Figure 94: Load/axial-displacement relationship

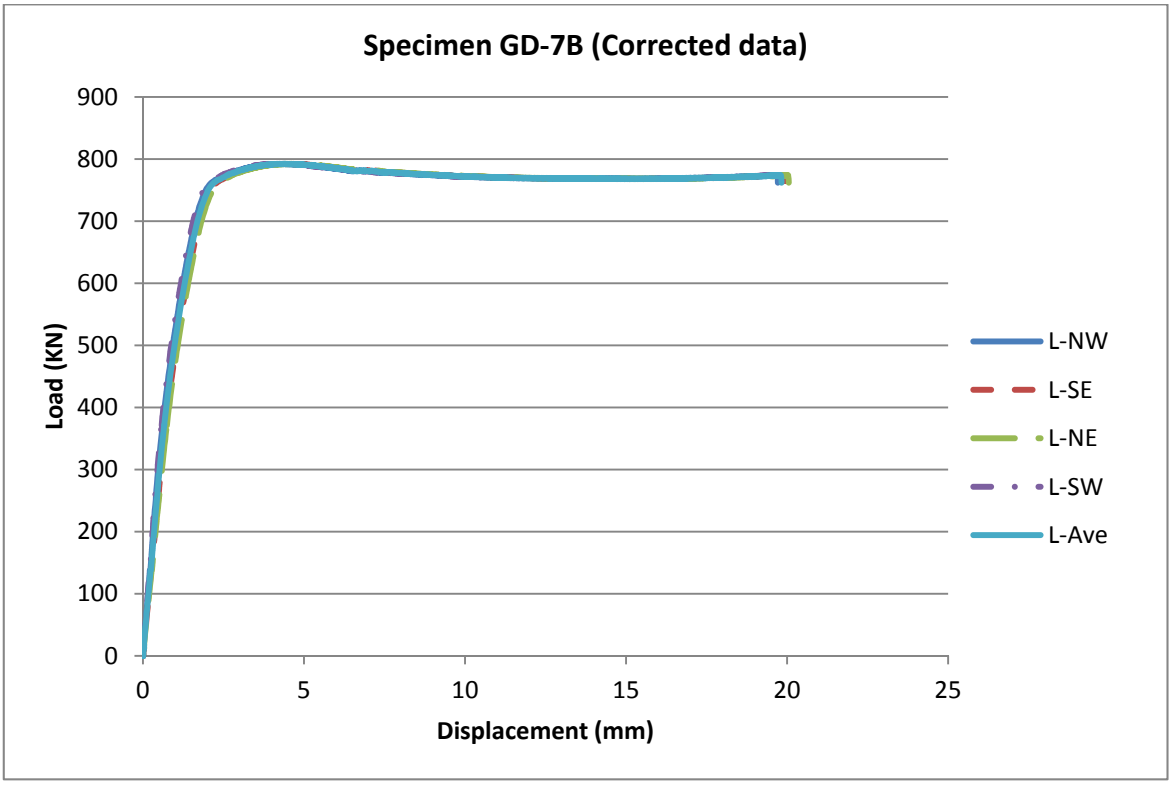

Figure 95: Load/axial-displacement relationship

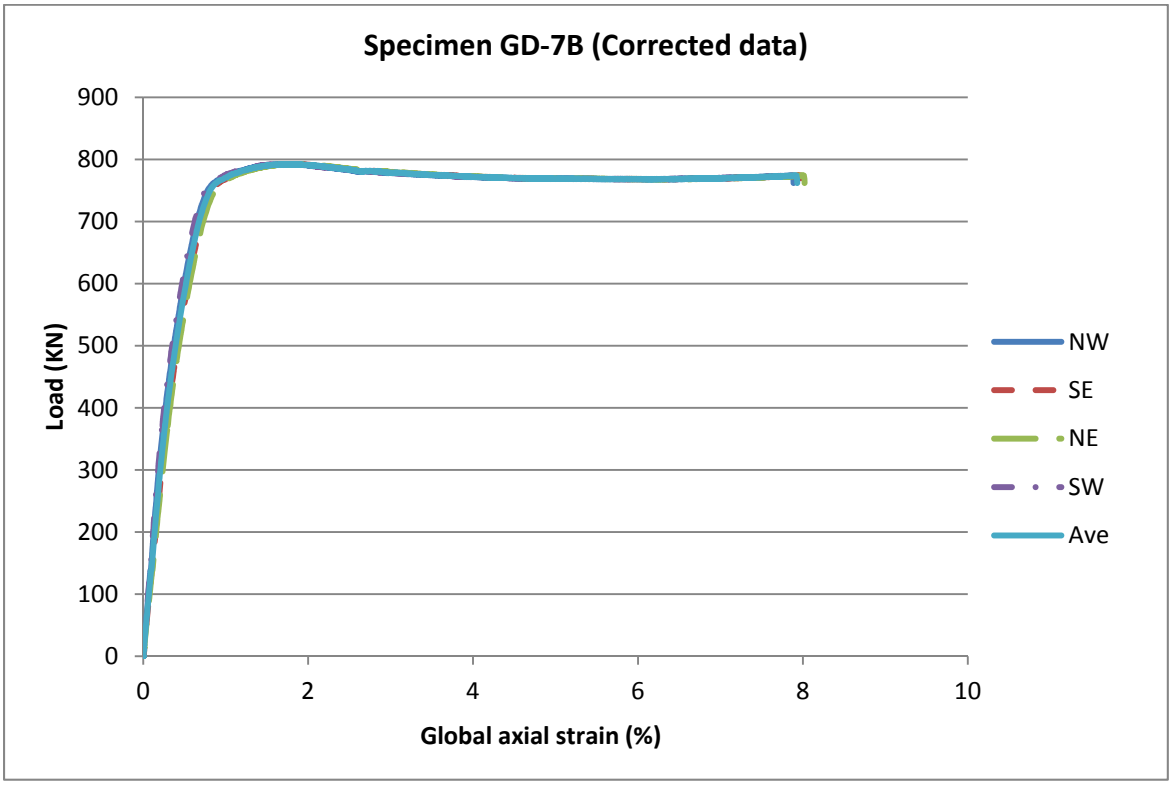

Figure 96: Load/global-axial-strain relationship

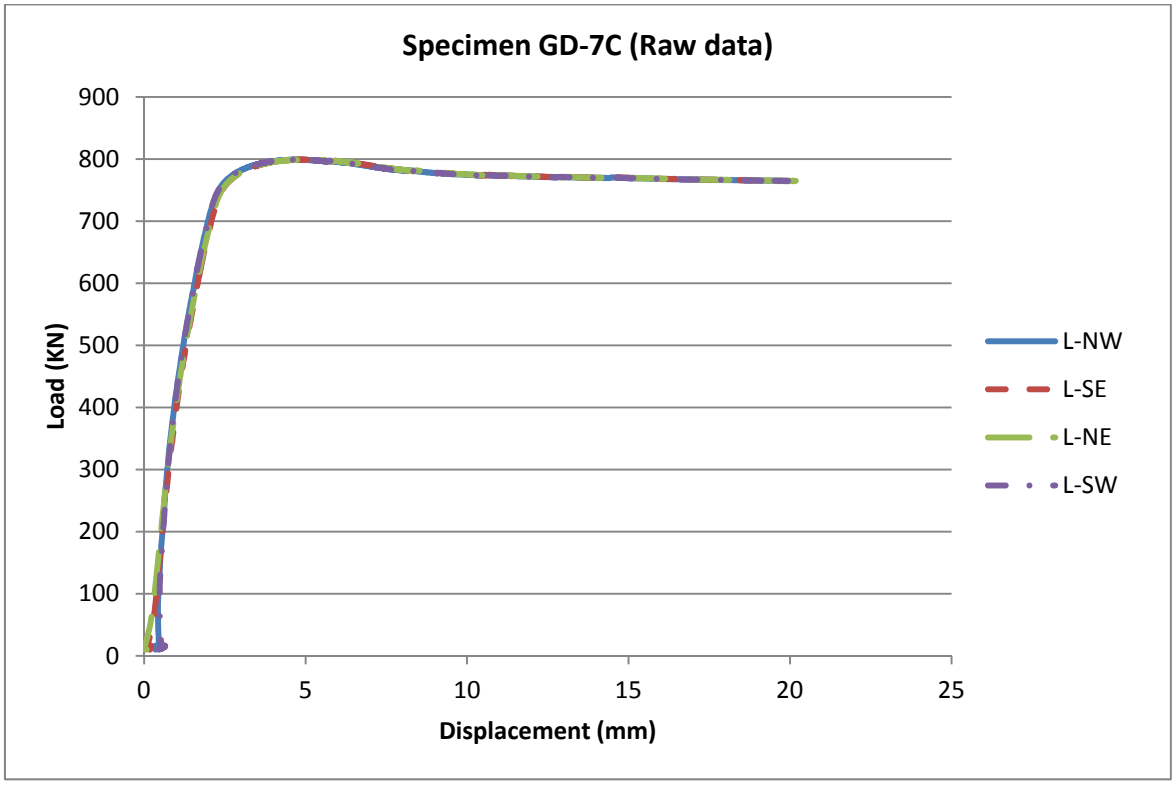

Figure 97: Load/axial-displacement relationship

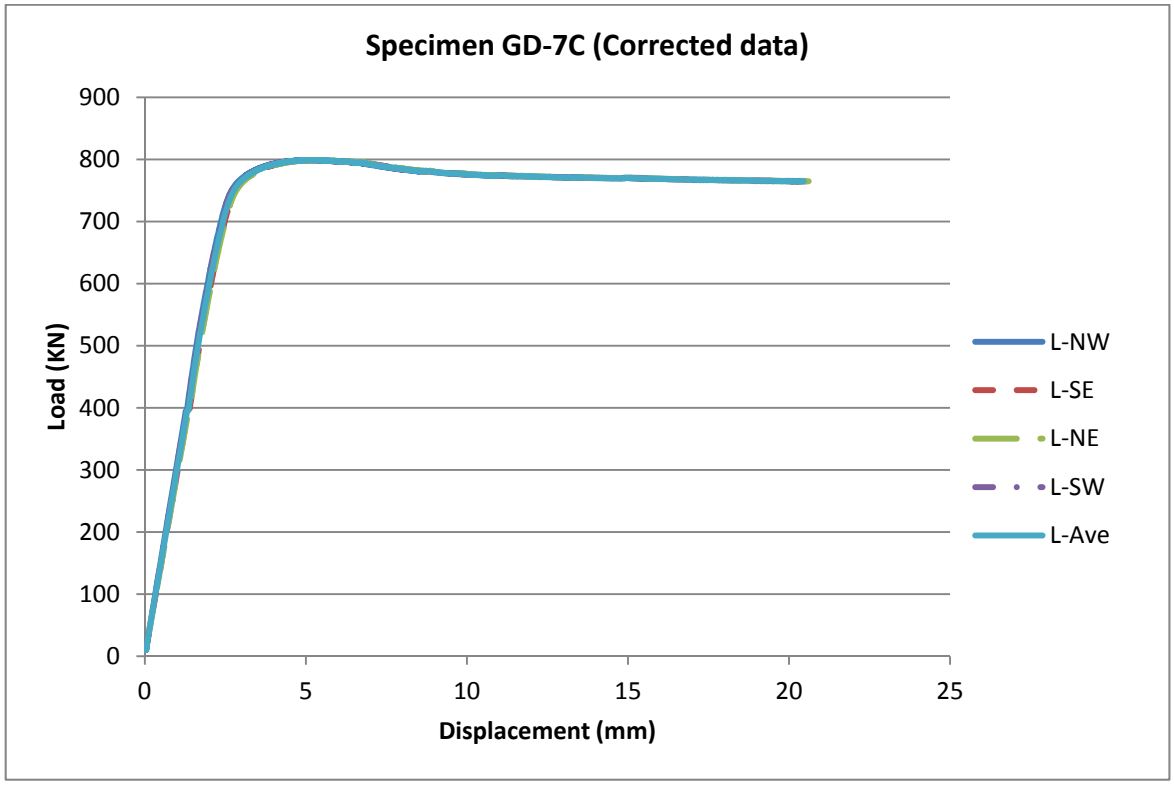

Figure 98: Load/axial-displacement relationship

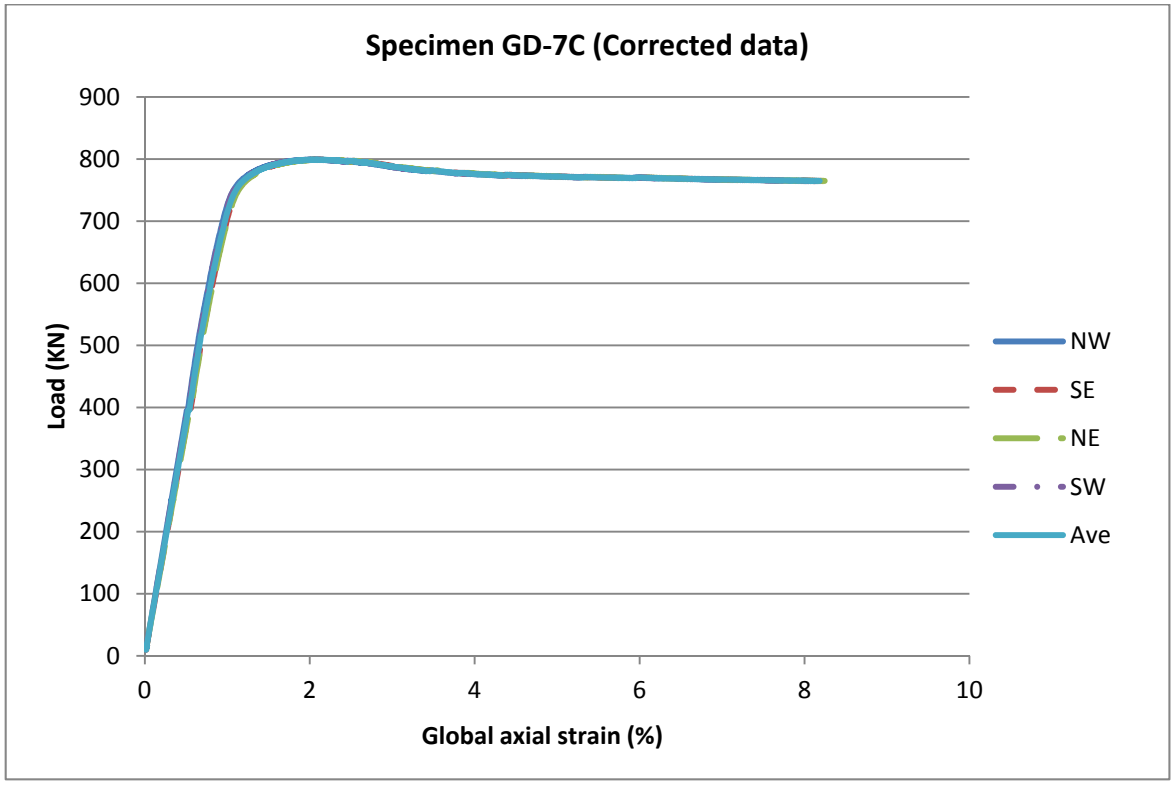

Figure 99: Load/global-axial-strain relationship

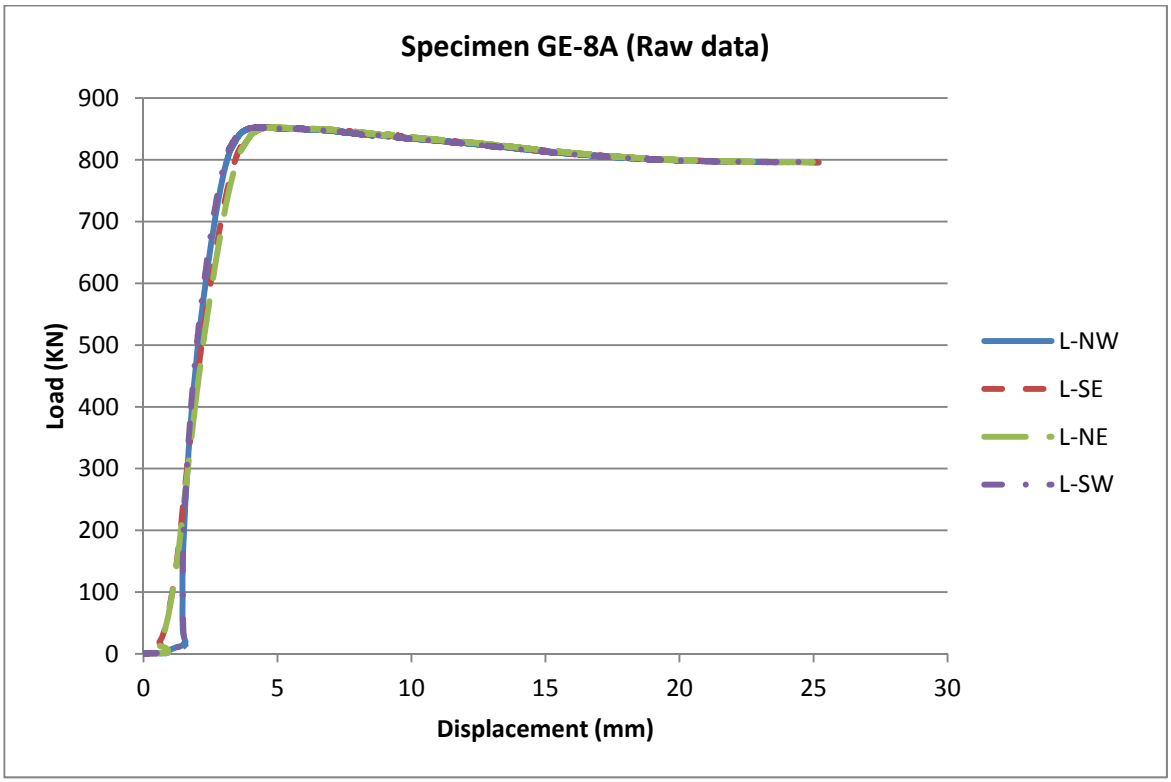

Figure 100: Load/axial-displacement relationship

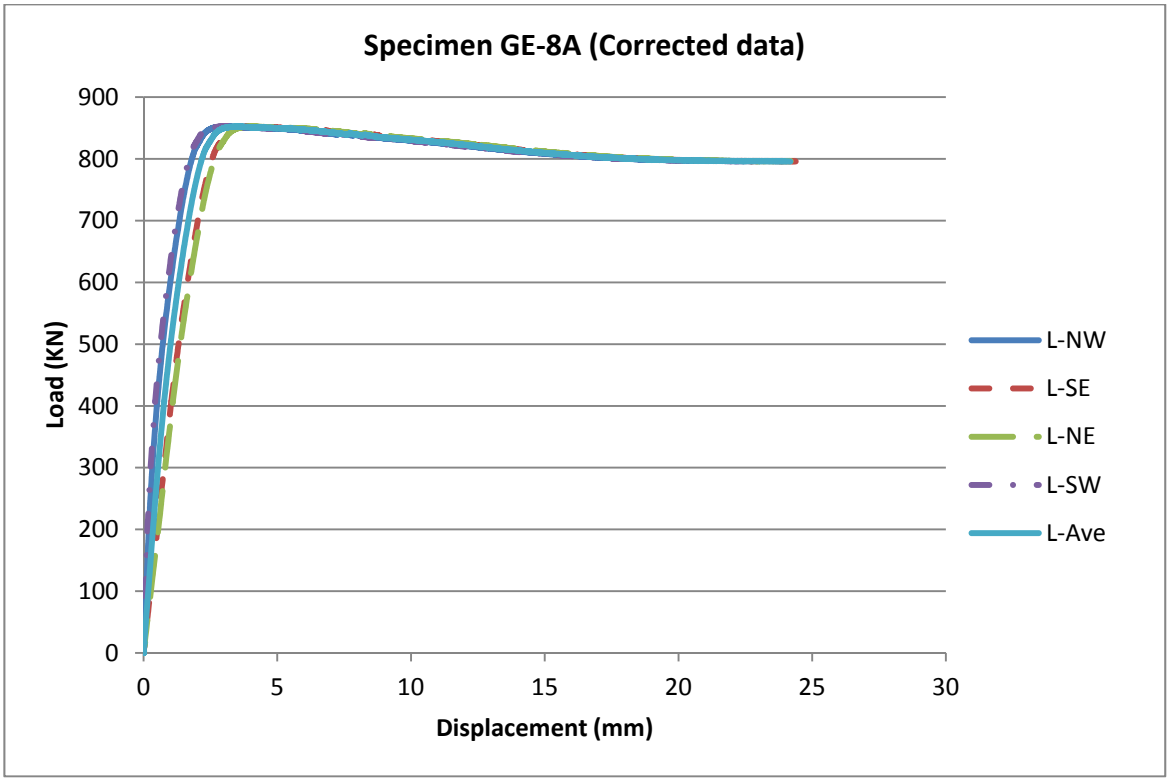

Figure 101: Load/axial-displacement relationship

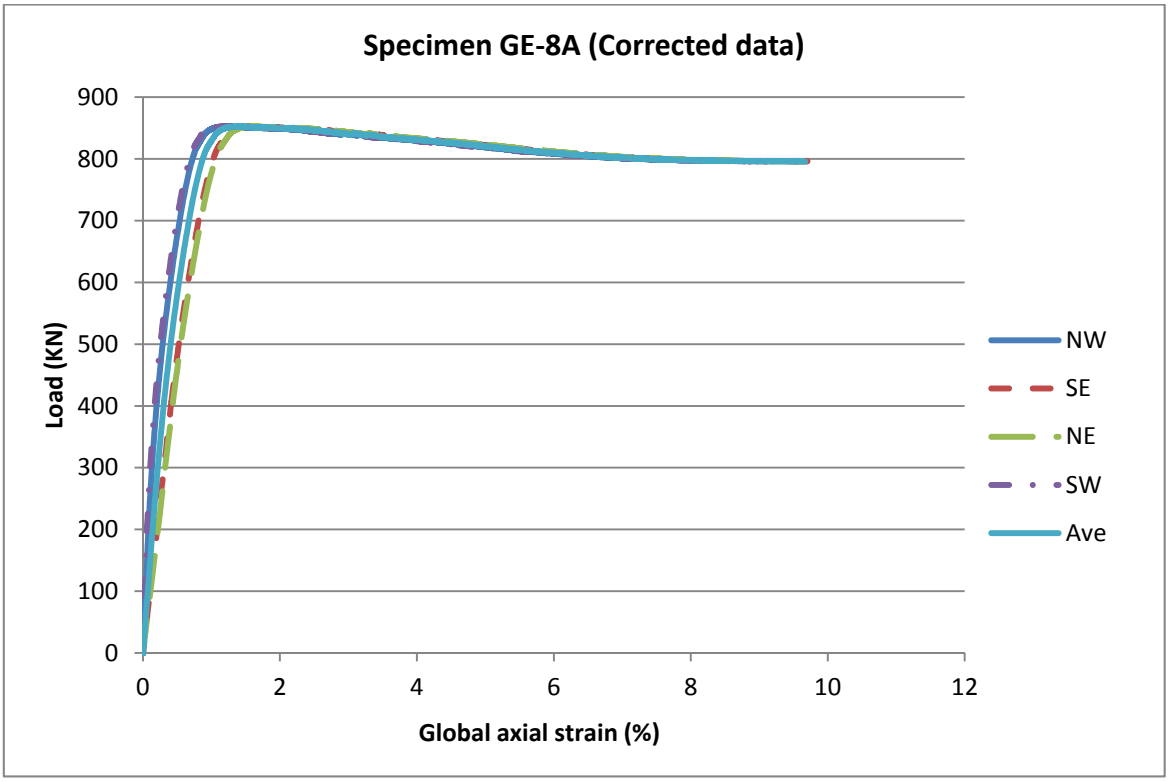

Figure 102: Load/global-axial-strain relationship

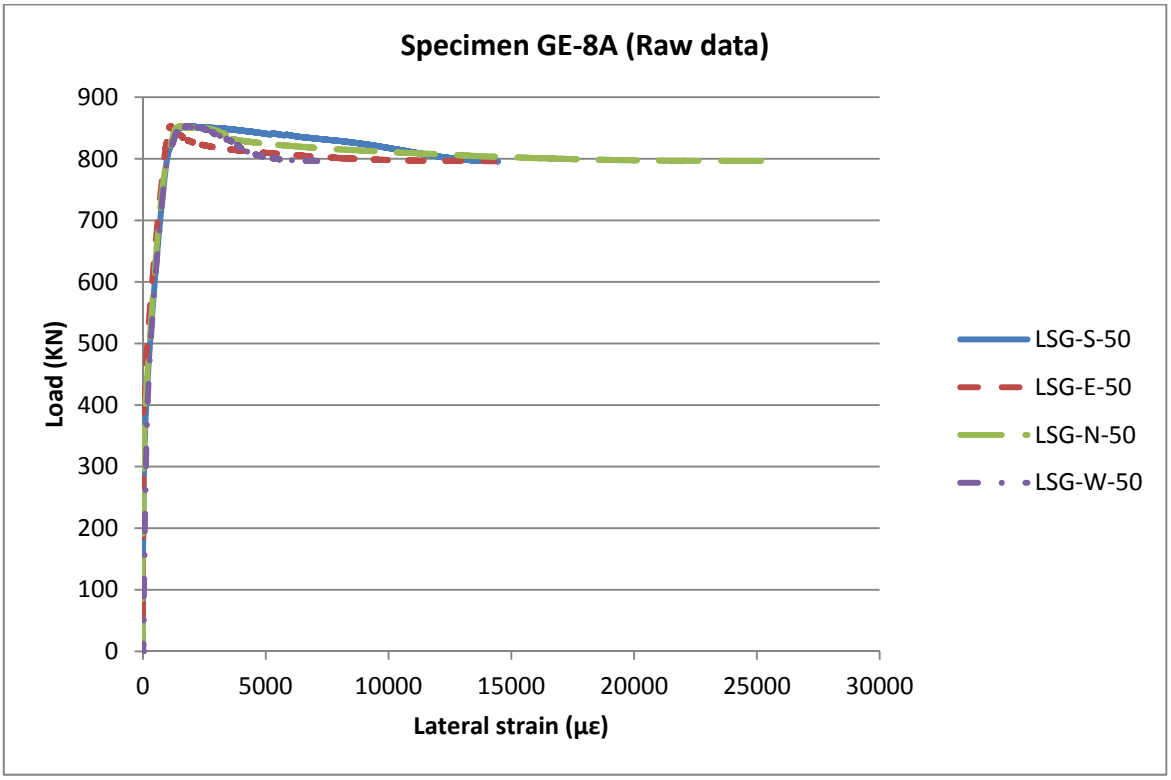

Figure 103: Load/lateral-strain relationship

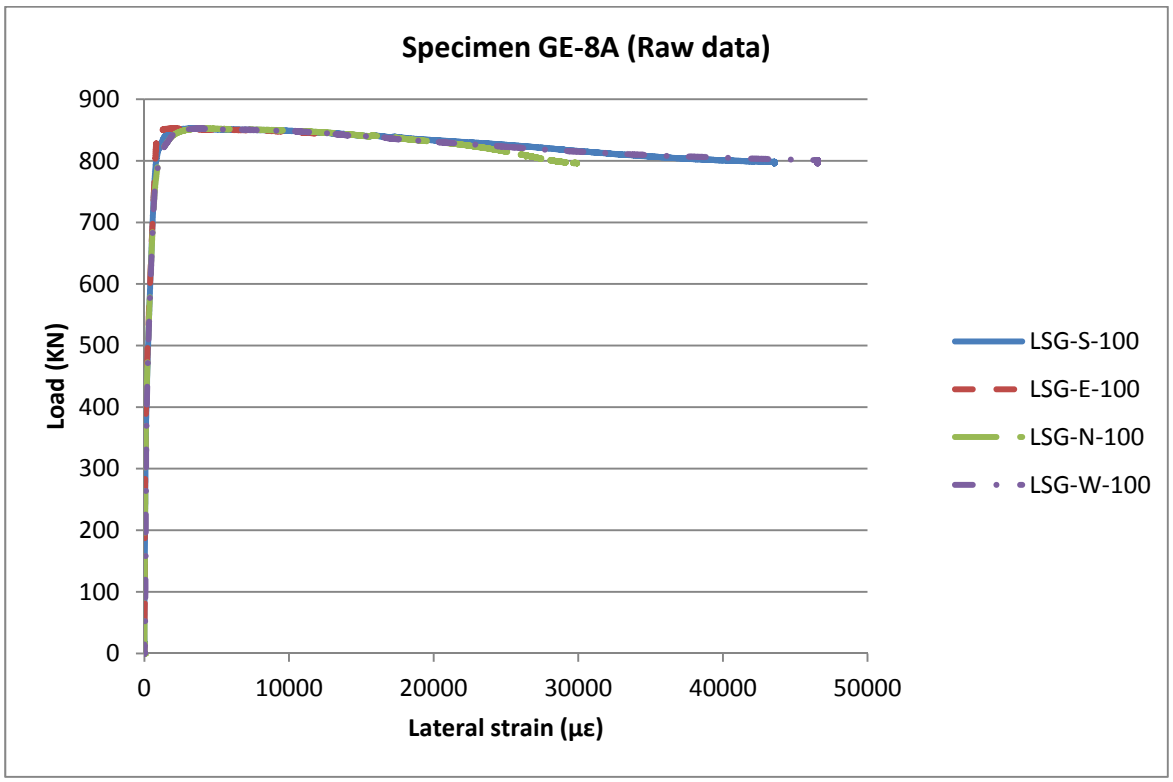

Figure 104: Load/lateral-strain relationship

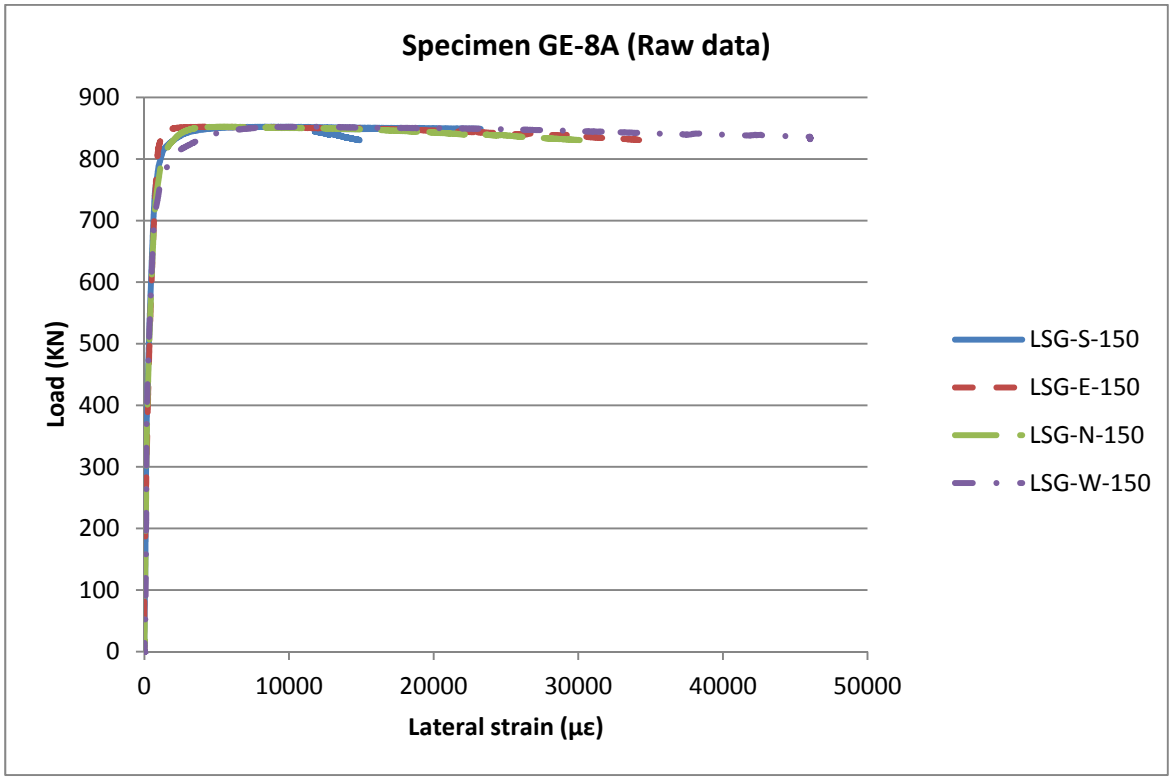

Figure 105: Load/lateral-strain relationship

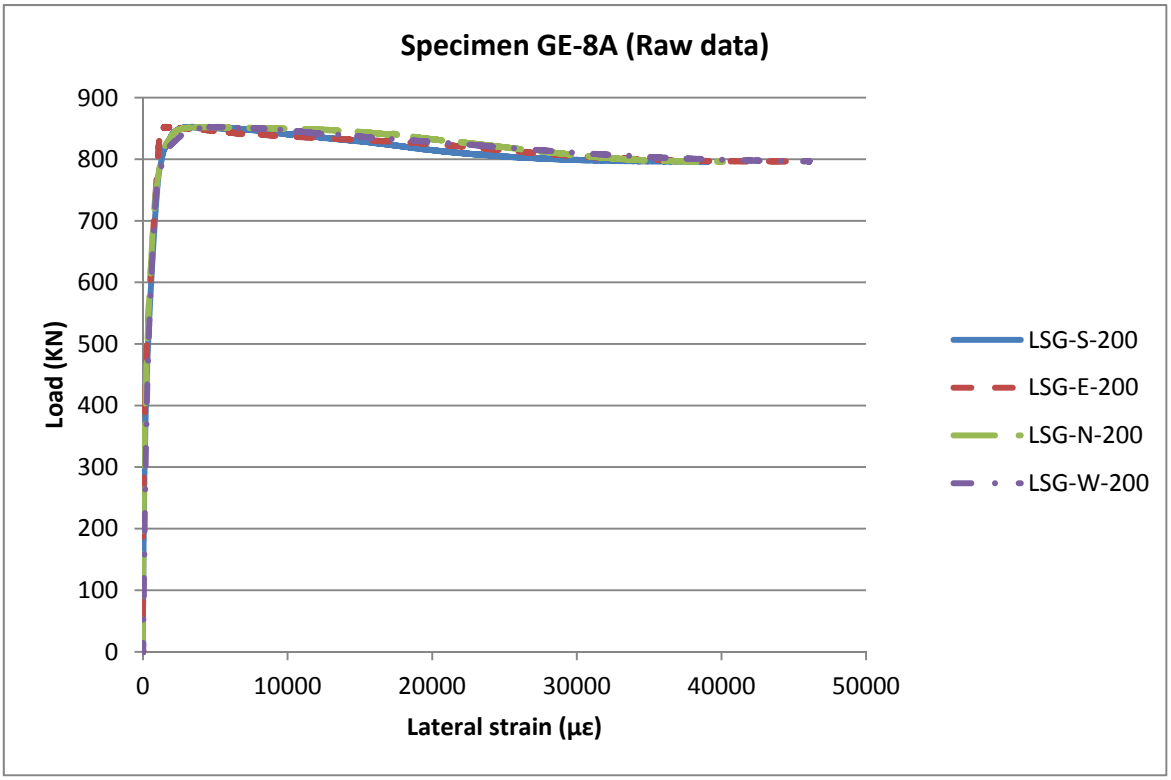

Figure 106: Load/lateral-strain relationship

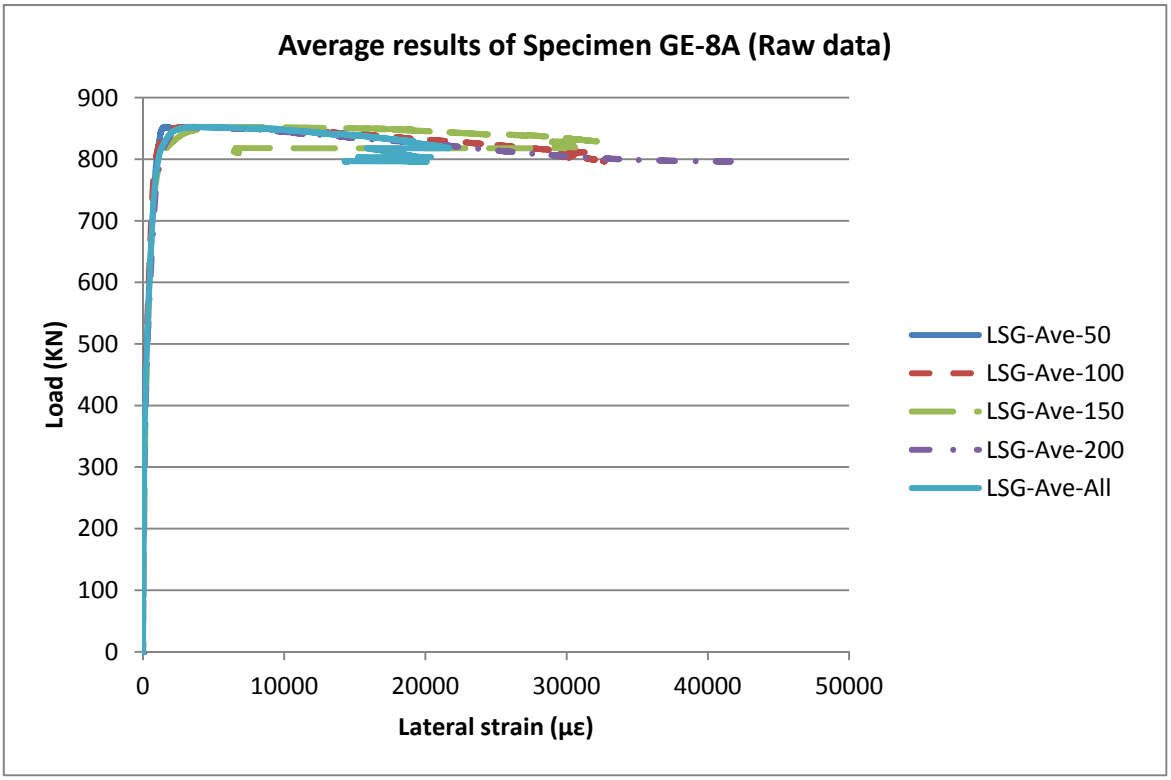

Figure 107: Load/lateral-strain relationship

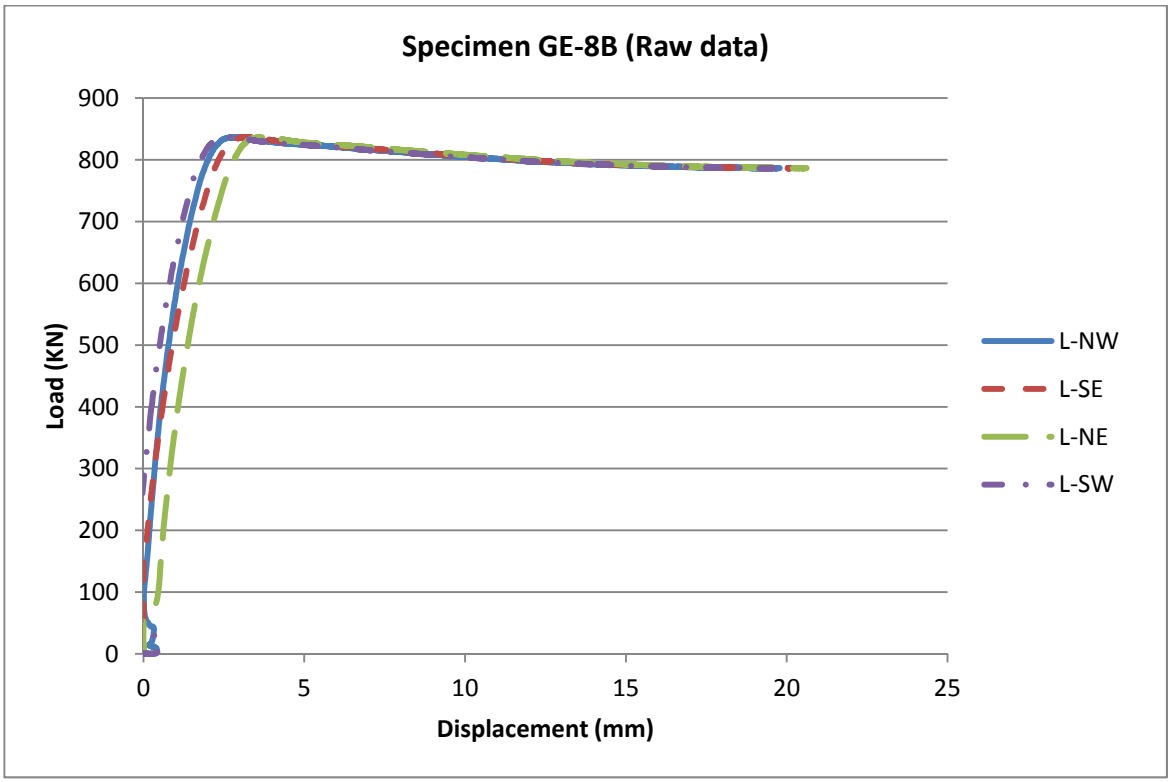

Figure 108: Load/axial-displacement relationship

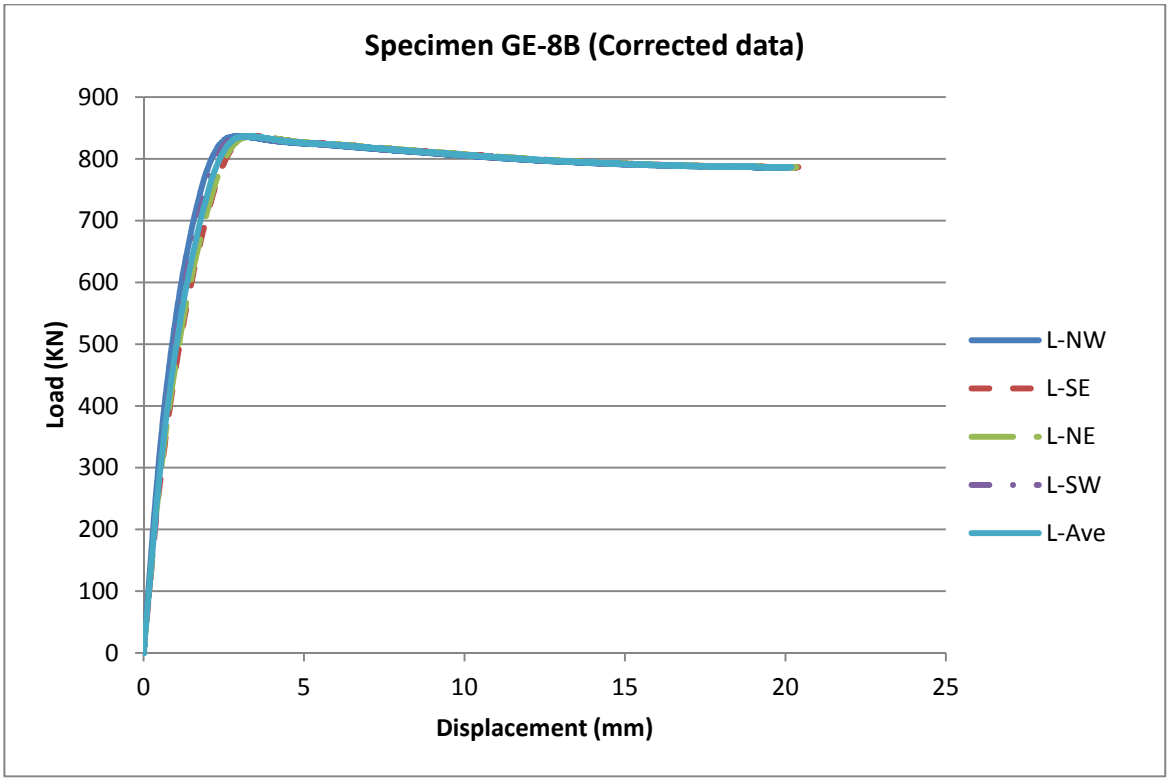

Figure 109: Load/axial-displacement relationship

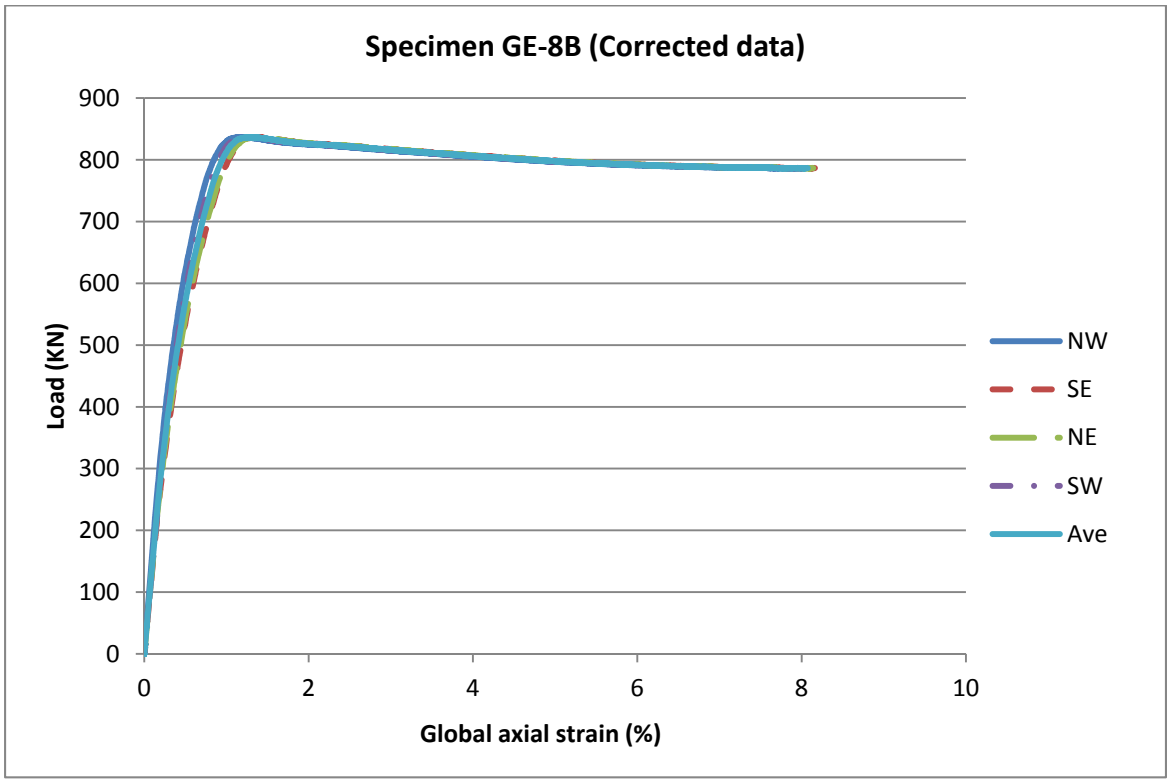

Figure 110: Load/global-axial-strain relationship

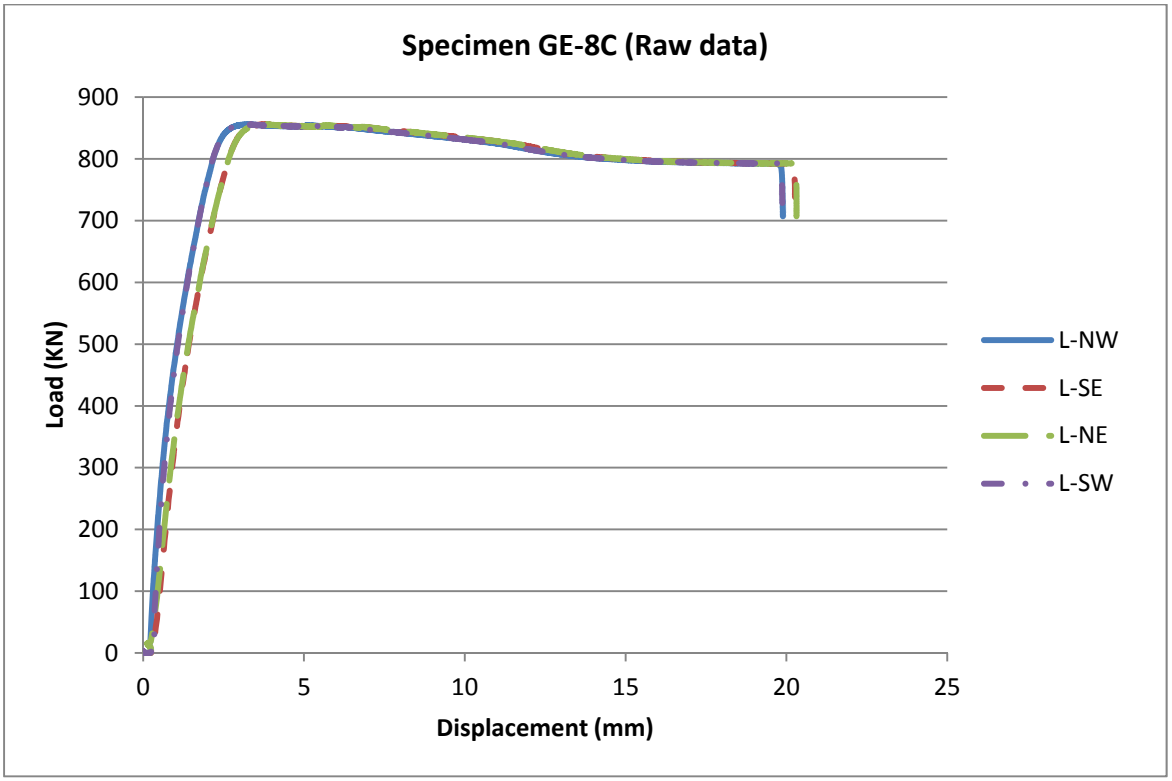

Figure 111: Load/axial-displacement relationship

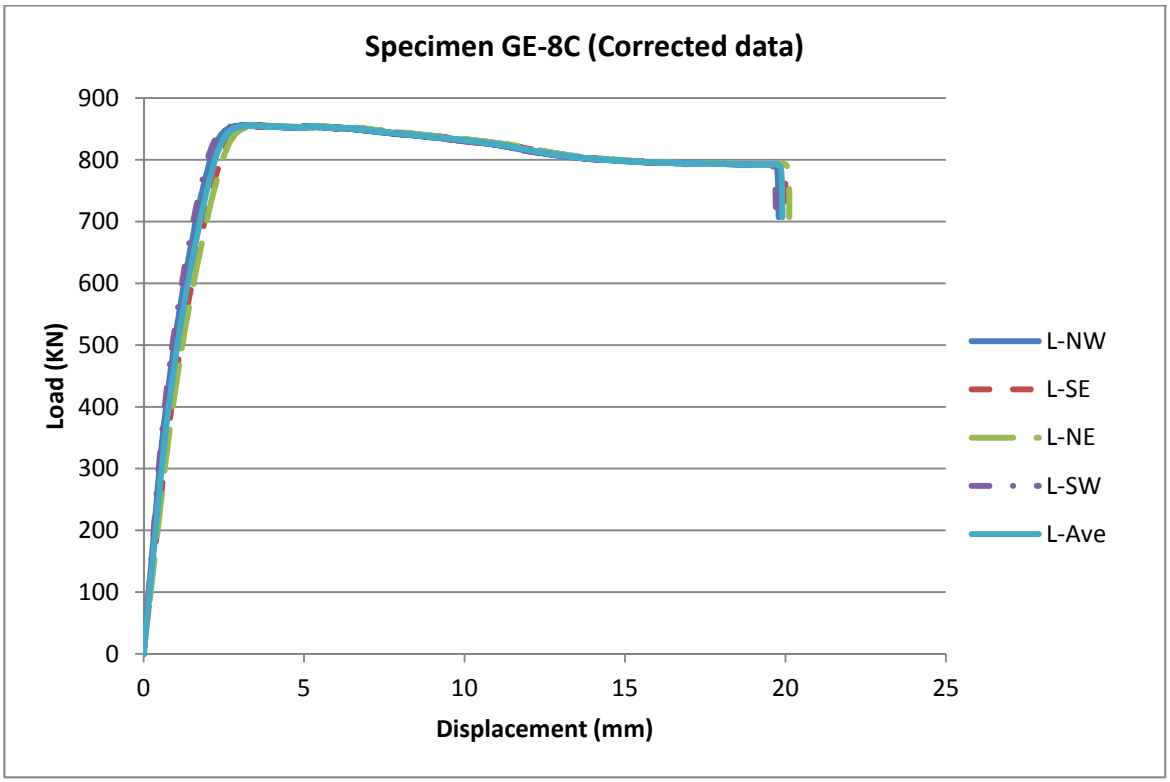

Figure 112: Load/axial-displacement relationship

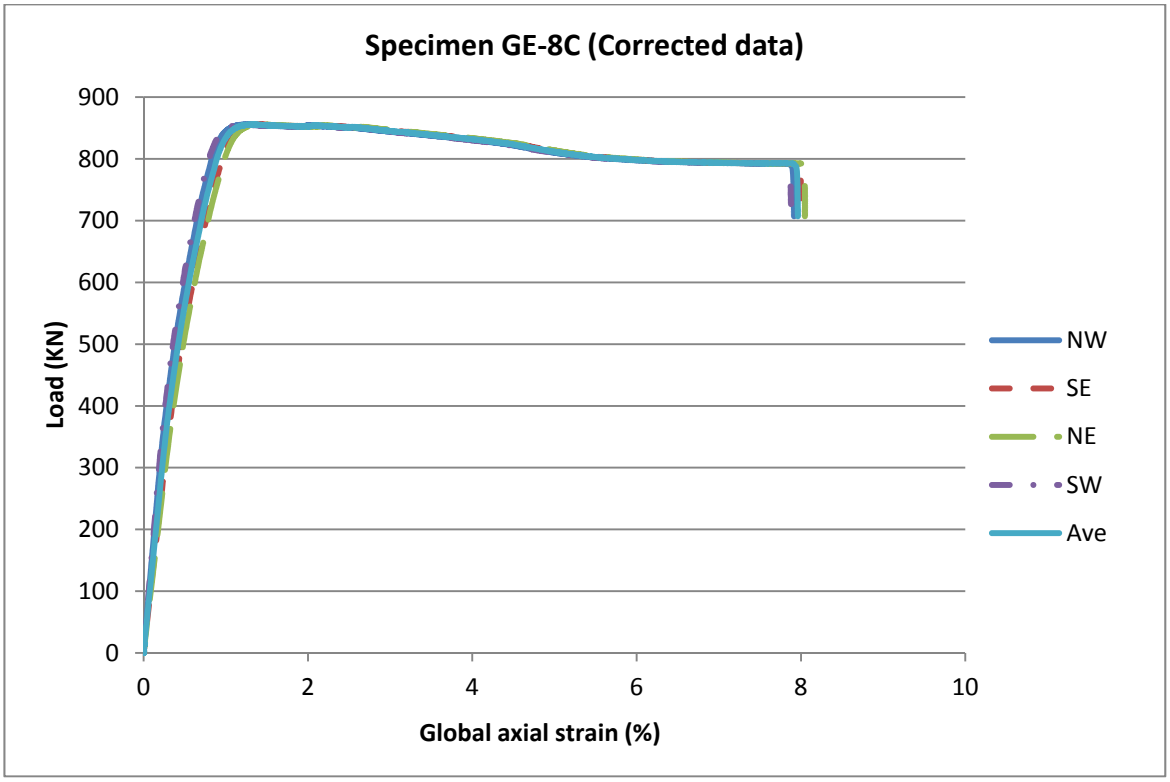

Figure 113: Load/global-axial-strain relationship

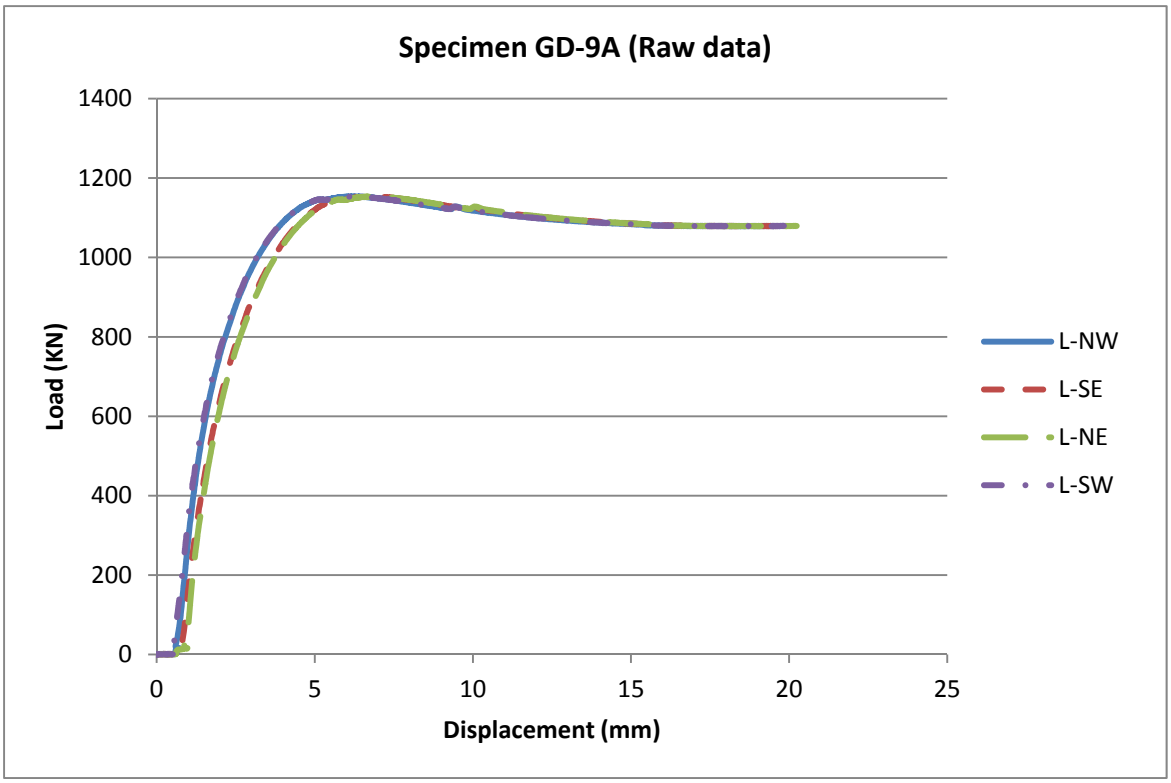

Figure 114: Load/axial-displacement relationship

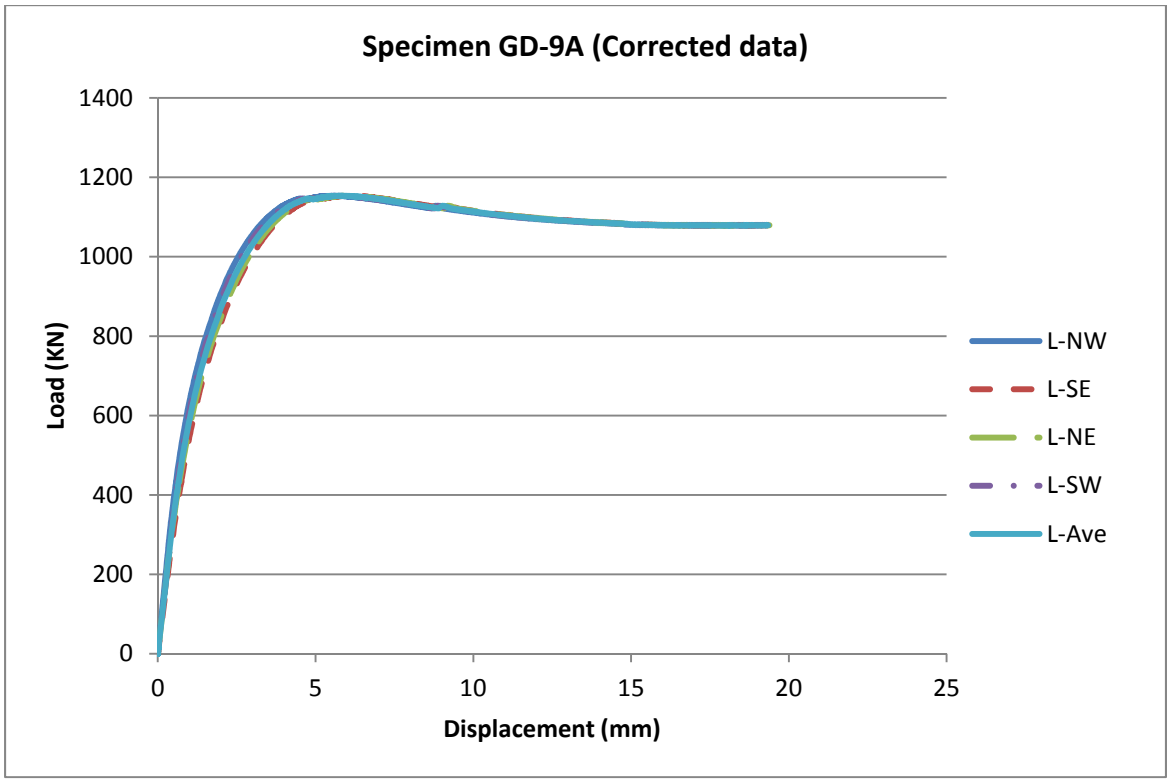

Figure 115: Load/axial-displacement relationship

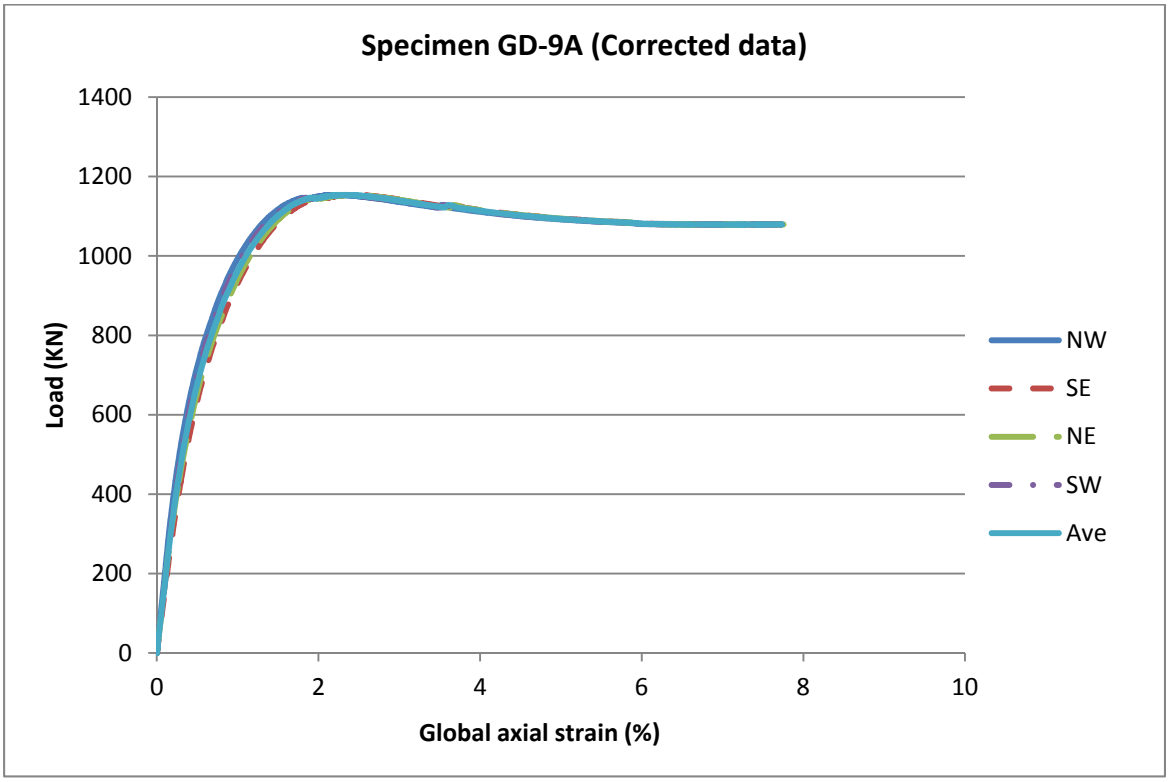

Figure 116: Load/global-axial-strain relationship

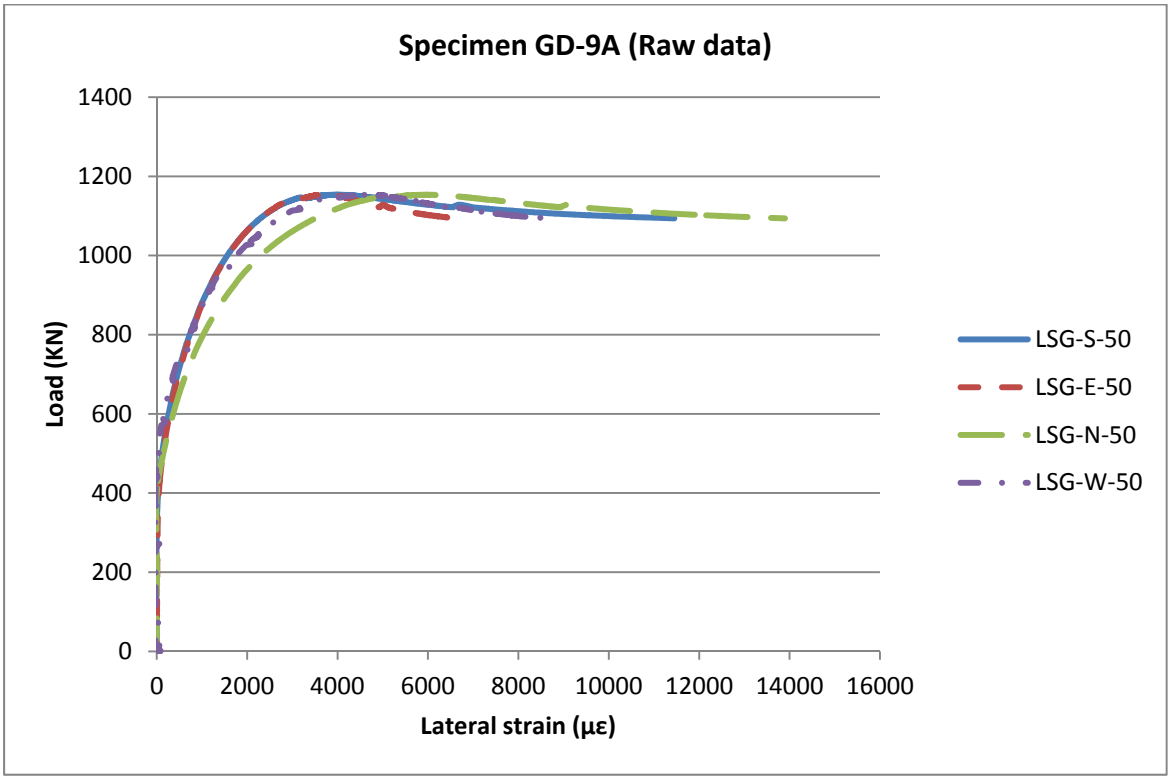

Figure 117: Load/lateral-strain relationship

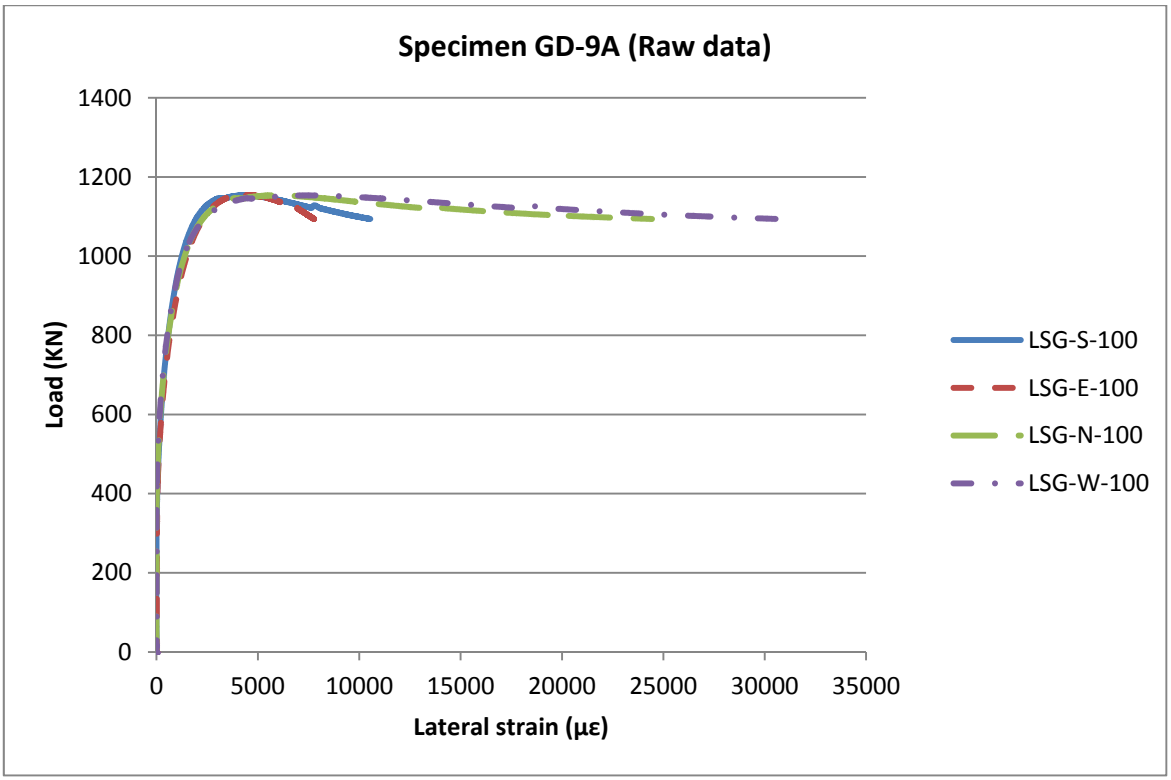

Figure 118: Load/lateral-strain relationship

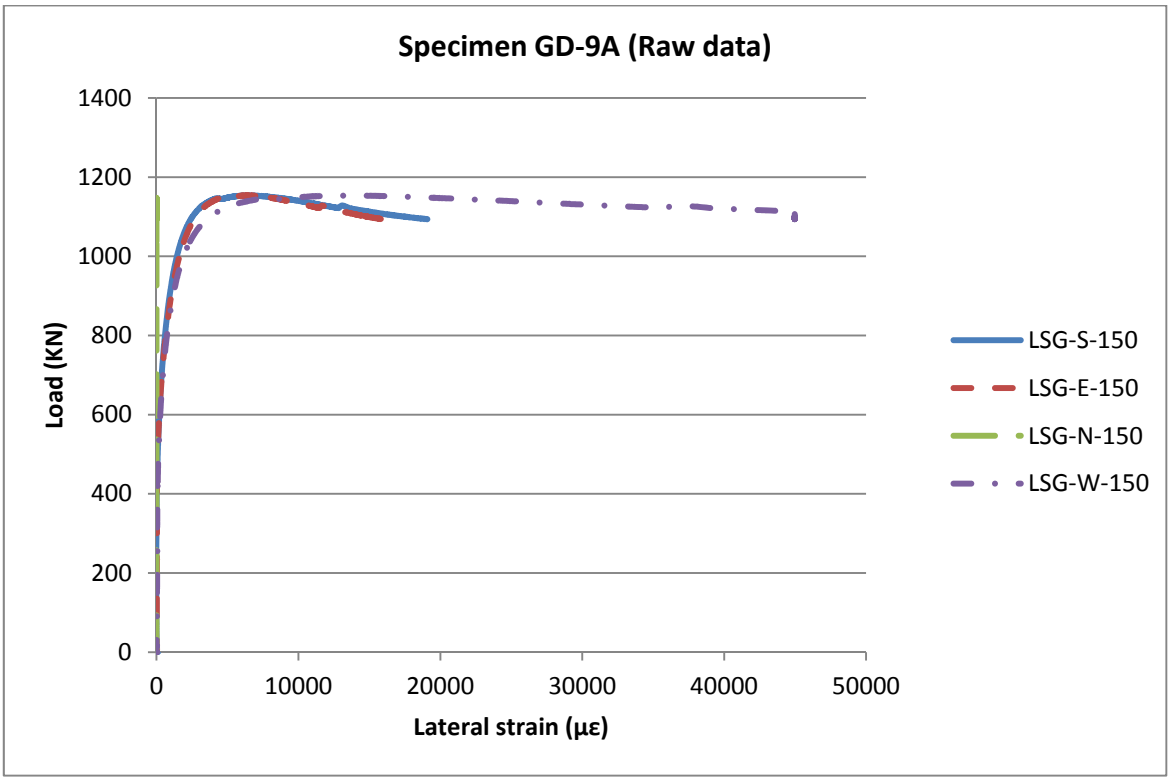

Figure 119: Load/lateral-strain relationship

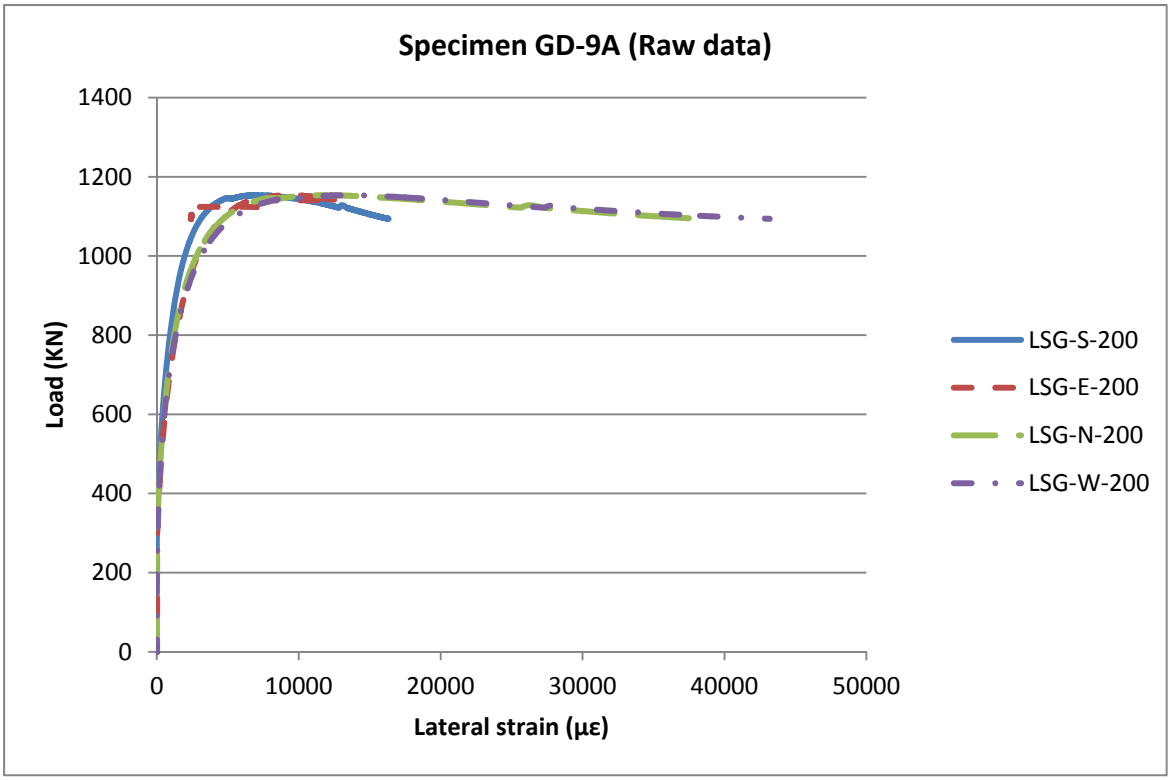

Figure 120: Load/lateral-strain relationship

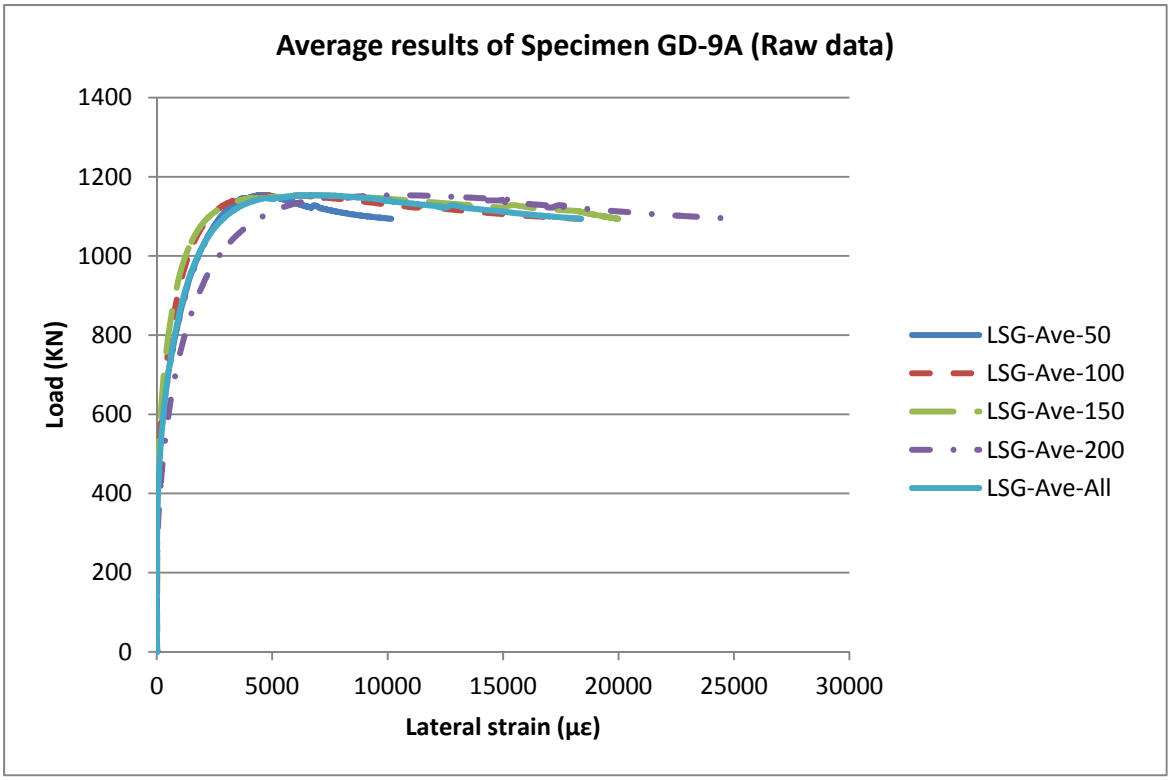

Figure 121: Load/lateral-strain relationship

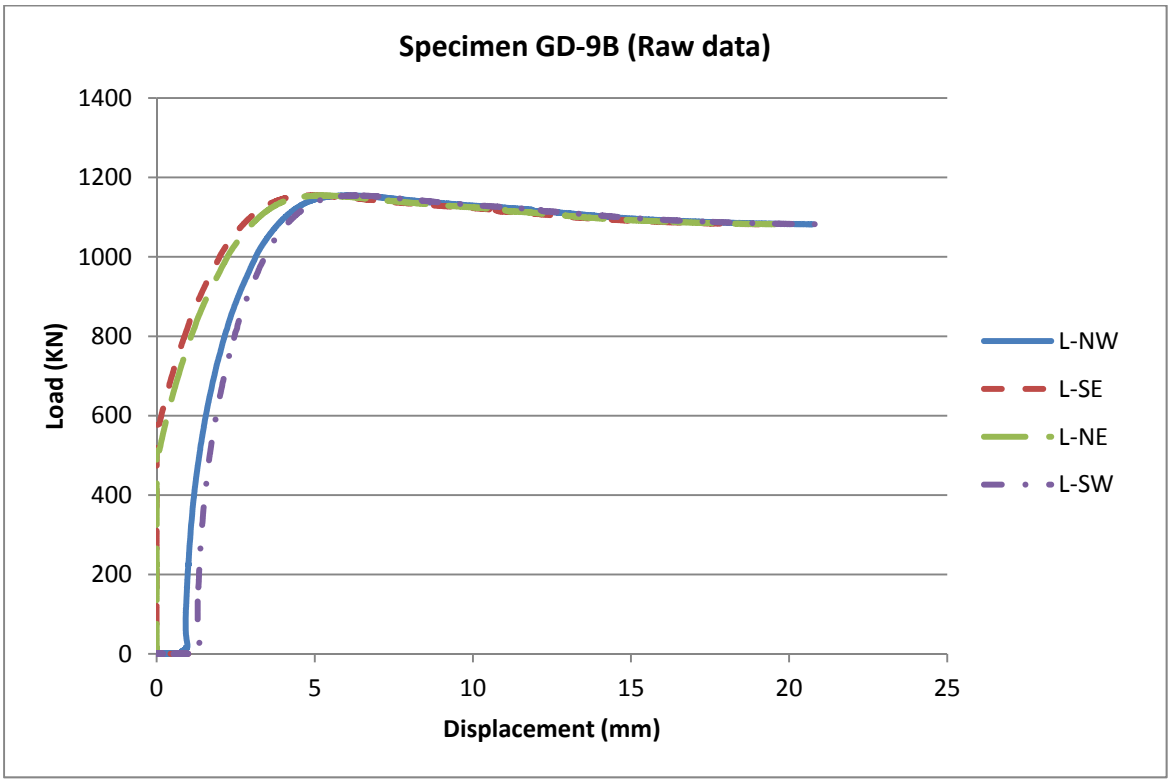

Figure 122: Load/axial-displacement relationship

Figure 123: Load/axial-displacement relationship

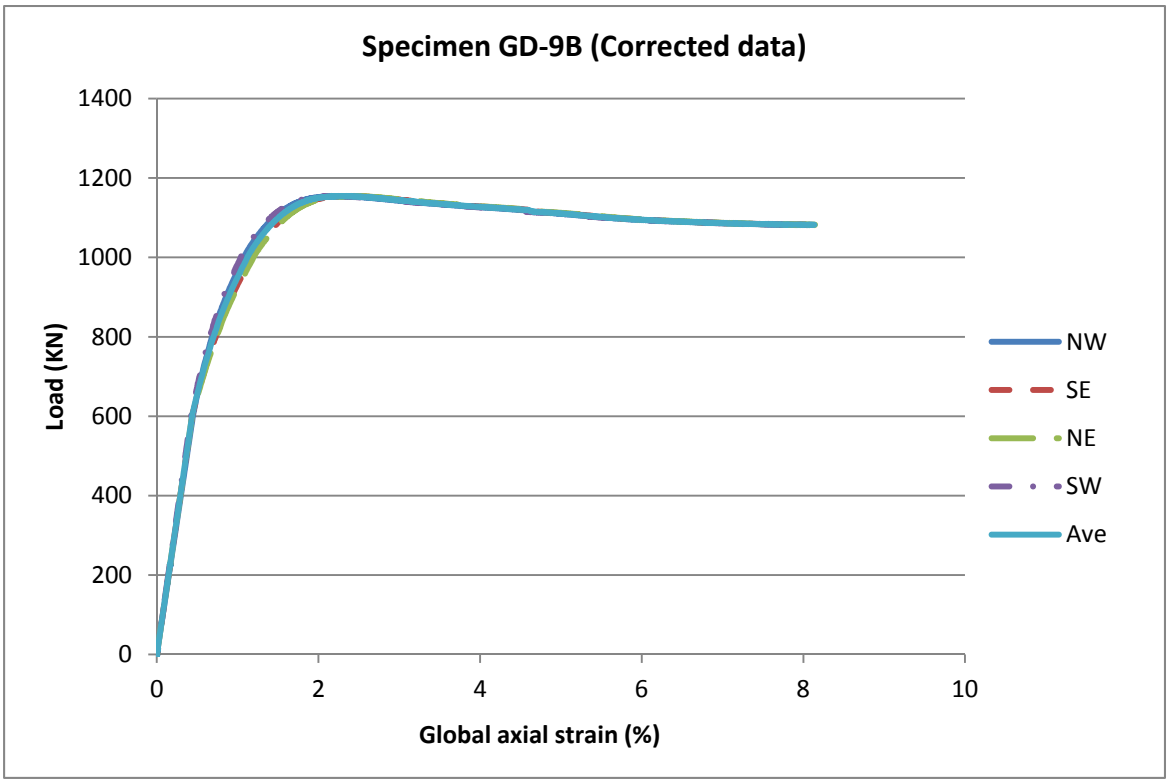

Figure 124: Load/global-axial-strain relationship

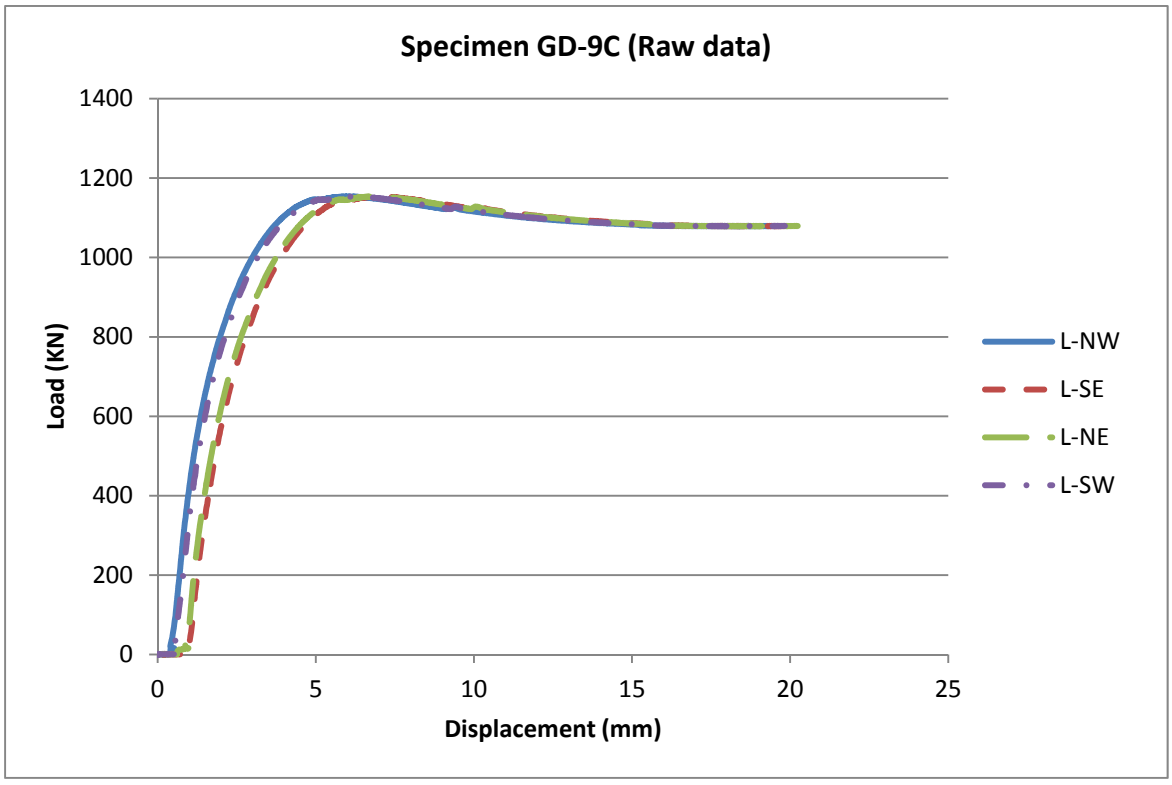

Figure 125: Load/axial-displacement relationship

Figure 126: Load/axial-displacement relationship

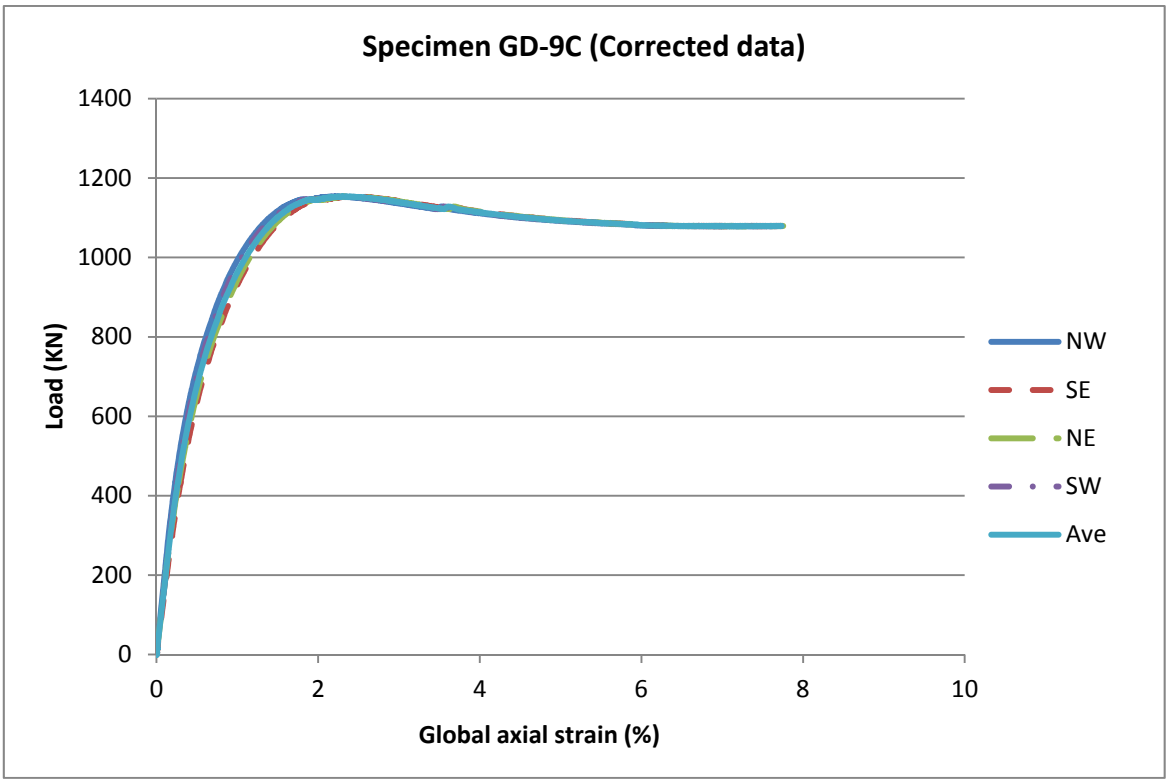

Figure 127: Load/global-axial-strain relationship

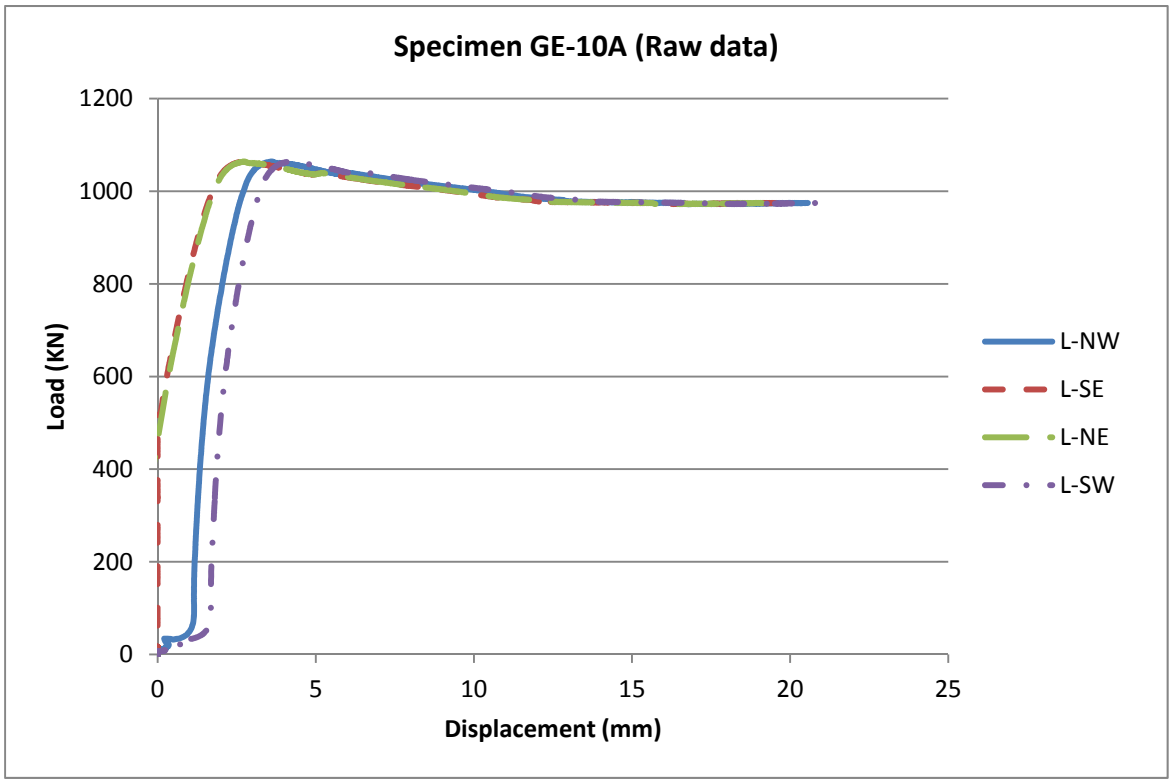

Figure 128: Load/axial-displacement relationship

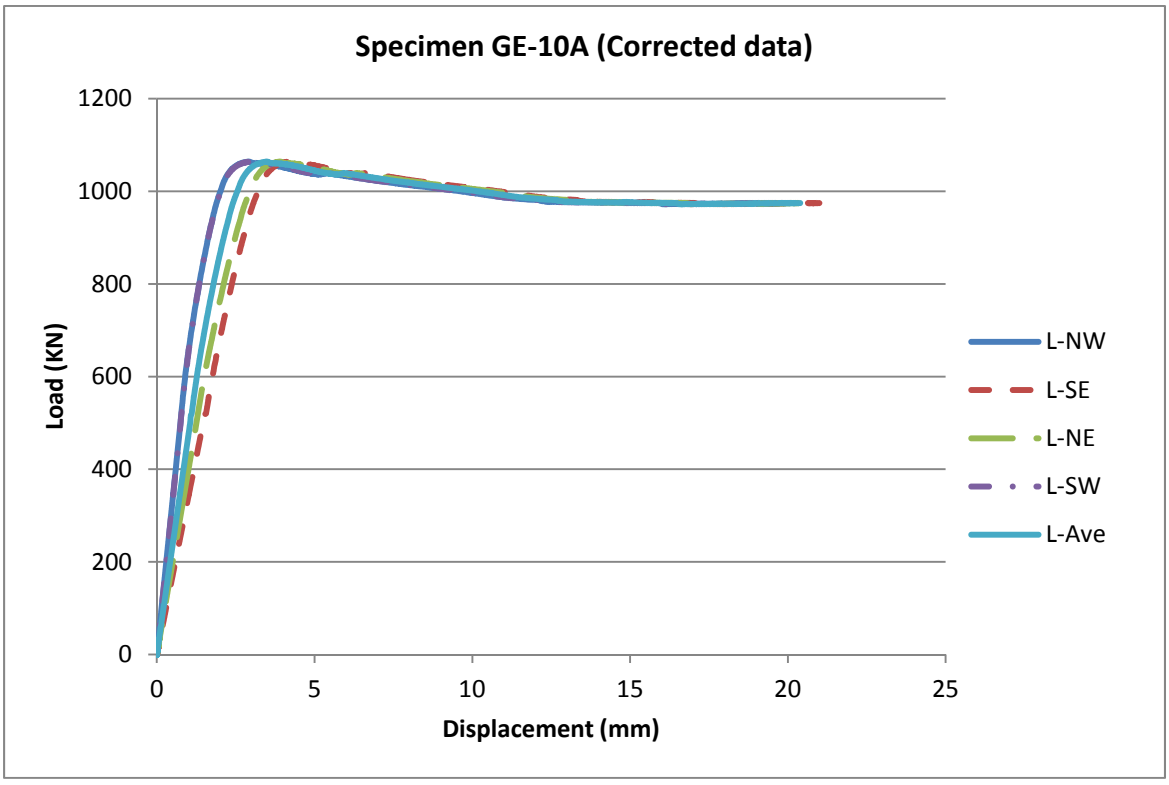

Figure 129: Load/axial-displacement relationship

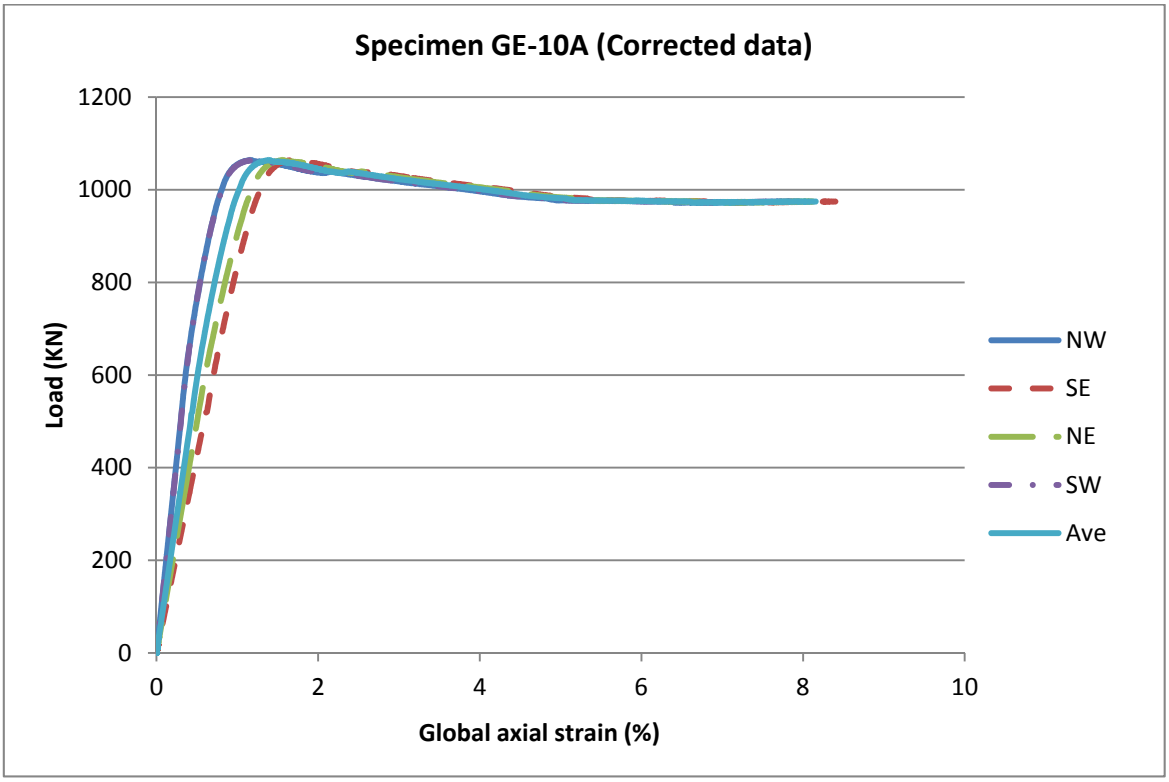

Figure 130: Load/global-axial-strain relationship

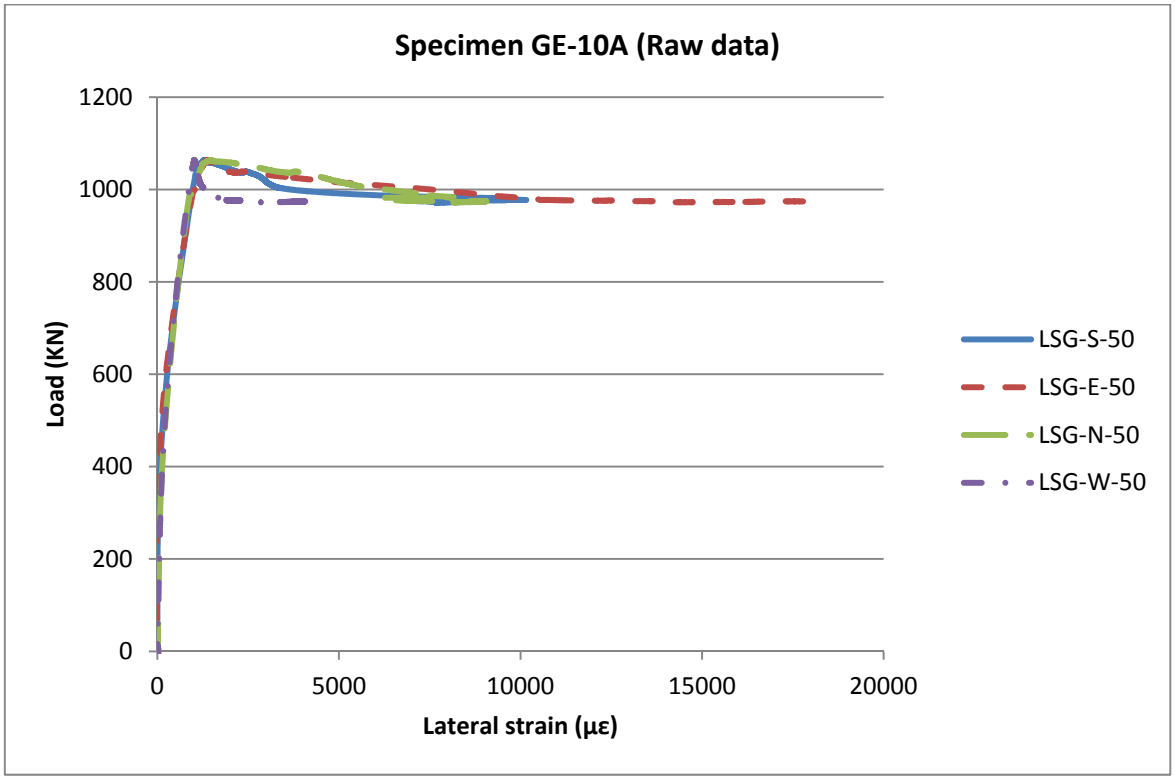

Figure 131: Load/lateral-strain relationship

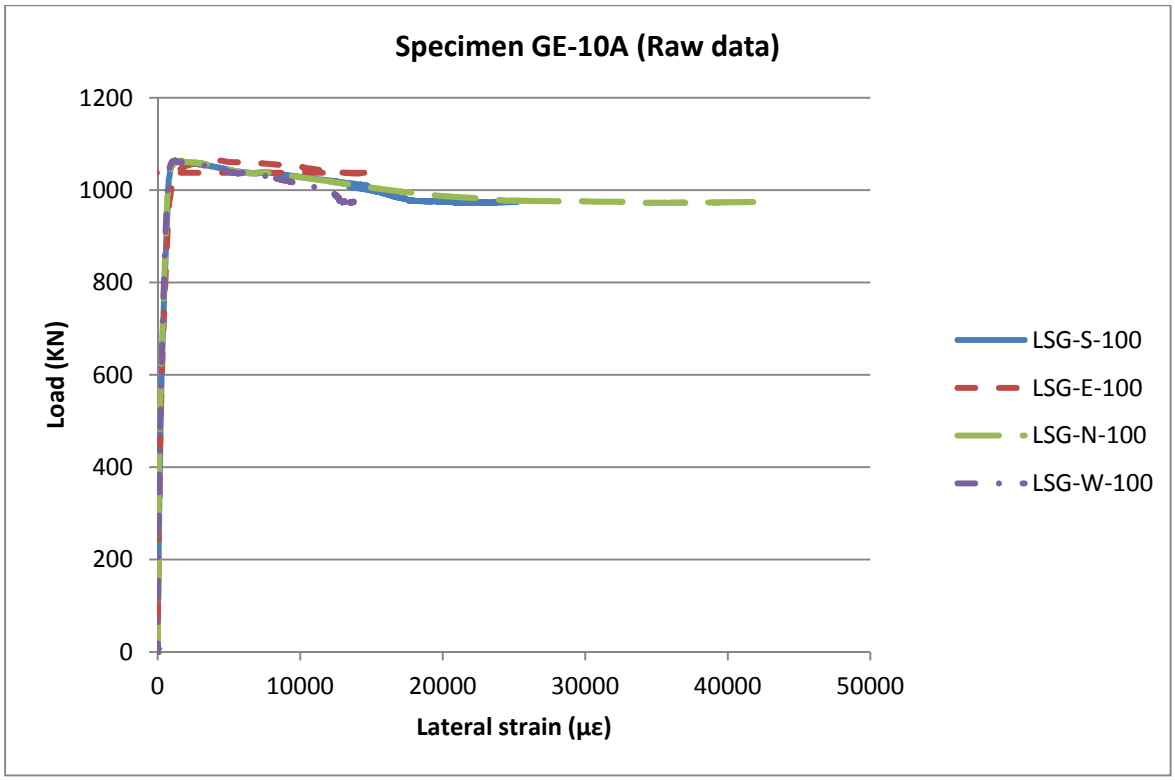

Figure 132: Load/lateral-strain relationship

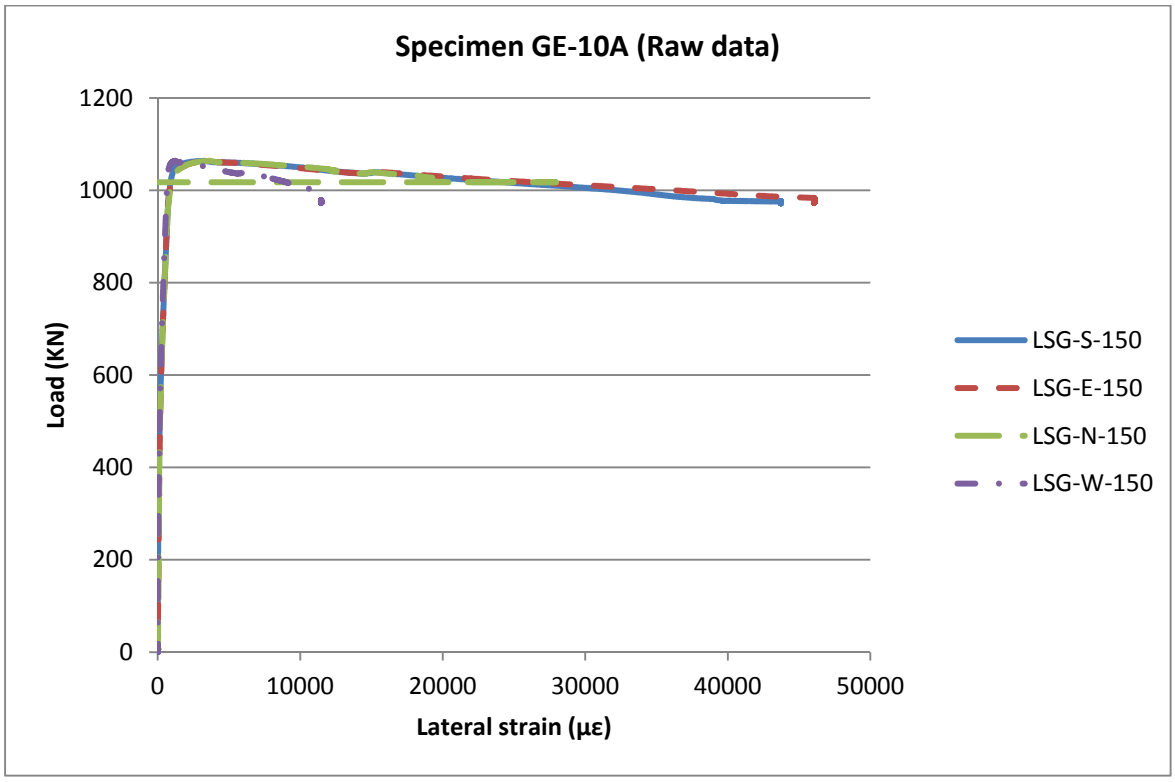

Figure 133: Load/lateral-strain relationship

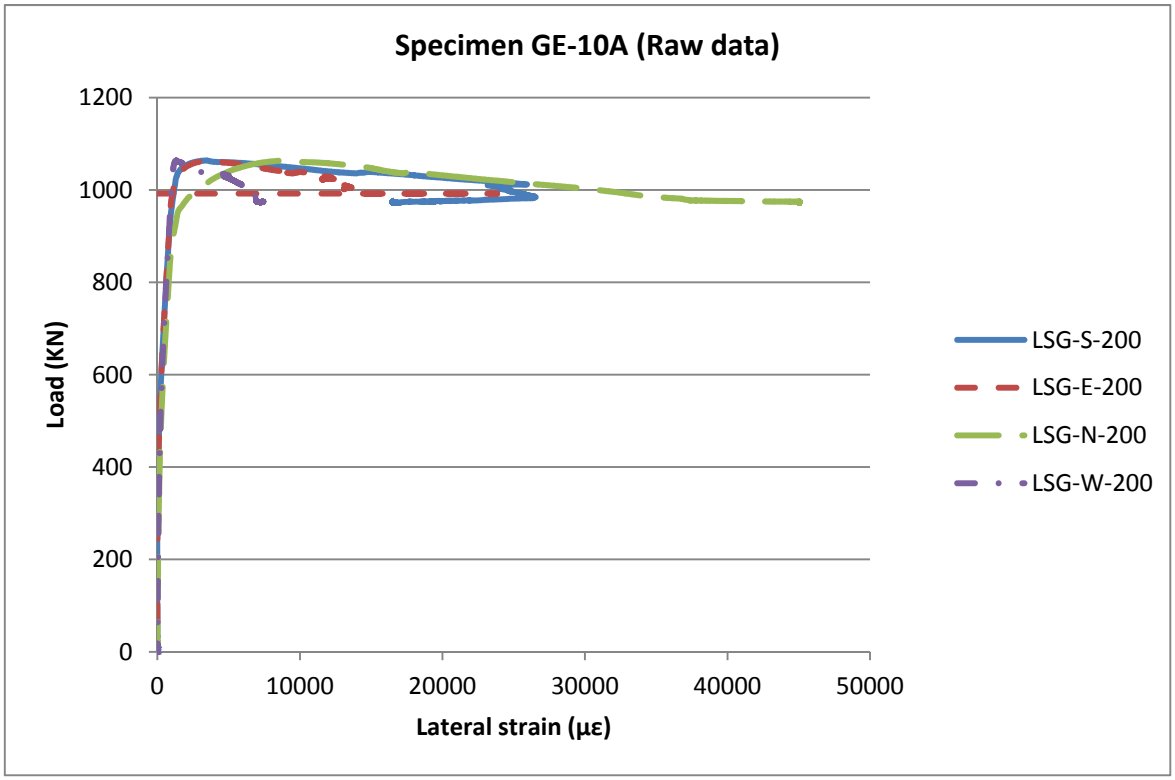

Figure 134: Load/lateral-strain relationship

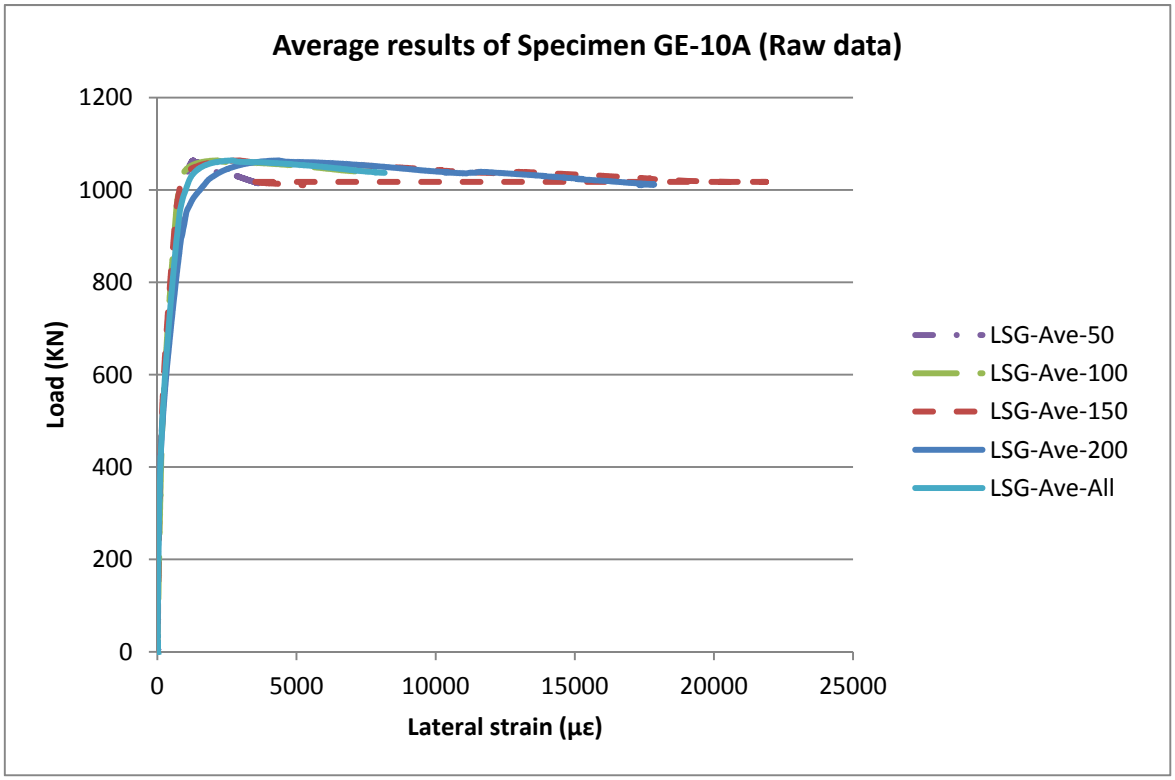

Figure 135: Load/lateral-strain relationship

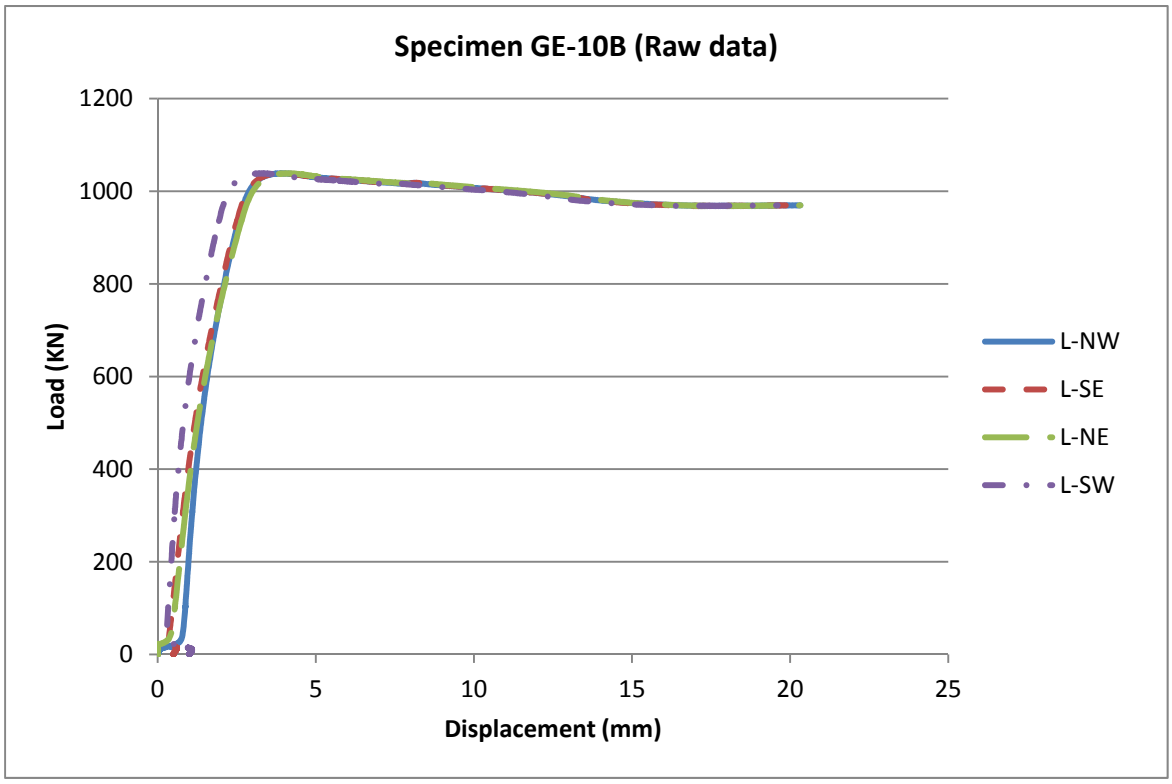

Figure 136: Load/axial-displacement relationship

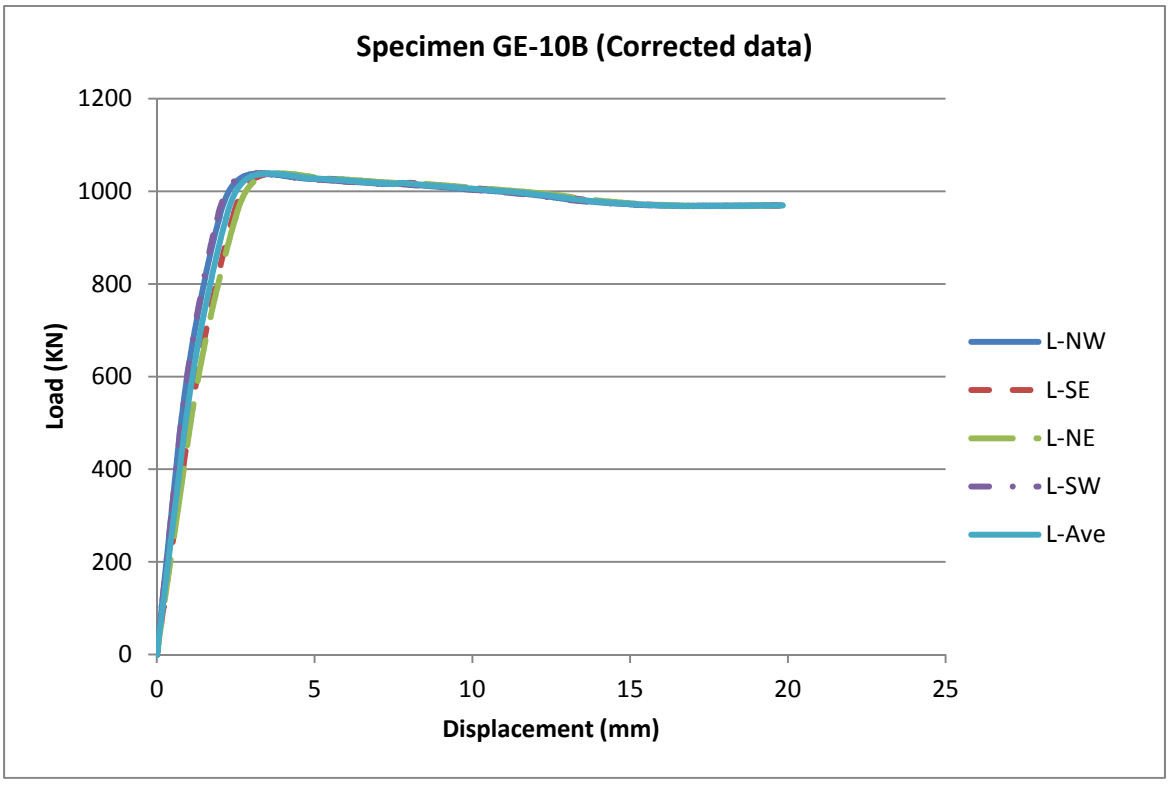

Figure 137: Load/axial-displacement relationship

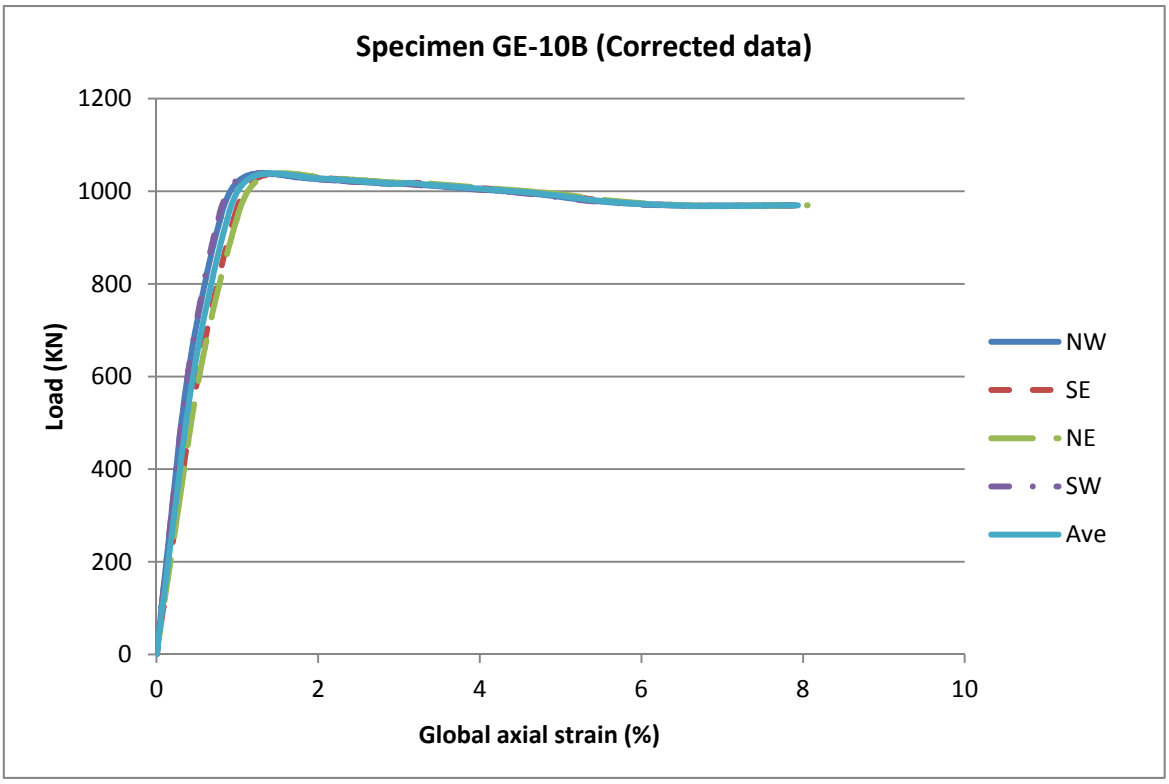

Figure 138: Load/global-axial-strain relationship

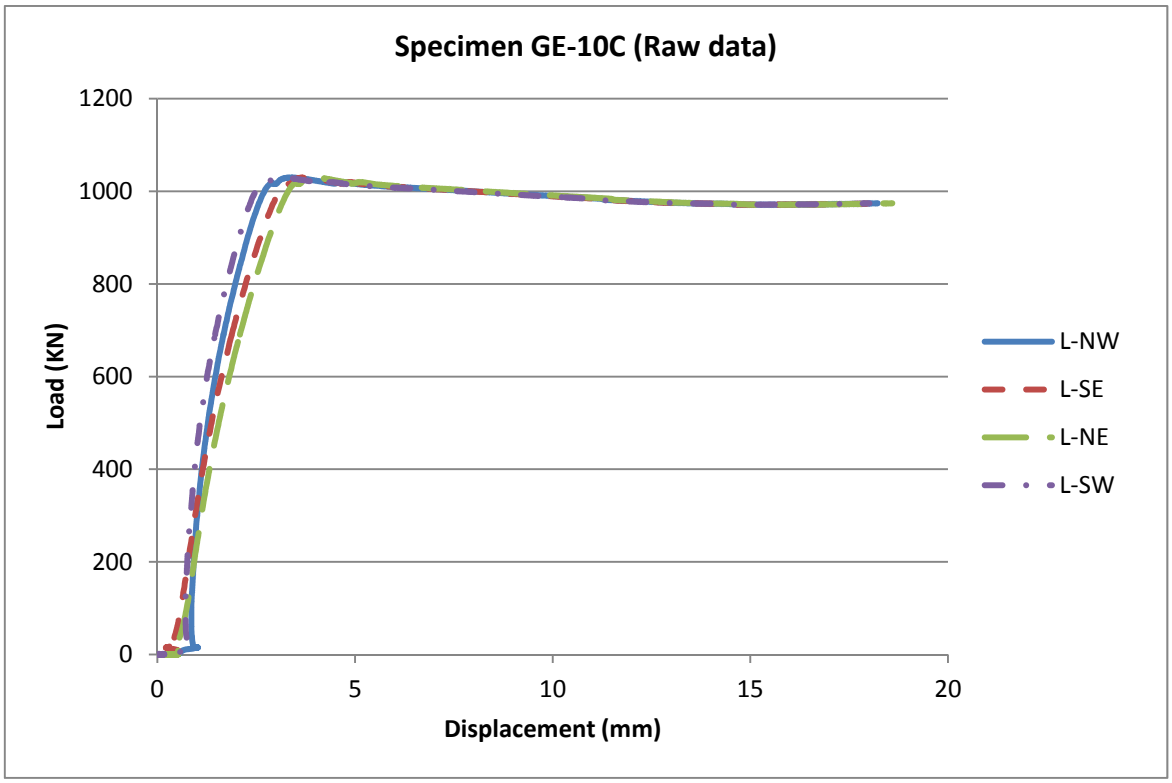

Figure 139: Load/axial-displacement relationship

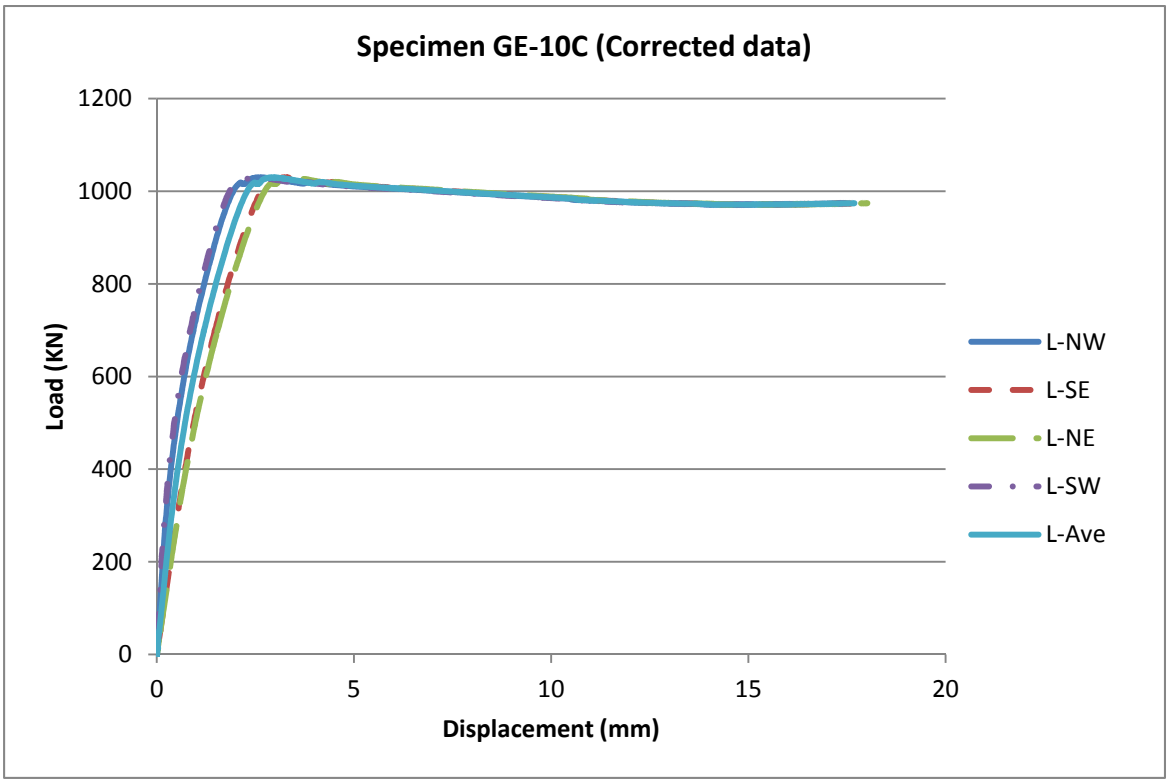

Figure 140: Load/axial-displacement relationship

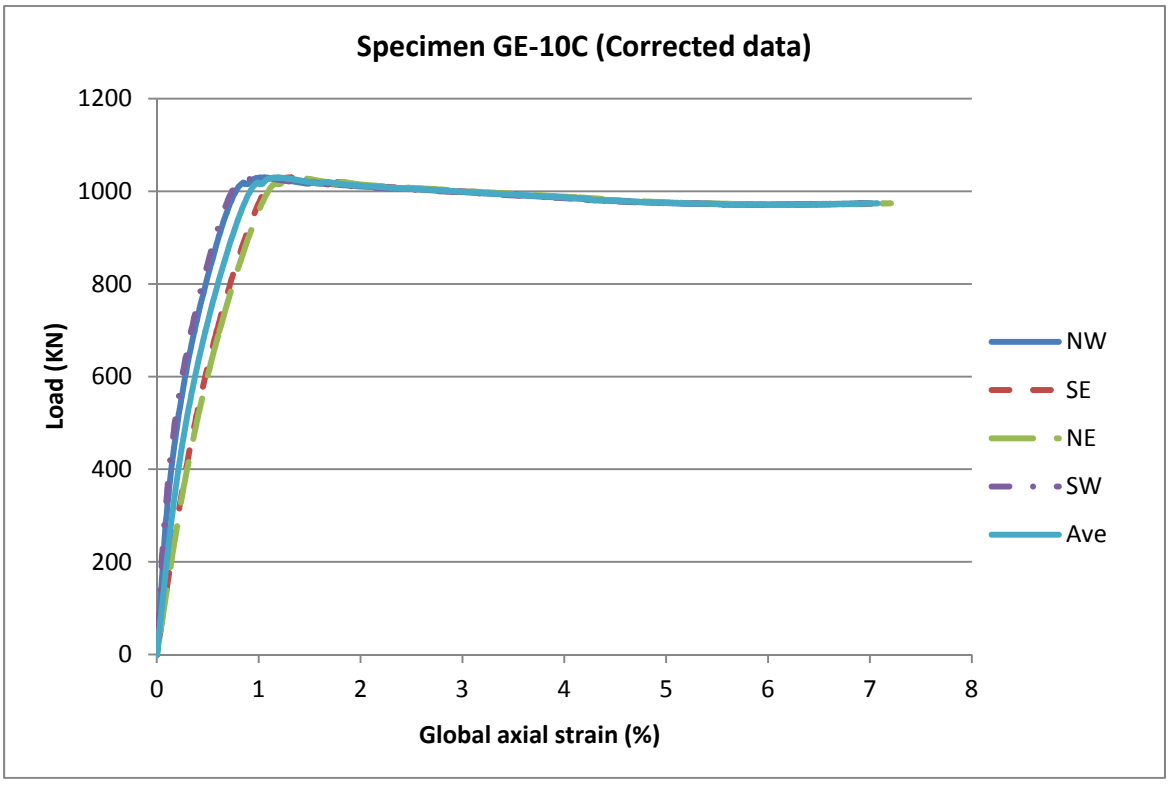

Figure 141: Load/global-axial-strain relationship

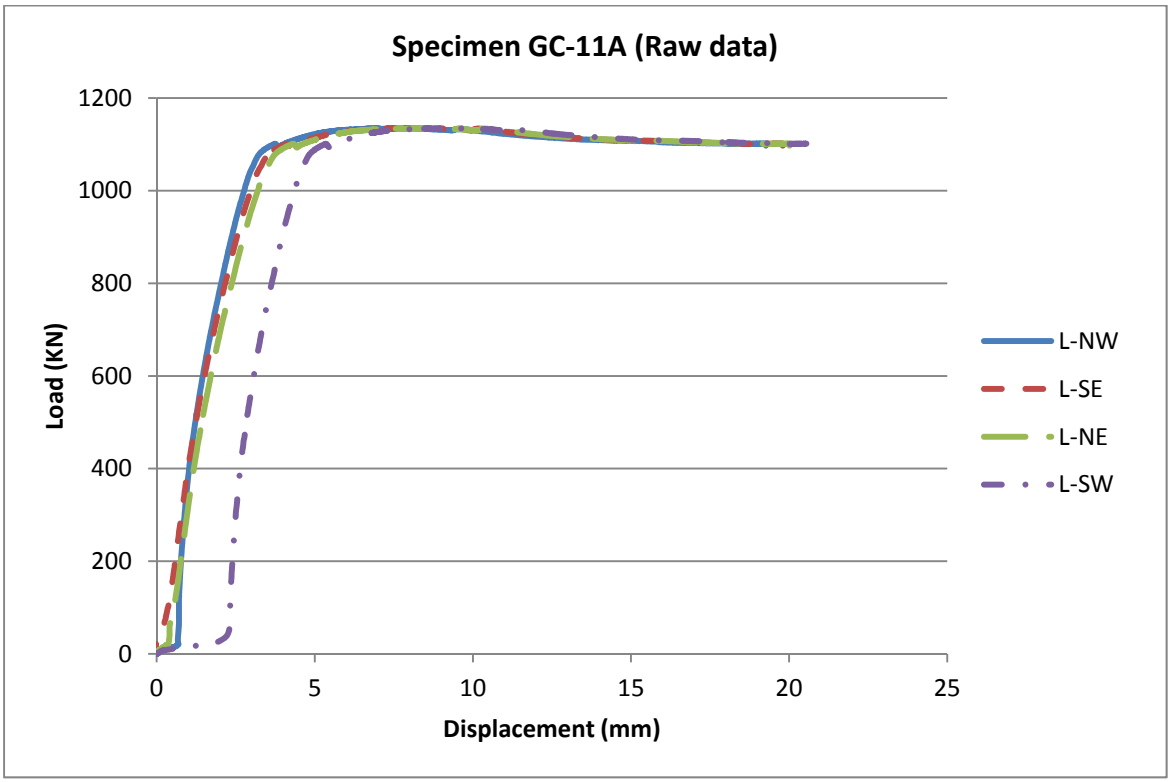

Figure 142: Load/axial-displacement relationship

Figure 143: Load/axial-displacement relationship

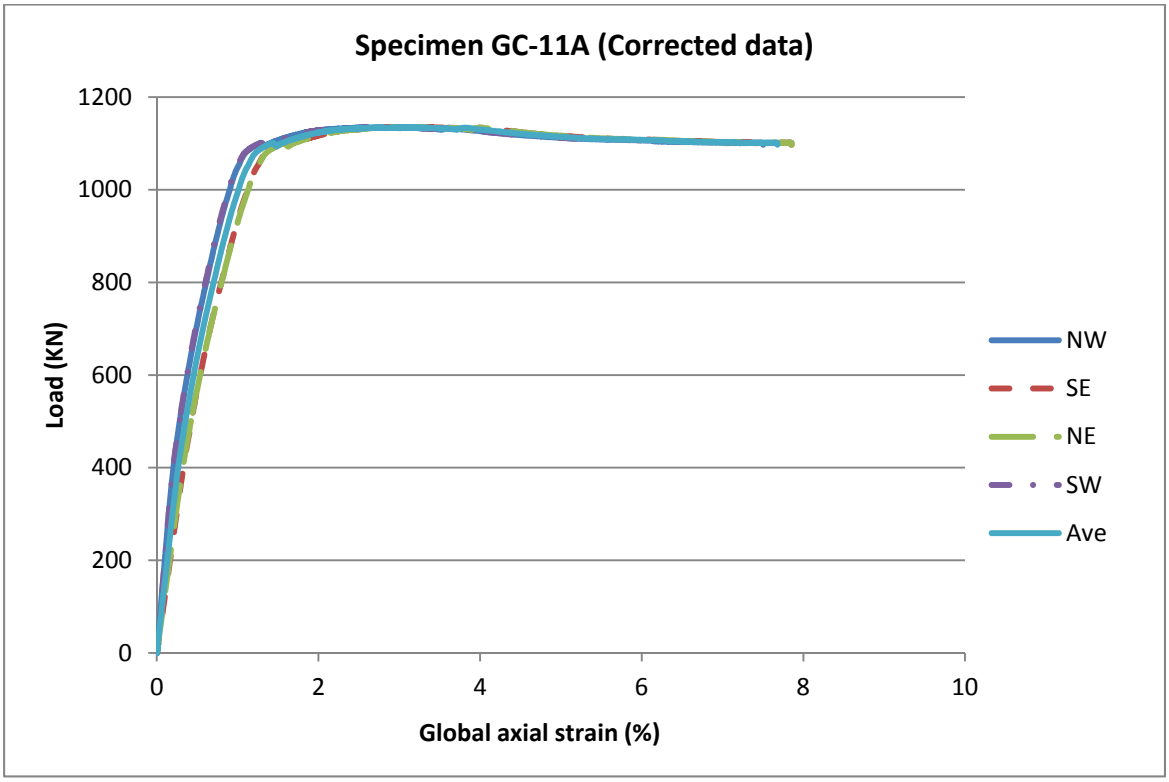

Figure 144: Load/global-axial-strain relationship

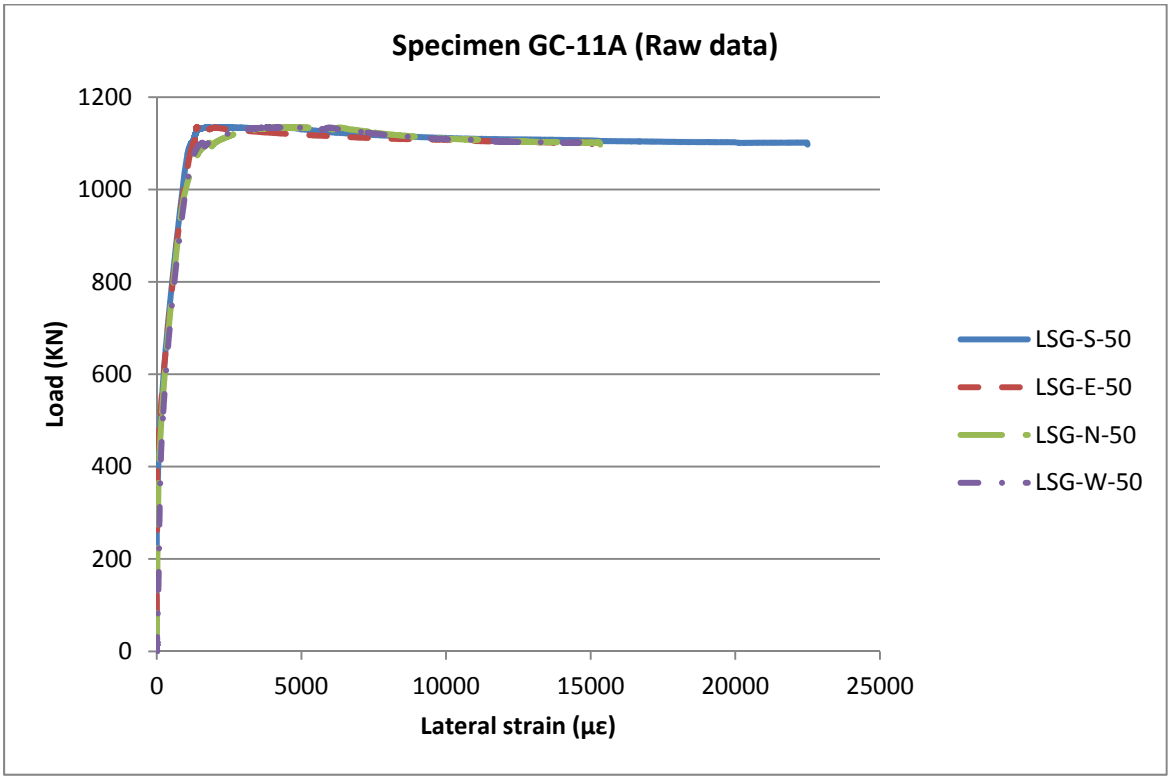

Figure 145: Load/lateral-strain relationship

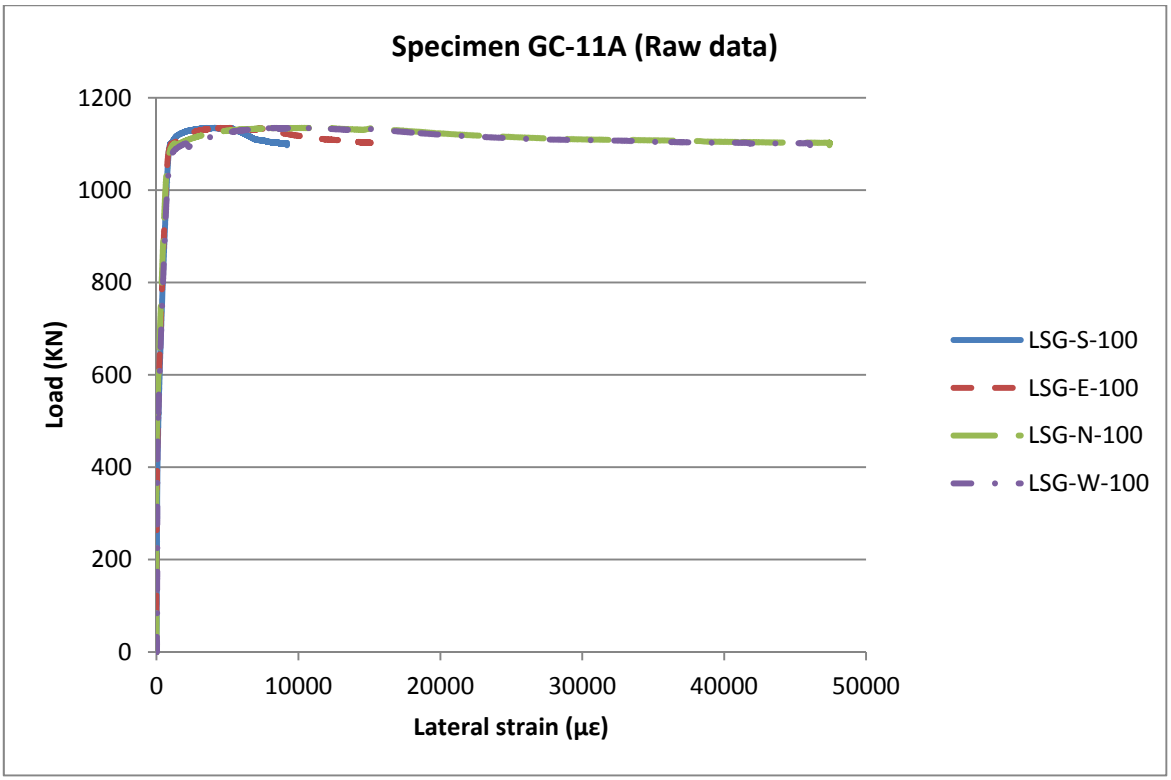

Figure 146: Load/lateral-strain relationship

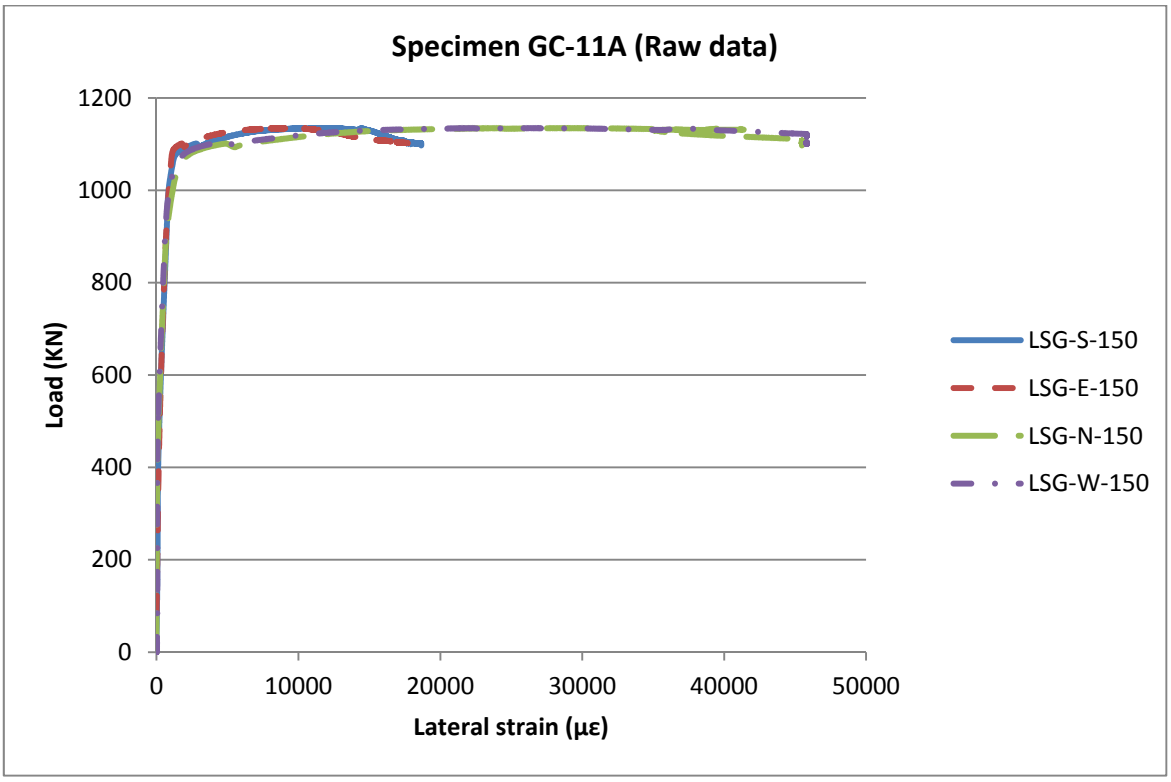

Figure 147: Load/lateral-strain relationship

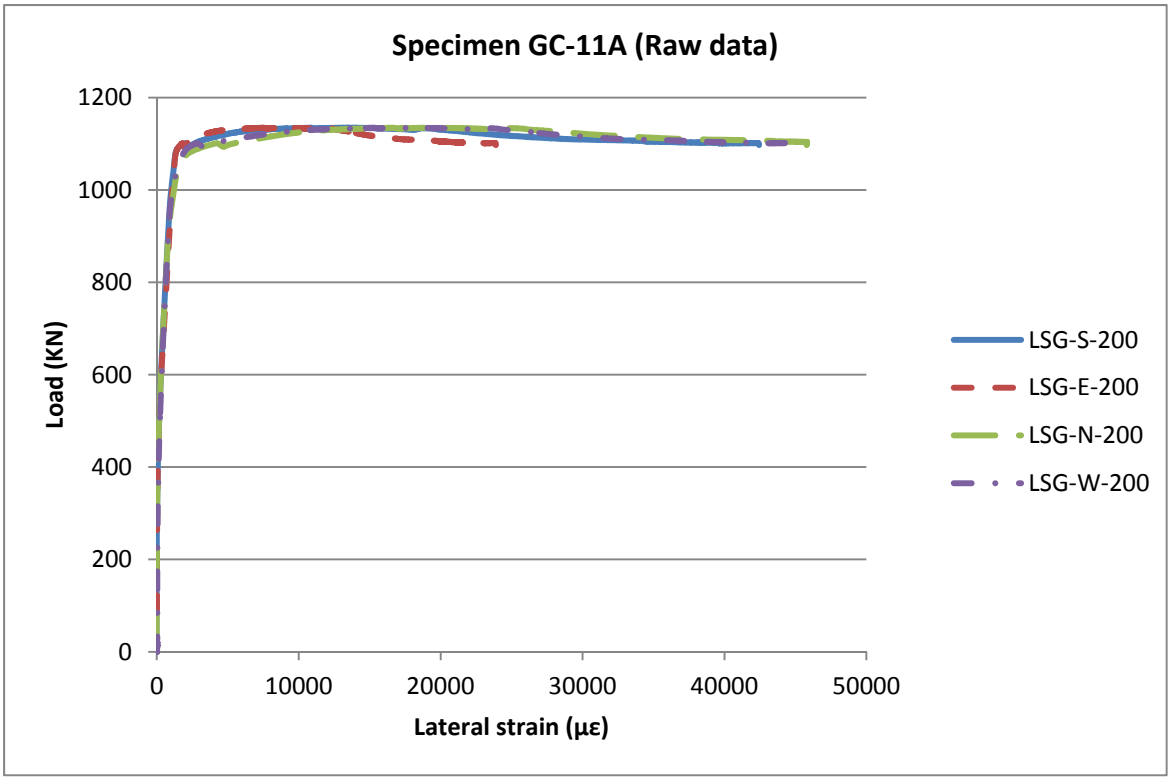

Figure 148: Load/lateral-strain relationship

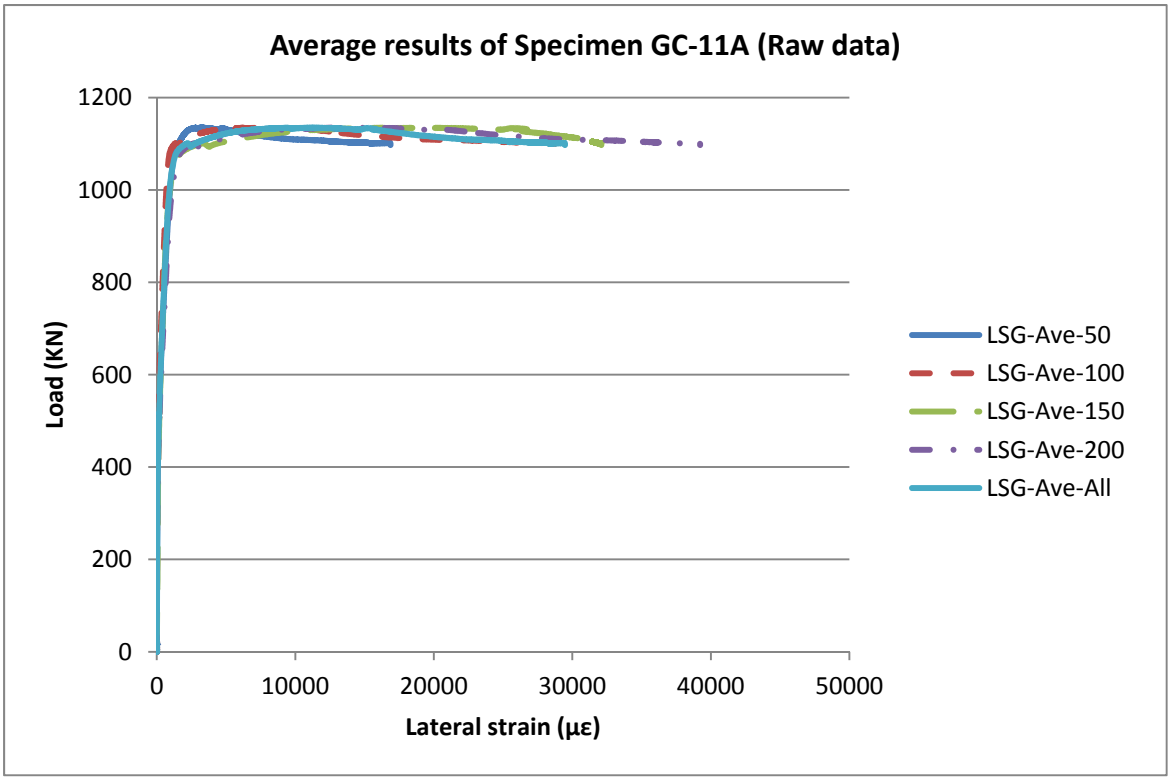

Figure 149: Load/lateral-strain relationship

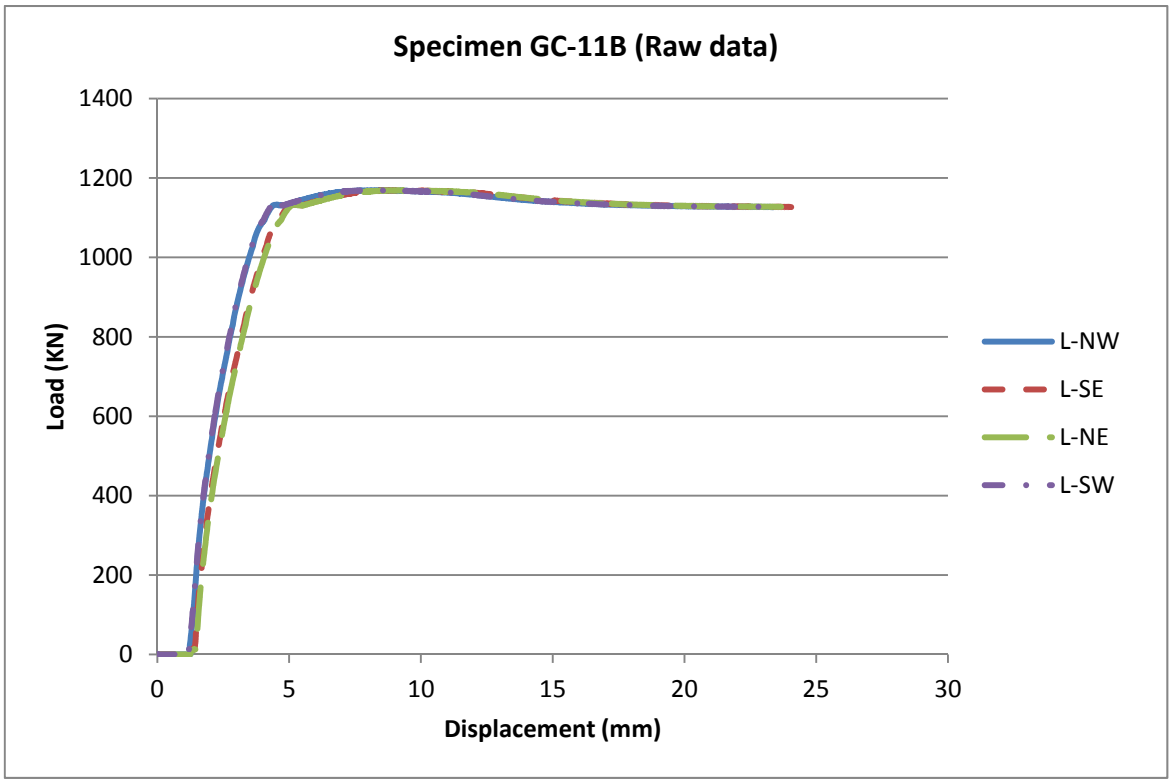

Figure 150: Load/axial-displacement relationship

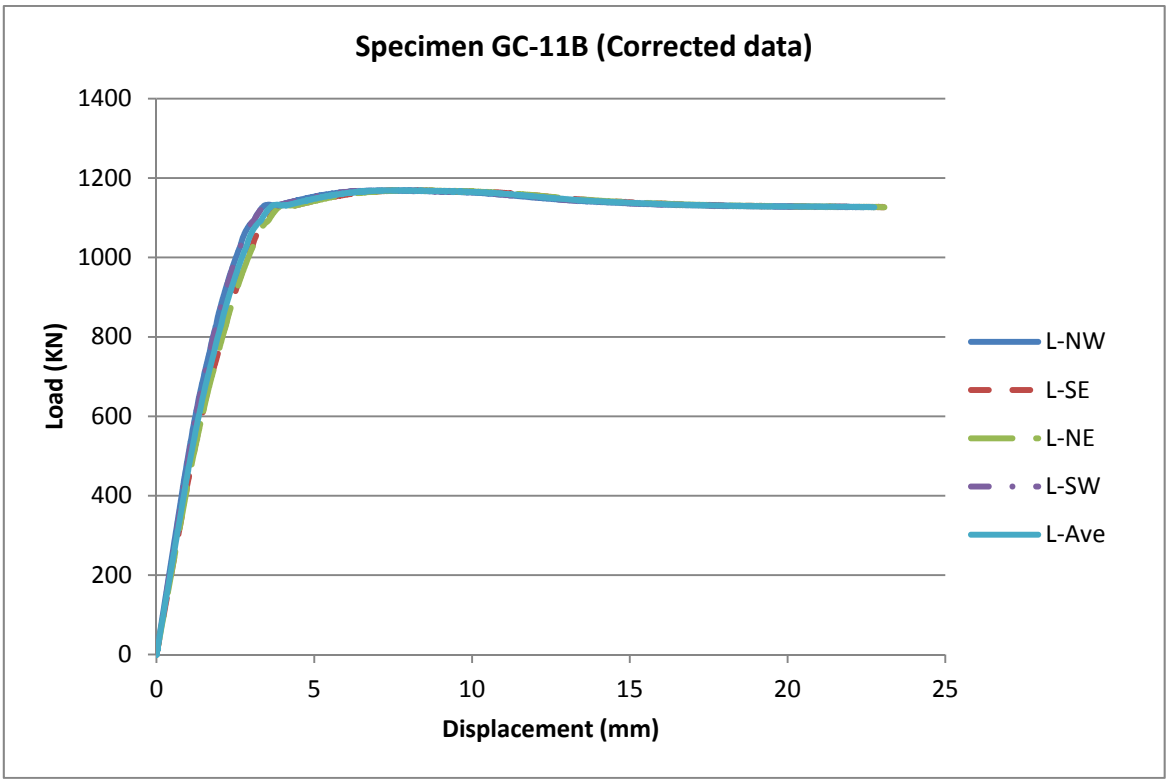

Figure 151: Load/axial-displacement relationship

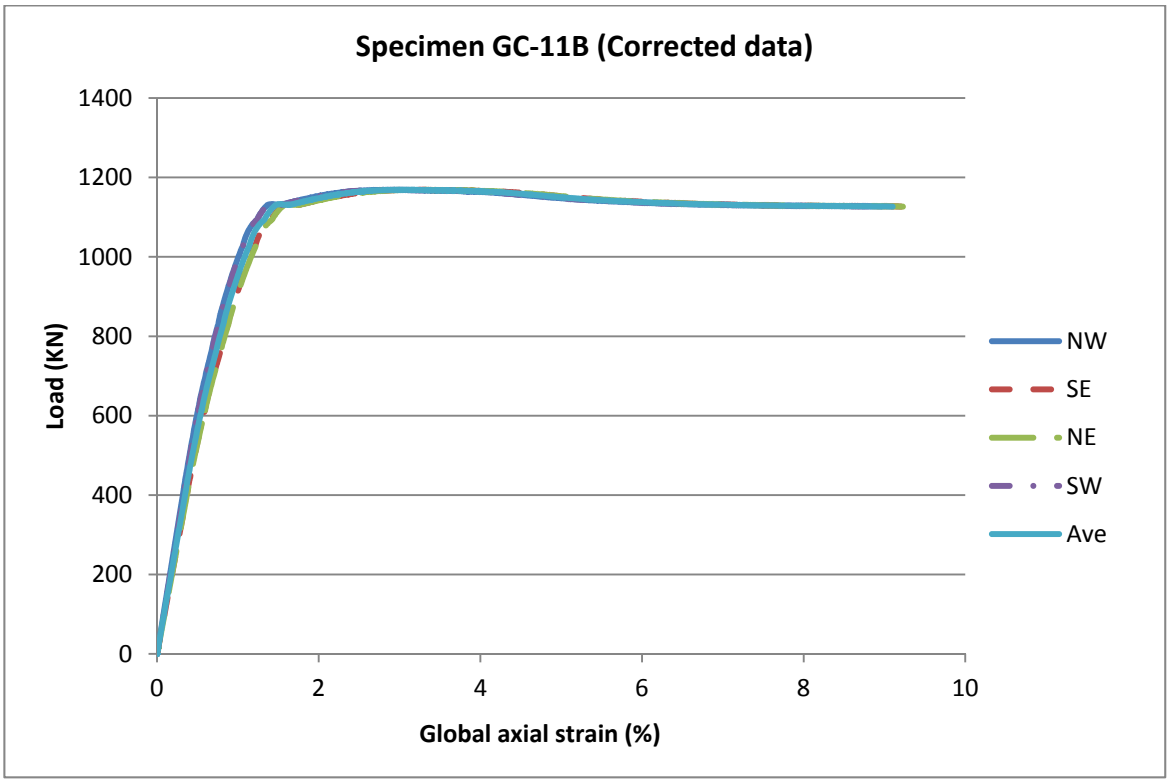

Figure 152: Load/global-axial-strain relationship

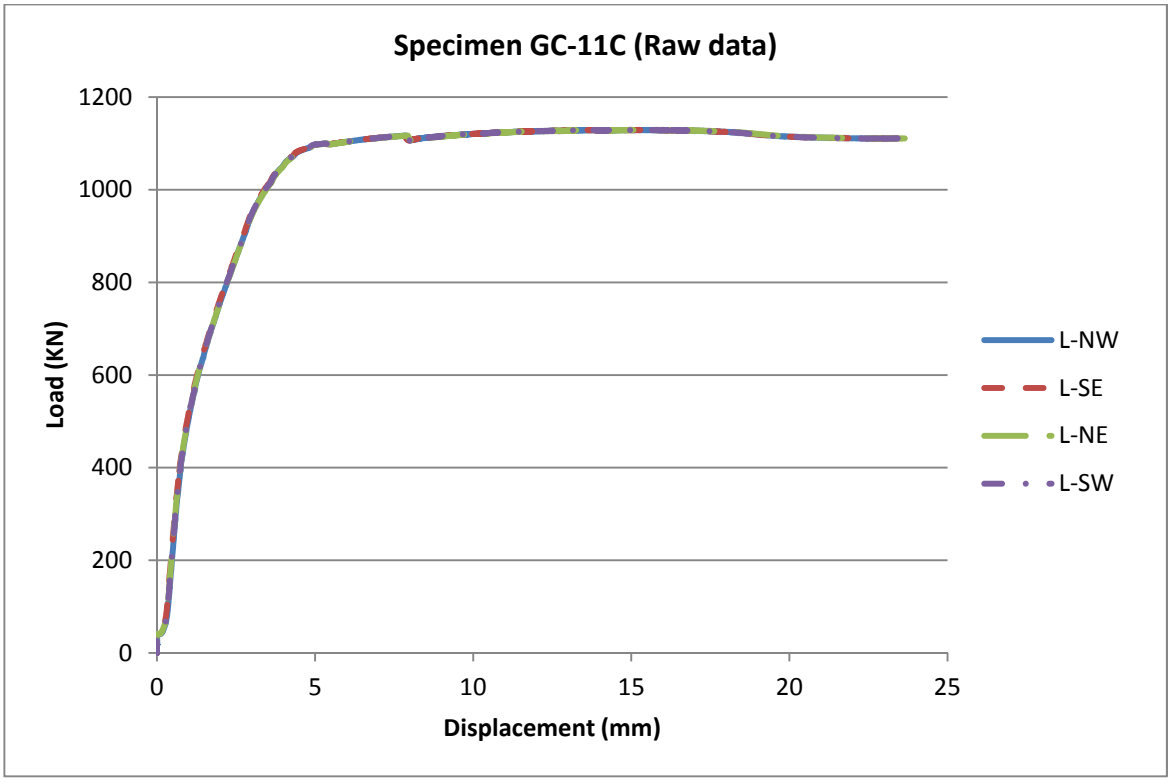

Figure 153: Load/axial-displacement relationship

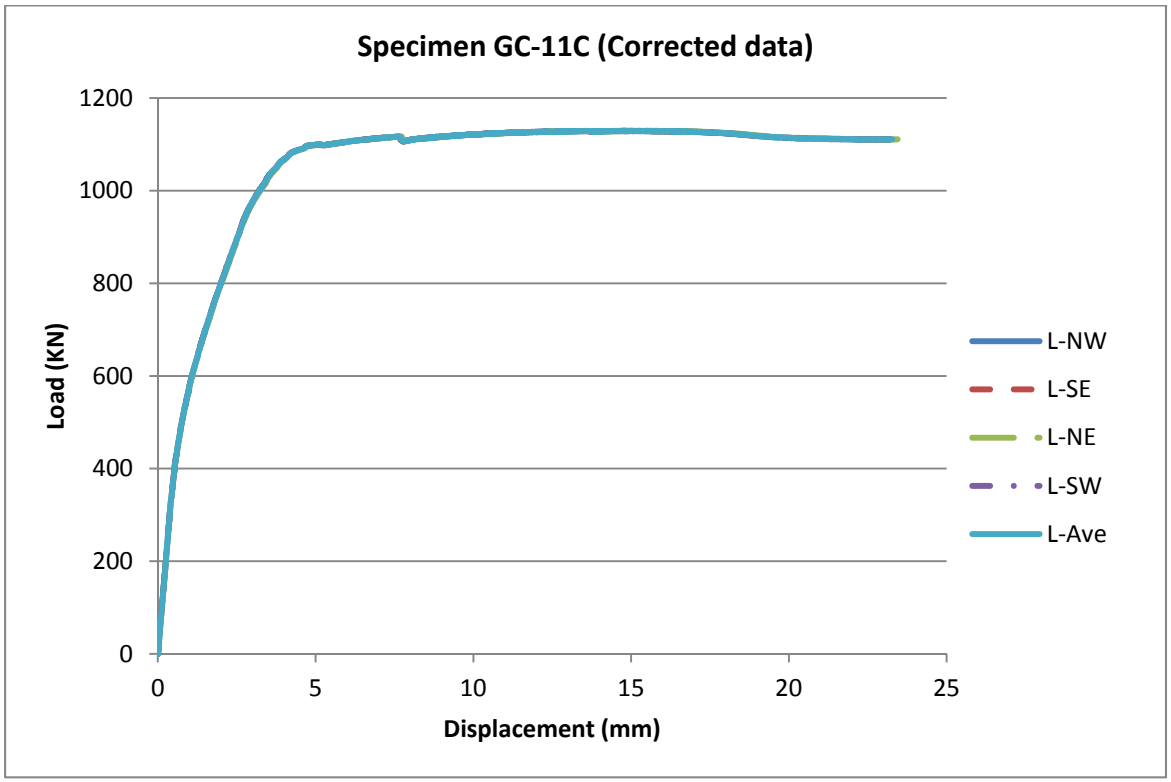

Figure 154: Load/axial-displacement relationship

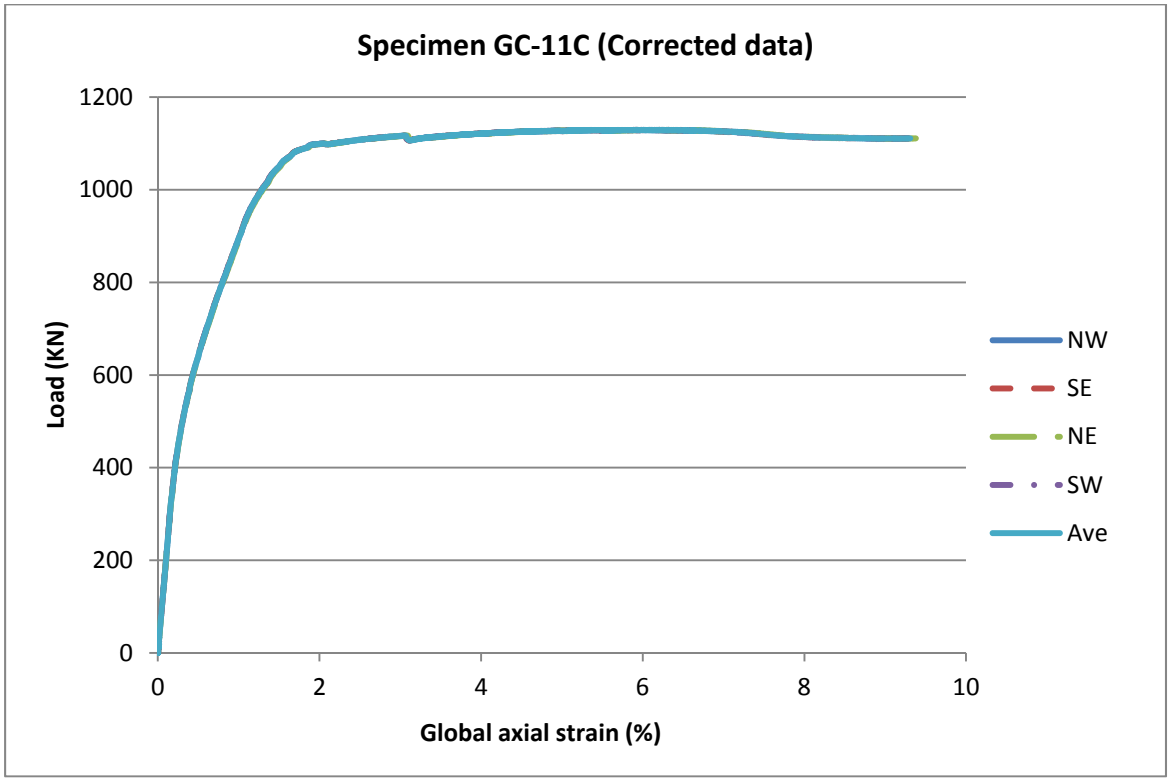

Figure 155: Load/global-axial-strain relationship

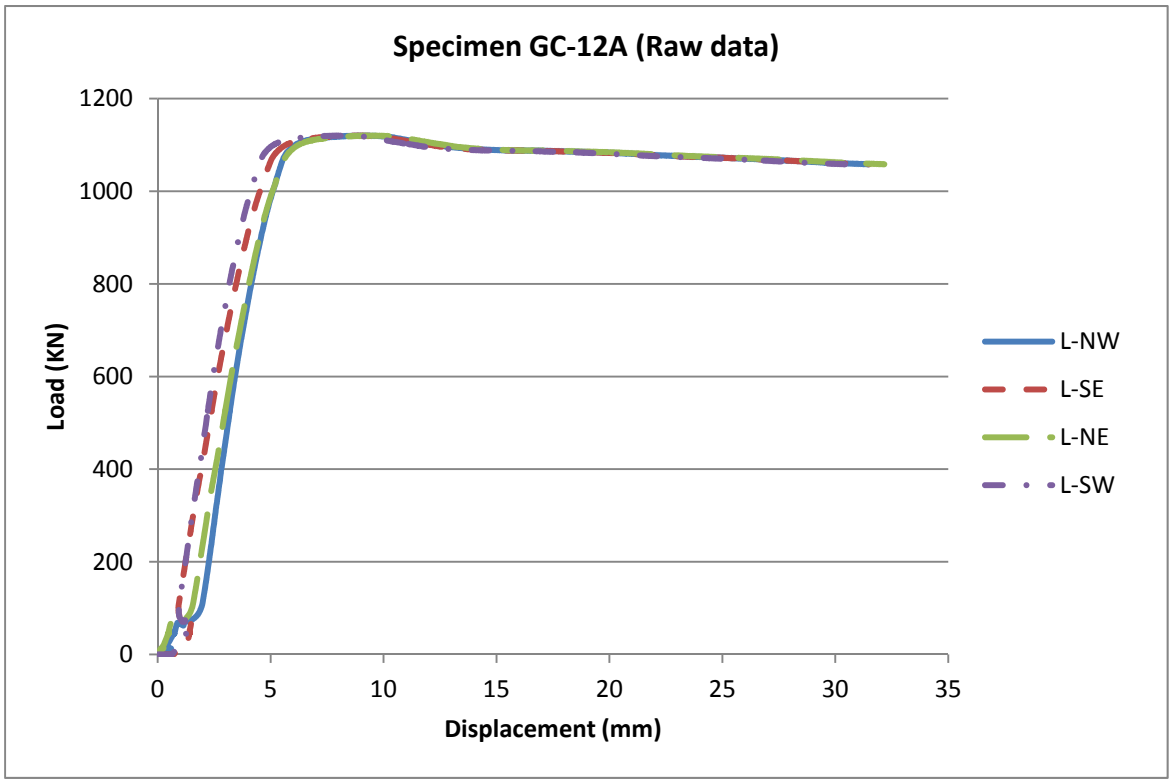

Figure 156: Load/axial-displacement relationship

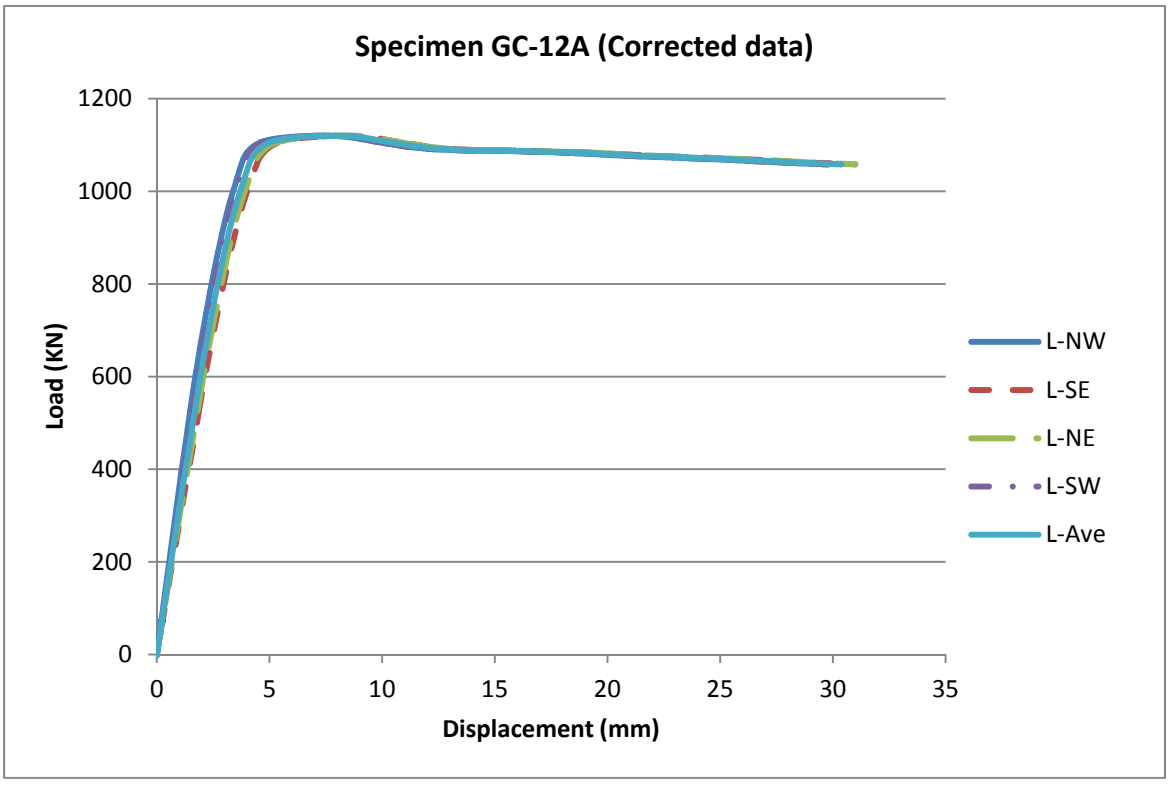

Figure 157: Load/axial-displacement relationship

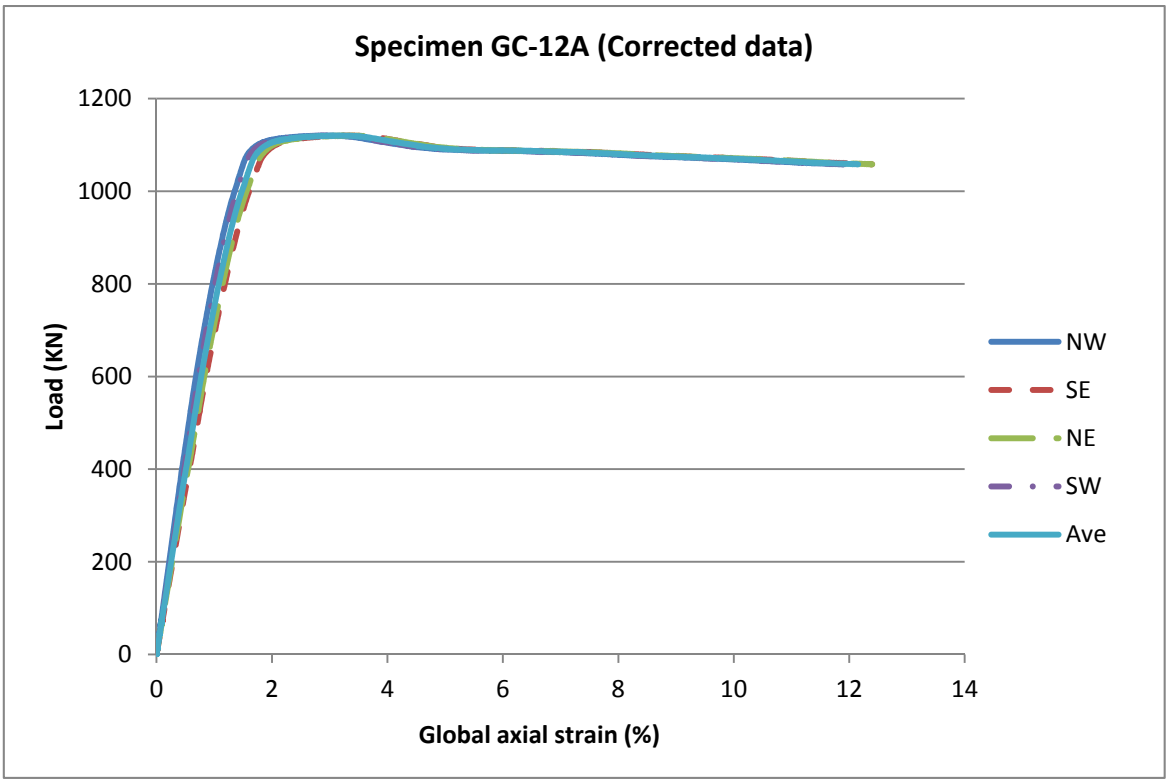

Figure 158: Load/global-axial-strain relationship

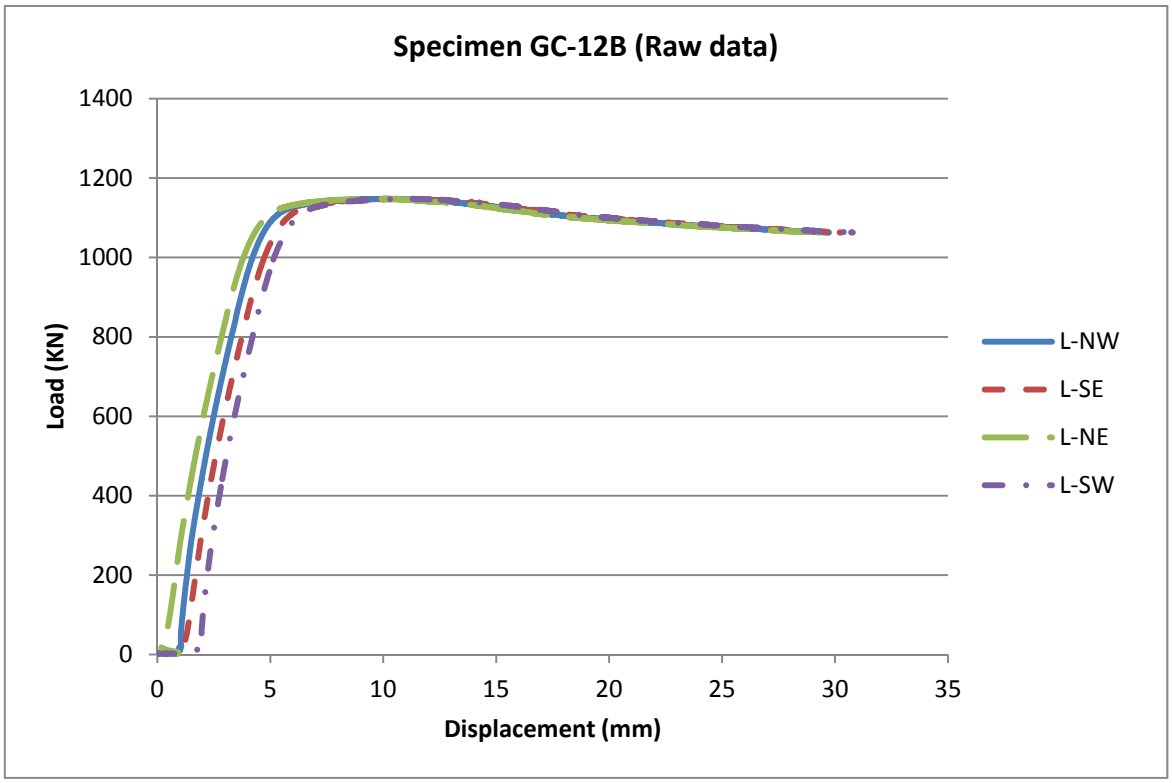

Figure 159: Load/axial-displacement relationship

Figure 160: Load/axial-displacement relationship

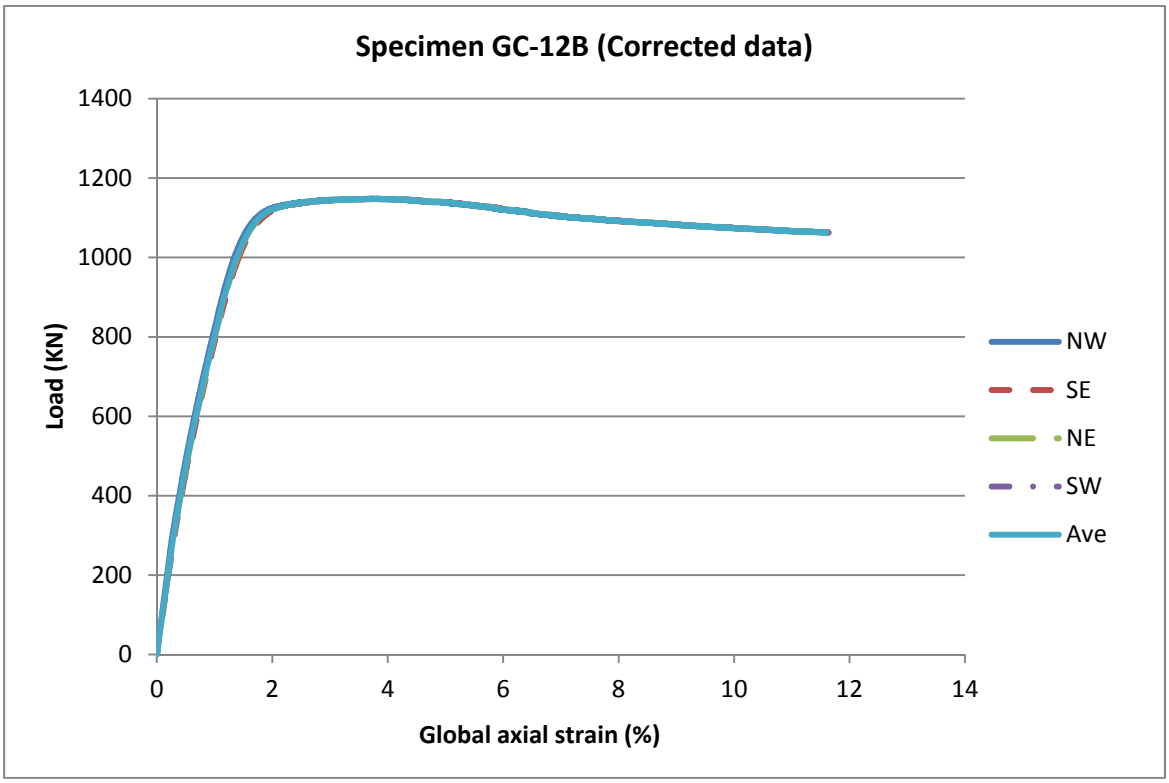

Figure 161: Load/global-axial-strain relationship

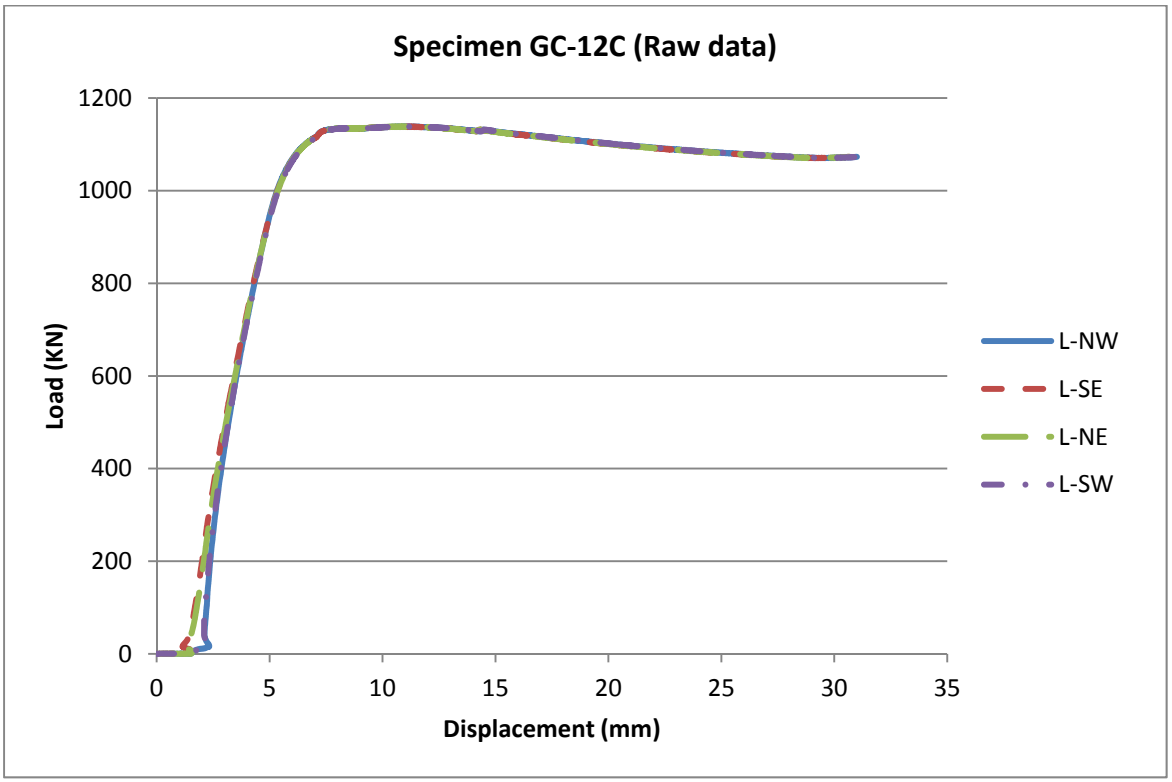

Figure 162: Load/axial-displacement relationship

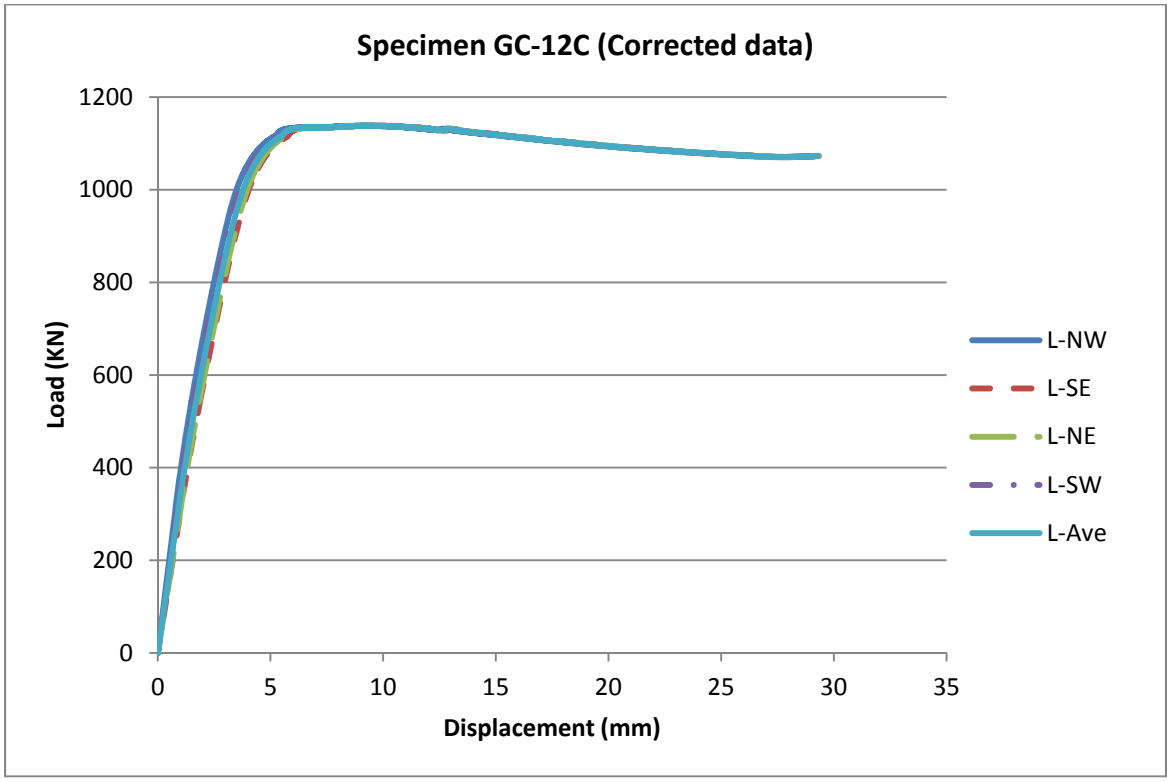

Figure 163: Load/axial-displacement relationship

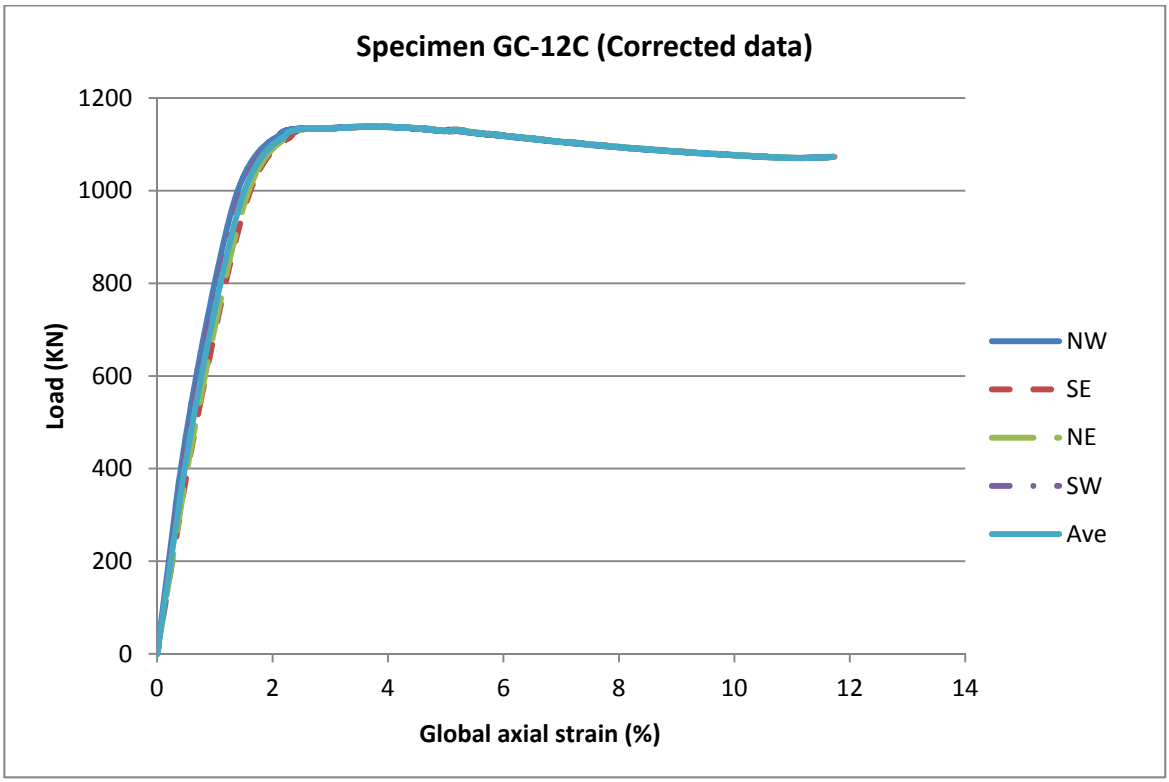

Figure 164: Load/global-axial-strain relationship

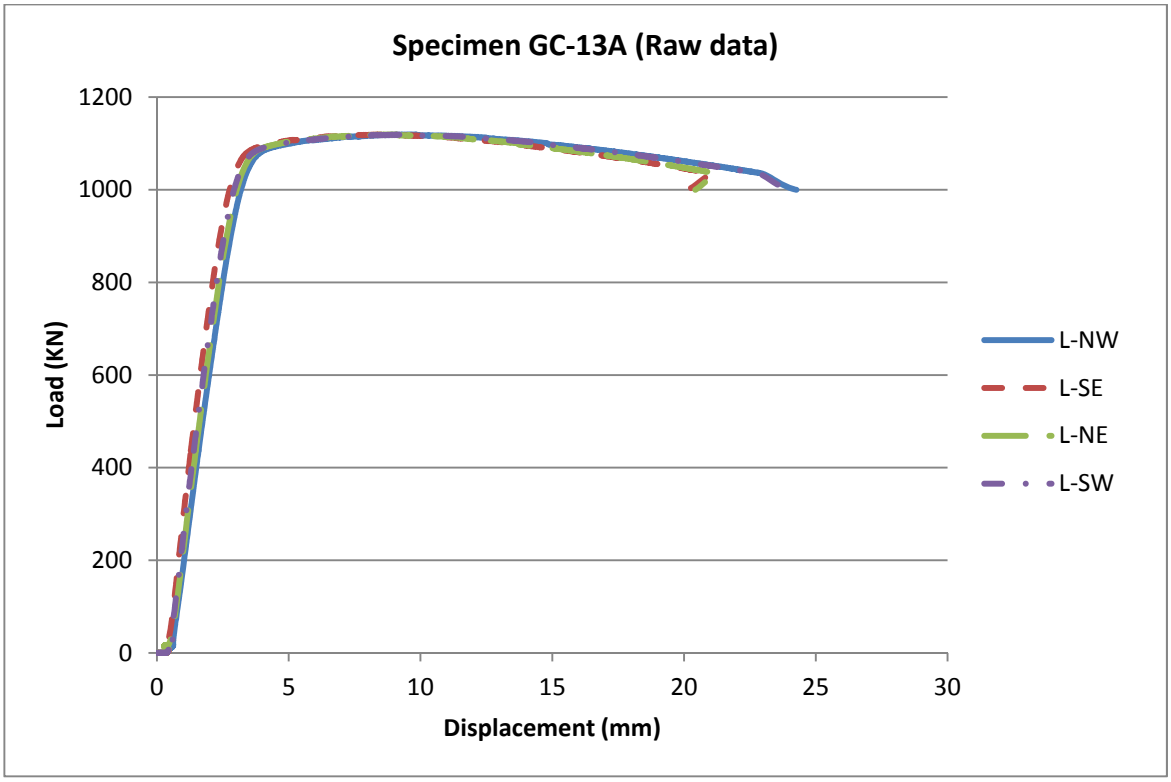

Figure 165: Load/axial-displacement relationship

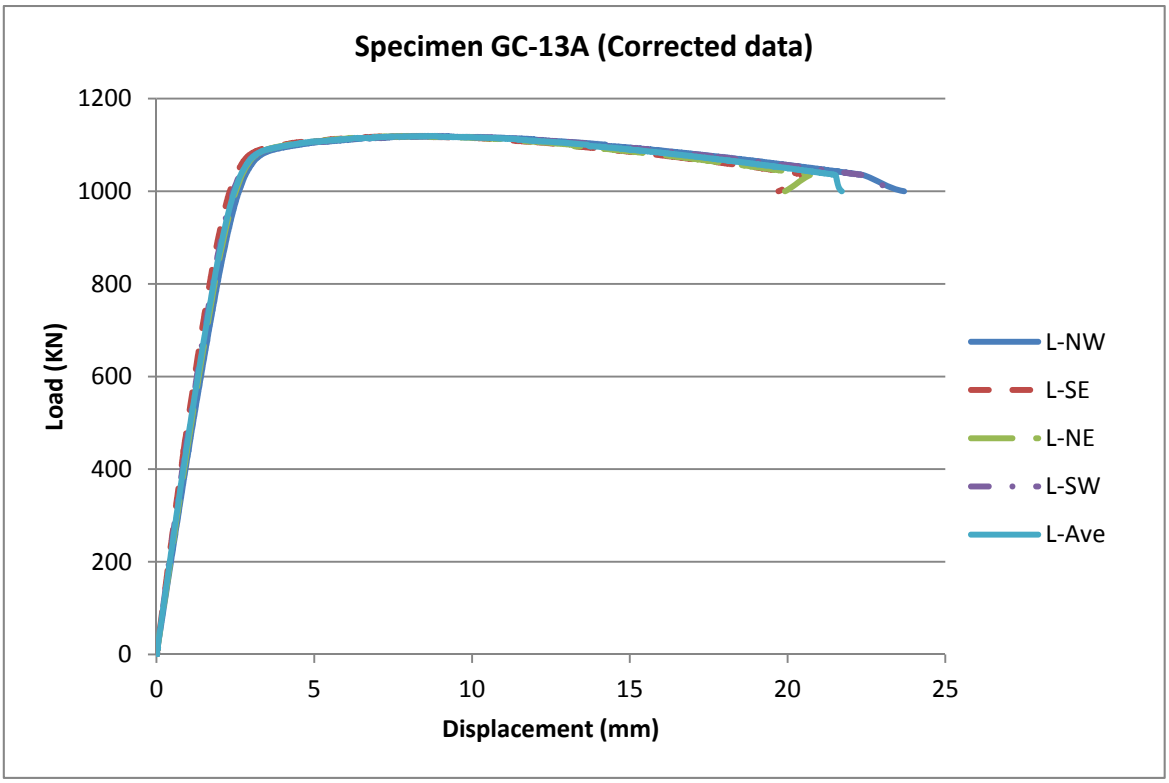

Figure 166: Load/axial-displacement relationship

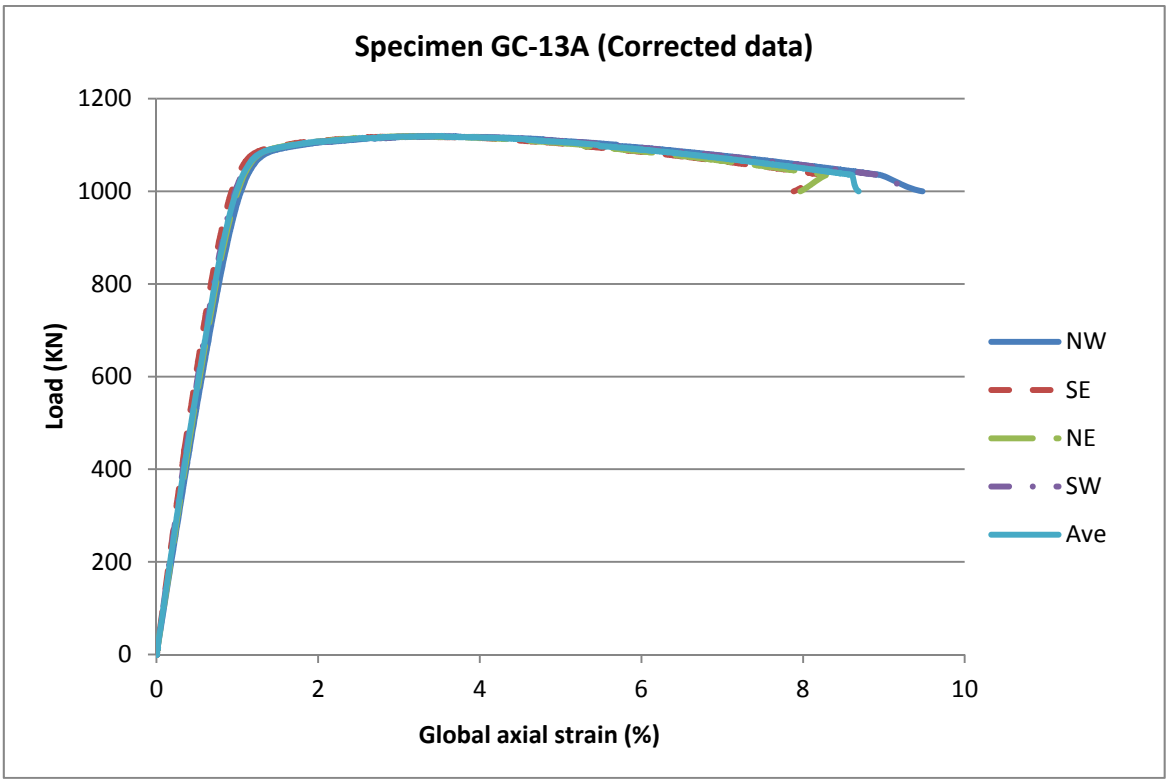

Figure 167: Load/global-axial-strain relationship

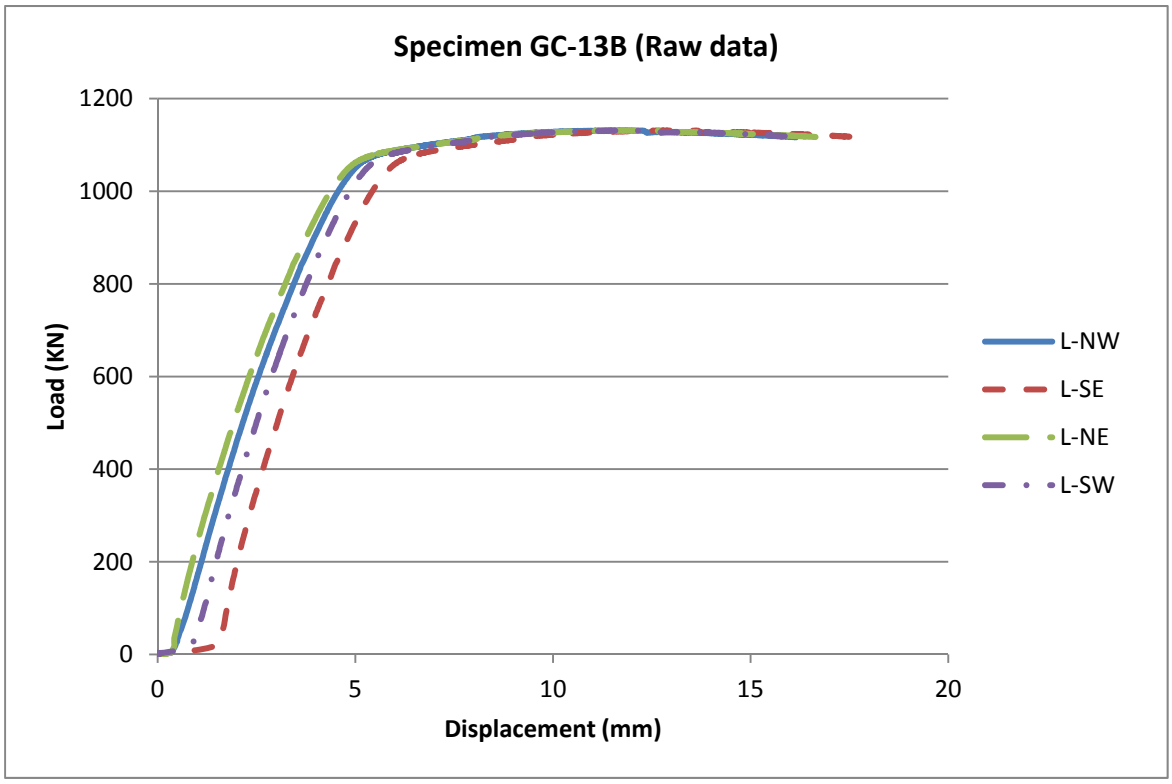

Figure 168: Load/axial-displacement relationship

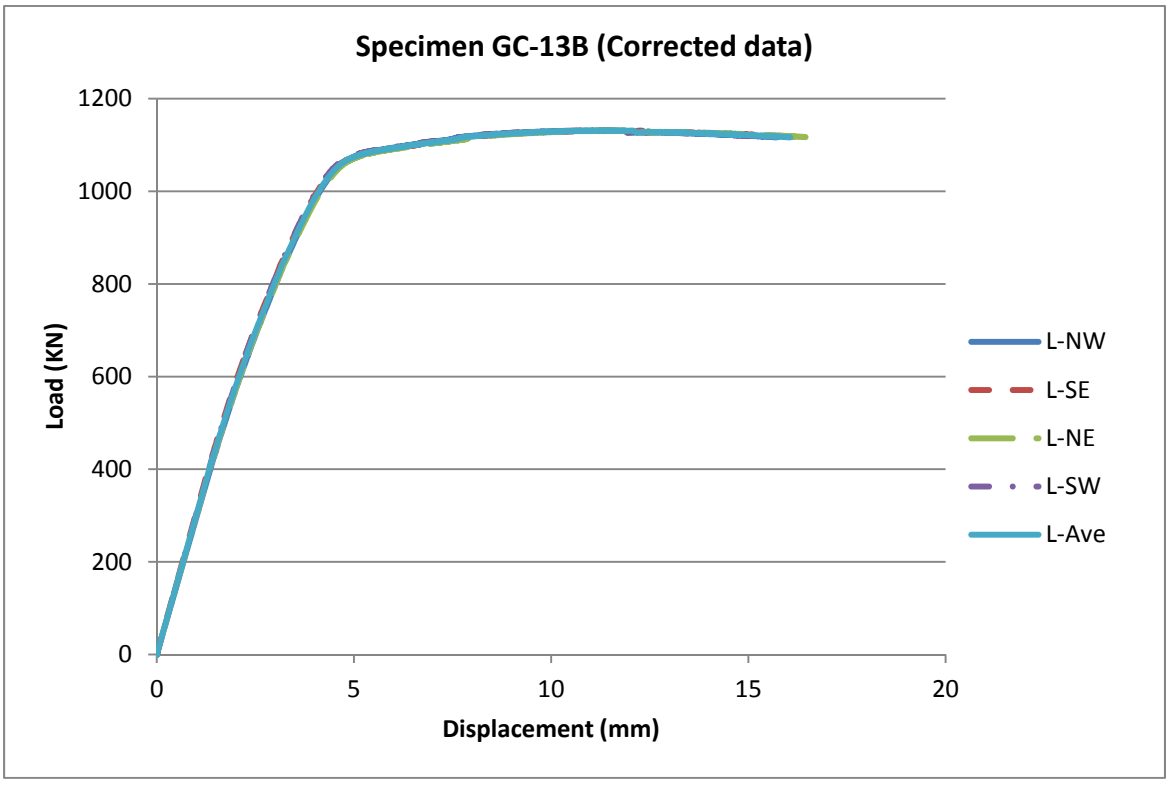

Figure 169: Load/axial-displacement relationship

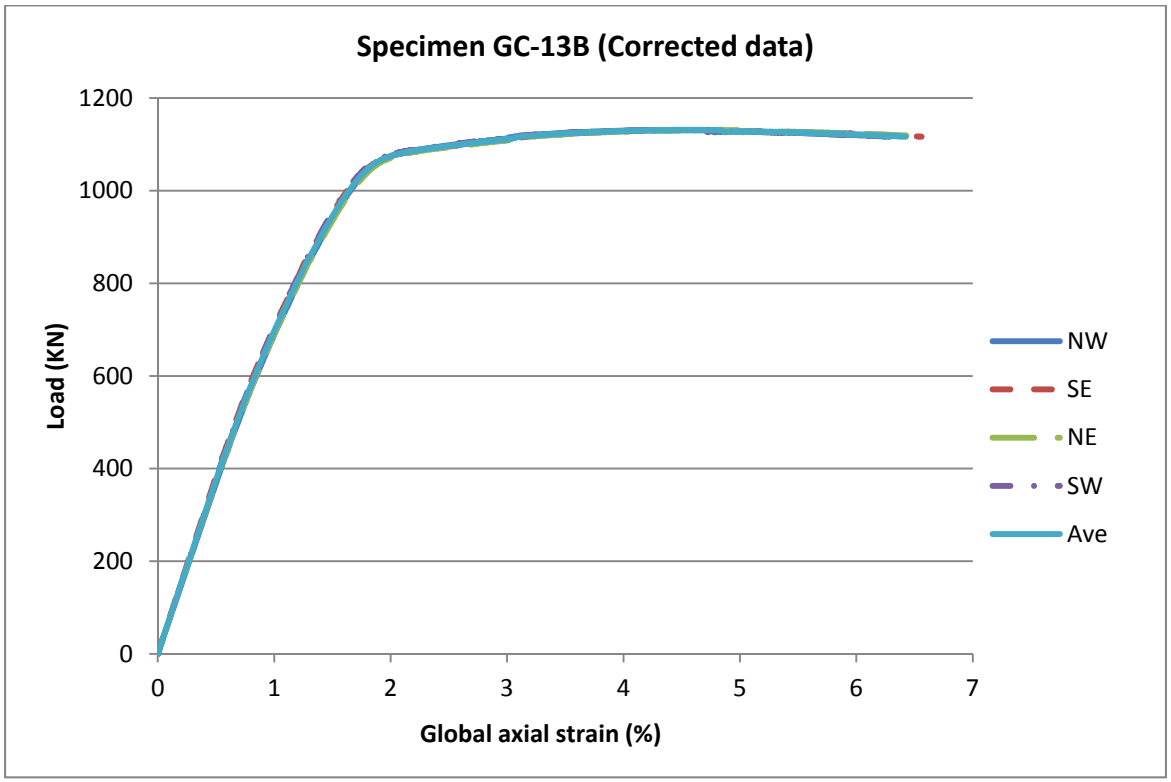

Figure 170: Load/global-axial-strain relationship

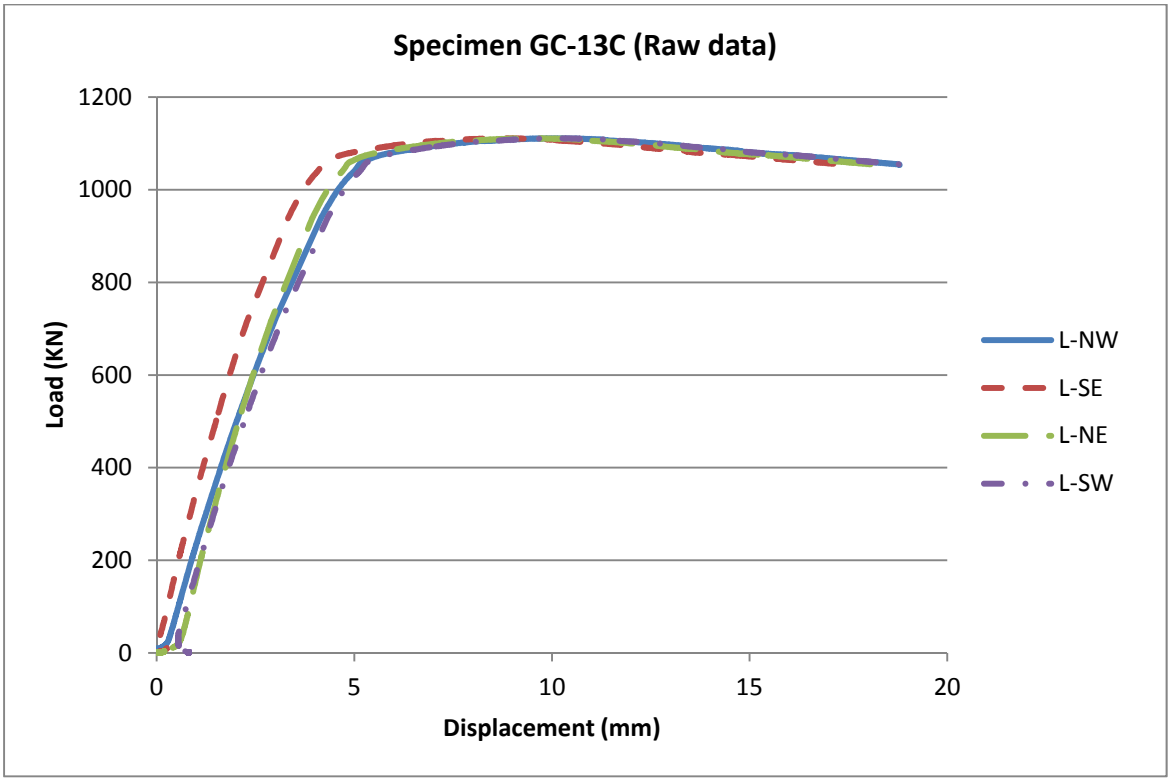

Figure 171: Load/axial-displacement relationship

Figure 172: Load/axial-displacement relationship

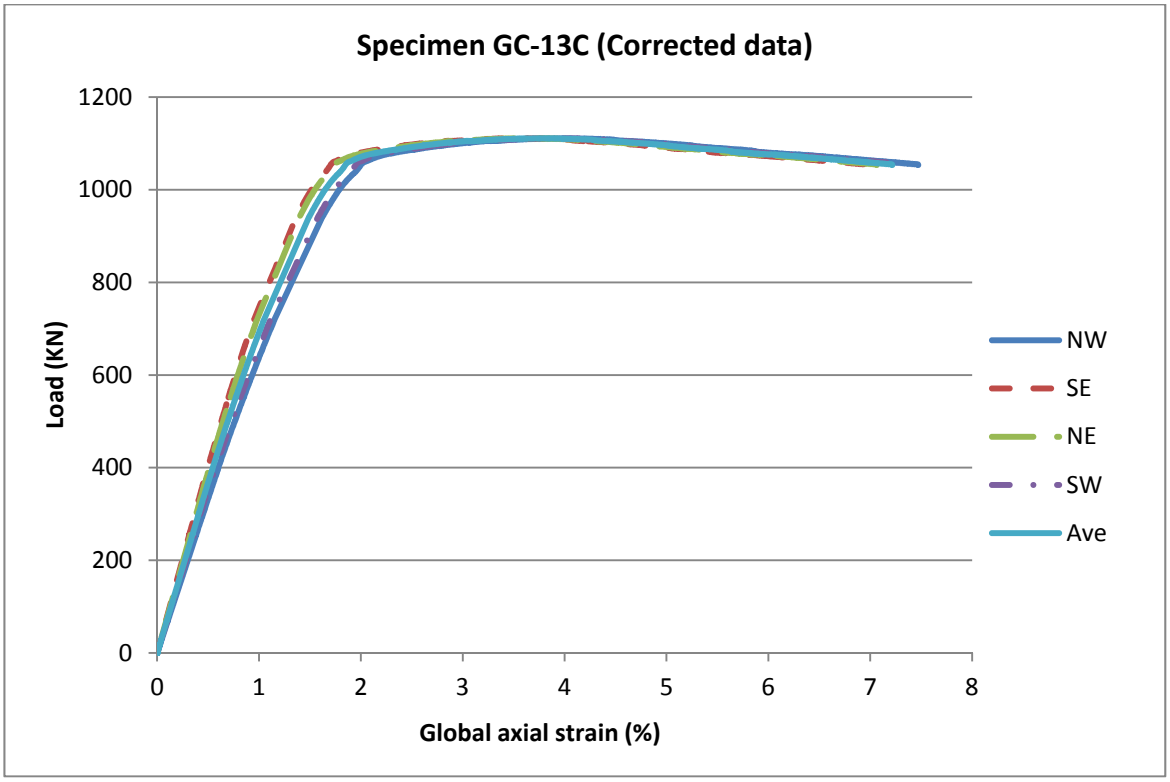

Figure 173: Load/global-axial-strain relationship

Table 5: Photos of tested specimens

No.	After test	Failure model	α_{Theo} (degree)	α_{Exp} (degree)	$\frac{\alpha_{Theo}}{\alpha_{Exp}}$
①	②	③	④	⑤	⑥
GA-1A		 single sliding plane	39.4	36.6	1.08
GA-1B		 single sliding plane	39.4	38.8	1.02
GA-1C		 single sliding plane	39.4	40.9	0.96

Table 5: Photos of tested specimens (continued)

No.	After test	Failure model	α_{Theo} (degree)	α_{Exp} (degree)	$\frac{\alpha_{Theo}}{\alpha_{Exp}}$
①	②	③	④	⑤	⑥
GA-2A		 single sliding plane	39.4	43.7	0.90
GA-2B		 Bending, shear failure	39.4	36.3	1.09
GA-2C		 Bending, shear failure	39.4	34.9	1.13

Table 5: Photos of tested specimens (continued)

No.	After test	Failure model	α_{Theo} (degree)	α_{Exp} (degree)	$\frac{\alpha_{Theo}}{\alpha_{Exp}}$
①	②	③	④	⑤	⑥
GA-3A		 single sliding plane	39.4	36.6	1.08
GA-3B		 single sliding plane	39.4	36.9	1.07

Table 5: Photos of tested specimens (continued)

No.	After test	Failure model	α_{Theo} (degree)	α_{Exp} (degree)	$\frac{\alpha_{Theo}}{\alpha_{Exp}}$
①	②	③	④	⑤	⑥
GB-4A		 single sliding plane	39.3	35.2	1.12
GB-4B		 circumferential wedge	39.3	33.7	1.17
GB-4C		 circumferential wedge	39.3	40.0	0.98

Table 5: Photos of tested specimens (continued)

No.	After test	Failure model	α_{Theo} (degree)	α_{Exp} (degree)	$\frac{\alpha_{Theo}}{\alpha_{Exp}}$
①	②	③	④	⑤	⑥
GB-5A		 circumferential wedge	39.3	30.0	1.31
GB-5B		 circumferential wedge	39.3	31.5	1.25
GB-5C		 single sliding plane	39.3	32.8	1.20

Table 5: Photos of tested specimens (continued)

No.	After test	Failure model	α_{Theo} (degree)	α_{Exp} (degree)	$\frac{\alpha_{Theo}}{\alpha_{Exp}}$
①	②	③	④	⑤	⑥
GB-6A		 single sliding plane	39.3	35.0	1.12
GB-6B		 single sliding plane	39.3	42.0	0.94
GB-6C		 single sliding plane	39.3	36.0	1.09

Table 5: Photos of tested specimens (continued)

No.	After test	Failure model	α_{Theo} (degree)	α_{Exp} (degree)	$\frac{\alpha_{Theo}}{\alpha_{Exp}}$
①	②	③	④	⑤	⑥
GD-7A		 single sliding plane	37.6	38.2	0.98
GD-7B		 Bending, shear failure	37.6	31.5	1.19
GD-7C		 circumferential wedge	37.6	42.0	0.89

Table 5: Photos of tested specimens (continued)

No.	After test	Failure model	α_{Theo} (degree)	α_{Exp} (degree)	$\frac{\alpha_{Theo}}{\alpha_{Exp}}$
①	②	③	④	⑤	⑥
GE-8A		 single sliding plane	36.9	60.0	0.62
GE-8B		 single sliding plane	36.9	42.0	0.88
GE-8C		 single sliding plane	36.9	81.0	0.46

Table 5: Photos of tested specimens (continued)

No.	After test	Failure model	α_{Theo} (degree)	α_{Exp} (degree)	$\frac{\alpha_{Theo}}{\alpha_{Exp}}$
①	②	③	④	⑤	⑥
GD-9A		 single sliding plane	37.6	39.0	0.96
GD-9B		 single sliding plane	37.6	34.5	1.09
GD-9C		 circumferential wedge	37.6	41.2	0.91

Table 5: Photos of tested specimens (continued)

No.	After test	Failure model	α_{Theo} (degree)	α_{Exp} (degree)	$\frac{\alpha_{Theo}}{\alpha_{Exp}}$
①	②	③	④	⑤	⑥
GE-10A		 single sliding plane	36.9	42.0	0.88
GE-10B		 single sliding plane	36.9	38.5	0.96
GE-10C		 single sliding plane	36.9	39.5	0.94

Table 5: Photos of tested specimens (continued)

No.	After test	Failure model	α_{Theo} (degree)	α_{Exp} (degree)	$\frac{\alpha_{Theo}}{\alpha_{Exp}}$
①	②	③	④	⑤	⑥
GC-11A		 single sliding plane	39.4	41.0	0.96
GC-11B		 single sliding plane	39.4	38.0	1.04
GC-11C		 single sliding plane	39.4	44.5	0.89

Table 5: Photos of tested specimens (continued)

No.	After test	Failure model	α_{Theo} (degree)	α_{Exp} (degree)	$\frac{\alpha_{Theo}}{\alpha_{Exp}}$
①	②	③	④	⑤	⑥
GC-12A		 single sliding plane	39.4	40.0	0.99
GC-12B		 single sliding plane	39.4	38.0	1.04
GC-12C		 Bending, shear failure	39.4	36.5	1.08

Table 5: Photos of tested specimens (continued)

No.	After test	Failure model	α_{Theo} (degree)	α_{Exp} (degree)	$\frac{\alpha_{Theo}}{\alpha_{Exp}}$
①	②	③	④	⑤	⑥
GC-13A		 single sliding plane	39.4	41.0	0.96
GC-13B		 single sliding plane	39.4	39.0	1.01
GC-13C		 single sliding plane	39.4	60.0	0.66

6. Results of analysis and discussion

6.1 Buckling

The loading platen is always flat during the loading process which forces the metal plate flat as well. Figure 174 shows the enlarged top end of specimen GA-2C after testing in which there is local crushing on left-side and small gap on right-side of the metal plate. Hence, even though some specimens, such as Specimen GA-2C as shown in Table 5, have significant curvature, the load/axial-displacement relationships recorded from different LVDTs, are still almost identical as shown in Figures 30 and 31. Hence this type of specimen was loaded uniformly so that failure is due to buckling inducing flexure and this has been referred to in Table 5 as *bending, shear failure* where *bending* relates to the moment induced whilst buckling and *shear failure* to the shear sliding wedges. It would, therefore, be expected that the stress/global-axial-strain relationship will have a steeper descent than expected from its material properties due to the moment induced by buckling.

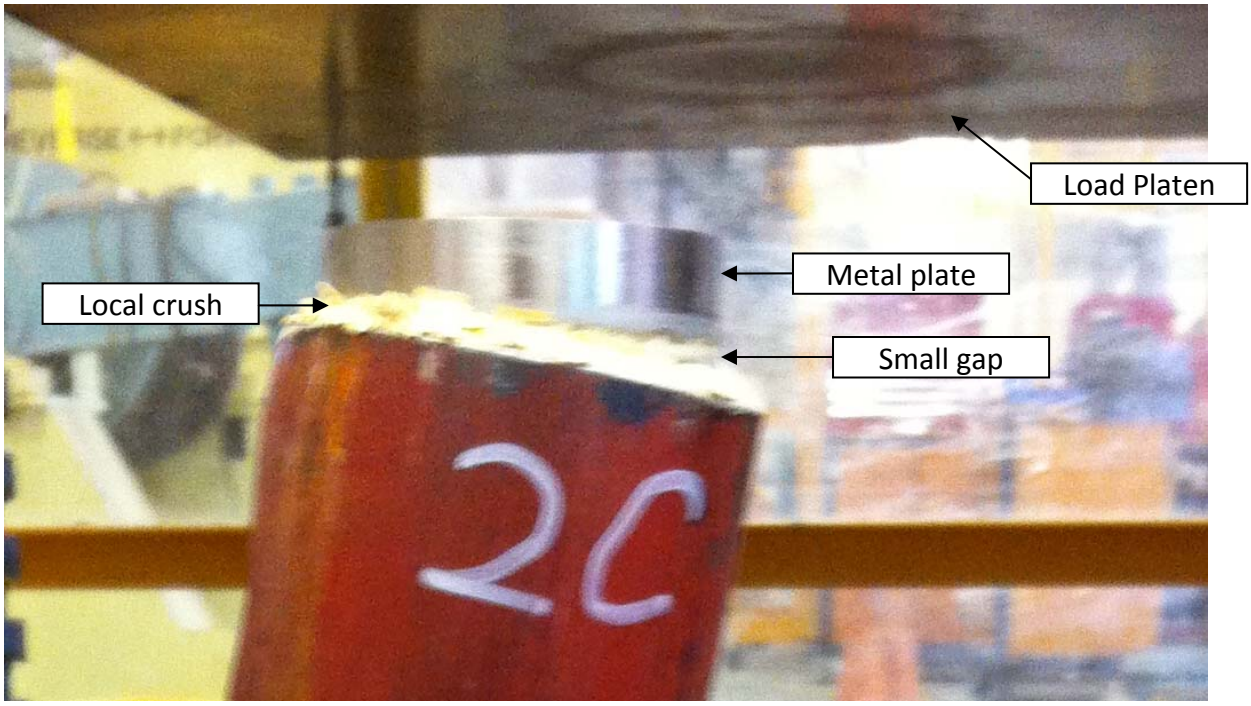

Figure 174: Enlarged top end of specimen GA-2C

6.2 Axial size effect

Three groups of specimen (Group A, Group B and Group C in Table 4), whose diameters are the same and lengths were varied in each group, were designed to verify the axial size effect expression, Equation 4, for the axial size of the specimen η_{ax}. For Group A, whose diameters were all 76.1 mm, and had lengths of 250, 500 and 750 mm, the load/mean-value-of-global-axial-strains relationships derived from individual test results of load/global-axial-strains relationship (Figures 12, 20, 23, 26, 29, 32, 35 and 38) are compared in Figure 175; it can be seen that there is little variation in the groups of identical specimens such as 2A, 2B and 2C. Similarly, the load/mean-value-of-global-axial-strains relationships for Group B and Group C are shown in Figures 176 and 177 separately.

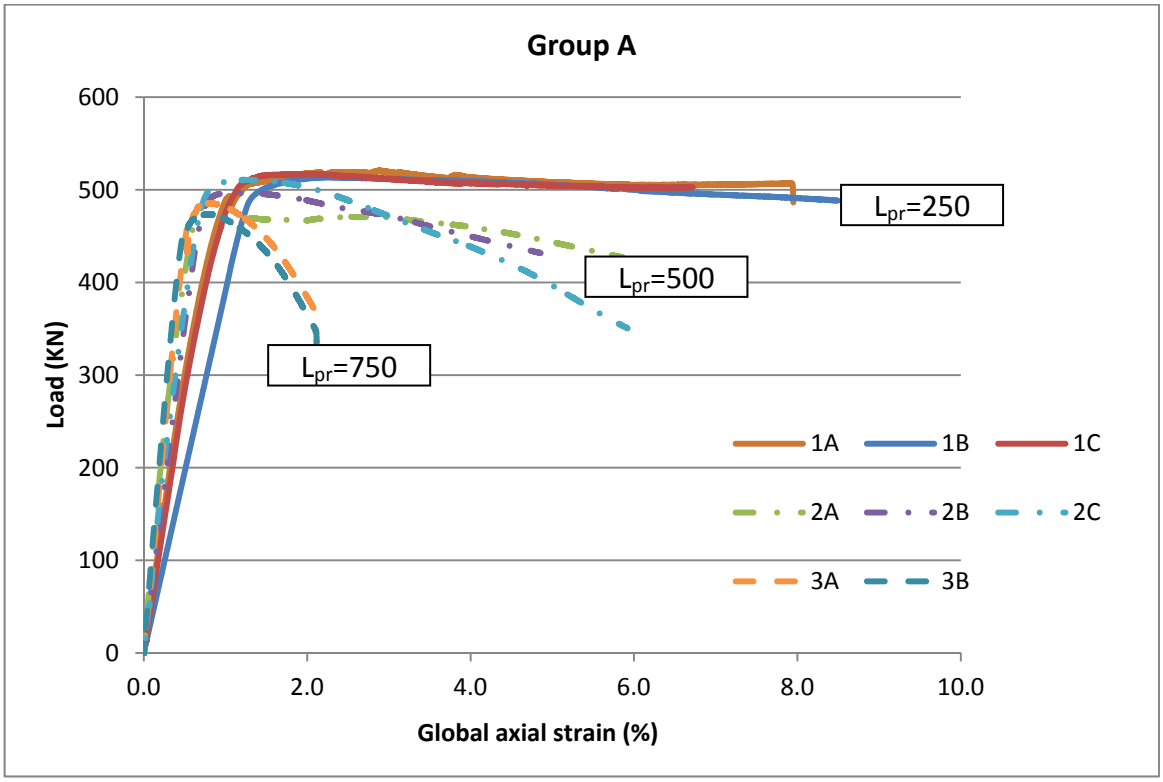

Figure 175: Load/mean-value-of-global-axial-strains relationships

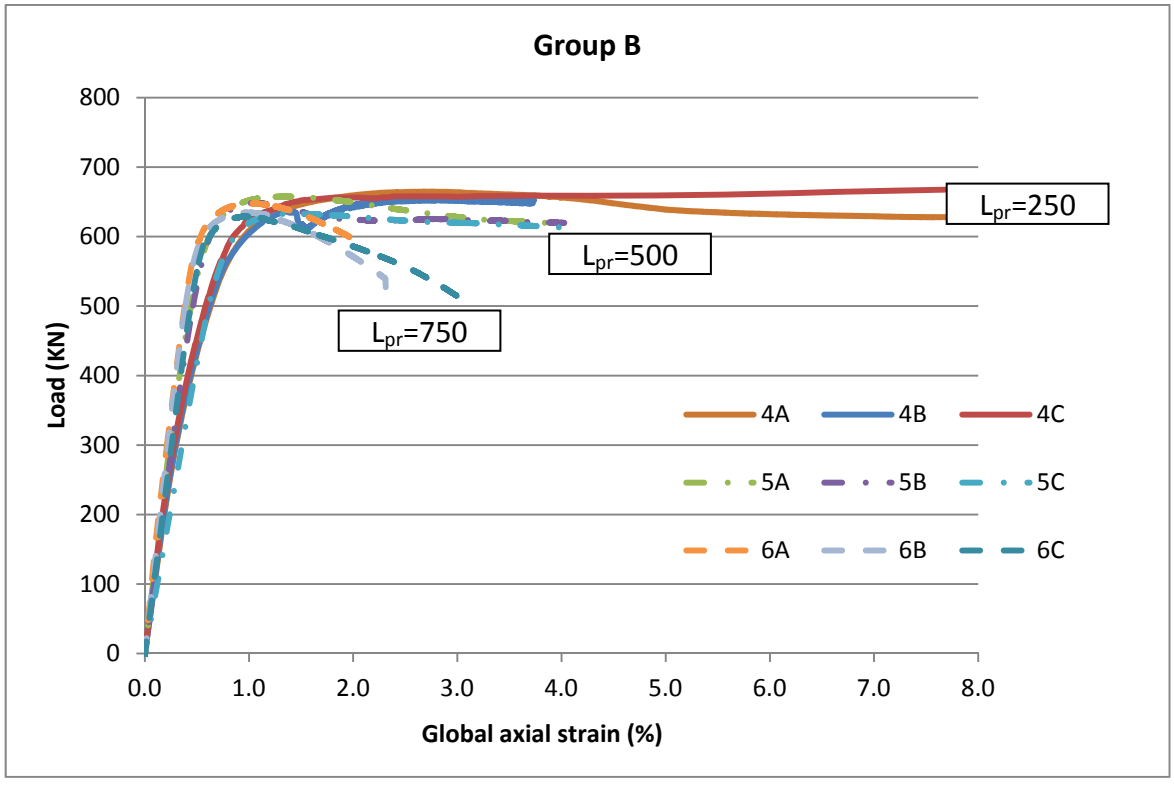

Figure 176: Load/mean-value-of-global-axial-strains relationships

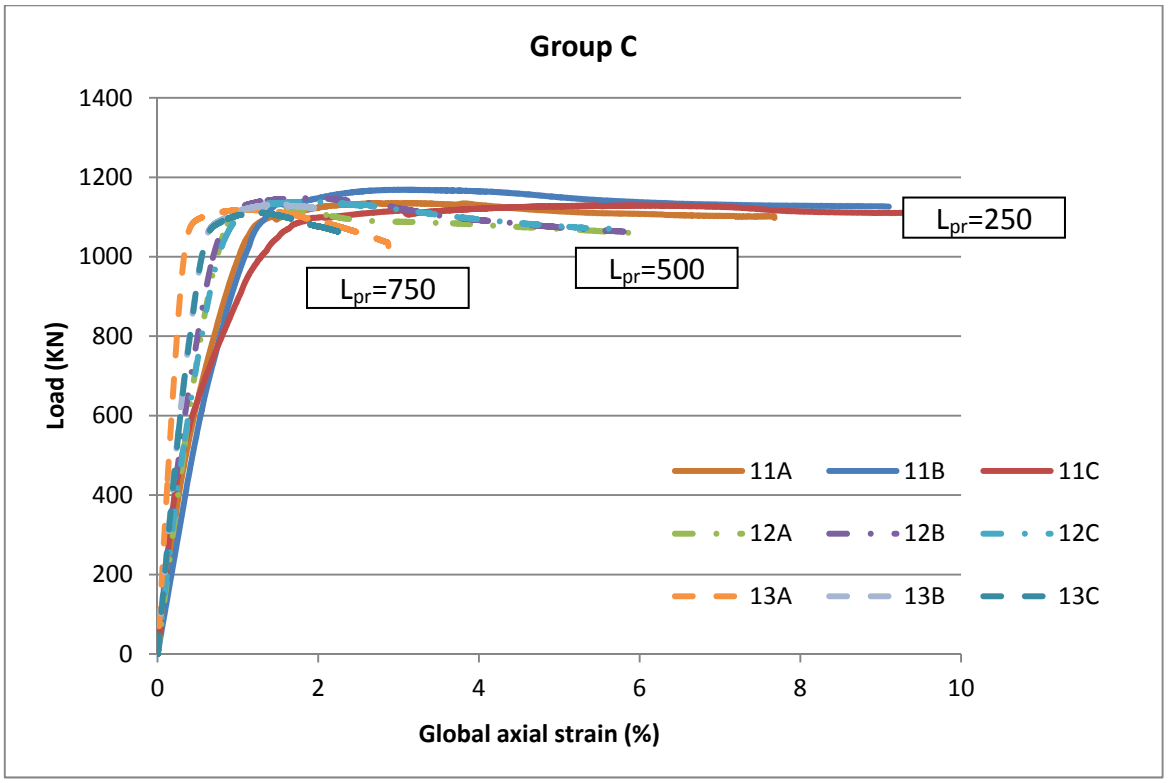

Figure 177: Load/mean-value-of-global-axial-strains relationships

It can be seen from Figure 175 that the stiffness of the ascending curves are only slightly different. However, the stiffnesses are obviously varying for the descending branch. For example, the solid lines in Figure 175 are the test results of specimens GA-1A, GA-1B and GA-1C that have the smallest decreasing slope for their shortest length or height of specimen 250 mm in Group A. When the length increases to 500 mm, the decreasing slope of specimens GA-2A, GA-2B and GA-2C is more rapid. Increasing the length to 750 mm will result in an even more rapid decreasing slope. Hence it can be said that the ascending branches are size independent, whereas, the descending branches are size dependent. Furthermore and very importantly the compressive concrete ductility decreases considerably with increases in height.

Figures 176 and 177 are the load/mean-value-of-global-axial-strains relationships for specimens in Group B and Group C separately that give the similar trends as those shown in Figure 175 for specimens in Group A. In summary:

1. The curves in Figures 175 to 177 are almost identical till the applied load reaches about 40% of peak load which can be defined as a diverging load;
2. Once the loading process passes the diverging point (appropriate 40% of peak load), the ascending curves are slightly more flexible for longer specimens;
3. The descending branch of each curve varies significantly that is decreasing quicker for longer specimens. However it may be worth noting that part of this is due to buckling as discussed in Section 6.1 that is it is not completely a material property.
4. The above two trends can also be combined as that once the loading process passes the diverging point (appropriate 40% of peak load), the variation of global axial

strains due to the varying of lengths is continuing to increase no matter whether in the loading or unloading period.

As discussed in the introduction, the axial size effect expression (Equation 4) can be used to derive the theoretical axial-stress/global-axial-strain relationships from one tested result for confined concrete specimens consisting of both identical concrete and confining steel tube material properties, and where the length of the specimen only varies. So, the mean test result of the 500 mm length specimens for each group is selected to be the base line from which the theoretical results of 250 and 750 mm length specimens are derived and shown in Figures 178 to 180 for Group A, Group B and Group C separately. The mean experimental result for each length of specimen is shown as solid lines in Figures 178 to 180 (Exp. L=750, Exp. L=500 and Exp. L=250) has reasonable correlation with the theoretical results (Theo. L=750 and Theo. L=250); bearing in mind that the stiffnesses of the 750 mm specimens are increased by buckling. More importantly, the theoretical results comply with all of the previous four trends concluded from test results of Figures 175 to 177. It is worthy to note that the test result of any length specimen can be treated as a base line (e.g. L_{pr}=250 mm or 750 mm) and the derived theoretical results still have reasonable correlation with the experimental results and comply with all of the previous four trends concluded from test results of Figures 175 to 177.

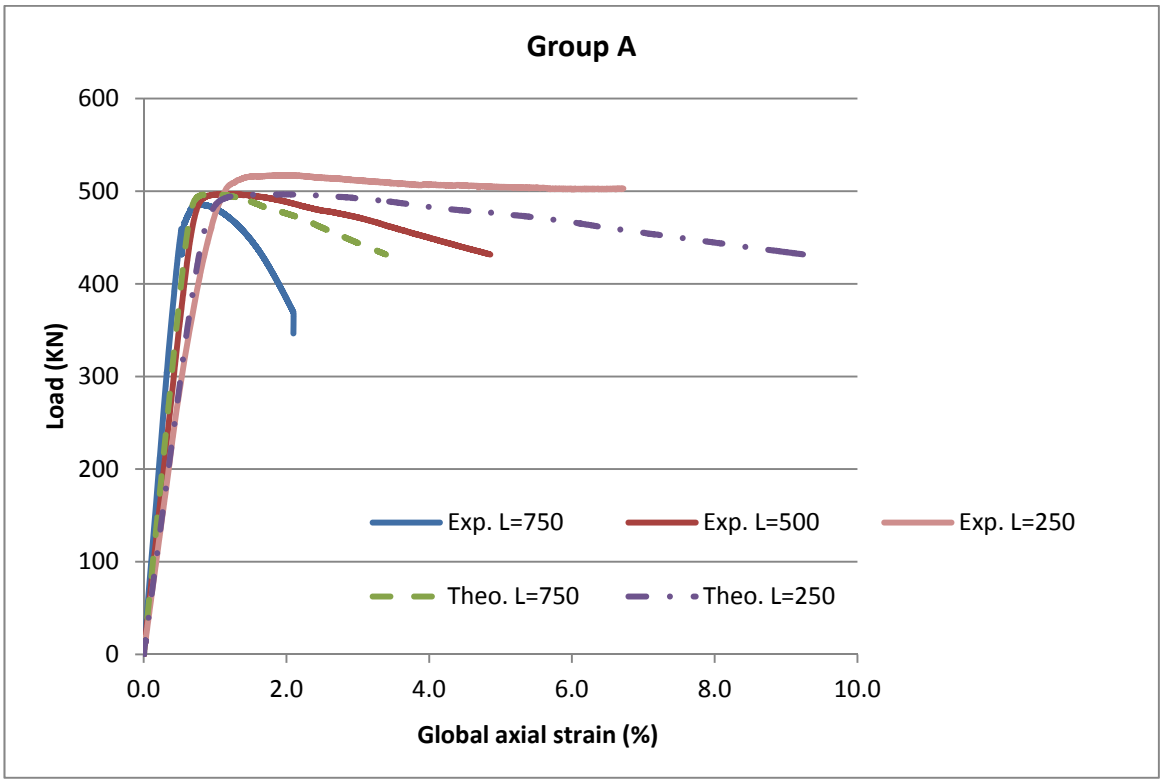

Figure 178: Equation 4 for specimens of Group A

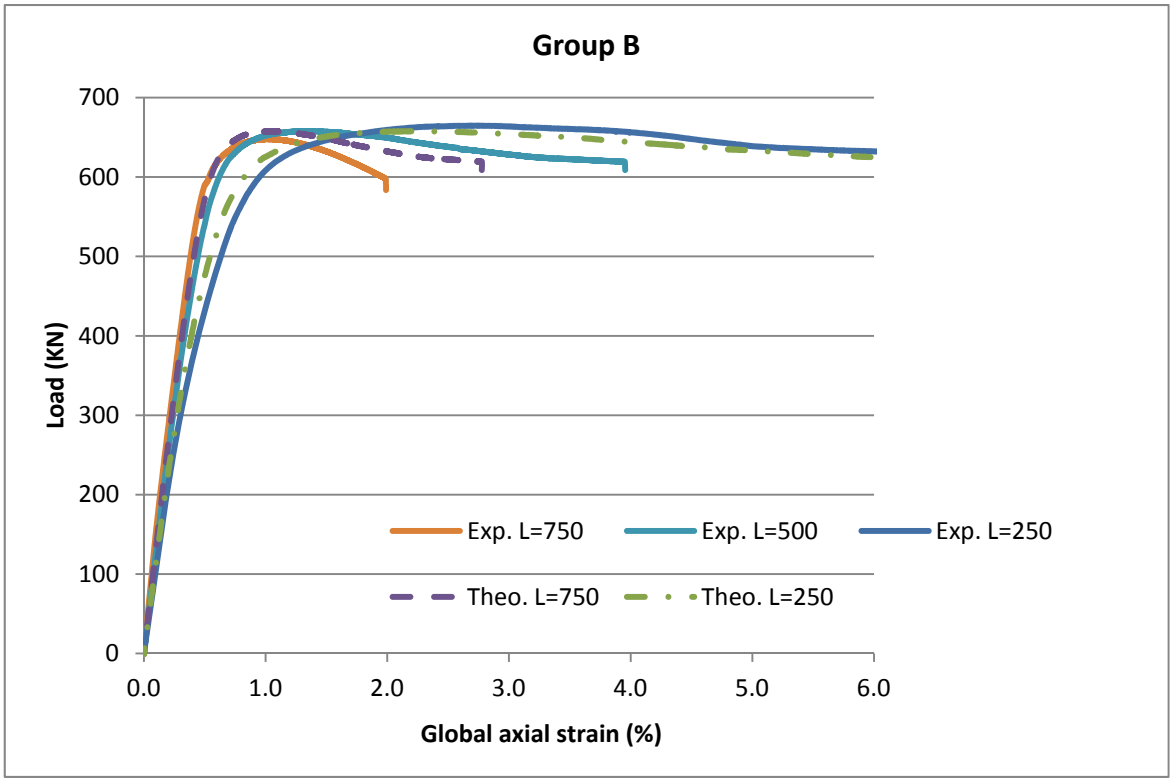

Figure 179: Equation 4 for specimens of Group B

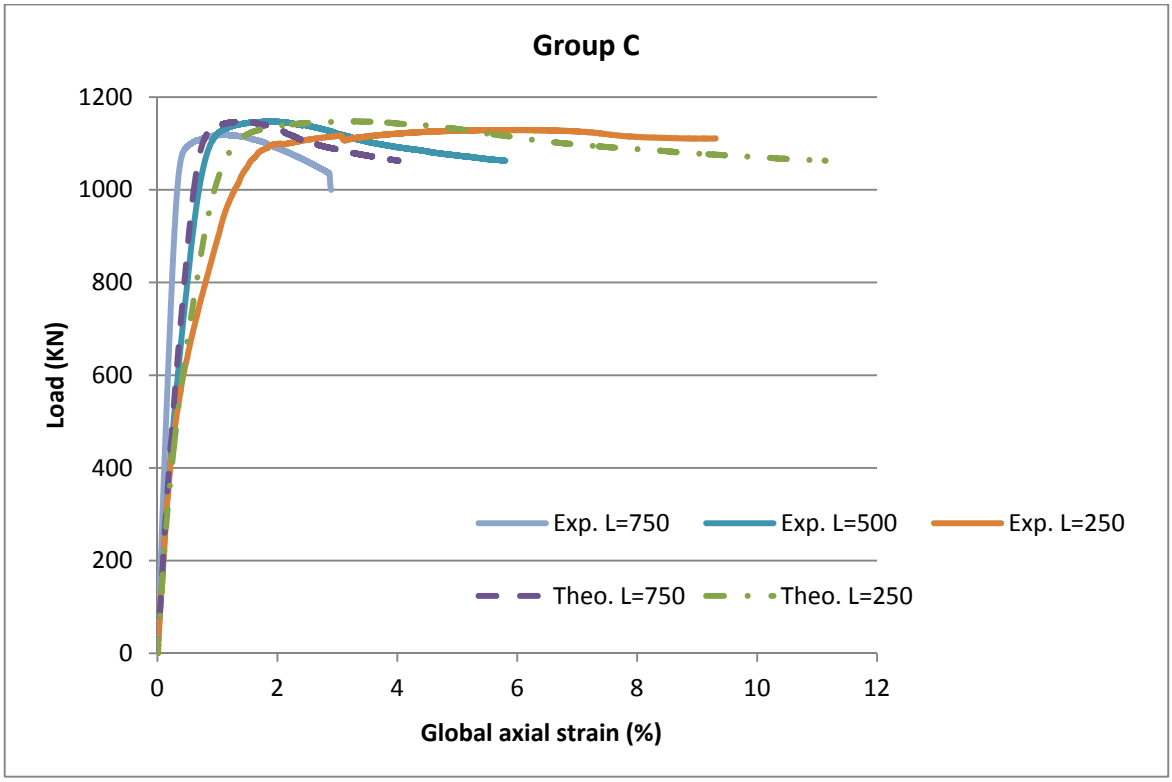

Figure 180: Equation 4 for specimens of Group C

6.3 Lateral size effect

Theoretical analysis in Chapter 4 of this thesis has shown that for specimen 1 with prism diameter d_{pr-1} and thickness of steel tube t_1, specimen 2 with prism diameter d_{pr-2} requires a thickness of steel tube t_2, where t_2 is adopted from Equation 5, to provide the same axial-stress/global-axial-strain relationship as specimen 1. Two groups of test series (Groups D and Group E), whose diameters are varied and lengths are constant in each group, were designed to verify the lateral size effect expression, equation 5, for lateral size of the specimen η_{lat}. The parameter of exponent x in Equation 5 is proposed by Chen et al. (2014d) in Chapter 4 of this thesis and valued at 1.08 in these two groups. For Group D, whose lengths are both 250 mm, and diameter is 101.6 and 114.3 mm, the axial-stress/mean-value-of-global-axial-strain relationships are derived from individual test result of load/global-axial-strain relationship (Figures 88, 96, 99, 116, 124 and 127) and compared in Figure 181. Similarly, the axial-stress/mean-value-of-global-axial-strain relationships for Groups E are shown in Figures 182.

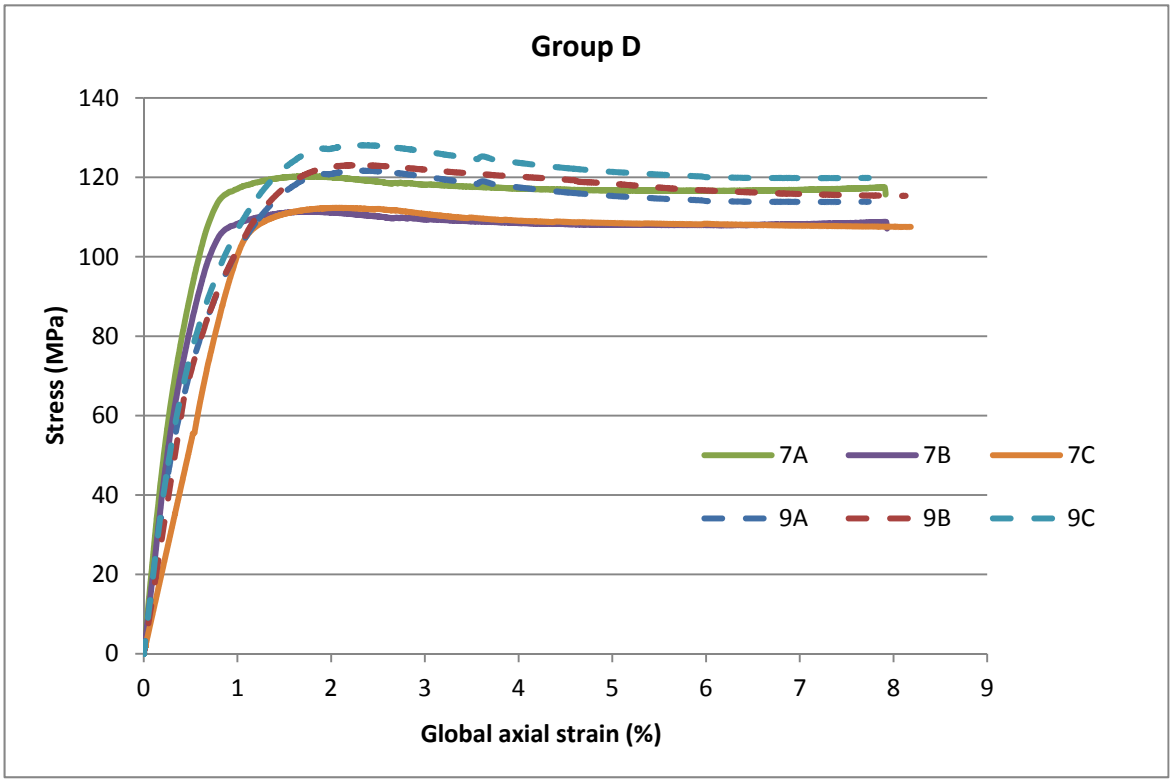

Figure 181: Equation 5 for specimens of Group D

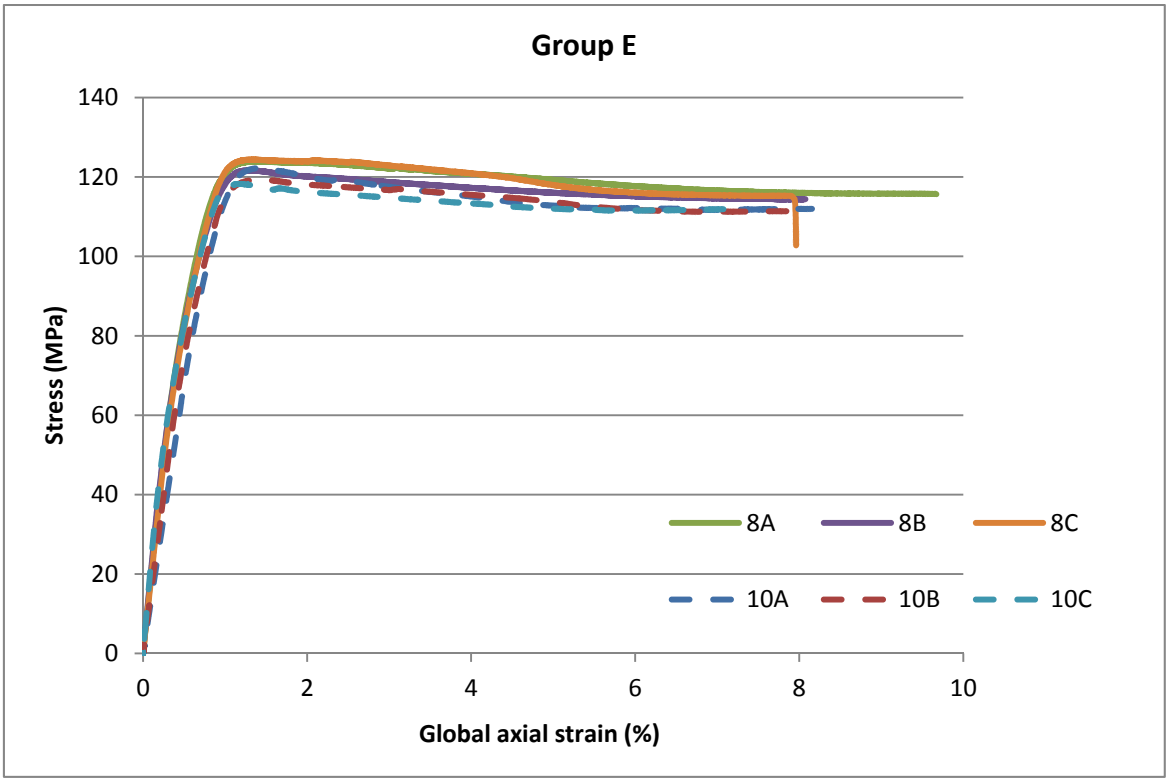

Figure 182: Equation 5 for specimens of Group E

It can be seen from Figures 181 and 182 that the axial-stress/global-axial-strain curves are almost identical for vary the diameters and steel tube thicknesses in which the lateral size effect expression, equation 5 is adopted.

6.4 Sliding angle α

The confinement stress σ_{con} can be calculated by inserting the yield stress of steel tube f_y (column 4 in Table 1) and the thickness of steel tube t (column 6 in Table 1) into Equation 7. Knowing the confinement stress σ_{con}, the theoretical result of sliding angle α_{Theo} can be determined by Equation 6 that is proposed in Chapter 2 of this thesis. These are compared in Table 5 with the experimental results. It can be seen from Figure 183 that except for 3 outliers (specimens GE-8A, GE-8C and GC-13C) the theoretical results α_{Theo} from Equation 6 have a good correlation with the experimental results α_{Exp}. Moreover, except for 3 outliers the statistics of the 35 results in Figure 183 are that mean value of $\alpha_{Theo}/\alpha_{Exp}$ is 103% with a standard derivation of 0.11.

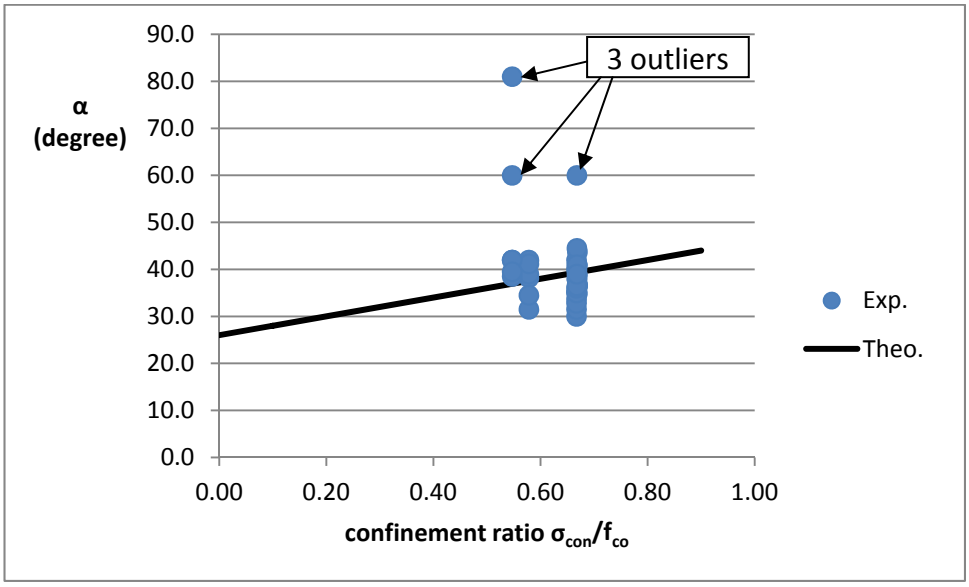

Figure 183: Equation 6

6.5 Wedge effect on global lateral strain

The general information for the specimens attached with lateral strain gauges is shown below in Table 6 where the eight columns show contents as follows in sequence: ①specimen name; ②Figure number; ③middle height of wedge region shown in the photo of Table 5; ④height of maximum lateral strain shown in Table 4; ⑤mean value of lateral strain gauges for the height of column (3) at peak load; ⑥mean value of lateral strain gauges for the height of column (3) at end of tested point; ⑦height of minimum lateral strain shown in Table 4; ⑧mean value of lateral strain gauges for the height of column (6) at peak load; ⑨mean value of lateral strain gauges for the height of column (6) at end of tested point; ⑩ratio of mean lateral strain for different heights at peak load point, column (5) to column (8); ⑪ratio of mean lateral strain for different heights at end of tested point, column (6) to column (9). The mean value of columns ⑤ to ⑥ and ⑧ to ⑪ has been shown in the last row of Table 6. *NA* in the last row of Table 6 means that this mean column value is useless. All the information of above columns ④ to ⑨ can be found in Table 4.

It has been theoretically discussed in Chapter 4 of this thesis that global lateral strain $\varepsilon_{lat\text{-}gbl}$ is composed by three components that are the material dilation strain due to σ_{ax}, the contracting strain caused by confinement stress σ_{con} and the expansion strain due to sliding of the wedge. The individual height shown in columns ③ and ④ of Table 6 agrees well as they are all the corresponding height of the above global lateral strain $\varepsilon_{lat\text{-}gbl}$.

However, the reading of lateral strain gauges that are at the heights of column ⑦ in Table 6 would not include the expansion strain due to sliding of the wedge as it are all attached out of the wedge region. As a result, the global lateral strain within wedge region (contents in columns ⑤ and ⑥ of Table 6) is always much higher than that for out of wedge region (contents in columns ⑧ and ⑨ of Table 6). The mean ratio between them is 4.4 at peak load point and 4.0 at end of tested point that has been shown in column ⑩ and ⑪ of Table 6 respectively.

For example, load/lateral strain relationship of specimen GA-1A (Figure 17) are almost identical on the rising branch for different layers of lateral strain gauges which suggests that the wedge effect on the rising branch can be ignored for all intents and purposes. However on the falling branch they vary considerably. The strain gauge at 150 mm height appears to have captured the wedge and it is about 10 times of those at 50 mm height as shown in column ⑩ and ⑪ of Table 6.

Therefore, the researchers have to capture the wedge to get the correct dilation for use in calculate the right confinement stress which is the key parameter to improve the compressive strength and ductility for confined specimens as discussed in Chapter 2 of this thesis.

Table 6: Wedge effect on global lateral strain

Specimen No.	Figure No.	Within wedge region				Out of wedge region			Ratio at peak load point	Ratio at end of tested point
		Middle height of Wedge region shown in the photo of Table 5 (mm)	Height of maximum lateral strain (mm)	Mean value of lateral strain gauges at this height		Height of minimum lateral strain (mm)	Mean value of lateral strain gauges at this height			
				At peak load point	At end of tested point		At peak load point	At end of tested point		
①	②	③	④	⑤	⑥	⑦	⑧	⑨	⑩	⑪
GA-1A	17	125	150	23459	39941	50	2420	3624	9.7	11.0
GB-4A	49	125	125	14939	31071	50	9807	27633	1.5	1.1
GB-4B	58	150	125	15384	16890	50	4822	4975	3.2	3.4
GB-4C	67	50	50	5216	5141	125	1855	1717	2.8	3.0
GB-7A	93	200	150	14189	34611	50	2408	4117	5.9	8.4
GB-8A	107	100	150	7009	32956	50	1558	15499	4.5	2.1
GB-9A	121	150	200	10412	25046	50	4570	10159	2.3	2.5
GB-10A	135	200	200	4364	22095	50	1299	9932	3.4	2.2
GB-11A	149	150	150	19308	32098	50	3250	16875	5.9	1.9
Mean column value	NA	NA	NA	12698	26650	NA	3554	10503	4.4	4.0

6.6 Failure models of confined concrete

From Table 5, it can be seen that in 28 of the total of 38 test specimens single sliding plane failure occurred; 6 specimens had circumferential wedge failure which were mainly in the short specimens; and 4 had material failure or bending failure due to the slenderness in the long specimens. It can be seen that the failure mode in material test specimens as in Figure 8 that is the circumferential wedge failure and from which most axial-stress/global-axial-strain relationships are developed only occurs in a minority of cases and therefore not fully representative of the behaviour in steel tube confined concrete.

Typically, the standard material test is always adopting small scale 2:1 aspect ratio specimens, as a result the majority of the failure mode in material test specimens is the circumferential wedge failure and from which most axial-stress/global-axial-strain relationships are developed. However, similar to the specimens studied in this test program, the aspect ratio of most practical steel tube confinement columns is more than 2, only occurs in a minority of cases for the circumferential wedge failure. Therefore, the empirical or semi-empirical equations developed from small scale concrete specimens are not truly representative of the actual behaviour of full-scale columns which have aspect ratios markedly different from the 2:1 ratio most commonly tested.

Detailed theoretical analysis for the effect of failure models on global lateral strain and confinement stress can be found in Chapter 4 of this thesis.

6.7 Bond between concrete and steel tube

As the axial size effect expression, Equation 4 and lateral size effect expression, Equation 5 are both derived based on the assumption of ignoring the bond between concrete and confinement material, it was not considered when we designed the test specimens. However, it can be seen from Figure 55 that the mean value of each layer of axial strain gauges for specimen GB-4B varies with height. Generally, the recording of the axial strain gauges attached at middle height (e.g. Local axial strain-125 in Figure 55) is always bigger than that of end positions (e.g. Local axial strain-50 in Figure 55). This phenomenon is very obviously for specimens GB-4A and GB-4C as shown in Figures 45 and 64 respectively.

7. Summary

1. Tests with constant tube diameters and thicknesses but with varying lengths showed that the global axial strain can be assumed to be size independent in the ascending branch but size dependent in the descending branch. The tests clearly showed that as the height of the specimens increased the axial-stress/global-axial-strain ductility reduced rapidly and that the trend was similar to theoretical approaches. The tests also showed that long specimens tended to buckling such that the axial-stress/global-axial-strain relationships were no longer material properties but affected by the moment induced by buckling.
2. In order to develop “equivalent” axial-stress/global-axial-strain relationships for different sized confined concrete specimens, the lateral size effect expression, equation 5 has been proposed in Chapter 4 of this thesis and adopted to apply in this test program. The larger and smaller confined concrete specimens consist of identical

concrete and confining steel tube properties, and where thickness of steel tube only varies as shown specimens 1 and 2 in Figure 1. Once the smaller specimen has been tested and its axial-stress/global-axial-strain curve determined, the proposed size effect expression can be applied to determine the thickness of steel tube required to provide the larger specimen with a axial-stress/global-axial-strain curve similar to the smaller specimen.

3. The proposed expression of sliding angle α that is dependent on the confinement stress and proposed in Chapter 2 of this thesis has a very good correlation with the experimental results.
4. The locally measured axial strain on the tube is significantly smaller than the global axial strain in the concrete and, hence, should not be used to try to quantify the concrete material properties.
5. In average, the global lateral strain within the wedge region is appropriate 4 times bigger than those out of the wedge region. Hence, the researchers have to capture the wedge to get the correct dilation for use in calculate the right confinement stress which is the key parameter to improve the compressive strength and ductility for confined specimens as discussed in Chapter 2 of this thesis.
6. Typically, the standard material test is always adopting small scale 2:1 aspect ratio specimens, as a result the majority of the failure mode in material test specimens is the circumferential wedge failure and from which most axial-stress/global-axial-strain relationships are developed. However, similar to the specimens studied in this test program, the aspect ratio of most practical steel tube confinement columns is more than 2, only occurs in a minority of cases for the circumferential wedge failure. Therefore, the empirical or semi-empirical equations developed from small scale concrete specimens are not truly representative of the actual behaviour of full-scale columns which have aspect ratios markedly different from the 2:1 ratio most commonly tested. Detailed theoretical analysis for the effect of failure models on global lateral strain, confinement stress and behaviour of full-scale columns can be found in Chapter 4 of this thesis.

8. References

American Concrete Institute (1999). “Building code requirements for structural concrete and commentary.” ACI 318-99, Detroit (USA).

American Institute of Steel Construction (1999). “Load and resistance factor design specification for structural Steel buildings.” AISC Specification, Chicago (USA).

Australian Standards AS3600 (1994). “Concrete structures.” Sydney (Australia).

Australian Standards AS4100 (1998). “Steel structures.” Sydney (Australia).

Balmer, G. G. (1949). “Shear strength of concrete under high triaxial stress – Computation of Mohr’s envelope as a curve.” Structural Research Laboratory Roport No. SP-23, Department of the interior bureau of reclamation, United States.

Bellotti, P. R. (1991). “Cylinder tests: experimental technique and results”. Materials and Structures, Vol. 24, 45-51.

Cai, S.H. (2003). “Steel Tube Confined Concrete Structures.” People’s Translation Press [in Chinese].

Candappa, D.P., Sanjayan, J.G., and Setunge, S. (2001), “Complete Triaxial Stress-strain Curves of High-strength Concrete”, Journal of Materials in Civil Engineering, Vol. 13, No. 3, 209-215.

Chen, Y. (2005). “Constitutive Model and Bearing Capacity of Confined Steel Reinforced Concrete Columns with Circular Steel Tube.” Nanjing, China: Southeast University [Masters’ Thesis, in Chinese].

Chen, Y., Visintin, P., Oehlers, D.J., and Alengaram, U. (2014a). “Size-Dependent Stress-Strain Model for Unconfined Concrete.” Journal of Structural Engineering, 140(4), 04013088.

Chen, Y., Visintin, P., and Oehlers, D.J. (2014b). “Concrete shear-friction material properties: derivation from actively confined compression cylinder tests.” Submitted to Advances in Structural Engineering on 26/03/2014.

Chen, Y., Zhang, T., Visintin, P., and Oehlers, D.J. (2014c). “Concrete shear-friction material properties: application to shear capacity of RC beams of all sizes.” Submitted to Advances in Structural Engineering on 26/03/2014.

Chen, Y., Visintin, P., and Oehlers, D.J. (2014d). “Closed-form solution of FRP confined cylinders using the shear friction mechanism.” To be submitted to Journal of Southeast University.

Chinese Standards GB50010 (2010). “Code for design of Concrete structures.” Beijing (China).

Gardner, N. J. (1969). “Triaxial behaviour of concrete”. ACI Journal, Title no. 66-15, 136-146.

Giakoumelis, G., and Lam, D. (2004). “Axial capacity of circular concrete-filled tube columns.” Journal of Constructional Steel Research, Vol. 60, No. 7, pp 1049–1068.

Han, L.H. (2007). “Concrete-filled steel tubular structures theory and practice.” Beijing, China: Science Press [in Chinese].

Harmon, T.G., Ramakrishnan, S. and Wang, E.H. (1998), “Confined concrete subjected to uniaxial monotonic loading”, Journal of Engineering Mechanics, Vol. 124, No.12, 1303-1309.

Hatzigeorgiou, G. D. (2008). “Numerical model for the behavior and capacity of circular CFT columns, Part I: Theory.” Engineering Structures, Vol. 30, No. 6, pp 1573–1578.

Huang, C. S., Yeh, Y. K., Hu, H.T., Tsai, K. C., Weng, Y. T., and Wang, S. H. (2002). “Axial load behavior of stiffened concrete-filled steel columns.” Journal of Structural Engineering, Vol. 128, No. 9, pp 1222–1230.

Imran, I., and Pantazopoulou, S. J. (1996). “Experimental Study of Plain Concrete under Triaxial Stress”. ACI Materials Journal, Vol. 93, No. 6, 589-601.

Jamet, P., Millard, A., and Nanas, G. (1984). “Triaxial behaviour of a Micro-concrete Complete Stress-Strain Curves for Confining Pressures Ranging From 0 to 100 MPa”. GIF SUR YVETTE CEDEX (France), Title no. 91191, 133-140.

Jiang, T., Teng, J. G. (2007). “Analysis-oriented stress-strain models for FRP confined concrete”. Engineering Structures, Vol. 29, No. 11, pp. 2968-2986.

Kotsovos, M. D. and Newman J. B. (1978). “Generalised stress-strain relations for concrete”. Journal of the Engineering Mechanics Division, ASCE, Vol. 104, No. EM4, pp. 845-856.

Kotsovos, M. D. and Newman J. B. (1979). “A mathematical description of the deformational behaviour of concrete complex loading”. Magazine of Concrete Research, Vol. 31, No. 107, pp. 77-90.

Lahlou, K., Aitcin, P. C. and Chaallal, O. (1992). “Behaviour of high-strength concrete under confined stresses”. Cement and Concrete Composites, 14, 185-193.

Lu, X. B., and Hsu, C. T. (2006). “Behavior of high strength concrete with and without steel fiber reinforcement in triaxial compression”. Cement and Concrete Research, 36, 1679-1685.

Richart, F. E., Brandtzaeg, A., and Brown, R. L. (1928). “Study of the Failure of Concrete under Combined Compressive Stresses,” Bulletin 185, University of Illinois Engineering Station, Urbana.

Richart, F. E., Brantzaeg, A., and Brown, R. L. (1929). “The failure of plain and spirally reinforced concrete in compression”. Bulletin No. 185, Engineering Experiment Station, University of Illinois, Urbana.

Sakino, K., Nakahara, H., Morino, S., and Nishiyama, I. (2004). “Behavior of centrally loaded concrete-filled steel-tube short columns.” Journal of Structural Engineering, Vol. 130, No. 2, pp 180–188.

Schneider S. P. (1998). “Axially loaded concrete-filled steel tubes.” Journal of Structural Engineering, Vol. 124, No. 10, pp 1125–1138.

Setunge, S., Attard, M. M., and Darvall, P. (1993). “ultimate strength of confined very high strength concrete”. ACI, Structure Journal, 90(6), 632-641.

Shanmugam, N. E., & Lakshmi, B. (2001). “State of the art report on steel–concrete composite columns.” Journal of Constructional Steel Research, Vol. 57, No. 10, pp 1041-1080.

Sfer, D., Carol, I., Gettu, R. and Etse, G. (2002). “Study of the behaviour of concrete under triaxial compression”. Journal of Engineering Mechanics, Vol. 128, No.2, 156-163.

Smith, S. S., William, K. J., Gerstle, K. H., and Sture, S. (1989). “Concrete over the top, or is there life after peak?”. ACI Materials Journal, Vol. 86, No. 5, 491-497.

Teng, J. G., Hu, Y. M., and Yu, T. (2013). “Stress–strain model for concrete in FRP-confined steel tubular columns.” Engineering Structures, Vol. 49, pp. 156-167.

Visintin, P., Chen, Y., and Oehlers, D.J. (2014). “Size dependent axial and lateral stress strain relationships for actively confined concrete.” Accepted for publication by Advances in Structural Engineering on 05/06/2014.

Xiao, Q. G., Teng, J. G., and Yu, T. (2010), “Behavior and Modeling of Confined High-strength Concrete”, Journal of Composites for Construction, Vol. 14, No. 3, pp 249-259.

Chapter 6: Concluding Remarks

This thesis details the extensive progress that has been made towards the shear-friction properties and size effect for the shear failure of concrete specimens. The following conclusions can be made:

1. Concrete under compression undergoes axial contractions and lateral expansions both due to material straining and the shear friction mechanism of wedge sliding. Since the shear friction properties which control wedge sliding are independent of size, for any size specimen this non-material deformation due to sliding is constant, while the material deformation scales with size. Hence it is this non material deformation which is responsible for both axial and lateral strain size dependency.

2. By separating the size independent and size dependent components of the deformation, it is possible to derive size dependent stress-strain relations for unconfined or confined concrete from tests using one specimen size and to derive the dilatory deformation directly from the axial deformation. This should considerably reduce the amount of testing required for new concretes as only one size of specimen needs be tested to obtain stress-strain relationships for all sizes.

3. The shear-friction material properties at all load levels can be derived from relatively inexpensive actively confined concrete compression cylinder tests. This should expedite the development of new types of concrete as large amounts of relatively expensive forms of testing such as the use of shear-sliding tests are no longer required.

4. The derived shear-friction material properties can be used directly to quantify the shear-sliding capacity and also can be used to analyse standard shear-sliding tests in order to extract more accurate shear-sliding capacities.

5. The shear friction approach is capable of predicting the response of specimens failing with either a circumferential wedge or a single sliding plane and hence can simulate, through mechanics, the dependency of the passively confined stress strain response on slenderness. Furthermore, the approach can be applied to specimens with any type of concrete or any type of FRP wrap provided the shear friction properties are known.

6. The proposed axial and lateral size expressions should enhance the value or usefulness of testing FRP confined cylinders as in theory the results from a single test can be adapted to apply to a wide range of shapes and sizes.

7. The standard material test always adopts small scale 2:1 aspect ratio specimens, as a result the majority of the failure modes in material test specimens is the circumferential wedge failure and from which most axial-stress/global-axial-strain relationships are developed. However, the aspect ratio of most practical steel tube confinement columns is more than 2. Hence only in a minority of cases does the circumferential wedge failure occur. Therefore, the empirical or semi-empirical equations developed from small scale concrete specimens are not truly representative of the actual behaviour of full-scale columns which have aspect ratios markedly different from the 2:1 ratio most commonly tested. Hence, it is suggested that, as in practice, members have a slenderness ratio greater than two. There is a need for empirical research to shift focus to experiments on slender specimens and in which the total axial deformation is measured.

Suggested Future Research

1. Though there has been much experimental research on quantifying the angle α of the sliding plane, a strict and consistent measurement process is still required to ensure that different researchers can reach an identical angle value for a given failure specimen.

2. The size and strength of aggregate is an important factor in shear-friction behaviour that should be quantified.

3. No matter what kind of confinement material, the bond is always an important factor to the shear-friction behaviour of confined concrete that should be quantified.

4. For steel tube confined concrete, the buckling of steel tube must be considered as it leads to longitudinal stress distribution and also impact the confinement depending on the direction of the buckling.